2018

Repairable Precast Buildings and Bridges

Abdullah Boudaqa
South Dakota State University

REPAIRABLE PRECAST BUILDINGS AND BRIDGES

BY

ABDULLAH BOUDAQA

A dissertation submitted in partial fulfillment of the requirements for the

Doctoral of Philosophy

Major in Civil Engineering

South Dakota State University

2018

REPAIRABLE PRECAST BUILDINGS AND BRIDGES

This dissertation is approved as a creditable and independent investigation by a candidate for the Doctoral of Philosophy in Civil Engineering Degree and is acceptable for meeting the thesis requirements for this degree. Acceptance of this thesis does not imply that the conclusions reached by the candidates are necessarily the conclusions of the major department.

Mostafa Tazarv, Ph.D., P.E.
Thesis Advisor
Civil and Environmental Engineering Date

Nadim Wehbe, Ph.D., P.E.
Department Head
Civil and Environmental Engineering Date

Kimchel C. Doerner, Ph.D.
Dean, Graduate School Date

To my mother, Wafaa Shaban, the strongest and most wonderful woman in the world who raised 10 successful children without complaints. This success story would not have been accomplished without her endless support and priceless encouragement.

This dissertation is also dedicated to all my family members who supported me unconditionally.

ACKNOWLEDGEMENTS

First, I would like to express my gratitude and appreciation to Dr. Mostafa Tazarv for his priceless guidance, amazing mentorship, and patience. His experience and knowledge have brought me a great educational experience. This paper would not have been completed without him.

I also wish to extend my thanks to Dr. Nadim Wehbe and Dr. Suzette Burckhard for their contribution and support.

Special thanks to Zachary Gutzmer and all my fellow graduate students, Ishtiaque Tuhin, Locus Bohn, Zachary Carnahan, Sandip Rimal, and Puskar Dahal for their assistance throughout this research.

I also owe a debt of gratitude to my friends, Ali Al-Qubbej, Hussein Aboamara, Amine Radoui, Abdelrahman Mohsen, and Mohammad Badawi for making my life easier during this journey.

Finally, I would like to thank my family, specifically my brother Mohammed, for all the encouragement, support, and love they have for me.

TABLE OF CONTENTS

LIST OF FIGURES

LIST OF TABLES

ABSTRACT

REPAIRABLE PRECAST BUILDINGS AND BRIDGES

ABDULLAH BOUDAQA

2018

A new moment-resisting precast connection is developed in the present work through experimental and analytical studies to accelerate construction of bridges and buildings, to improve their seismic performance, and to quickly repair them through replacement of exposed reinforcement. The new precast joint detailing incorporates (1) detachable external reinforcing steel bars restrained against buckling, which is referred to as buckling restrained reinforcement (BRR), to develop plastic bending moments, (2) a steel pipe connecting the precast members through a pin connection to resist plastic shear forces, and (3) detachable mechanical bar splices to assemble and disassemble BRR at any time specifically after server event as a quick repair method. Feasibility and performance of a new type of BRR that can be used as detachable external reinforcing steel bars, were experimentally investigated. Furthermore, a simple design method for BRR with or without a section modification (e.g. dog-bone) is presented to further help engineers with the design of external reinforcement and energy dissipaters. The seismic performance of the proposed repairable precast connections was investigated through cyclic testing of four half-scale beam-column specimens detailed based on a nine-story building designed for Los Angeles, which is a high seismic region. A reference cast-in-place beam-column specimen was also included for comparison. The test results showed

that the repairable precast connections can withstand more than fourteen times the design level earthquake with insignificant damage and ability to be repaired afterward. Furthermore, a comprehensive analytical study including pushover and nonlinear response history analyses was performed to investigate the seismic performance of three-, six-, and nine-story repairable precast and cast-in-place (CIP) buildings, and repairable precast bridge columns. It was found that the stiffness of the proposed precast system is 60% of conventional cast-in-place structures but the displacement capacity of the proposed precast structures can be four times higher than that in the conventional structures. The increase in the displacement demands of the precast systems due to lower initial stiffness is usually within the design limits and there is no need to increase the member sizes. Based on the construction, and experimental and analytical studies, it can be concluded that the proposed precast connection detailing is expected to improve the seismic performance of bridges and buildings, to expedite the construction, and to eliminate the need of structure total replacement after severe earthquakes since the repair is done by replacement of exposed bars.

Chapter 1: Introduction

1.1 Introduction

A new precast reinforced concrete (RC) connection is developed in the present work through experimental and analytical studies to accelerate construction of bridges and buildings, to improve their seismic performance, and to quickly repair them through replacement of exposed reinforcement. A summary of the findings of the literature review, the research objectives, and the dissertation outlines are presented in this chapter.

1.2 Backgrounds and Applications

The proposed precast connection detailing (Ch. 3) incorporates a few components that have been developed in previous studies. This section presents a summary of the related literature utilizing these components.

1.2.1 Hybrid Rocking Systems

Figure 1-1 shows the hysteretic behavior for conventional and rocking columns. A rocking system includes structural elements (e.g., columns, walls, beam-column joints) that swing on rocking surfaces and return to their original positions (self-centering behavior) usually using post-tensioning tendons. This system, simple rocking system, usually dissipates very low energy during lateral displacements (Fig. 1-1b). Internal or external energy dissipaters are added to rocking systems to improve the energy

dissipation and to reduce lateral displacement demands. A hybrid rocking system includes two types of reinforcement, one to increase self-centering, and one to dissipate energy.

It can be seen in Fig. 1-1a that a conventional column shows wide hysteretic loops with high energy dissipation and usually large residual displacements. Large energy dissipation of conventional RC columns is due to the yielding of longitudinal reinforcement. A simple rocking column exhibits self-centering behavior, but large lateral displacement demands under lateral excitation such as earthquakes (Fig.1-1b). When energy dissipaters are added to simple rocking columns (hybrid rocking columns), the displacement demands are reduced but the self-centering behavior will be preserved as shown in Fig. 1-1c.

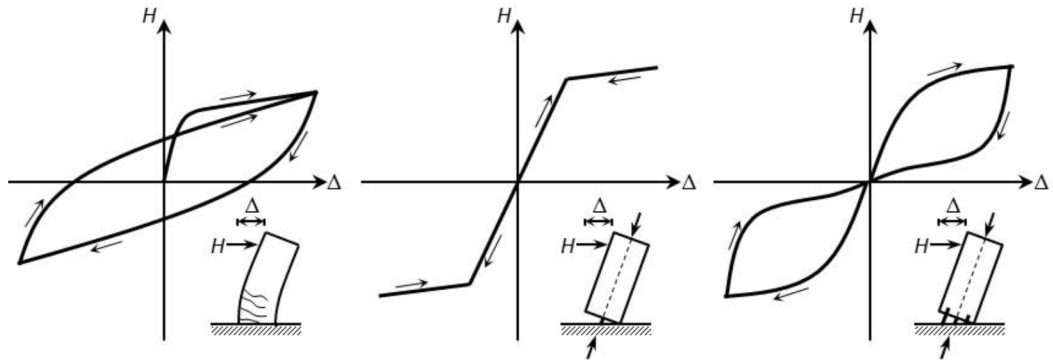

(a) Conventional Detailing (b) Simple Rocking (c) Hybrid Rocking

Figure 1-1. Hysteretic Behavior of Conventional and Rocking Columns (Guerrini et al., 2015)

Energy dissipation of hybrid rocking columns can be provided using internal dissipaters (longitudinal reinforcement in Fig. 1-2a) or external energy dissipaters (Fig. 1-2b).

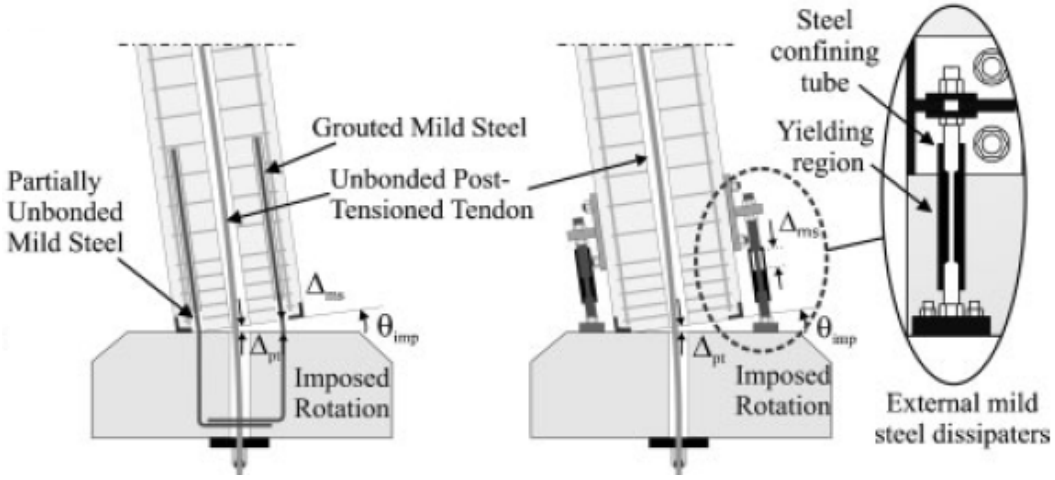

(a) Internal Dissipater (b) External Dissipater

Figure 1-2. Energy Dissipaters in Hybrid Rocking Columns (Marriott et al., 2011)

1.2.2 Buckling Restrained Reinforcement (BRR)

When external energy dissipaters are used in hybrid rocking structures, the bar has to be either restrained against buckling or free in compression (tension-only member). Otherwise, it will fail by low cycle fatigue. Most exciting anti-buckling fuses (Fig. 2b) consist of dog-bone shape steel or aluminum bars encased in steel tubes. Grout or epoxy are usually used to fill the gap between the bar and the tube. Buckling restrained reinforcement with dog-bone shape steel core has been used in all previous studies as external energy dissipaters. Chapter 2 of this dissertation is dedicated to buckling restrained reinforcement (BRR).

1.2.3 Bar Coupler connections

To assure continuity in reinforced concrete members, reinforcing steel bars must be spliced, which is done by either lap splicing (Fig. 1-3a), overlapping two adjoining reinforcement bars, or using mechanical bar splices (Fig. 1-3b). Mechanical bar splices can reduce the length and width of the splice compared to conventional lap splicing.

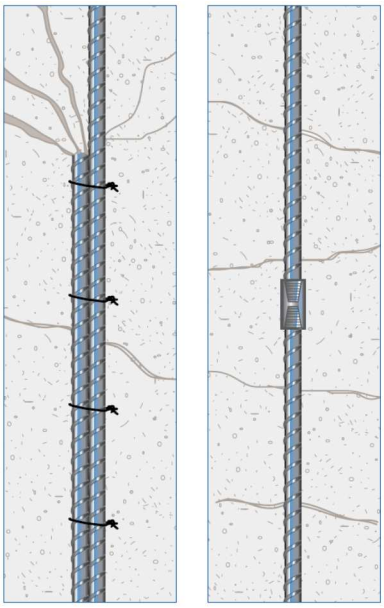

a) Lap Splicing b) Mechanical Bar Splicing

Figure 1-3. Illustration of Lap and Mechanical Splicing (Lenton, 2017)

The use of mechanical bar splice (which is usually referred to as couplers) has multiple advantages such as:

- Reduction of bar congestion in joints.
- Improvement of loading path and structural integrity since connected bars are acting as a continuous bar.
- Acceleration of construction when couplers are used in precast member connections.
- Splicing of large-size reinforcing steel bars (No. 14 and No. 18). Lap splicing for these bars is prohibited.

There are different coupler types available in the US market. A few of which are shown in Fig. 1-4. Based on Tazarv and Saiidi (2015), couplers can be generally grouped in five categories: 1) shear screw coupler, 2) headed bar coupler, 3) grounded sleeve coupler, 4) threaded coupler, and 5) swaged coupler.

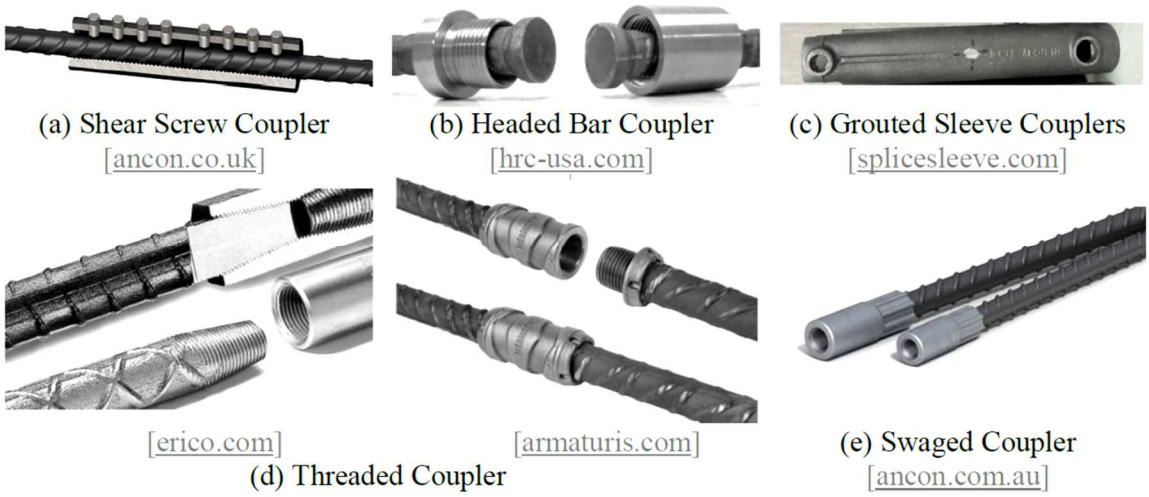

Figure 1-4. Diferent Types of Mechanical Bar Splices (Tazarv and Saiidi, 2015)

1.2.4 Pipe-Pin Connections

Pipe-pin hinges are used in concrete structures to provide shear resistance and to eliminate moment (Fig. 1-5). This hinge usually consists of a heavy-duty steel pipe embedded in one element (e.g., bridge column) and extended into the adjacent element (e.g., bridge bent cap or footing) where a steel cup is embedded. The hinge mechanism can be achieved by providing a gap between the pipe and the cup. This gap allows rotation of the pipe inside the cup. Note that long pipes and minimal gaps will lead to dual curvature deformations for the pipe making the joint partially fixed.

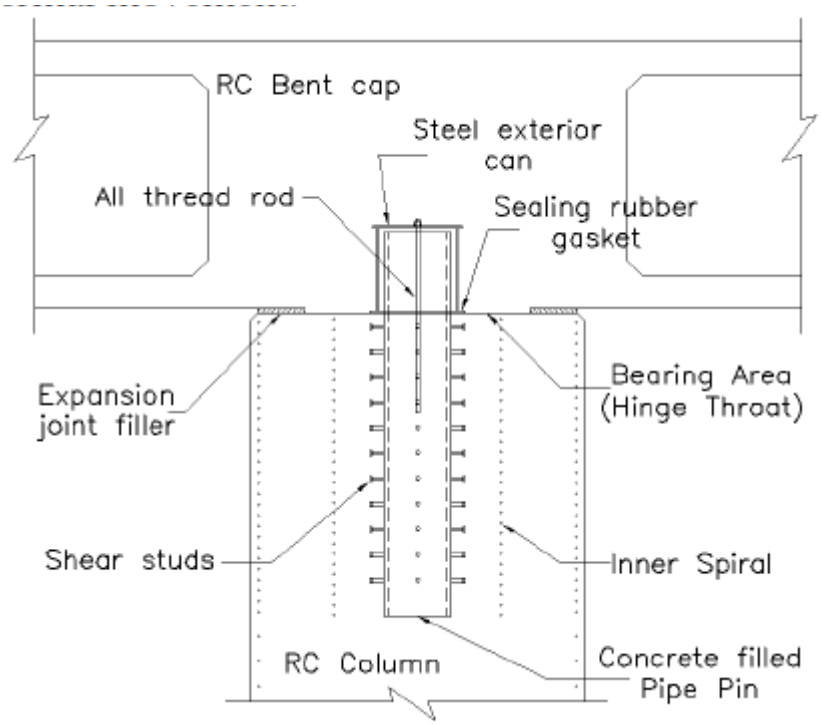

Figure 1-5. Pipe-Pin Detail (Zaghi and Saiidi, 2010)

Shear forces is transferred when the pipe and the cup are in contact. Although current design codes do not have any specific provisions for shear pipe-pin design, Zaghi and Saiidi (2010) investigated the seismic performance of pipe-pin hinges through extensive experimental and analytical studies and developed design guidelines.

1.2.5 Shape Memory Alloy (SMA) Reinforcing Bar

Steel is considered as one of the most used material in civil engineering. Reinforcing steel bars are used in concrete structure to resist tensile stresses since concrete has negligible tensile strength. Using steel as reinforcing concrete material has major setbacks since steel experiences large permanent deformation after yielding. In addition, steel in vulnerable to corrosion and fatigue. New materials are emerging to overcome these problems.

One of the new materials that can replace steel is shape memory alloys (SMA). SMA is a class of metallic material that has a unique ability to undergo large plastic strains and recover its original shape upon heating (shape memory effects) or unloading (superelastic effect). SMA is superelastic at any temperature above the austenite finish temperature, A_f, (Brinson, 1993).

There are several alloys that falls under SMA calcification but most of the previous studies were focused on Nickel-Titanium (NiTi) SMA. NiTi SMA consists of equal weight portion of Nickel and Titanium and considered as the most desirable SMA for structural application due to its high superelastic properties and its high resistance to corrosion and fatigue. Figure 1-6 shows the stress-strain relationship for No. 10 NiTi SMA and steel bars. It can be seen that a NiTi SMA bar exhibits negligible residual strains even after a 6% strain cycle while the residual strains of a steel bar are significant.

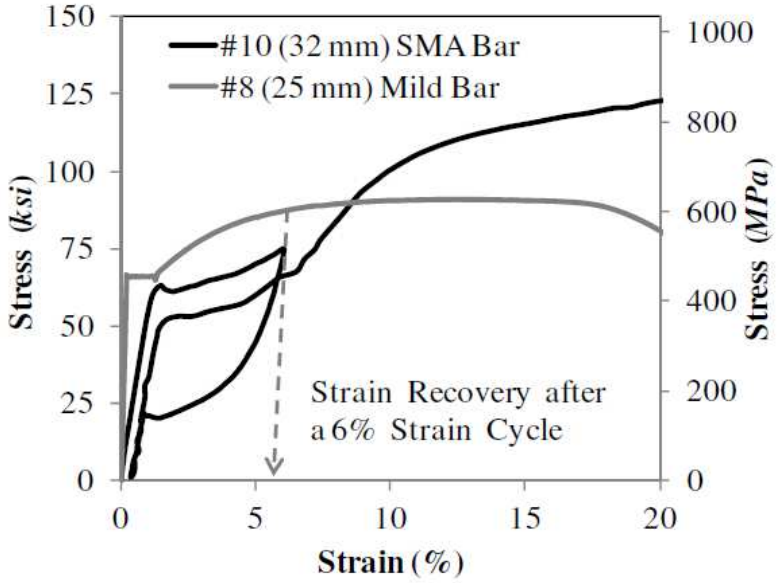

Figure 1-6. Stress-Strain Relationship for No.10 NiTi SMA and Steel Bars (Tazarv and Saiidi, 2014)

Tazarv and Saiidi (2014) developed a material model for reinforcing SMA bars (Fig. 1-7 and Table 1-1) and proposed design values. The main mechanical properties were defined, according to Tazarv and Saiidi (2014), as:

- Observed yield strength (f_{yo}) is the stress at the initiation of nonlinearity on the first cycle of loading to the upper plateau.
- Austenite modulus (k_1) is the average slope between 15 to 70% of f_{yo}.
- Post yield stiffness (k_2) is the average slope of curve between 2.5% and 3.5% of strain on the upper plateau of the first cycle of loading to 6% strain.
- Austenite yield strength (f_y) is the stress at intersection of line passing through origin with slope of k_1 and line passing through stress at 3% strain with slope of k_2.
- Lower plateau inflection strength (f_i) is the stress at the inflection point of lower
- Plateau during unloading from the first cycle to 6% strain.
- Lower plateau stress factor, $\beta = 1 - (f_i/f_y)$.
- Residual strain (ε_{res}) is the tensile strain after one cycle to 6% and unloading to 1 *ksi* (7 *Mpa*).
- Recoverable superelastic strain (ε_r) is maximum strain with at least 90% strain recovery capacity ($\varepsilon_r \leq 6\%$).
- Martensite modulus (k_3) is the slope of the curve between 8 to 9% strain, subsequent to one cycle of loading to 6% strain, unloading to 1 *ksi* (7 *MPa*) and reloading to the ultimate stress.
- Secondary post-yield stiffness ratio, $\alpha = k_3/k_1$.
- Ultimate strain (ε_u) is strain at failure.

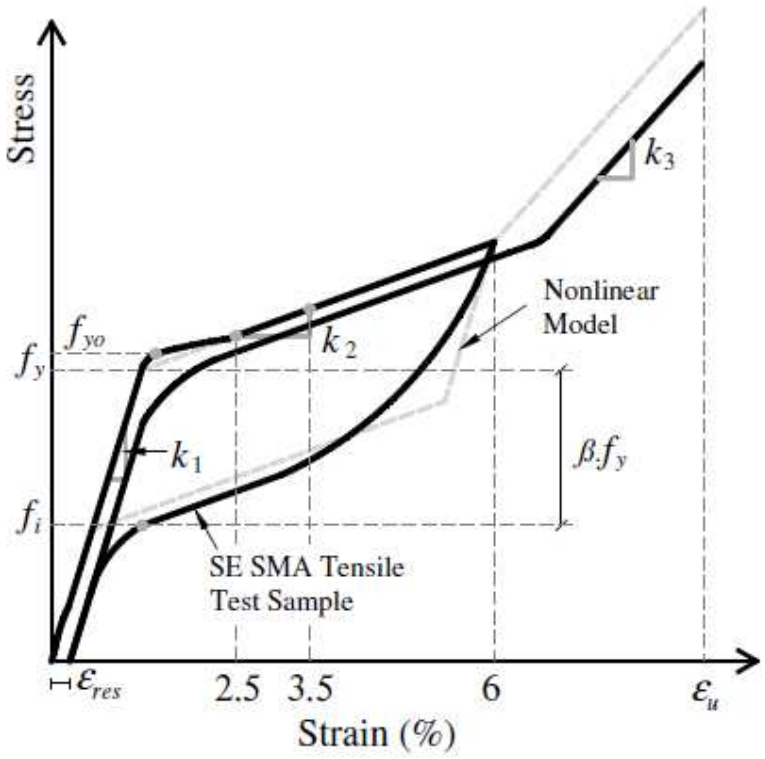

Figure 1-6. NiTi SMA Nonlinear Model (Tazarv and Saiidi, 2014)

Table 1-1. Expected Tensile NiTi SMA Mechanical Properties

Specimen ID	Bar No. (mm)
Austenite modulus, k_1	5500 ksi (37900 MPa)
Post yield stiffness, k_2	250 ksi (1725 MPa)
Austenite yield strength, f_y	55 ksi (380 MPa))
Lower plateau stress factor, β	0.65
Recoverable superelastic strain, ε_r	6%
Secondary post-yield stiffness ratio, α	0.3
Ultimate strain, ε_u	10%

1.2.6 Past Studies on Beam-Column Joints

Several studies have investigated the behavior of beam-column connections under cyclic loading. Most of these studies were specifically focused on the joint detailing and behavior thus only few of which successfully included the actual boundary conditions in the test. A summary of selected studies on beam-column connection behavior is reviewed herein to better understand the performance of beam-column connection during

lab testing and to adapt the ideal boundary condition for exterior beam-column connection.

1.2.6.1 Study by Ehsani and Wight (1985)

Six beam-column connections were tested under cyclic loading by Ehsani and Wight (1985). Figure 1-7 shows the setup used to test all beam-column connections. The test variables were (1) flexural capacity, (2) joint shear stresses, and (3) the transverse reinforcement. The following findings were concluded: a column to beam flexural strength ratio of 1.4 and higher eliminates the plastic hinge formation in the connection, a shear stress of $12\sqrt{f_c'}$ (psi) or lower significantly improve the connection behavior, and additional transverse reinforcement enhances the general connection behavior.

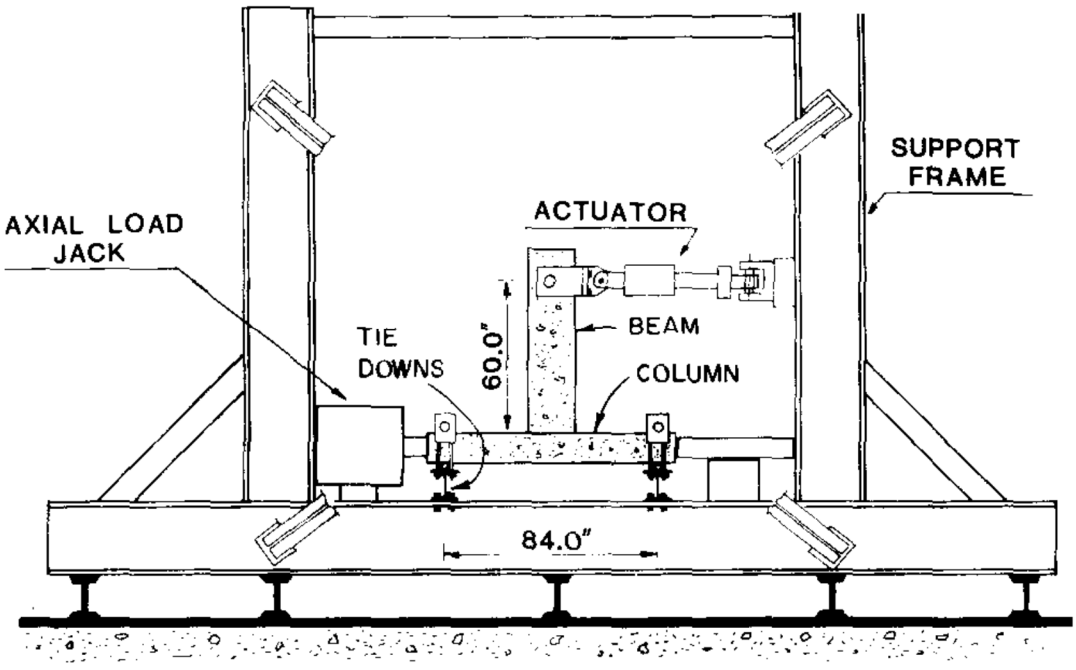

Figure 1-7. Beam-Column Test Setup used in Ehsani and Wight (1985)

1.2.6.2 Study by Ehsani et al. (1987)

Four exterior beam-column connections incorporating both normal strength concrete (NSC) and high strength concrete (HSC) were tested under cyclic loading by Ehsani et al. (1987). The study (Fig. 1-8) concluded that the connections with HSC provides sufficient ductility and comparable hysteretic response to the connections with NSC. Another finding was that large displacement capacities can be achieved for specimens with high beam to column flexural strength ratio and low joint shear stresses.

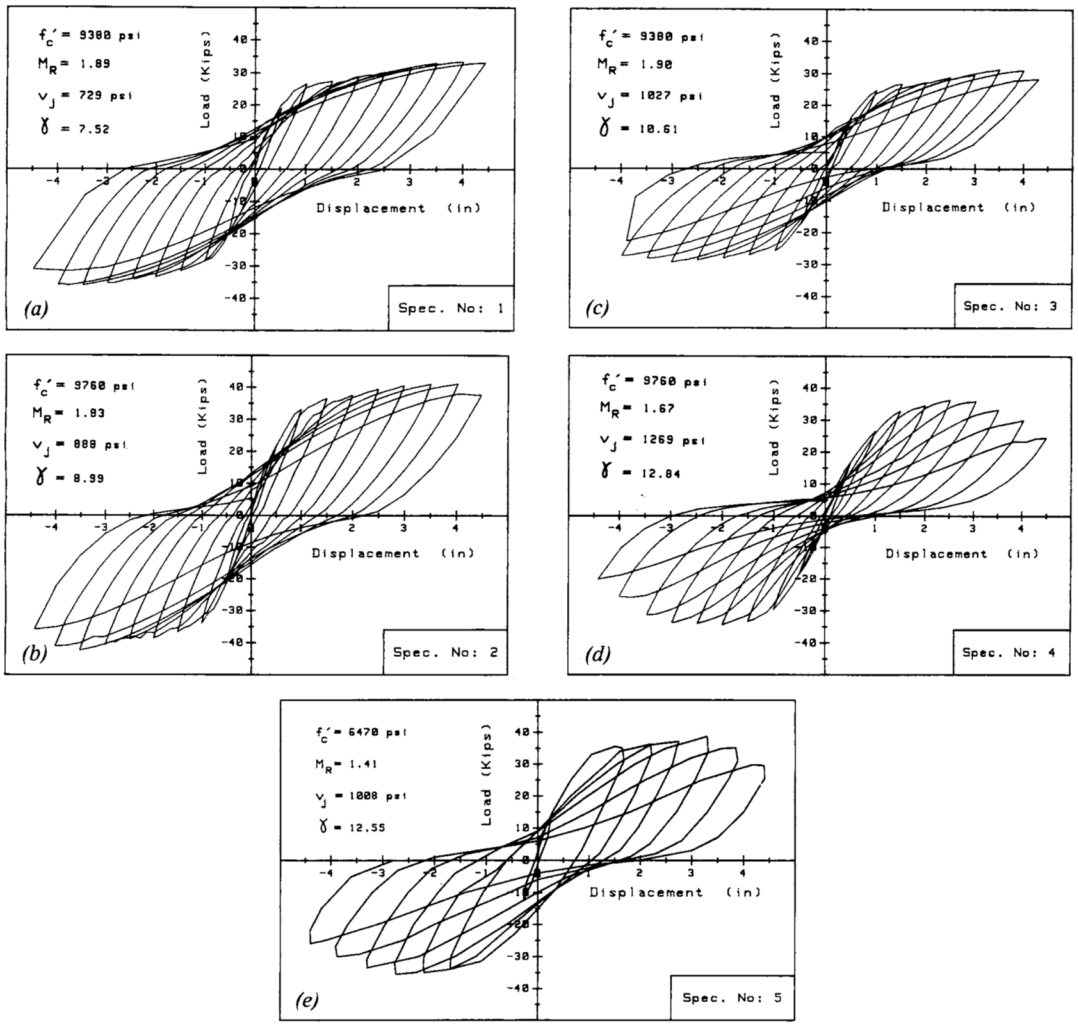

Figure 1-8. Force-Diplacement Relationships of Beam-Column Specimens (Ehsani et al., 1987)

1.2.6.3 Study by Joh et al. (1991)

Joh et al. (1991) investigated the bond deterioration of beam reinforcement through testing two RC beam-column connections. Figure 1-9 shows the test setup. The study found that the connections with sufficient transverse reinforcement exhibit minimal bond-slip effects. Another conclusion was that the bond deterioration can be prevented by shifting the plastic hinge regions away from the column face.

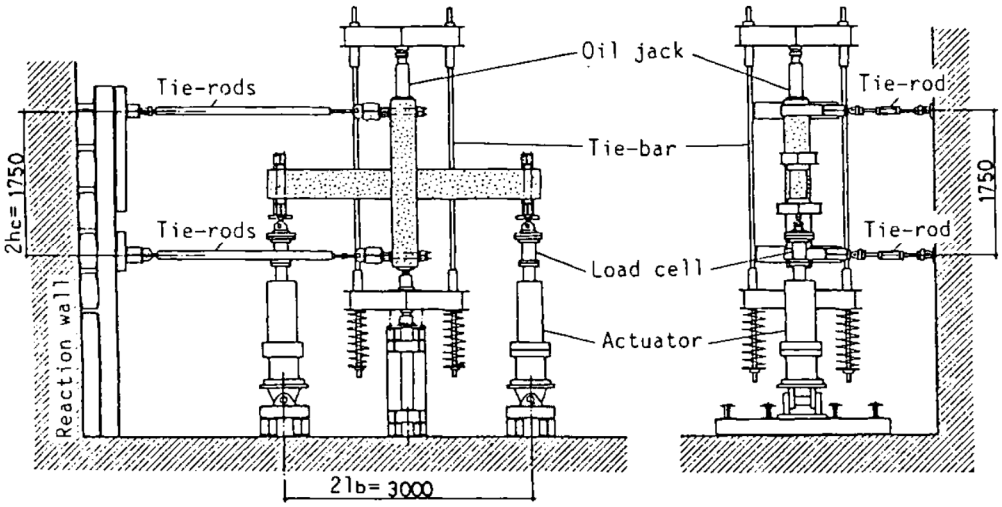

Figure 1-9. Beam-Column Test Setup used in Joh et al. (1991)

1.2.6.4 Study by William et al. (1995)

William et al. (1995) experimentally tested 10 hybrid precast beam-column connections under cyclic loading protocols. Figure 1-10 shows the detailing of the precast specimens. The hybrid precast specimens consist of mild steel to dissipate energy and post-tensioning steel tendons to provide shear resistance. The experimental results showed that hybrid precast connections can be designed to match or exceed the performance of conventional connections in term of strength, energy dissipation, and drift capacity.

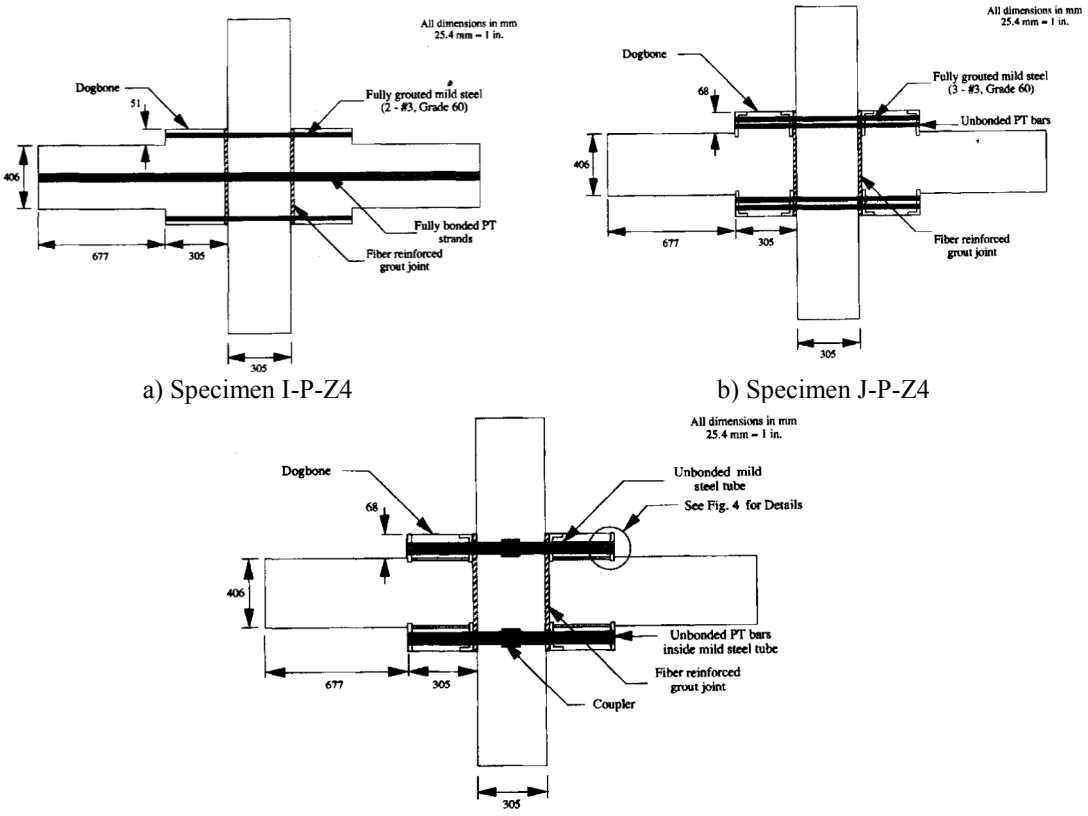

Figure 1-10. Precast Hybrid Rocking Beam-Column Specimen Details (Scott, 1996)

1.2.6.4 Study by Scott (1996)

Scott (1996) experimentally tested 17 beam-column connections under both cyclic and monotonic loading protocols. The key test variables were steel ratio and reinforcement detailing in the beam region, the beam depth, and the force applied on column. A comparison between theoretical and experimental moment capacities were presented. It was found that the connections with beam reinforcement bent-down and U-shape bars show better agreement than those connections with beam reinforcement bent-up (Fig. 1-11).

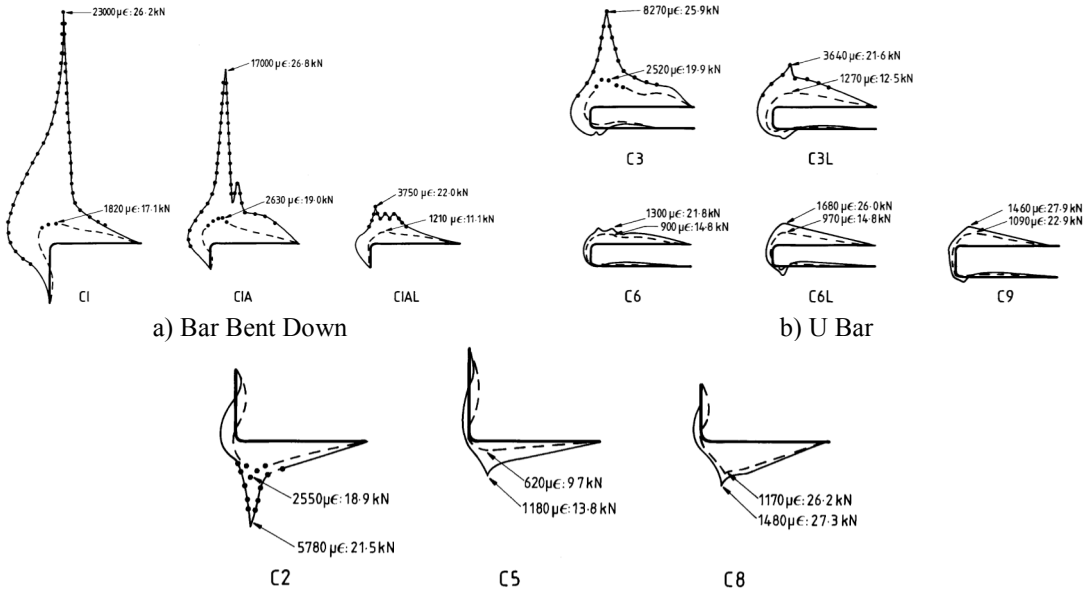

Figure 1-11. Strain Distribution in Beam-Column Specimens (Scott, 1996)

1.2.6.5 Study by Conley et al. (2002)

Conley et al. (2002) constructed and tested sixty-percent scaled five-story building under pseudo-dynamic loading. Four precast concrete frames could resist the lateral load in one direction while jointed precast panel wall system was used to resist the lateral load in the other direction (Fig. 1-12). The panel connections consisted of energy dissipaters, unbonded post-tensioning bars, and U-shape flexural plates. The building was designed following the direct displacement-based design approach. An analytical model was developed and verified, using the experimental data, to predict the seismic response of the building. A minimal damage of the wall panel at 2.63% drift ratio was observed. The building experienced a low residual drift (0.06%) at 1.8% drift ratio. Overall, the performance of the jointed panel system could be categorized as "immediate occupancy" after 150% of the design level earthquake.

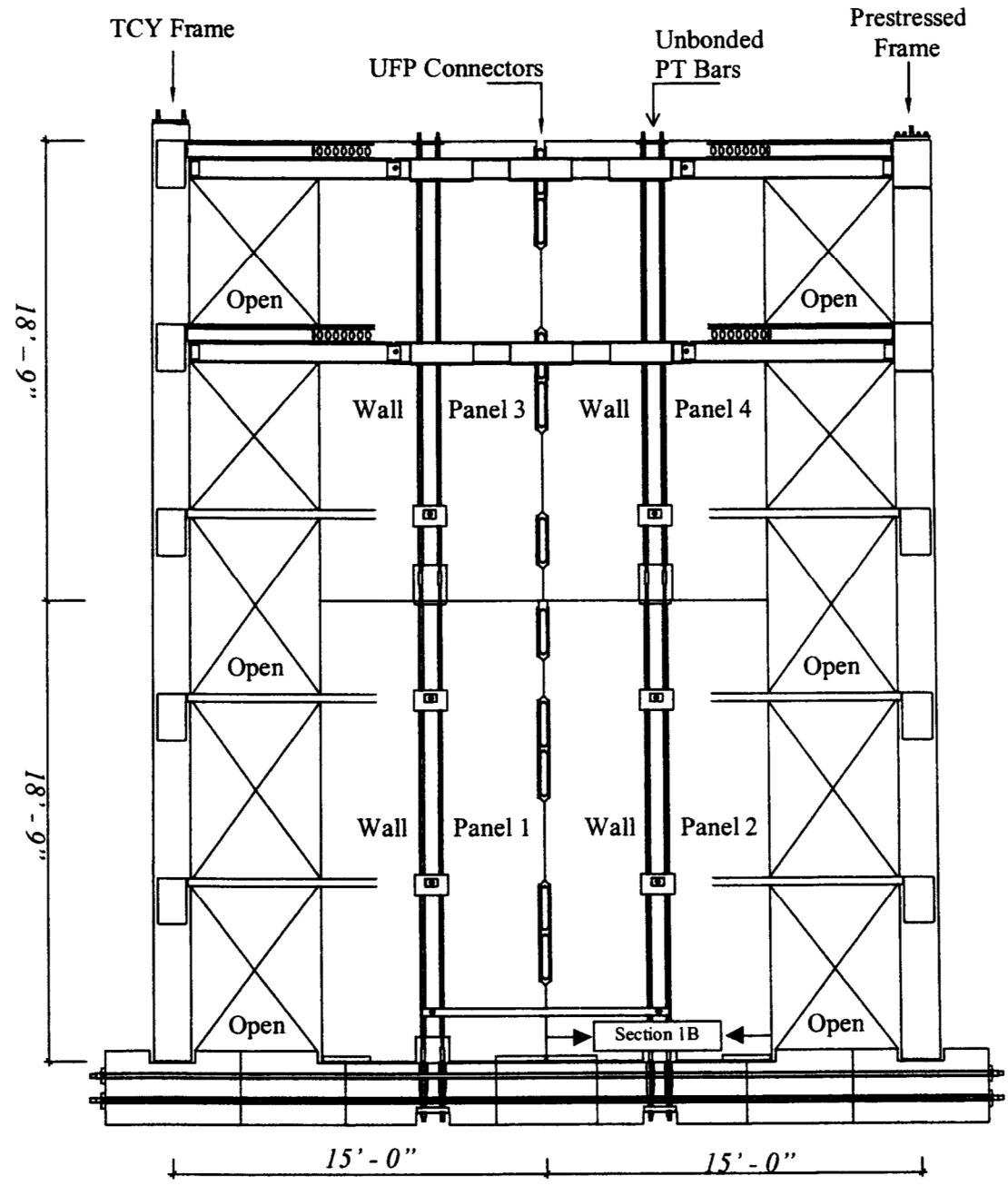

Figure 1-12. Frame Test Setup in Conley et al. (2002)

1.2.6.6 Study by Tsonos (2007)

Tsonos (2007) tested four half-scale beam-column connections under cyclic loading. "Strong column-week beam" philosophy was adopted in this study following the Eurocode and ACI318-05 codes. Two specimens experienced excessive damage in the joint region and exhibited shear failure during the early stages of loading (Fig. 1-13). The shear failure was due to higher shear stress demands than the connection ultimate shear strength.

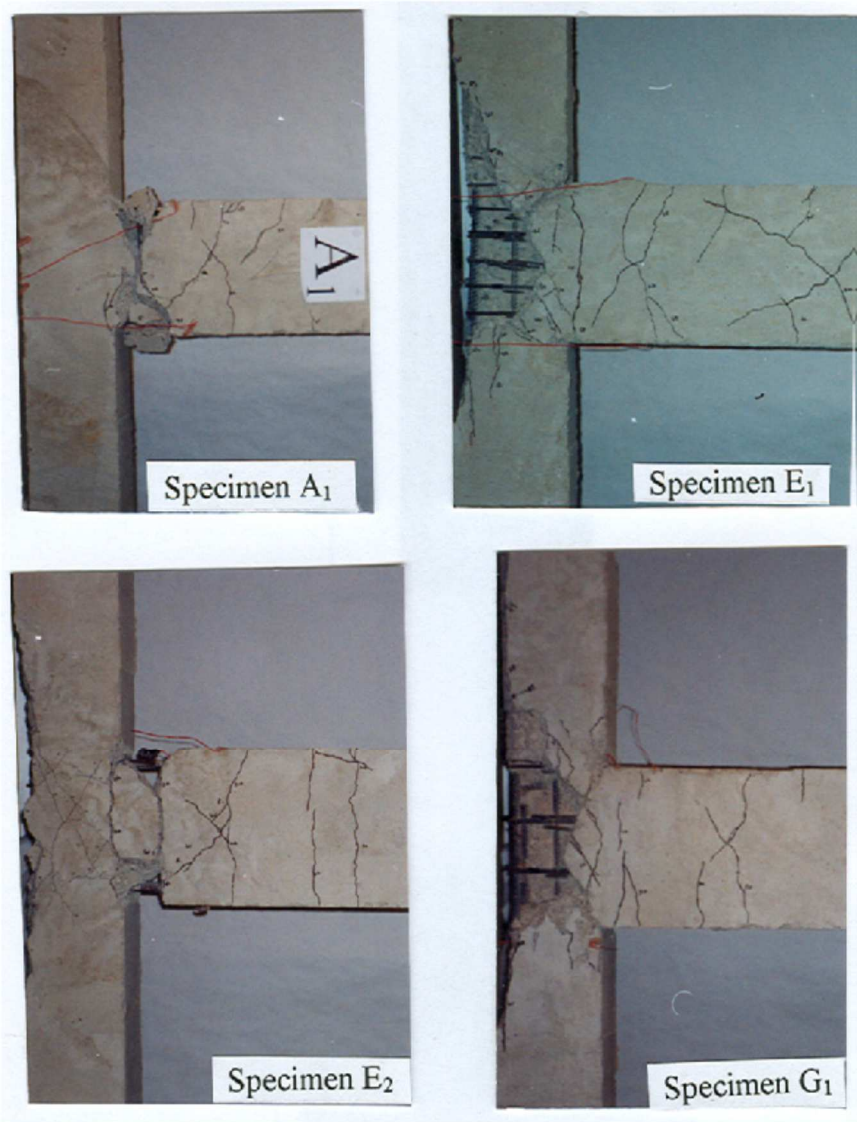

Figure 1-13. Damege of Beam-Column Specimens in Tsonos (2007)

1.2.6.7 Study by Walsh et al. (2016)

Three precast beam-column connections, extracted from a building damaged in 2016 Christchurch earthquake, were tested under cyclic loading by Walsh et al. (2016). The main finding of this study is that precast beams with shear ductile properties exhibited lower displacement capacity comparing to typically detailed beams.

1.2.6.8 Study by Dongzhi et al. (2016)

A new precast beam-column connection was proposed by Dongzhi et al. (2016) for moment-resisting frames (Fig. 1-14). An experimental study on five full-scale beam-column connections was carried out including the monolithic specimen. All beam-column specimens were tested under cyclic loading. The study reported that the proposed precast connection showed good seismic performance and can be used in high seismic regions.

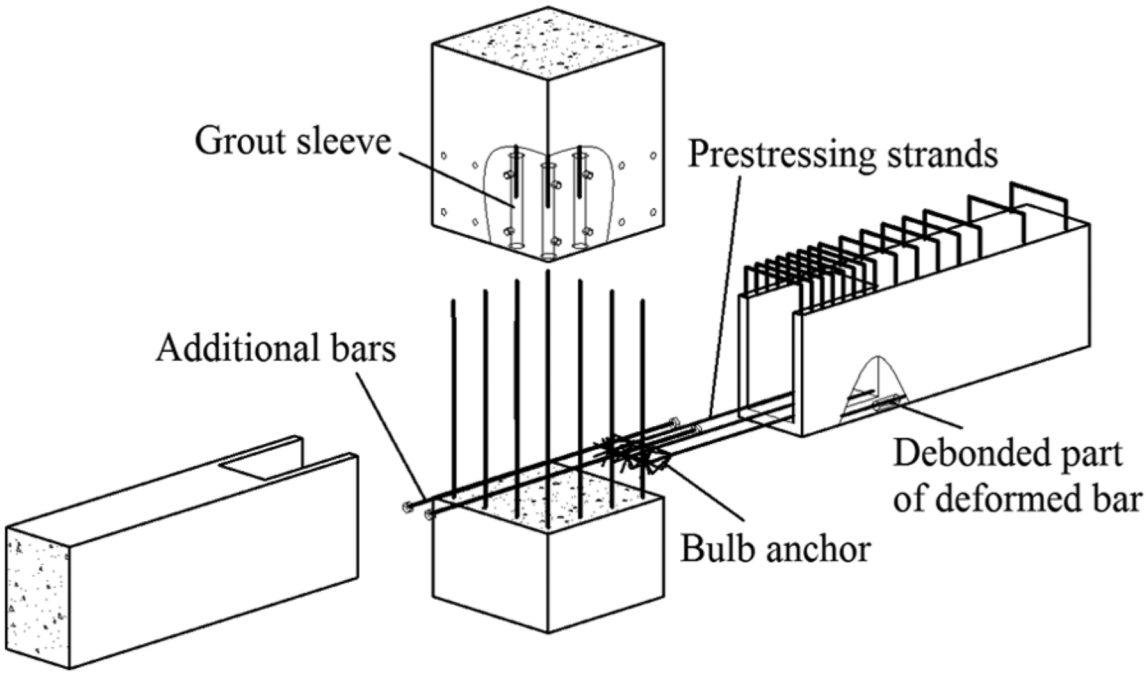

Figure 1-14. Precast Beam-Column Connection Detailed by Donghzi et al. (2016)

Only a few of the past studies simulated the actual boundary conditions of a beam-column connections. Many studies simply applied cyclic loads to the specimen at the end of beam. A number of studies (Carlos et al., 2001 and Tsonos, 2009) installed the actuator at the tip of the column but failed to allow the beam to sway with the column. Li et al., (2009) successfully incorporated the actual boundary conditions but without applying axial load at column head. In addition, the latter study did not allow beam horizontal movement. Finally, Tuhin (2016) successfully incorporated the actual boundary conditions in the beam-column connection test specimen in which both column and beam could rotate and sway. Figure 1-15 shows the boundary conditions for an exterior beam-column connection used in Tuhin (2016). The present study adopted the test setup used in Tuhin (2016).

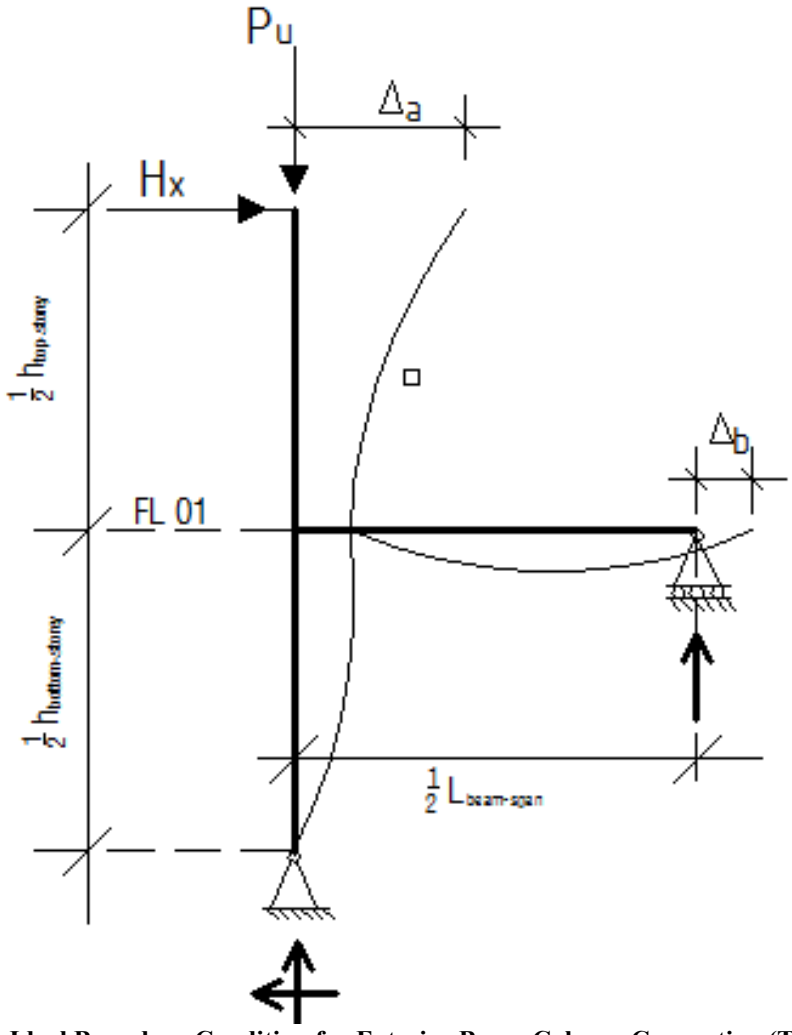

Figure 1-15. Ideal Boundary Condition for Exterior Beam-Column Connection (Tuhin, 2016)

1.3 Objectives and Scope

The main objective of this study is to develop a new generation of precast buildings and bridges, which can be built quickly, exhibit improved seismic performance compared to conventional RC structures, and can be repaired in a few hours after severe events with minimal cost and labor through replacement of exposed reinforcement.

Experimental and analytical programs were completed to achieve the abovementioned objective: (1) design guidelines were developed for buckling restrained reinforcement (BRR), (2) four half-scale precast beam-column specimens incorporating

the proposed detailing were tested under a cyclic loading protocol, (3) analytical studies were performed to investigate the seismic performance of precast building incorporating the proposed detailing, and (4) analytical studies were carried out to establish the behavior of repairable precast bridge columns.

1.4 Dissertation Outline

Chapter 1 presents introduction and scope of the work done. Chapter 2 presents experimental investigation of BRR (or external energy dissipaters) to observe their compressive behavior and to propose a new design methodology. Chapter 3 presents the results of repairable precast beam-column specimen tests and includes a comparison with a reference conventional beam-column specimen. Chapter 4 includes modeling methods for the proposed beam-column specimens and the summary of analytical study findings on precast and conventional building frames. The findings of a parametric study on repairable precast bridge columns incorporating the innovative detailing are summarized in Ch. 5. The summary and conclusions of the study are presented in Ch. 6.

1.5 References

1. Guerrini, G., Restrepo, J., Vervelidis, A., Massari, M. (2015). “Self-Centering Precast Concrete Dual-Steel-Shell Columns for Accelerated Bridge Construction: Seismic Performance, Analysis, and Design,” PEER Report No. 2015/13, Pacific Earthquake Engineering Research Center, Headquarters at the University of California, Berkeley.
2. Marriott, D., Pampanin, S., and Palermo, A. (2011). “Biaxial Testing of Unbonded Post□Tensioned Rocking Bridge Piers with External Replaceable Dissipaters. Earthquake Engineering & Structural Dynamics,” 40(15), 1723-1741.

3. Lenton. (2017). Retrived June 30, 2017, from https://www.erico.com/catalog/literature/RSB-WWEN.pdf.
4. Tazarv, M. and Saiidi, M.S. (2015). "Design and construction of bridge columns incorporating mechanical bar splices in plastic hinge zones," Center for Civil Engineering Earthquake Research, Department of Civil and Environmental Engineering, University of Nevada, Reno, Nevada, Report No. CCEER-13-07, 149 pp.
5. Tazarv, M. and Saiidi, M.S. (2016). "Seismic design of bridge columns incorporating mechanical bar splices in plastic hinge regions," Engineering Structures, DOI: 10.1016/j.engstruct.2016.06.041, Vol 124, 507-520.
6. Tazarv, M., and Saiidi, MS. (2014). "Next Generation of Bridge Columns for Accelerated Bridge Construction in High Seismic Zones," CCEER Report No. 14-06, Center for Civil Engineering Earthquake Research, University of Nevada, Reno, NV.
7. Zaghi, A., and Saiidi, M.S. (2010). "Seismic Design of pipe pin connections in Concrete Bridges," Center for Civil Engineering Earthquake Research, University of Nevada, Reno, Nevada. CCEER Report No. 10-01.
8. Brinson L., C. (1993). "One-Dimensional Constitutive Behavior of Shape Memory Alloys: 109 Thermomechanical Derivation with Non-Constant Material Functions and Redefined Martensite Internal Variable," Journal of Intelligent Material Systems and Structures, 4, 229-242.
9. Burton, D.S., and Gao, X. (2006). "Finite Element Simulation of a Self-Healing Shape Memory Alloy Composite," Mechanics of Materials, 38 (1), 525-537.

10. Cho, M., and Kim, S. (2005). “Structural Morphing Using Two-Way Shape Memory Effect of SMA,” International Journal of Solids and Structures, 42 (1), 1759 pp.
11. DesRoches, R., and Smith, B. (2004). “Shape Memory Alloys in Seismic resistant designand retrofit: a critical review of their potential and limitations” Journal of EarthquakeEngineering, 8 (3), 415-429.
12. Dolce, M., and Cardone, D. (2006). “Theoretical and Experimental Studies for the Application of Shape Memory Alloys in Civil Engineering,” Journal of Engineering Materials and Technology, 128 (1), 302-311.
13. DesRoches, R., McCormick, J., and Delemont, M. (2004). “Cyclic Properties of Superelastic Shape Memory Alloy Wires and Bars” Journal of Structural Engineering, 130 (1), 38-46.
14. Youssef, M.A., Alam, M.S. and Nehdi, M. (2008). "Experimental Investigation on the Seismic Behavior of Beam-Column Joints Reinforced with Superelastic Shape Memory Alloys," Journal of Earthquake Engineering, 12(7), 1205-1222.
15. Dolce, M. and Cardone, D. (2006). “Theoretical and Experimental Studies for the Application of Shape Memory Alloys in Civil Engineering,” Journal of Engineering Materials and Technology, 128 (1), 302-311.
16. Ehsani, M., Moussa, A., and Valenilla, C. (1987). "Comparison of inelastic behavior of reinforced ordinary-and high-strength concrete frames," Structural Journal, 84(2), 161-169.

17. Ehsani, M., and Wight, J. (1985). "Exterior reinforced concrete beam-to-column connections subjected to earthquake-type loading," Paper presented at the Journal Proceedings.
18. IEBC Standard (2012). "International existing building code," International code council, Inc., Country Club Hills, IL.
19. Joh, O., Goto, Y., and Shibata, T. (1991). "Influence of Transverse Joint and Beam Reinforcement and Relocation of Plastic Hinge Region on Beam Column Joint Stiffness Deterioration," Special Publication, 123, 187-224.
20. William, C., Geraldine, S., and John, F. (1995). "Performance of Hybrid Moment-Resisting Precast Beam-Column Concrete Connections Subjected to Cyclic Loading," ACI Structural Journal, 99(S22), 229-249.
21. Scott, R. H. (1996). "Intrinsic mechanisms in reinforced concrete beam-column connection behavior," ACI Structural Journal," 93(3), 336-346.
22. Li, B., Tran, C.T.N. and Pan, T.C. (2009). "Experimental and numerical investigations on the seismic behavior of lightly reinforced concrete beam-column joints," Journal of structural engineering, 135(9), pp.1007-1018.
23. Tsonos, A.G. (1999). "Lateral load response of strengthened reinforced concrete beam-to-column joints," ACI Structural Journal, 96, pp.46-56.
24. Conley, J., Sritharan, S., and Priestley, M. (2002). "Precast Seismic Structural Systems PRESSS-3: The Five-Story Precast Test Building Vol:3.5: Wall Direction Response," SSRP Report No. 99-19, Structural System Research Project, University of California, San Diego, CA.

25. Tsonos, A. G. (2007). "Cyclic load behavior of reinforced concrete beam-column subassemblages of modern structures," ACI Structural Journal, 104(4), 468.
26. Dongzhi, G., Zhengxing, G., Quandong, X., and Yongfeng, Z. (2016). "Experimental Study of a New Beam-to-Column Connection for Precast Concrete Frames Under Reversal Cyclic Loading," Advances in Structural Engineering Journal, 19(3), 529-545.
27. Zhou, H. (2009). "Reconsideration of seismic performance and design of beam-column joints of earthquake-resistant reinforced concrete frames," Journal of structural engineering, 135(7), 762-773.
28. Tuhin, I.A. (2016). “Application of New Materials and Innovative Detailing for Reinforced Concrete Structures,” MSc thesis, South Dakota State University, Brookings, SD.

Chapter 2: Buckling Restrained Reinforcement (BRR)

2.1 Introduction

Reinforce concrete (RC) bridges and buildings are currently designed to withstand severe earthquakes without collapse. This design objective is attained by providing large displacement capacities through the yielding of reinforcement. However, the repair of RC structures is often inevitable under extreme earthquakes mainly due damage of concrete, reinforcement, and sometimes large residual displacements. The repairable of damaged RC structures will be impractical when the longitudinal reinforcement fractures or the repair cost exceeds 50% of the replacement cost.

External reinforcing bars have been used in previous studies to increase energy dissipation of rocking columns and post-tensioned concrete buildings. Only buckling restrained reinforcement with dog-bone shapes (BRRD) have been used in previous studies. Furthermore, steel bars used in BRRD were not usually conventional reinforcing steel bars allowed by current bridge and building codes. With some modification, external energy dissipaters can be used as the longitudinal reinforcement of RC members. Feasibility and performance of a new type of external energy dissipater were experimentally investigated and the results are presented herein. Furthermore, a simple design method for buckling restrained reinforcement (BRR) with or without a section

modification (e.g. dog-bone) is presented to further help engineers with the design of external reinforcement and energy dissipaters.

2.2 Research Objectives

Dog-bone mild steel or aluminum bars, which have been used as energy dissipaters, showed promising performance in previous experimental studies. In an attempt to avoid bar machining and to reduce the cost, conventional reinforcing steel bars without any section reduction enclosed in tubes were proposed as external energy dissipaters in this study. The main objective of this chapter is to experimentally investigate the feasibility and performance of conventional steel bars without any machining in BRR. A simple design method for buckling restrained reinforcement is also proposed.

2.3 Past Research on Buckling Restrained Reinforcement

As mentioned in the previous sections, external bars have been used in rocking structures to increase energy dissipation (Guerrini et Al. (2014), Pampanin (2015) Sarti et al. (2013) and Cattanach et al. 2008). Of different forms, dissipaters made of mild steel or aluminum bars encased in steel tubes (Fig. 2-1) are the focus of this chapter. Grout or epoxy are usually used in this dissipater type as tube filler. The purpose of enclosing a bar in a steel tube is to avoid its buckling. Note bucking restrained reinforcement without any section modification is called BRR, and with a fuse-like shape (e.g. dog-bone) is called BRRD in present study. A brief review of past studies on buckling restrained reinforcement is presented herein.

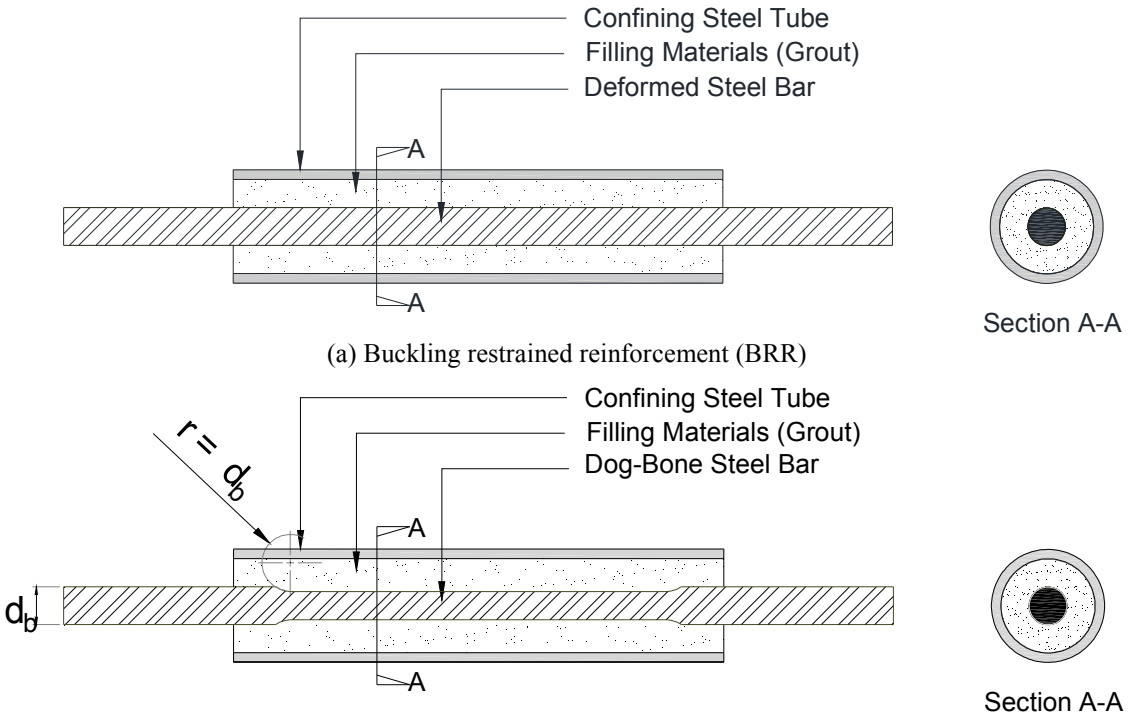

(a) Buckling restrained reinforcement (BRR)

(b) Dog-bone buckling restrained reinforcement (BRRD)

Figure 2-1. Different Types of External Energy Dissipaters

2.3.1 Study by Marriot el al. (2009)

Marriot el al. (2009) utilized BRRD as external energy dissipaters in hybrid rocking bridge columns (Fig. 2-2). A structure is usually called hybrid rocking when two or more types of reinforcement (e.g. steel bars and steel tendons) are utilized. Three different fuse geometries were used to construct these external dissipaters, 75-mm (3 in.) long with 13.5-mm (0.53 in) diameter, 75-mm (3 in.) long with 10-mm (0.4 in) diameter, and 115-mm (4.5 in.) long with 8-mm (0.31 in.) diameter. The fuse is referred to a portion of a bar where the section is reduced. All bars were encased within 34-mm (1.34 in.) long tube with a wall thickness of 2 mm (0.08 in.). Epoxy was used as the tube filler material.

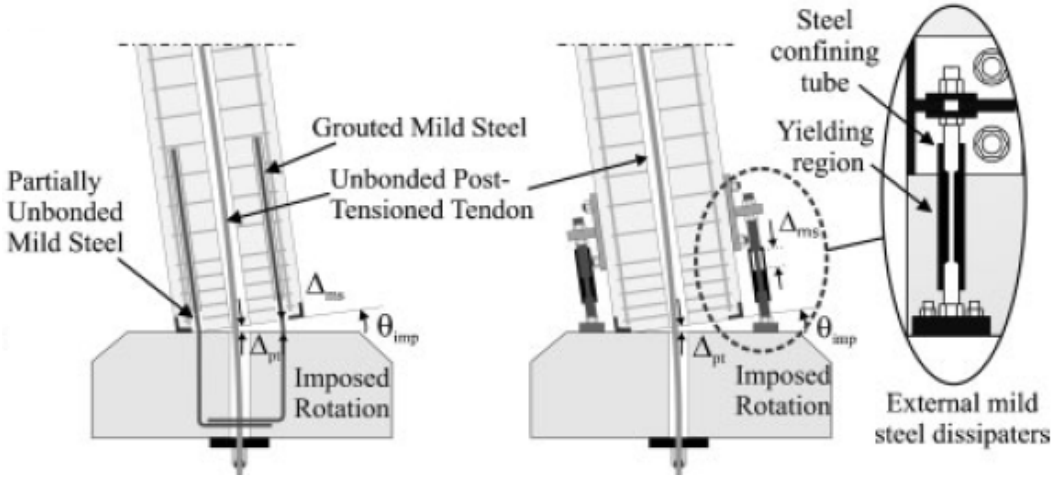

Figure 2-2. Dog-bone Shape External Energy Dissipaters for Rocking Columns (Marriott et al., 2011)

The performance of these dissipaters under cyclic loads was experimentally investigated prior to the column testing. These BRRD exhibited large hysteresis before failure at 12% strains. One sample load-strain relationship is shown in Fig. 2-3a. Furthermore, no pinching was observed during cyclic loading indicating that large inelastic deformations can be achieved without reinforcement buckling. Another finding was that the stiffness of BRRD in compression was 10% higher than that in tension by. The increase in the stiffness can be attributed to the gap closure between the grout and the unreduced section of the bar as shown in Fig. 2-3b.

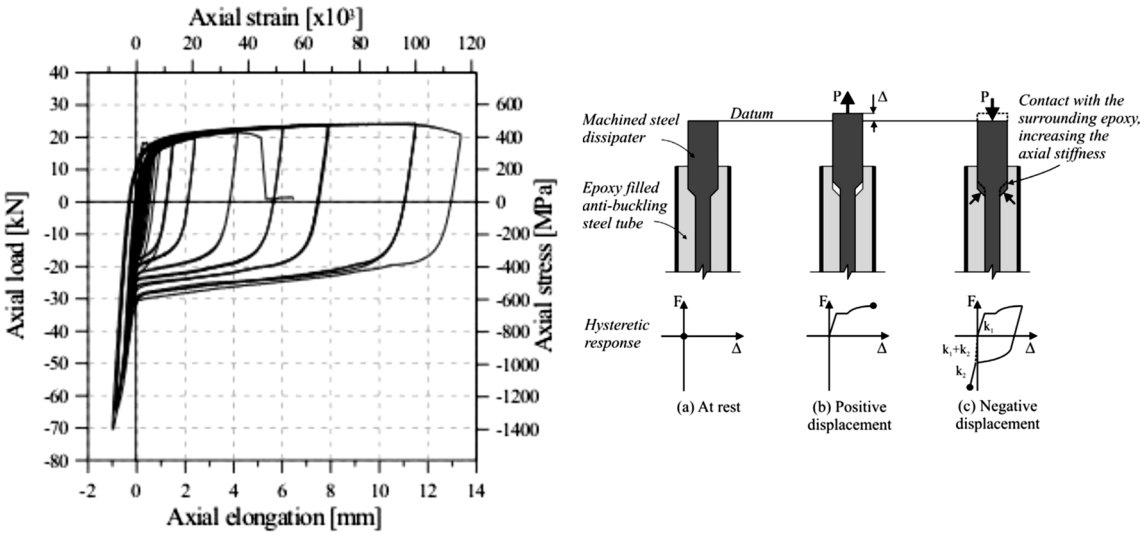

(a) Cyclic and monotonic behavior of dissipater (b) Compression behavior of dissipater

Figure 2-3. Cyclic Behavior of External Energy Dissipater (Marriott et al., 2009)

Two bridge columns incorporating the previously discussed external energy dissipaters were tested, one with eight external dissipaters and another with four external dissipaters. Moreover, one conventional RC bridge column was tested as a benchmark model. All columns were tested under pseudo-dynamic loading protocols. The axial load was 300 kN (67.44 kips) for each column. The hybrid rocking columns showed satisfactory energy dissipation and a re-centering characteristic. The hybrid rocking columns damage was insignificant due to the steel tube jacketing around the plastic hinge region. The columns failed at 3.5% drift ratio due to rapture of external energy dissipaters.

2.3.2 Study by Mesa and Dario (2010)

Mesa and Dario (2010) tested three BRRD as external energy dissipaters: one 90-mm (3.5-in.) long bar with a 7-mm (0.28-in.) fuse diameter, one 90-mm (3.5-in.) long bar with a 10-mm (0.4-in) fuse diameter, and one 90-mm (3.5-in.) long bar with a 13-mm (0.5-in.) fuse diameter. The bars were confined with 34-mm (1.34-in.) long tube with a

wall thickness of 3 mm (0.12 in.). The performance of these dissipaters was investigated using uniaxial monotonic and cyclic loading.

Figure 2-4 shows measured stress-strain responses for two dissipaters with 7-mm (0.28-in.) and 8-mm (0.31-in.) fuse diameters. The ultimate compressive strain was 9% for that the BRR with 7-mm (0.28-in.) fuse diameter and 11% for the BRR with 8-mm (0.31-in.) fuse diameter, respectively.

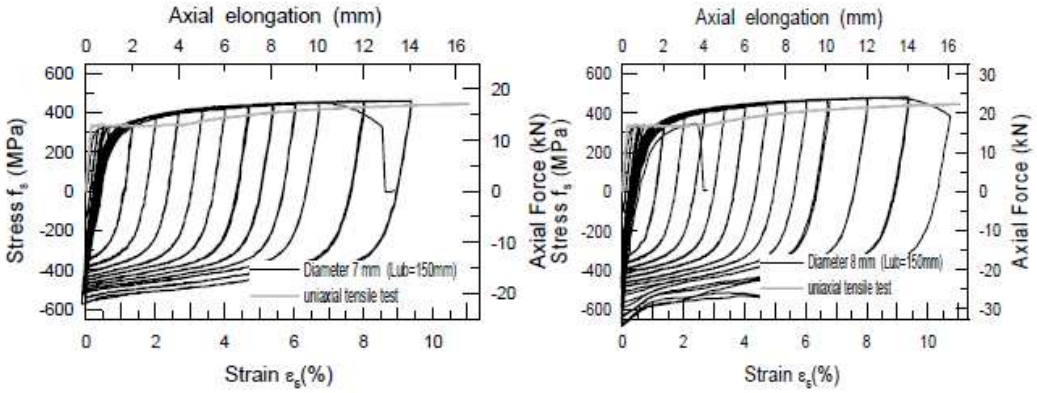

(a) Dissepater with 7-mm fuse diameter (b) Dissepater with 9-mm fuse diameter

Figure 2-4. Stress-Strain Relationships for External Energy Dissipaters (Mesa and Dario, 2010)

2.3.3 Study by Marriott et al. (2011)

Marriott et al. (2011) performed another experimental study to investigate the performance of hybrid rocking bridge columns similar to those tested in 2009 but under a biaxial loading protocol. Concrete spalling at 2% drift ratio was observed for conventional bridge column followed by reinforcement buckling at 2.5% drift ratio and reinforcement fracture at 3.5% drift ratio. The hybrid rocking columns showed insignificant damage and minimal strength degradation up to 2.5% drift ratio where one of the dissipaters fractured.

2.3.4 Study by Lukkunaprasit et al. (2011)

Lukkunaprasit el al. (2011) conducted experimental study on buckling restrained reinforcement (BRR) energy dissipaters. Mild steel bars with a 16-mm (0.63 in.) diameter were used in BRR. Twenty-eight-mm (1.1-in.) long tubes with 4 mm-thickness (0.16 in.) were used to confine the steel bars. Non-shrink grout was used as the filler material. Overall, the test showed that BRR can prevent buckling of slender vertical bars under a significantly high axial load.

Subsequently, two one-half scale bridge columns incorporating internal BRR within the plastic hinge region and two conventional bridge columns were tested in this study. The column tests showed that shear failure can be deferred or even eliminated when BRR is provided in the critical zone (Fig. 2-5a). Furthermore, incorporating BRR into bridge columns can increase the column drift capacity up to 125% compared to conventional columns (Fig. 2-5b).

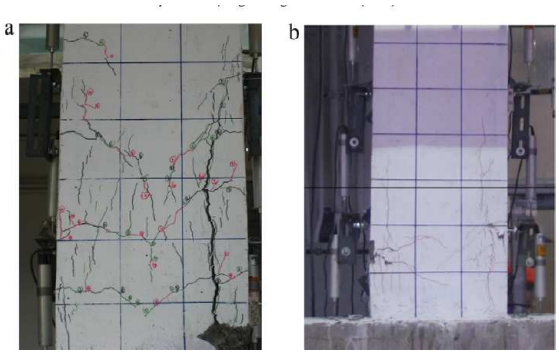

(a) Damage observed for both conventional and columns with BRR

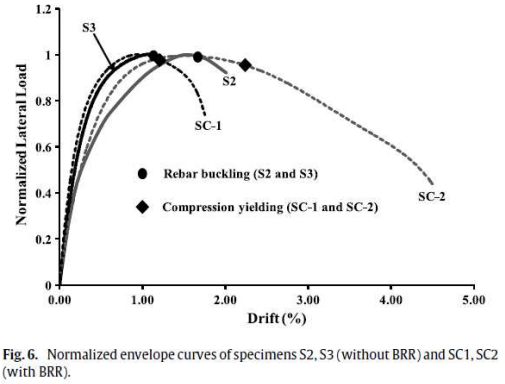

Fig. 6. Normalized envelope curves of specimens S2, S3 (without BRR) and SC1, SC2 (with BRR).

(b) Force-drift relationships for conventional and columns with BRR

Figure 2-5. Hysteretic Behavior of External Energy Dissipaters Constructed with Aluminum Bar (Lukkunaprasit et al., 2011)

2.3.5 Study by Mashal et al. (2014)

The seismic performance of low-damage and high-damage two-column bridge bents was investigated by Mashal et al. (2014). Low-damage Bridge bent used hybrid rocking columns incorporating dog-bone shape external energy dissipaters while high-damage Bridge bent consisted of precast columns with member socket connection at the column-to-footing interface and grouted duct connection at the column-cap interface. The test results and details of energy dissipaters were proprietary and were not available. The columns were confined using steel jackets to attach the dissipater. The specimens were tested under cyclic loads. The column axial load was 390 kN (87.68 kips). The rocking columns incorporating external dissipaters showed no damage, low residual displacements, and high energy dissipation (Fig. 2-6) up to 3.5% drift ratio where the test was stopped.

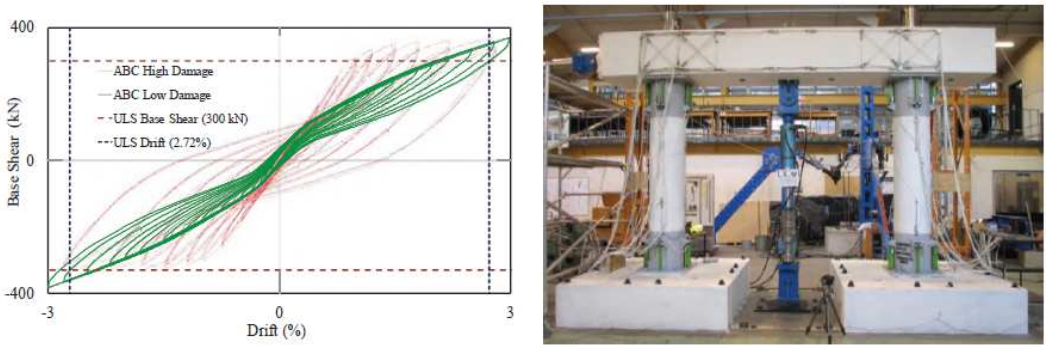

(a) Force – displacement response (b) bent after testing

Figure 2-6. Force-Displacement Relationship for Low-Damage and High-Damage Bridge Bents (Mashal et al., 2014)

2.3.6 Study by Guerrini et al. (2014)

Guerrini et al. (2014) performed an experimental study on hybrid rocking columns incorporating buckling restrained energy dissipaters. Dog-bone shape ASTM A576 Grade 1018 hot rolled steel bars were used in BRRD (Fig. 2-7). The yield and ultimate strength of the bars were 190 MPa (27.56 ksi) and 331 MPa (48 ksi),

respectively. Figure 2-8 shows the hysteretic behavior of the external dissipaters. The test results showed that the BRRD ultimate compressive stress is higher than its ultimate tensile stress due to a partial composite behavior in the dissipaters. The ultimate BRRD compressive strain was 4%.

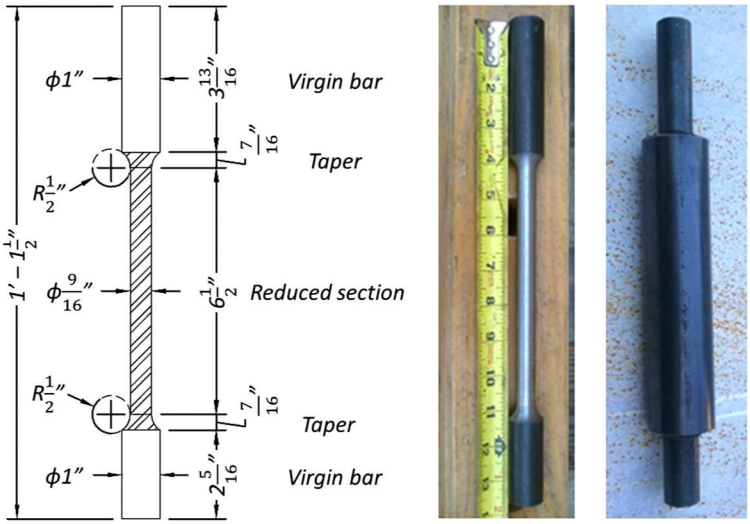

Figure 2-7. Buckling Restrained Energy Dissipaters in Guerrini et al. (2014)

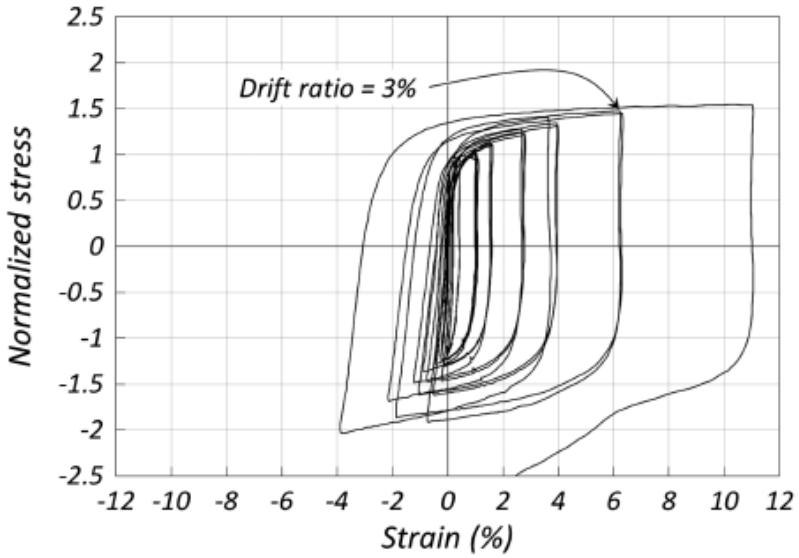

Figure 2-8. Hysteretic Behavior of Buckling Restrained Energy Dissipaters in Guerrini et al. (2014)

Followed by BRRD testing, these external energy dissipaters were incorporated into a dual shell hybrid rocking bridge column (Fig. 2-9a). The performance of the

column was tested under quasi-static reversed cyclic loading. Two hollow hydraulic jacks were used to apply 63 kips (280 kN) axial load on the column. The first BRRD deformed at 3% drift ratio which was the target design drift for this column. One dissipater fractured at 7.5% drift ratio followed by the fracture of two more dissipaters at subsequent cycles. Figure 2-9b shows the hysteretic behavior of the column up to 10% drift ratio where the test was stopped.

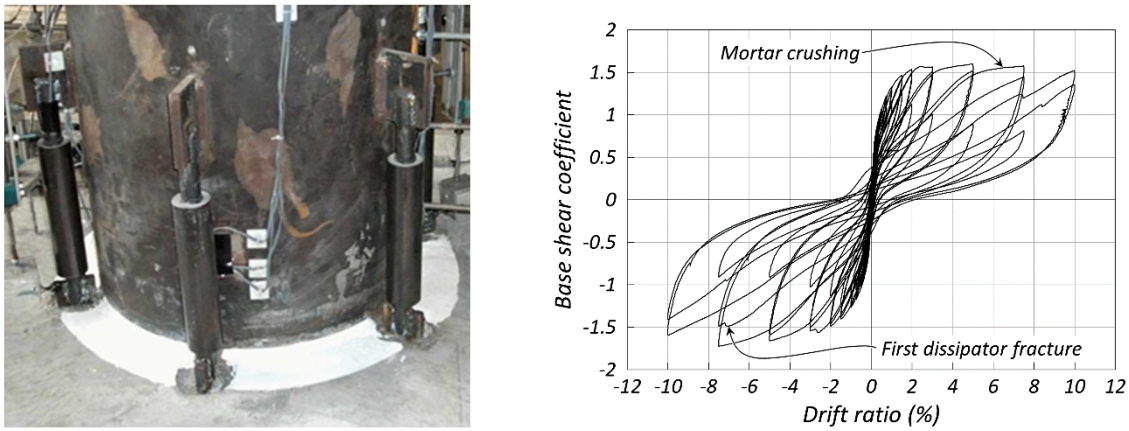

a) Bridge column incorporate external energy dissipater

b) Hysteretic lateral force-displacement response

Figure 2-9. Dual-Shell Hybrid Rocking Bridge Column (Guerrini et al., 2014)

2.3.7 Study by Guo et al. (2015)

Guo et al. (2015) investigated the behavior of three hybrid rocking bridge columns with external energy dissipaters under cyclic loading. Aluminum bars with an original diameter of 25 mm (1 in.) and a fuse diameter of 15 mm (0.59 in) were used to form the external dissipaters. All bars had a fuse length of 100 mm (4 in.) but one which had a 200-mm (8 in.) fuse length. No test was carried out on individual dissipaters in this study. Three one-third scale hybrid rocking bridge columns incorporating aluminum external dissipaters and one conventional bridge column were tested in this study (Fig. 2-10a). The test showed that these columns are low damage up to 4% drift ratio where the

test was stopped. The conventional column had a significant damage and large residual displacements at only 2.25% drift ratio. Furthermore, the hybrid columns exhibited large energy dissipation even though a few dissipaters raptured at 2% drift ratio. Figure 2-10b shows stress-strain relationships, which were recorded during the columns tests, of aluminum external dissipaters.

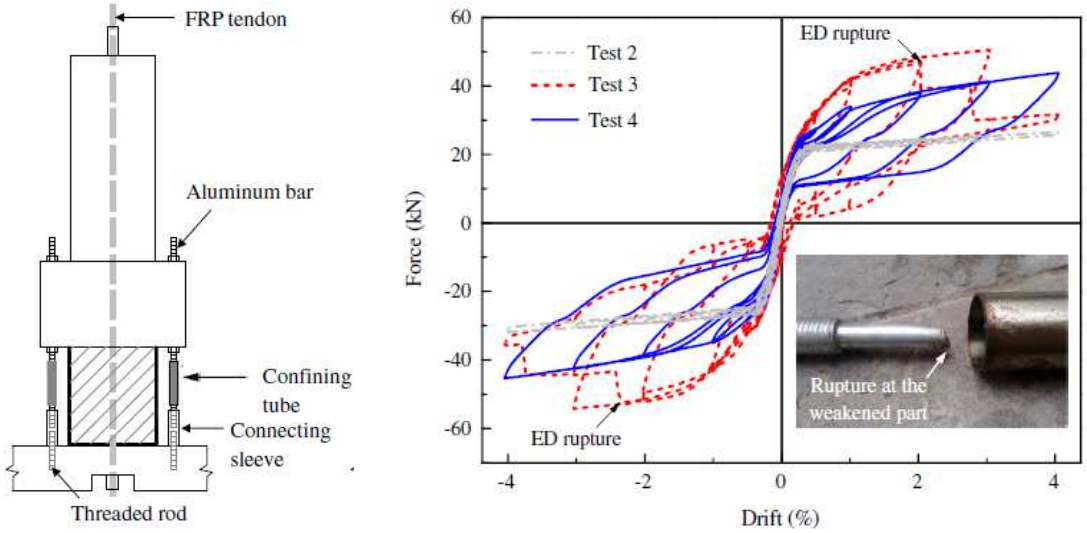

(a) Bridge pier with dissipater (b) Hysteretic behavior

Figure 2-10. Hysteretic Behavior of External Energy Dissipaters Constructed with Aluminum Bar (Guo et al., 2015)

2.3.8 Study by White and Palermo (2016)

White and Palermo (2016) experimentally investigated the behavior of two hybrid rocking bridge columns with external energy dissipaters. Grade 300 (43.5 ksi) steel bars with an original diameter of 30 mm (1.18 in.) and a fuse diameter of 24 mm (0.95 in.) were used as external energy dissipaters as shown in Fig. 2-11. Two types of cross-section were proposed for the fuse portion: circular and grooved. It was claimed that the grooved section provides higher resistance against buckling due to the relatively high radius of gyration. No test results were provided for individual dissipaters in this study.

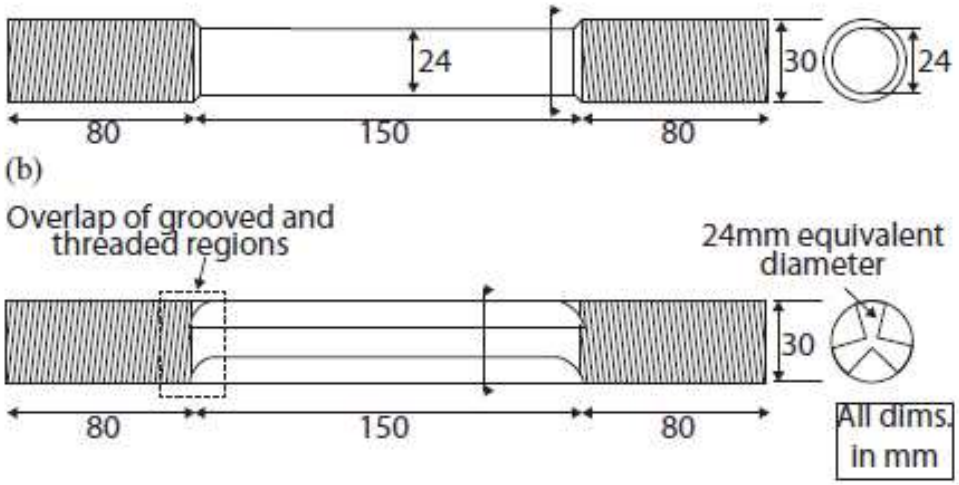

Figure 2-11. Geometric Configuration for External Energy Dissipaters (White & Palermo, 2016)

2.3.9 Study by Sarti et al. (2016)

Sarti el al. (2016) conducted experimental and analytical studies on six dog-bone shape buckling restrained energy dissipaters. Grade 300 (43.5 ksi) mild steel bars were used in BRRD. AS/NZS 1163 grade C250L0 tubes were used to confine the steel bars. Both epoxy and grout were used as the filler materials. Different dissipater geometries were included (Fig. 2-12) to investigate their effects on the dissipater failure mechanism. The experimental results showed a noticeable improvement in dissipater stiffness under negative displacement comparing to unrestrained bars which means a significant improvement in dissipater compression behavior. Two failure modes were reported for BRRD: (1) bar fracture within the fuse portion of the dissipater due to low cyclic fatigue, and (2) buckling of the dissipater (including bar, grout, and tube). Overall, the test results showed stable hysteretic behavior for the dissipaters up to 6% compressive strain. Another finding was that the dissipater compressive ultimate stress was higher that the

tensile strength due to a composite action between the bar and grout in compression. Furthermore, the filler material had no effect on the dissipater behavior.

The study recommended the fuse slenderness ratio, which is defined as the fuse length divided by the fuse diameter, should be no more than 60. Finally, design equations, to determine design parameters such as peak force in dissipaters, were developed based on an extensive parametric analysis. Equation 2-1 presents the design peak force in these energy dissipaters:

$$\frac{Fmax}{Fy} = 30.9\ \lambda_{tot}^{-0.76} \tag{2-1}$$

where F_{max} is the design peak force of the BRRD, F_y is the yield stress of the bar, and λ_{tot} is the effective slenderness ratio.

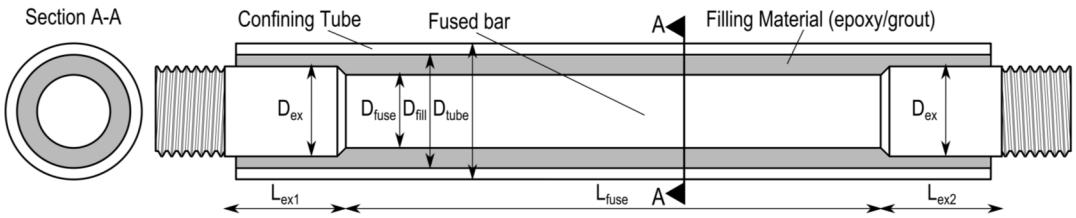

Figure 2-12. Geometric Configuration for Dog-Bone Energy Dissipaters (Sarti et al., 2016)

2.4 BRR Experimental Programs

The feasibility and performance of buckling restrained reinforcement (BRR) was investigated by testing 16 BRR under axial compressive loading at the Lohr Structures Laboratory at South Dakota State University. The experimental test was performed in collaboration with Tuhin (2016). The test matrix, setup, and loading protocols for BRR are presented herein.

2.4.1 Test Matrix

A total of 16 specimens (Table 2-1) including four reference deformed bars, three deformed bars restrained with a series of steel nuts, and nine BRR were constructed and tested under monotonic and cyclic axial compressive loading to failure. Two different sizes of deformed steel bars, No. 4 (13 mm) and No. 8 (25 mm) were used in this experimental investigation. Furthermore, three BRR slenderness ratios of 10, 15, and 20 were included in the experiment. The BRR slenderness ratio is defined as the ratio of the tube length to the bar diameter. Grout filled steel tubes with different geometries were used to prevent buckling of reinforcement. The main purpose of using the grout is to increase the moment of inertia of the section and to enhance the durability. Loading for all specimens was monotonic except "No4-BL14.81d-TL7.5s-TG13-G0.50," which was cyclic. Guide on the specimen naming system is presented in the table footnote.

Table 2-1. Test Matrix for Buckling Restrained Reinforcement

Specimen ID	Bar No. (mm)	Bar Length, in. (mm)	Tube O.D., in. (mm)	Tube Gage	Tube Length, in. (mm)	Filler
No4-BL11.00d	4 (Ø13)	11.00 (279.4)	N.A.	N.A.	N.A.	N.A.
No4-BL10.94d	4 Ø13)	11.00 (279.4)	N.A.	N.A.	N.A.	N.A.
No8-BL16.91d	8 (Ø25)	16.96 (430.8)	N.A.	N.A.	N.A.	N.A.
No8-BL10.25d	8 (Ø25)	10.25 (260.4)	N.A.	N.A.	N.A.	N.A.
No4-BL11.00d-Nuts-G0.875	4 (Ø13)	11.00 (279.4)	N.A.	N.A.	N.A.	Steel Nuts
No4-BL11.00d-Nuts-G0.42	4 (Ø13)	11.00 (279.4)	N.A.	N.A.	N.A.	Steel Nuts
No4-BL11.00d-Nuts-G0.20	4 (Ø13)	11.00 (279.4)	N.A.	N.A.	N.A.	Steel Nuts
No4-BL11.00d-TL5.0s-TG18-G3.00	4 (Ø13)	11.00 (279.4)	1 ¼ (31.8)	18 GA	5 (127)	Grout
No4-BL10.94d-TL5.0s-TG16-G2.94	4 (Ø13)	10.94 (277.9)	1 ¼ (31.8)	16 GA	5 (127)	Grout
No4-BL12.28d-TL7.5s-TG16-G0.50	4 (Ø13)	12.06 (320)	1 ¼ (31.8)	16 GA	7.5 (190.5)	Grout
No4-BL12.20d-TL7.5s-TG14-G0.50	4 (Ø13)	12.20 (209.9)	1 ¼ (31.8)	14 GA	7.5 (190.5)	Grout
No4-BL14.81d-TL7.5s-TG14-G0.50	4 (Ø13)	14.81 (376.2)	1 ¼ (31.8)	14 GA	10 (254)	Grout
No4-BL14.81d-TL7.5s-TG13-G0.50	4 (Ø13)	14.81 (376.2)	1 ¼ (31.8)	13 GA	10 (254)	Grout
No8-BL14.56d-TL10.0s-TG13-G0.50	8 (Ø25)	14.56 (369.8)	2 ¼ (57.2)	13 GA	10 (254)	Grout
No8-BL17.00d-TL10.0s-TG11-G1.00	8 (Ø25)	17.00 (431.8)	2 ¼ (57.2)	11 GA	10 (254)	Grout
No8-BL19.62d-TL15.0s-TG11-G0.50	8 (Ø25)	19.62 (498.3)	2 ¼ (57.2)	11 GA	15 (254)	Grout

Note: Guide for Specimen Identification:
Example: No4-BL10.94d-TL5.0s-TG16-G0.5
First Term - Bar Size: No4 or No8.
Second Term - Bar Length and Deformation Type (d for deformed and p for plain).
Third Term - Tube Length and Material (s for steel, a for aluminum).
Fourth Term - Tube Gage.
Last Term - Total Gap at the Ends of the Reinforcement.

2.4.2 Material Properties

Each BRR is made of three components: (1) reinforcing steel bar, (2) steel tube, and (3) filler material (Fig. 2-1). Constitutive materials of each component were tested according to ASTM standards and a summary of the material properties is presented herein:

- Reinforcing Steel Bar: ASTM A706 Grade 60 deformed steel bars were used in BRR. The measured yield and ultimate strengths of the bar were 77.25 ksi (532.6 MPa) and 118.25 ksi (815.3 MPa), respectively.
- Steel Tube: Tubes encasing reinforcing bars were made of ASTM A513 Grade 1026 carbon steel. The yield and the ultimate strengths of the steel tubes were 66 ksi (455 MPa) and 75 ksi (517.1 MPa), respectively.
- Non-Shrink Grout: Conventional non-shrink fine-aggregate high-flow grout was used to fill the gap between reinforcing bars and steel tubes. The test-day measured compressive strength of the grout was 6.78 ksi (46.8 MPa) to 10.19 ksi (70.3 MPa).

2.4.3 BRR Test Setup

Figure 2-13 and 2-14 show the self-reacting compressive setup used for BRR testing. This setup consisted of four post-tensioning rods passing through three steel plates (grade ASTM A36) each with a thickness of 1 in. (25.4 mm) and one 200-kips (889.6-kN) hydraulic jack. Two steel plates were equipped with steel cups at the center of the plates to secure the test specimen from any movement during loading. The average displacement rate of the hydraulic jack, which was controlled manually, was 0.0052 in./sec (132 mm/sec).

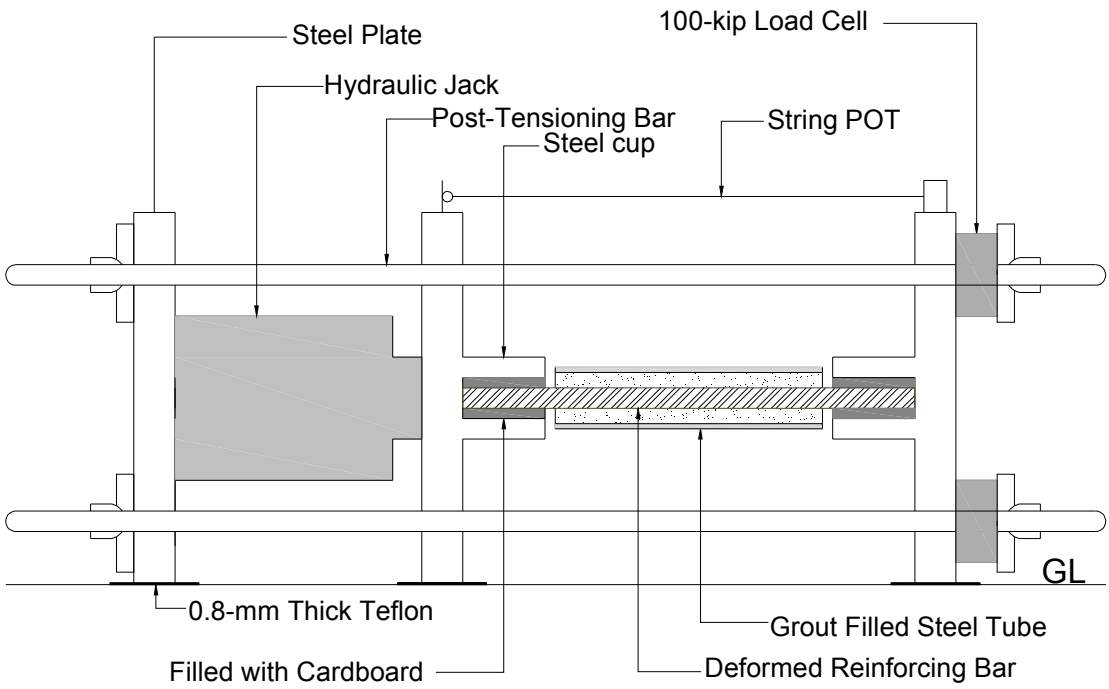

Figure 2-13. Elevation View of BRR Test Setup

Figure 2-14. Photograph of BRR Test Setup

2.5 BRR Experimental Results

All BRR specimens were tested according to the details presented in the previous

section. A summary of the test results is presented herein.

2.5.1 BRR Failure Mechanism

Figure 2-15a shows the failure mode of a reference deformed No. 4 (13 mm) bar with a total length of 11 in. (279 mm or 22 times the bar diameter, d_b) under compression in which the No. 4 (13 mm) bar buckled at a compressive stress of 23.45 ksi (161.7 MPa). In an attempt to improve the bar buckling resistance, bars were passed through a series of steel hex nuts. The gap between the nuts and the face of the steel cups in the axial direction (Fig. 2-15b, c and d) was varied by changing the number of the nuts. It was found that the compressive behavior of a nut-encased reinforcement is the same as that of the unrestrained steel bar (Fig. 2-15a) if the gap is not filled during the testing (or when the gap is large). Furthermore, a reinforcing steel bar can be restrained against buckling and the compressive strength can exceed the yield strength of the bar if the total gap in the series of the nuts does not exceed $0.5d_b$. Based on these findings, nine BRR were subsequently tested to failure to further validate the initial findings and to investigate the compressive performance.

(a) No4-BL11.00d
(b) No4-BL11.00d-Nuts-G0.875
(c) No4-BL11.00d-Nuts-G0.42
(d) No4-BL11.00d-Nuts-G0.20
(e) No4-BL11.00d-TL5.0s-TG18-G3.0
(f) No4-BL10.94d-TL5.0s-TG16-G2.94
(g) No4-BL12.20d-TL7.5s-TG14-G0.5
(h) No4-BL12.28d-TL7.5s-TG16-G0.29
(i) No4-BL14.81d-TL7.5s-TG13-G0.5
(j) No4-BL14.81d-TL7.5s-TG14-G0.5
(k) No8-BL17.00d-TL10.0s-TG11-G1.0
(l) No8-BL14.56d-TL10.0s-TG13-G0.5
(m) No8-BL19.62d-TL15.0s-TG11-G0.5

Figure 2-15. Failure of BRR Specimens (Tuhin, 2016)

Figure 2-15 shows failure modes of the nine BRR specimens under compressive loads. For No. 4 (13 mm) BRR, the device buckled at very large stresses [200 ksi (1379 MPa)] where the total axial gap between the tube and the cup was not more than $0.5d_b$. For cases in which the gap was more than $0.5d_b$, the specimen deformed in a "Z-shape" manner (Fig. 2-15g and h). Larger gaps resulted in lower compressive strength before bucking. Similar to No. 4 (13 mm) BRR, No. 8 (25 mm) BRR showed large compressive stresses before failure when the total axial gap was $0.5d_b$.

In summary, it was found that a short BRR exhibits higher compressive stress and strain capacities compared to a long BRR with the same properties. BRR with thicker tubes achieve higher stress and strain capacities compared to those with thinner tubes. Finally, the axial gap between the tube and the support plays a significant role to control the compressive behavior of BRR. This gap should be limited to one half of the bar diameter.

2.5.2 BRR Stress-Strain Relationships

Table 2-2 presents the peak stress and strain values obtained from BRR tests. The stress-strain data show that deformed steel bar can achieve high stresses, even higher than the ultimate compressive strength of the bar, when the total axial gap is less than half the bar diameter. Those high stresses can be explained due to the engagement of the nuts in compression after the closure of the gap. It is worth mentioning that the strain corresponding to peak stress was approximately 3%.

Table 2-2. Stress-Strain Peak Values for All Specimens

Specimen ID	Peak Stress, ksi (MPa)	Strain at Peak Stress (in./in.)
No4-BL11.00d	23.45 (161.7)	0.005
No4-BL10.94d	21.06 (145.2)	0.003
No8-BL16.91d	51.48 (354.9)	0.007
No8-BL10.25d	53.19 (366.7)	0.008
No4-BL11.00d-Nuts-G0.875	28.14 (194)	0.005
No4-BL11.00d-Nuts-G0.42	40.46 (279)	0.034
No4-BL11.00d-Nuts-G0.20	144.71 (997.7)	0.034
No4-BL11.00d-TL5.0s-TG18-G3.00	42.46 (292.7)	0.021
No4-BL10.94d-TL5.0s-TG16-G2.94	68.61 (473)	0.033
No4-BL12.28d-TL7.5s-TG16-G0.50	168.03 (1158.5)	0.062
No4-BL12.20d-TL7.5s-TG14-G0.50	222.97 (1537.3)	0.078
No4-BL14.81d-TL7.5s-TG14-G0.50	196.24 (1353)	0.052
No4-BL14.81d-TL7.5s-TG13-G0.50	191.63 (1321.2)	0.056
No8-BL14.56d-TL10.0s-TG13-G0.50	150.04 (1034.5)	0.113
No8-BL17.00d-TL10.0s-TG11-G1.00	112.2 (773.6)	0.064
No8-BL19.62d-TL15.0s-TG11-G0.50	Setup Limit	Setup Limit

Figure 2-16 shows stress-strain relationships of all buckling restrained reinforcement and the reference bars. It can be seen that the unrestrained steel bars buckled under low compressive stresses (less than the yield strength). Also, with proper detailing (e.g. minimal total axial gap, sufficient tube diameter, and tube wall thickness), it is possible to achieve large stress and strain capacities for the proposed buckling restrained reinforcement. Note the dashed horizontal lines in Fig. 2-16 are the measured tensile yield and ultimate strength for the steel bars used in BRR assuming that the steel bar stress-strain behavior is symmetric in tension and compression.

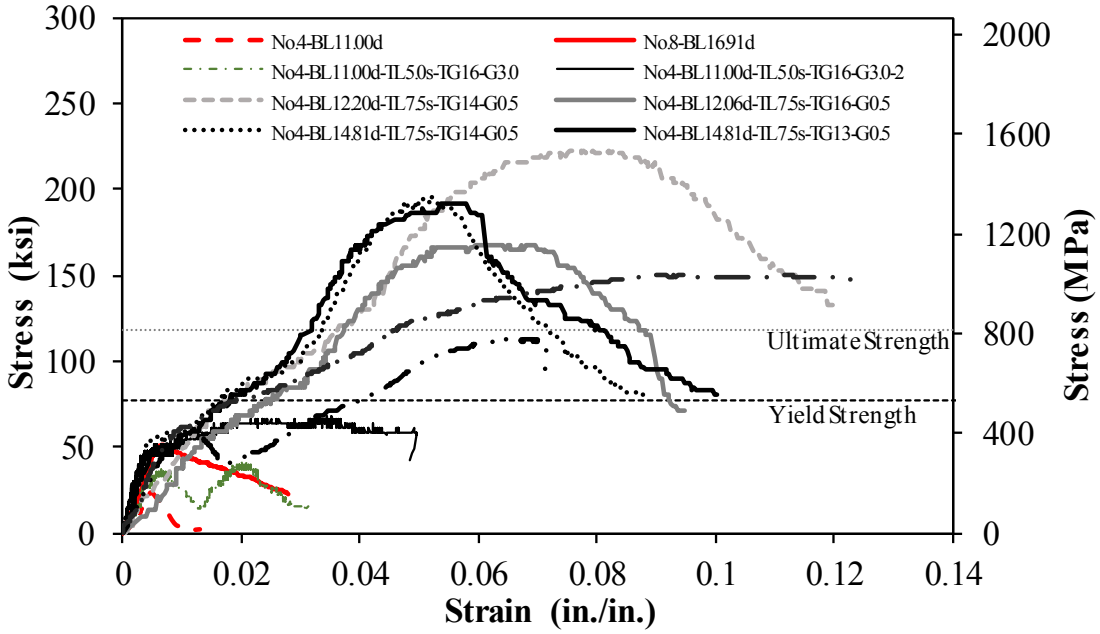

Figure 2-16. Stress-Strain Relationships for Buckling Restrained Reinforcement

The compressive stress of BRR can exceed the ultimate strength of the bar because of the contribution of the tube/grout after the gap closure. The compressive strain at the peak stress can exceed 5%, which will be sufficient in most practical cases since the strain of compressive reinforcement in a concrete section is usually controlled by the core concrete strains. The core concrete strain capacity even in a highly confined section does not exceed 5%.

2.6 Proposed Design Methodology for Buckling Restrained Reinforcement

Sarti et al. (2016) investigated the compressive behavior of BRRD through experimental and analytical studies. They proposed an equation to estimate the buckling force of the device. However, no systematic design method was proposed for buckling restrained reinforcement. A simple design method for both BRR and BRRD was developed in the present study and is summarized herein.

Figure 2-17 shows BRR/BRRD design parameters assuming that the tube is not filled with grout. In this case, bar will locally buckle under compressive loads until touching the inner side of the tube causing bending of the tube as a beam. Based on the experimental findings, BRR/BRRD with a longitudinal gap of half the bar diameter ($0.5d_b$) or less will fail at very high stresses (twice the ultimate strength of the bar) thus other modes of failure (e.g. Z-shape bending) is prevented meeting this gap requirement. It can be assumed that the steel bar inside the tube acts as a truss element. Therefore, three plastic hinges are needed to make the bar unstable. It was assumed that two hinges are at the locations where the bar buckles (Fig. 2-17b and c) inside the tube and one hinge forms on the bar at the middle of the tube.

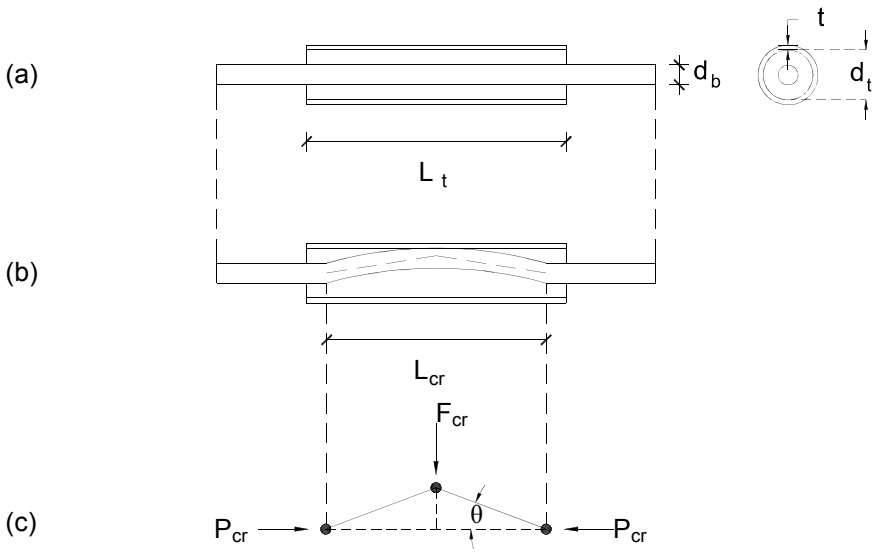

Figure 2-17. Design Parameters for Buckling Restrained Reinforcement

The buckling load of a bar can be estimated using the Euler's buckling equation:

$$P_{cr} = \frac{\pi^2 \mathrm{EI}}{(KL)^2} \tag{2-2}$$

where E is the modulus of elasticity of the bar, I is the moment of inertia of the bar, L is the length of the bar, and K is the effective length factor. K=1 for pinned-pinned elements, thus, the critical length required to cause bar buckling is

$$L_{cr} = \sqrt{\frac{\pi^2 \mathrm{EI}}{P_{cr}}} \tag{2-3}$$

The maximum possible compressive strength of a bar is equal to the plastic force of the bar, which is the product of the bar area (A_b) and the bar ultimate stress (f_{ub}), which was conservatively assumed to be 1.5 times the yield strength (f_{yb}) for ASTM A706 and ASTM A615 bars. These two types of reinforcement are extensively utilized in buildings and bridges.

$$P_{cr} = A_b \times f_{ub} = 1.5 \times A_b \times f_{yb} \tag{2-4}$$

Substituting Eq. 2-4 in Eq. 2-2

$$L_{cr} = \sqrt{\frac{\pi^2 \mathrm{EI}}{1.5 A_b . f_{yb}}} = 0.64 d_b \sqrt{\frac{\mathrm{E}}{f_{yb}}} \tag{2-5}$$

Since the bar is enclosed in a tube, it can be assumed that there is a resisting vertical force (F_{cr} in Fig. 2-17c) at the middle hinge when the vertical gap between the inner side of the tube and the bar is closed (assuming there is no grout). The maximum vertical displacement of the bar before touching the tube can be obtained from the geometry. A relationship between P_{cr} and F_{cr} can be determined using the equilibrium at the truss joint as:

$$F_{cr} = 2 P_{cr} \times \tan(\theta) = 2 P_{cr} \times \frac{d_t - d_b}{L_{cr}} \tag{2-6}$$

where d_t is the inner tube diameter. By substituting Eq. 2-5 in Eq. 2-6:

$$F_{cr} = 3.1 P_{cr} \frac{d_t - d_b}{d_b} \sqrt{\frac{f_{yb}}{E}} \quad (2\text{-}7)$$

The lateral load on the tube (F) tends to bend the tube. The maximum bending stress can be assumed to be equal to the yield stress of the tube (f_{yt}):

$$f_{yt} = \frac{M}{S_{xt}} \quad (2\text{-}8)$$

where M is the bending moment at the mid-length of the tube ($F_{cr}.L_t/4$), L_t is the length of the tube, and S_{xt} is the tube section modulus. By substituting Eq. 2-7 in Eq. 2-8:

$$S_{xt-demand} = \frac{F_{cr} L_t}{4 f_{yt}} \quad (2\text{-}9)$$

From strength of material, $S_{xt} = I_t / y_t$ where I_t is the tube moment of inertia and $y_t = (d_t+2t)/2$ for a tube, where t is the wall-thickness of the tube. The tube section modulus can be expressed as:

$$S_{xt-capacity} = \frac{\pi[(d_t + 2t)^4 - d_t^4]}{32(d_t + 2t)} \quad (2\text{-}10)$$

Knowing the geometrical and mechanical properties for the bar and the tube, the tube thickness (t) for any bar diameter (d_b) can be estimated by equating Eq. 2-9 with Eq. 2-10. Alternately, any tube thickness that results in $S_{xt\text{-}capacity}$ greater than $S_{xt\text{-}demand}$ can be used for BRR.

2.7 Design Methodology Validation

The results of the BRR tests (Section 2.5) and experimental data from Sarti et al. (2016) were used to validate the proposed BRR design methodology. Since the mechanical properties of the steel bars and tubes were known, the critical buckling load for each BRR was calculated using the design methodology discussed in Sec. 2.6 and was

compared to the measured peak load for the corresponding specimen (Table 2-3). Note the proposed design method only includes the cases where BRR buckles but not Z-shape bending thus they are not reported in the table. It can be concluded that the calculated BRR capacities are always smaller than those measured in the tests indicating that the proposed design method is conservative and may be used to determine the tube sizes (Fig. 2-18). The proposed method is conservative since the contribution of grout to the BRR strength was not included.

Table 2-3. Measured and Calculated Buckling Forces for Buckling Restrained Reinforcement

Specimen ID	Bar/Fuse Dia., in. (mm)	Tube Length, in.(mm)	Measured Peak Load, kips (kN)	Calculated Peak Load, kips (kN)
No4-BL12.28d-TL7.5s-TG16-G0.5	0.5 (12.7)	7.0 (190.5)	33.60 (149.46)	12.52 (55.69)
No4-BL12.20d-TL7.5s-TG14-G0.5	0.5 (12.7)	7.5 (190.5)	44.59 (198.34)	15.91 (70.77)
No4-BL14.81d-TL7.5s-TG14-G0.5	0.5 (12.7)	7.5 (190.5)	39.24 (174.54)	15.91 (70.77)
No4-BL14.81d-TL7.5s-TG13-G0.5	0.5 (12.7)	7.5 (190.5)	38.33 (170.50)	19.45 (86.51)
No8-BL14.56d-TL10.0s-TG13-G0.5	1.0 (25.4)	10.0 (254)	118.53 (527.24)	55.41 (246.47)
No8-BL17.00d-TL10.0s-TG11-G1.0	1.0 (25.4)	10.0 (254)	88.63 (394.24)	75.14 (334.24)
D12L180 (Sarti et al., 2016)	0.5 (12)	7 (180)	19.65 (87.30)	14.2 (63.07)
D20L300 (Sarti et al., 2016)	0.8 (20)	11.8 (300)	41.00 (182.50)	28.06 (124.73)
D24L360 (Sarti et al., 2016)	0.95 (24)	14.2 (360)	82.10 (364.80)	43.70 (194.20)
D26L390 (Sarti et al., 2016)	1.0 (26)	15.4 (390)	80.33 (357.00)	49.80 (221.36)
D26L488 (Sarti et al., 2016)	1.0 (26)	19.2 (488)	68.69 (305.30)	39.80 (176.91)
D26L585 (Sarti et al., 2016)	1.0 (26)	23.0 (585)	65.68 (291.90)	33.21 (147.58)

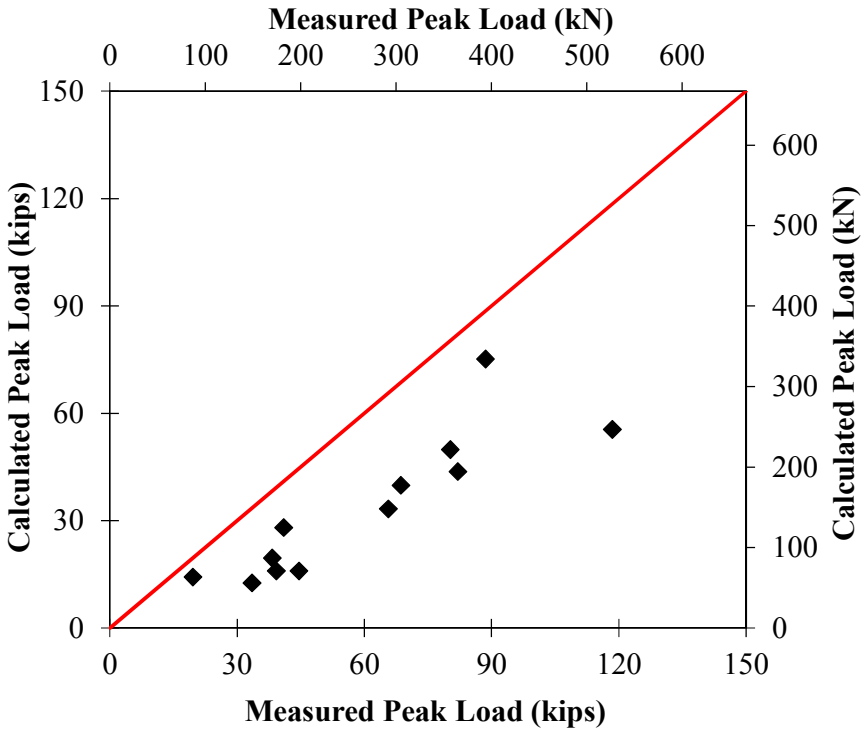

Figure 2-18. Measured versus Calculated Peak load

2.8 Summary and Conclusions

Previous studies demonstrated that dog-bone energy dissipaters play a significant role in improving the performance of hybrid rocking columns. In an attempt to reduce the cost accompanied with machining down these energy dissipating bars, conventional deformed steel bars were proposed in this study as a new energy dissipater, which was referred to as buckling restrained reinforcement (BRR). An experimental study was carried out by Tuhin (2016) to investigate the feasibility and performance of the proposed BRR.

A simple design method was proposed in the present study for both dog-bone and unreduced diameter BRR, and was validated using experimental data. The following conclusions can be drawn from the experimental (performed by Tuhin, 2016) and analytical investigations:

- The total axial gap between the support and BRR tube significantly affects the overall performance of BRR. A gap less than one half the bar diameter can lead to a BRR compressive strength that is higher than the ultimate reinforcing bar strength.
- The strain of BRR corresponding to its peak stress can exceed 5%, which will be sufficient in most practical cases since the strain of compressive reinforcement in a concrete section is usually controlled by the core concrete strains.
- Bar length can affect the overall BRR stress and strain capacities in a way that shorter bars provide higher compressive capacities than longer bars.
- Tube thickness has insignificant effect on the BRR performance if the tube is designed properly according to the proposed design method.

- The proposed BRR design method is conservative and may be used for the design of buckling restrained reinforcement.

2.9 References

1. Cattanach, A., Pampanin, S. (2008). "1st Century Precast: The Detailing and Manufacture of NZ's First Multi-Storey PRESSS-Building." NZ Concrete Industry Conference. Rotorua.
2. Pampanin, S. (2005). "Emerging Solutions for High Seismic Performance of Precast/Prestressed Concrete Buildings." Journal of Advanced Concrete Technology, 3(2), pp. 207-223.
3. Palermo, A., and Pampanin, S. (2008). "Enhanced Seismic Performance of Hybrid Bridge Systems: Comparison with Traditional Monolithic Solutions," Journal of Earthquake Engineering, 12(8), 1267-1295.
4. ASTM Standard E8/E8M-11 (2011). "Standard Test Methods for Tension Testing of Metallic Materials," ASTM International, West Conshohocken, PA.
5. ASTM Standard C39-12 (2012). "Standard Test Method for Compressive Strength of Cylinder Concrete Specimens," ASTM International, West Conshohocken, PA.
6. Marriott, D., Pampanin, S., and Palermo, A. (2009). "Quasi□Static and Pseudo□Dynamic Testing of Unbonded Post-Tensioned Rocking Bridge Piers with External Replaceable Dissipaters," Earthquake Engineering & Structural Dynamics, 38(3), 331-354.

7. Mesa, A., and Dario, A. (2010). “Developments of Advanced Solutions for Seismic Resisting Precast Concrete Frames,” PhD thesis, University of Canterbury, Christchurch, New Zealand.
8. Marriott, D., Pampanin, S., and Palermo, A. (2011). “Biaxial Testing of Unbonded Post□Tensioned Rocking Bridge Piers with External Replaceable Dissipaters. Earthquake Engineering & Structural Dynamics,” 40(15), 1723-1741.
9. Lukkunaprasit, P., Tangbunchoo, T., and Rodsin, K. (2011). “Enhancement of Seismic Performance of Reinforced Concrete Columns with Buckling-Restrained Reinforcement,” Engineering Structures, 33(2011), 3311-3316.
10. Mashal, M., Palermo, A., and Chegini, Z. (2014). “Quasi-Static Cyclic Tests of Half-Scale Fully Precast Bridge Bents Incorporating Emulative and Posttensioned Low Damage Solutions,” Paper presented at the 2nd European Conf. of Earthquake Engineering and Seismology, Turkish Earthquake Foundation, Istanbul, Turkey.
11. Guerrini, G., Restrepo, J. I., Massari, M., and Vervelidis, A. (2014). “Seismic Behavior of Posttensioned Self-Centering Precast Concrete Dual-Shell Steel Columns,” Journal of structural engineering, 141(4), 04014115.
12. Guerrini, G., Restrepo, J., Vervelidis, A., Massari, M. (2015). “Self-Centering Precast Concrete Dual-Steel-Shell Columns for Accelerated Bridge Construction: Seismic Performance, Analysis, and Design,” PEER Report No. 2015/13, Pacific Earthquake Engineering Research Center, Headquarters at the University of California, Berkeley

13. Guo, T., Cao, Z., Xu, Z., and Lu, S. (2015). "Cyclic Load Tests On Self-Centering Concrete Pier with External Dissipaters And Enhanced Durability," Journal of structural engineering, 142(1), 04015088.

14. White, S., and Palermo, A. (2016). "Quasi-Static Testing of Posttensioned Nonemulative Column-Footing Connections for Bridge Piers," Journal of Bridge Engineering, 21(6), 04016025.

15. Sarti, F., Palermo, A., and Pampanin, S. (2016). "Fuse-Type External Replaceable Dissipaters: Experimental Program and Numerical Modeling," Journal of structural engineering, 04016134.

16. Tuhin, I.A. (2016). “Application of New Materials and Innovative Detailing for Reinforced Concrete Structures,” MSc thesis, South Dakota State University, Brookings, SD.

Chapter 3: Repairable Precast Connections – Experimental Investigations

3.1 Introduction

The structural integrity of reinforced concrete buildings depends upon the performance of beam-column connections. Reinforced concrete (RC) moment-resisting frames (MRFs) are frequently used in seismic regions as lateral load resisting systems. Even though seismic detailing based on current design specifications ensure life safety performance level for buildings, damage of structural components is expected in extreme events. Minor damages may be repaired. Nevertheless, severely structurally damaged buildings are usually replaced which may impose substantial economic and social costs to the owners and public. An innovative detailing was developed for precast buildings in which all components are precast and the damages is limited to replaceable reinforcement, which was referred to as buckling restrained reinforcement (BRR) in Ch. 2, to eliminate the building total replacement. The feasibility of the new detailing for precast MRFs was experimentally and analytically investigated. This chapter presents the details of the experimental study. The findings of the analytical study are presented in the following chapter.

First, a prototype nine-story conventional RC MRF was designed then a half-scale cast-in-place beam-column specimen (CIP) was tested to failure under slow cyclic loading to serve as the benchmark model. This phase was completed by Tuhin (2016). The design, detailing, and testing of a new repairable beam-column joint were performed under the present study and are discussed in this chapter. The detailing of the proposed precast connection is presented first. Then, the test matrix and the design of the precast specimens are discussed. The test setup, loading protocol, instrumentation, and the test results are presented subsequently for each specimen. Finally, the seismic performance of all specimens is evaluated for comparison.

3.2 Proposed Precast Connection Detailing

Figure 3-1 shows the main components of the proposed precast beam-column specimen, which includes (1) fully precast beams and columns with exposed longitudinal reinforcement, (2) a shear pin made of steel pipe to be inserted into a steel cup placed in the column, (3) mechanical bar splices that can be detached, (4) external reinforcement restrained against buckling (BRR) to connect the precast beam reinforcement to the column reinforcement, and (5) a steel plate between the precast column and the beam to prevent damage during lateral deformations. The beam section has to be reduced at the end, which is referred to as “neck” region hereafter, to align BRR with the beam and column reinforcement. All components are designed as capacity protected members except BRR, which is allowed to yield and fracture. The proposed connection is repairable since the exposed reinforcement, BRR, can be replaced after a severe event without the use of any other repair methods such as patching, jacketing, etc.

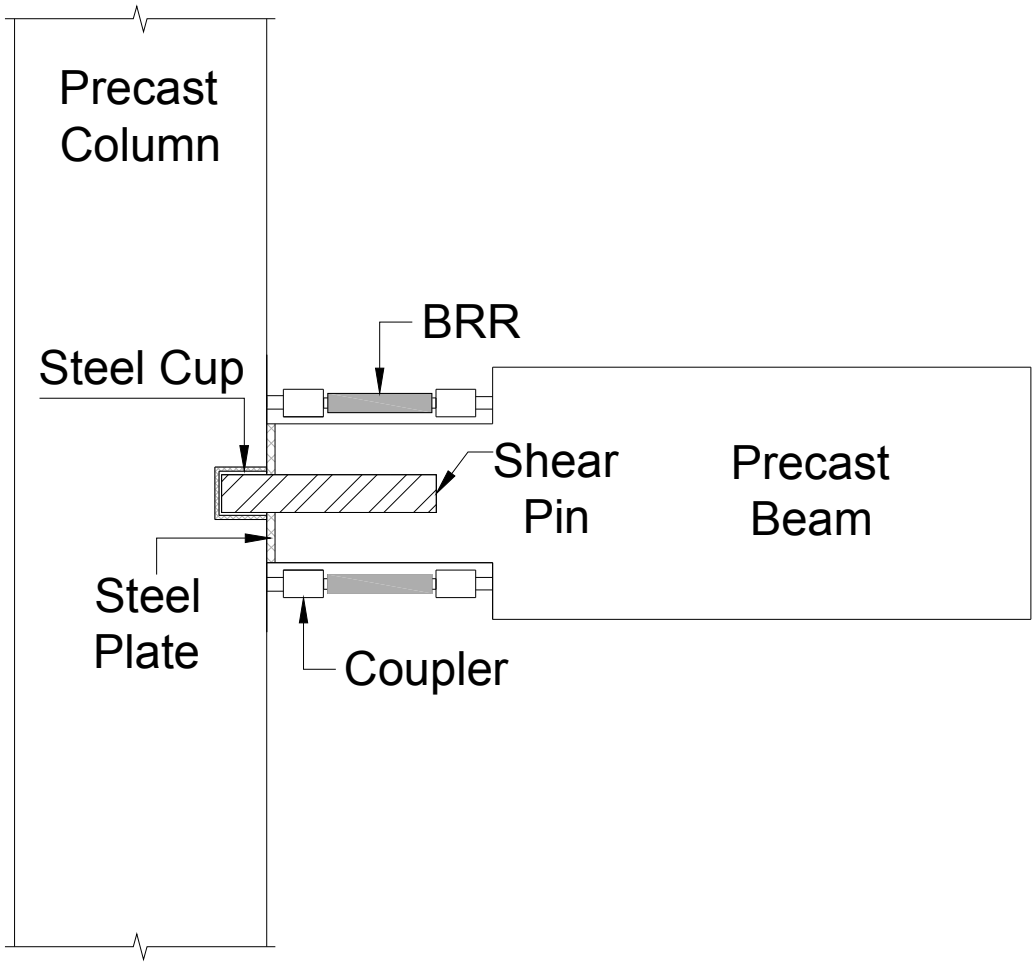

Figure 3-1. Proposed Precast Beam-Column Connection Details

The precast beam-column connection can be designed using current codes (e.g. ACI 318-14). A heavy-duty steel pipe embedded in the beam is used as a shear pin to transfer plastic shear forces. The steel pipe can be extended into the column where a steel cup is embedded. A gap between the pipe and the cup will allow rotation of the pipe inside the cup. Shear pipe-pin design guidelines proposed in by Zaghi and Saiidi (2010) were adopted in the present study.

Detachable mechanical bar splices are utilized to connect the precast beam longitudinal reinforcement, replaceable exposed bars or BRR, and the precast column reinforcement. A steel plate can be used at the interface of the two concrete members to

avoid damage of concrete during lateral movements. Exposed reinforcing steel bars cannot resist compressive forces since they buckle at low compressive loads. Therefore, they should be restrained against buckling. Refer to Ch. 2 to the proposed design method for BRR.

3.3 Test Matrix for Beam-Column Specimens

Three specimens (Table 3-1) including one reference CIP beam-column model and two repairable precast beam-column models were constructed and tested under a cyclic loading protocol. Each repairable specimen was tested twice, before and after the repair, by replacing the exposed reinforcement with either the same but new steel BRR or new shape memory alloy (SMA) BRR. It was decided to assign a different label to each precast specimen before and after the repair for the ease of comparison. Table 3-1 presents the test matrix for the five beam-column specimens including geometry and BRR type. Note the four precast specimens were consisted of only one precast column and two precast beams as identified in the table footnote.

Table 3-1. Test Matrix for Half-Scale Beam-Column Specimens

Specimen ID	Beam Cross Section, in. (mm)	Neck Cross Section, in. (mm)	Column Cross Section, in. (mm)	Steel Plate Thickness, in., (mm)	BRR Type	Long. Bar Area, in^2 (mm^2)
CIP	15×10 (381×254)	N/A	15×15 (381×381)	N/A	None	Top: 0.62 (400) Bot: 0.4 (258)
PBC1-D	15×10[(a)] (381×254)	8.25×10 (210×254)	15×15[(c)] (381×381)	0.5, (13)	Dog-Bone Steel	Top: 0.6 (387) Bot: 0.33 (213)
PBC1-D-R	15×10[(a)] (381×254)	8.25×10 (210×254)	15×15[(c)] (381×381)	0.5, (13)	Dog-Bone Steel	Top: 0.6 (387) Bot: 0.33 (213)
PBC2-D	15×10[(b)] (381×254)	8.25×10 (210×254)	15×15[(c)] (381×381)	1.0, (25)	Dog-Bone Steel	Top: 0.6 (387) Bot: 0.33 (213)
PBC2-SMA	15×10[(b)] (381×254)	8.25×10 (210×254)	15×15[(c)] (381×381)	0.5, (13)	SMA	Top: 0.6 (387) Bot: 0.6 (387)

Note: CIP: Cast-in-Place; BRR: Buckling Restrained Reinforcement; SMA: Shape Memory Alloy.
[(a)] Only one precast beam was used in PBC1-D and PBC1-D-R.
[(b)] Only one precast beam was used in PBC2-D and PBC2-D-SMA.
[(c)] Only one precast column was used in all four precast specimens.

3.4 Design and Construction of Beam-Column Specimens

The five beam-column specimens discussed above were designed, constructed, and tested at the Lohr Structures Laboratory at South Dakota State University. The CIP specimen was a half-scale model of an exterior beam-column connection located at the first story of a nine-story prototype special moment-resisting frame (SMRF). Subsequently, the precast specimens were detailed based on the CIP specimen but incorporating the new detailing. This section discusses the design of the nine-story prototype RC SMRF, design of test specimens, and construction of each beam-column specimen.

3.4.1 Design of Test Specimens

3.4.1.1 Introduction

Ordinary, intermediate, and special RC MRFs are used in different seismic regions of the country to accommodate the different seismic demands. SMRFs are usually used in high seismic regions since they are detailed to exhibit large lateral

displacements before collapse. In SMRFs, "strong column – weak beam" design philosophy is preserved to achieve large displacement capacities. A SMRF was utilized in the present study since SMRFs are the most ductile RC structures thus they can be used as the baseline to comment the performance of the proposed precast buildings.

3.4.1.2 Design of Nine-Story RC Special Moment-Resisting Building

The nine-story RC SMRF building was designed based on the requirements of ASCE 7-10 (2010) and was seismically detailed based on the requirements of ACI318-14 (2014).

3.4.1.3 Design of Prototype Beam-Column Specimen

Figure 3-2 and 3-3 show the plan view and the elevation of the prototype building, respectively. The five-by-five bay nine-story RC SMRF building was assumed to be located in Los Angeles, CA, which is a high seismic region. The building was designed in a way that each three stories had the same beams and columns in terms of section dimensions. The floor plan was assumed to be the same for all levels. SAP2000 software was utilized to design the prototype building. The concrete compressive strength was assumed to 5000 psi (34.47 MPa). ASTM A706 Grade 60 (2009) reinforcing steel bars were used as the longitudinal and transverse reinforcement in the prototype building. More information about the design of the prototype nine-story building can be found in Tuhin (2016).

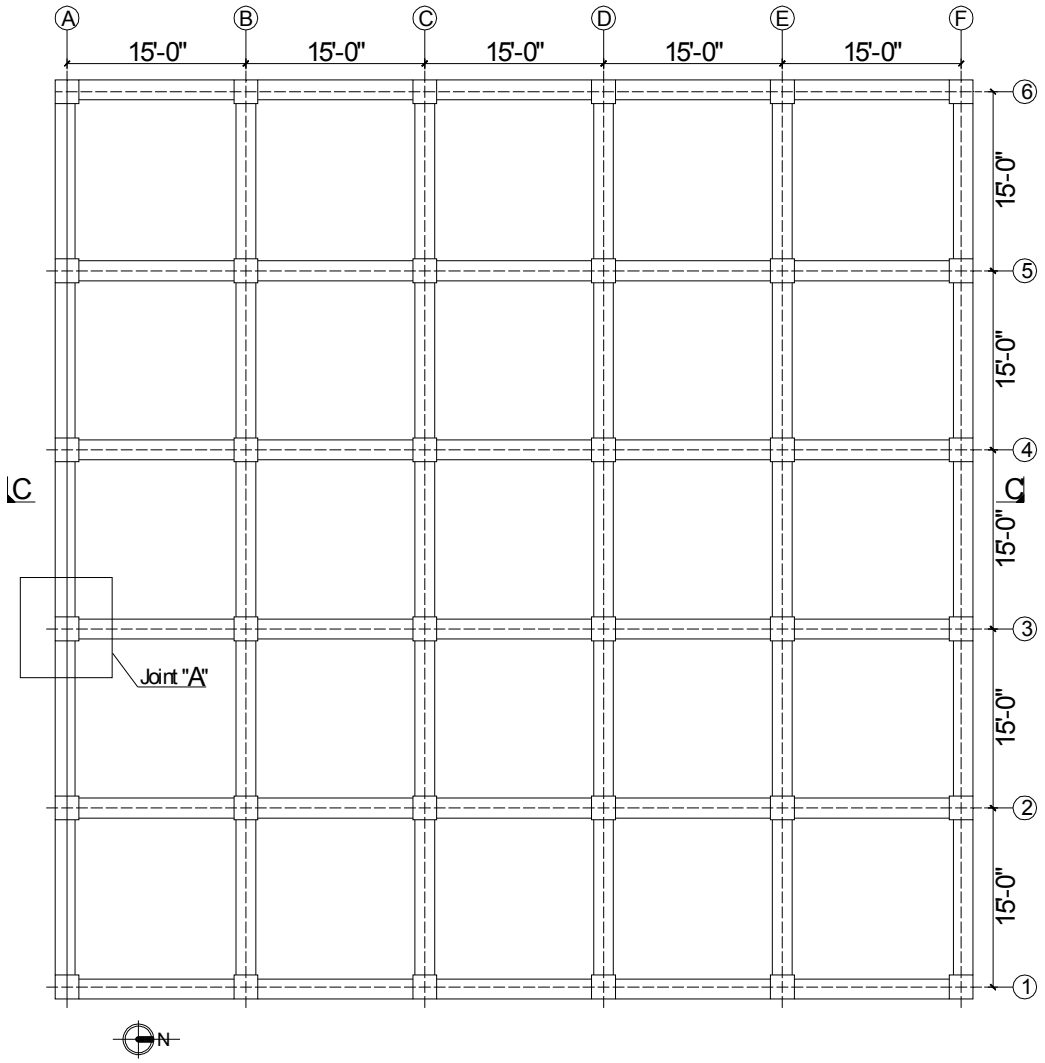

Figure 3-2. Plan View of Nine-Story RC Building (Tuhin, 2016)

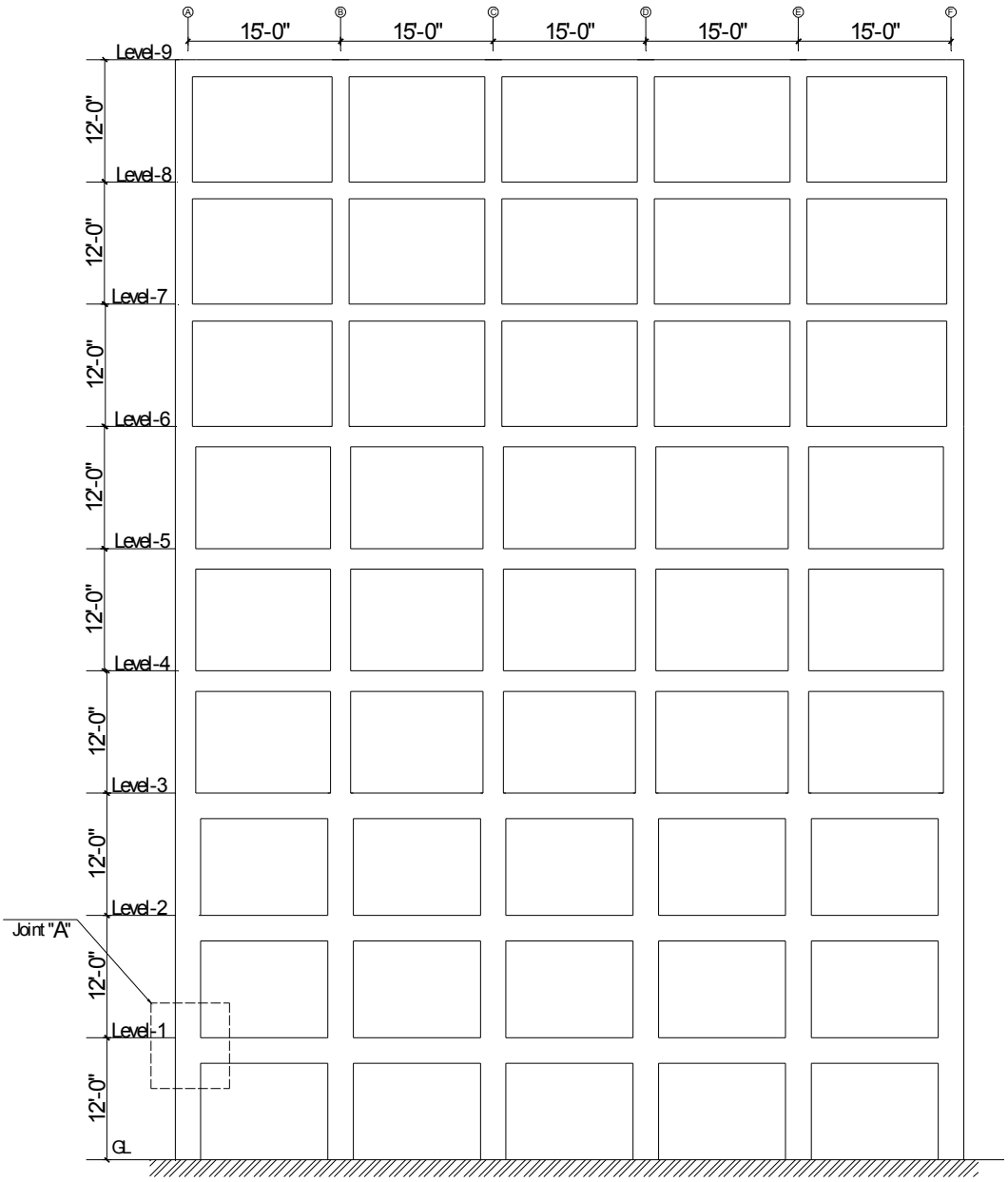

Figure 3-3. Elevation View of Nine-Story Building (Tuhin, 2016)

External joint A as marked in Fig. 3-3 was selected as the prototype beam-column specimen. Figure 3-4 shows the details of the prototype beam-column specimen. The dimension of the prototype beam and the column was 20 × 30 in. (508×762 mm) and 30 × 30 in. (762×762 mm), respectively. The column was longitudinally reinforced with 8 No. 10 (32 mm) bars and the beam was longitudinally reinforced with 3 No. 8 (25 mm)

bars at the top and 3 No. 7 (22 mm) bars at the bottom. No. 3 (10 mm) transverse bars spaced 6 in. (152 mm) was used to confine the beam sections.

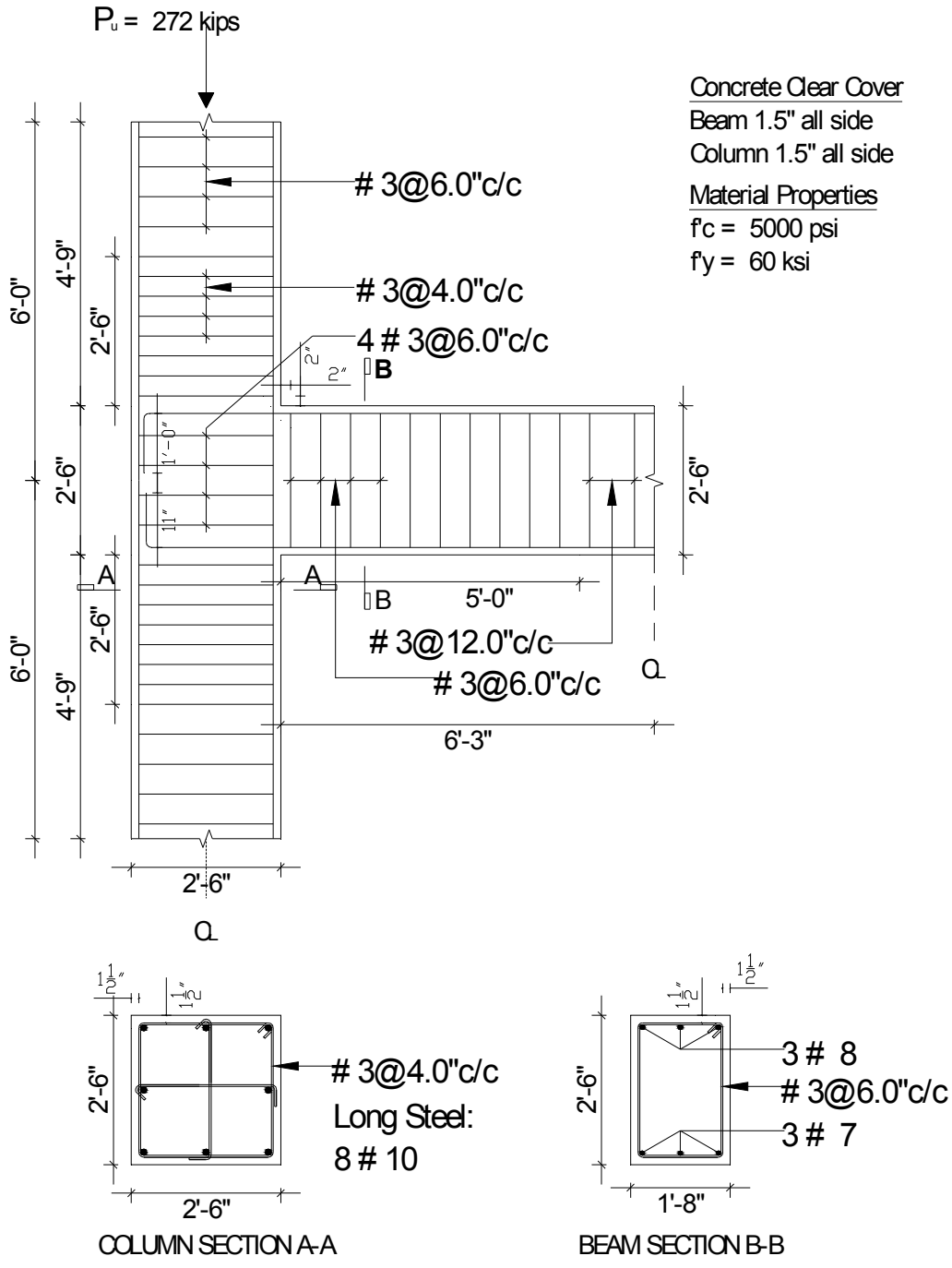

Figure 3-4. Detailing of Prototype Exterior Beam-Column Specimen (Tuhin, 2016)

3.4.1.4 Design of Half-Scale Beam-Column Specimen (CIP)

A half-scale beam-column specimen (Fig. 3-5) based on the prototype connection was selected to serve as the reference CIP test specimen. The scaling procedure proposed by Krawlnkler and Piotr (1982) was followed. The transverse bar size, spacing, and type of the scaled model was changed to keep the confinement the same (using the model proposed by Mander et al., 1998) as that in the prototype specimen.

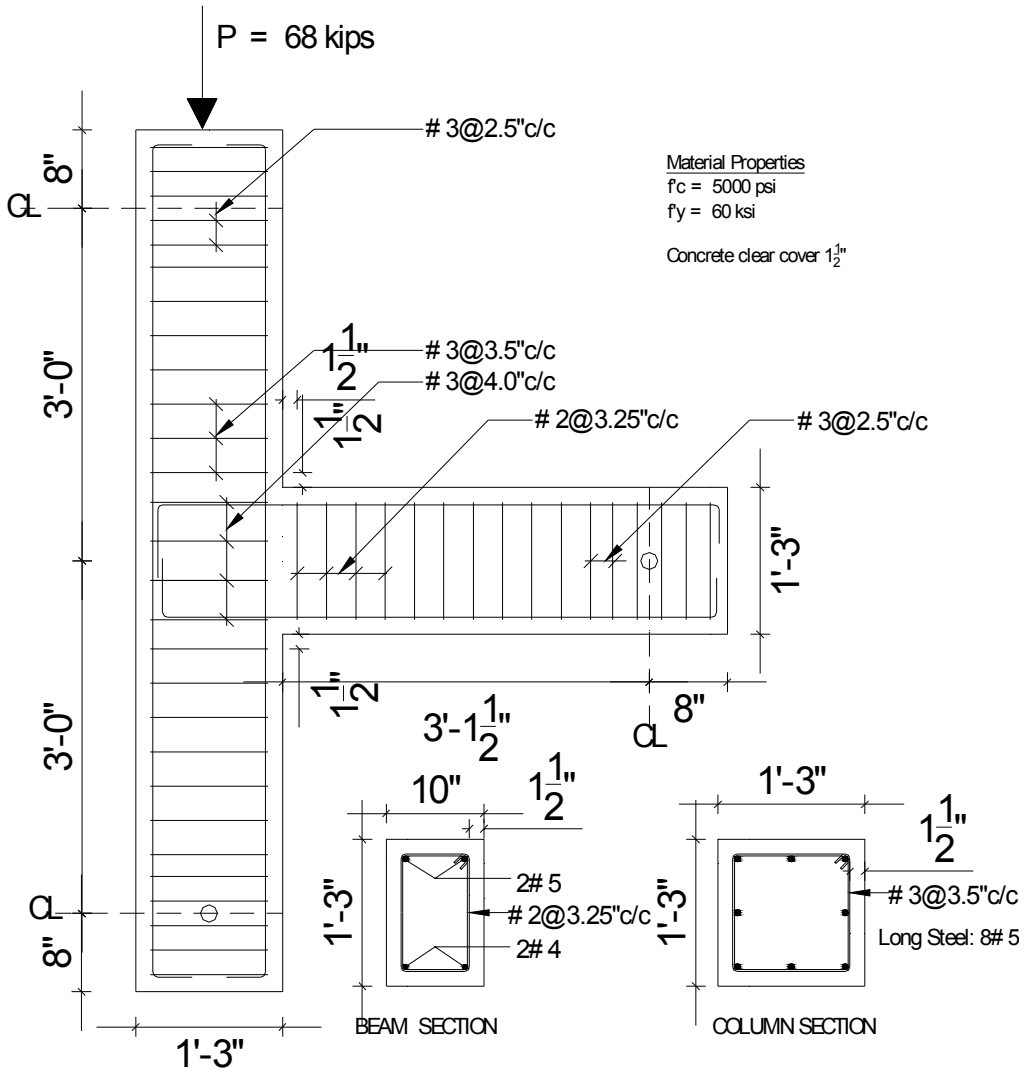

Figure 3-5. Detailing of CIP Beam-Column Specimen (Tuhin, 2016)

The dimension of the beam and the column of the half-scale CIP specimen was 10 × 15 in. (254×381 mm) and 15 × 15 in. (381×381 mm), respectively. The test beam and column lengths were 45 in. (1143 mm) and 72 in. (1829 mm), respectively. The concrete properties, and the longitudinal reinforcement types and properties were the same as those in prototype model. The column was longitudinally reinforced with 8 No. 5 (16 mm) bars and the beam was longitudinally reinforced with 2 No. 5 (16 mm) bars at the top and 2 No. 3 (13 mm) bars at the bottom. The transverse reinforcement for the beam was No. 2 steel wires conforming to ASTM A496 (Table 3-2). The design axial load for the half-scale column specimen (P) was 68 kips (302.5 kN).

Table 3-2. Mechanical Properties of ASTM A496 Grade 75 Steel Wires Used as Beam Stirrups

Mechanical property	Value
Yield Stress, f_y, ksi (MPa)	75 (517)
Modulus of Elasticity, E_s, ksi (MPa)	29000 (200000)
Ultimate Tensile Strength, f_u, ksi (MPa)	85 (586)

3.4.1.5 Design of Precast Beam-Column Specimens

Two precast beams (pilot, and improved detailing) and one precast column were designed and constructed to be used in the four precast beam-column specimens discussed in Sec. 3.3. The detailing of these precast beams and column is presented herein.

3.4.1.5.1 Design of Pilot Half-Scale Precast Beam-Column Specimen (PBC1)

A pilot half-scale fully precast beam-column specimen, which is referred to as PBC1 hereafter, was developed by modifying the CIP beam-column specimen (Sec. 3.4.1.4) incorporating the proposed precast detailing (Sec. 3.2) as shown in Fig. 3.6. The precast specimen has the same geometry, reinforcement type, and material properties as those in CIP but incorporating the new connection detailing.

The depth of the neck was 8.25 in. (210 mm) while the beam depth was 15 in. (381 mm) The column longitudinal and transverse reinforcement in PBC1 specimen were 12 No. 4 (13 mm) and No. 3 (10 mm) ties at 3.5 in. (89 mm) center to center, respectively. Both top and bottom reinforcement in the beam of PBC1 were oversized to 3 No. 6 (19 mm) compared to the CIP model to ensure the yielding of steel will only occur within the BRR. ASTM A706 Grade 60 reinforcing steel bars were chosen for both longitudinal and transverse reinforcement in both specimens. The target compressive strength of concrete was 5000 psi and the concrete cover was 1.5 in (38 mm). Three BRR with a fuse length of 5 in. (127 mm) and a reduced diameter of 0.5 in. (12.7 mm) were used as top reinforcement while three BRR with a fuse length of 5 in. (127mm) and a reduced diameter of 0.375 in. (10 mm) were used at bottom to match the reinforcement area in CIP specimen. All BRR where made of ASTM A706 Grade 60 reinforcing steel bars encased in ASTM A513 Grade 1026 carbon steel tubes. The gap between the steel bar and the tube was filled with non-shrink grout. The same but new BRR were used in for the repair and retesting of PBC1.

Headed couplers were used to adjoin the BRR to the adjacent reinforcement in the precast beam and column. A 0.5-in. (13-mm) thick Grade 36 (250 MPa) steel plate was utilized at the beam-column interface to distribute the compressive stresses and to prevent concrete crushing. A shear pin embedded in the beam and extended into the column through a steel cup was used to resist the shear force. The design of the shear pin, which was based on Zaghi and Saiidi (2010), is illustrated in Appendix A.

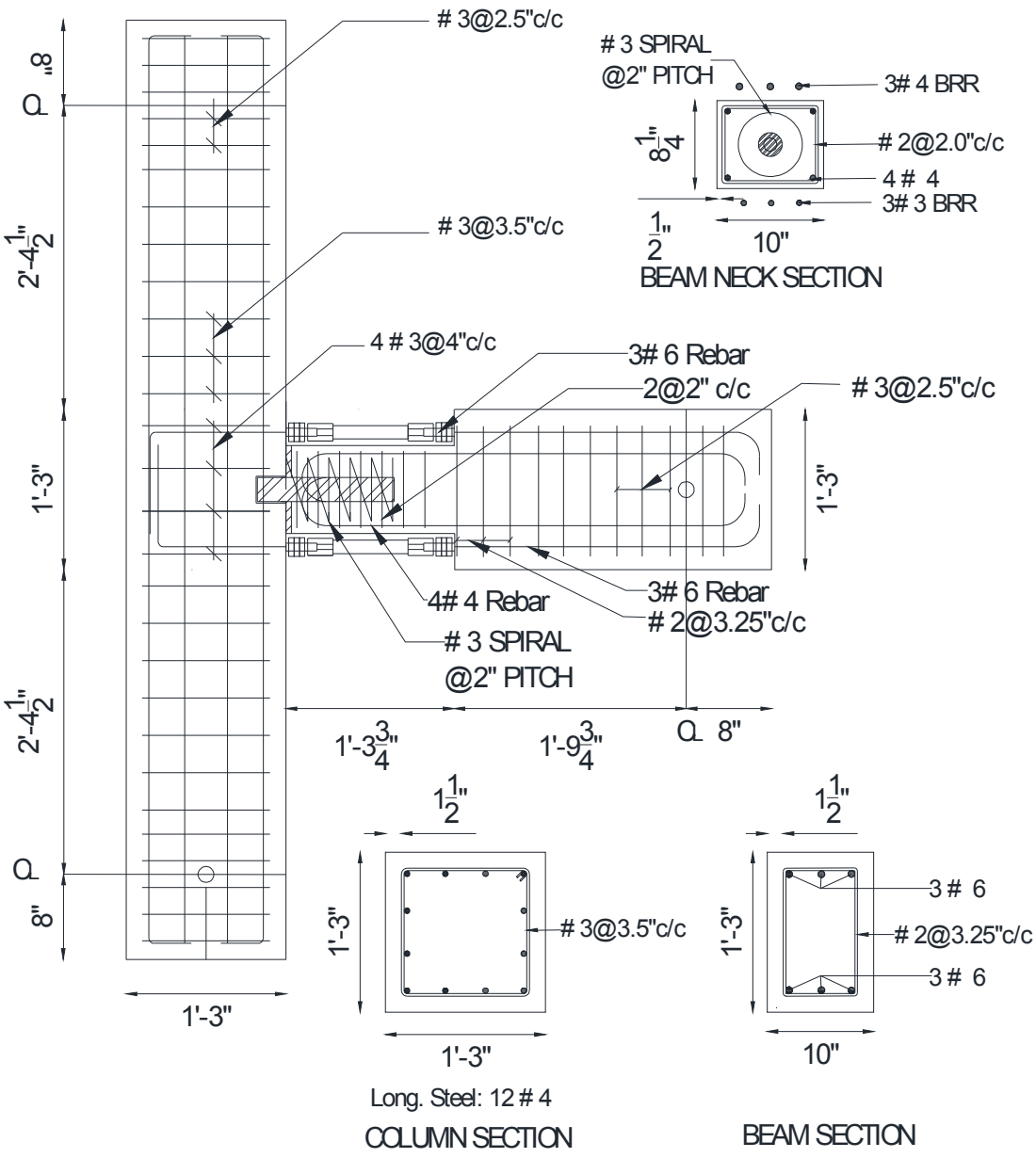

Figure 3-6. Detailing of Pilot Precast Beam-Column Specimen, PBC1

3.4.1.5.2 Design of Improved Half-Scale Beam-Column Specimen (PBC2)

After testing PBC1, another half-scale precast beam similar to that in PBC1 was constructed to enhance the structural performance. The specimen consisted of the improved beam detailing and the column which was used in PBC1 is referred to as PBC2. The overall geometry and reinforcement of the precast beam in PBC2 is similar to those

in PBC1. Figure 3-7 shows the detailing of PBC2. PBC2 had more longitudinal reinforcement (10 No. 5 [16 mm]) within the neck region compared to that in PBC1 to resist 1.25 of the plastic moment of the neck (Fig. 3-8).

The neck reinforcement was developed 3 ft (914 mm) beyond the beam depth change inside the beam to comply with the ACI318-14 development length requirements. To avoid bar strain concentration where the section depth changes, the precast beam longitudinal reinforcement (No. 6 [19 mm]) was debonded from the concrete with a length of 5 in. (127 mm) as shown in Fig. 3-7. Debonding was done by wrapping the bar with two layers of duct tape.

Dog-bone steel BRR with the geometry similar to that discussed in PBC1 were used in PBC2-D. After this test, the steel BRR were replaced with shape memory alloy BRR (PBC2-SMA) to exercise the repair by bar replacement and to minimize residual displacements. Each SMA BRR was 9-in. (229 mm) long with a diameter of 0.5 in. (12.7 mm). Six SMA BRR were used at the top or bottom of the precast beam, three bars per side.

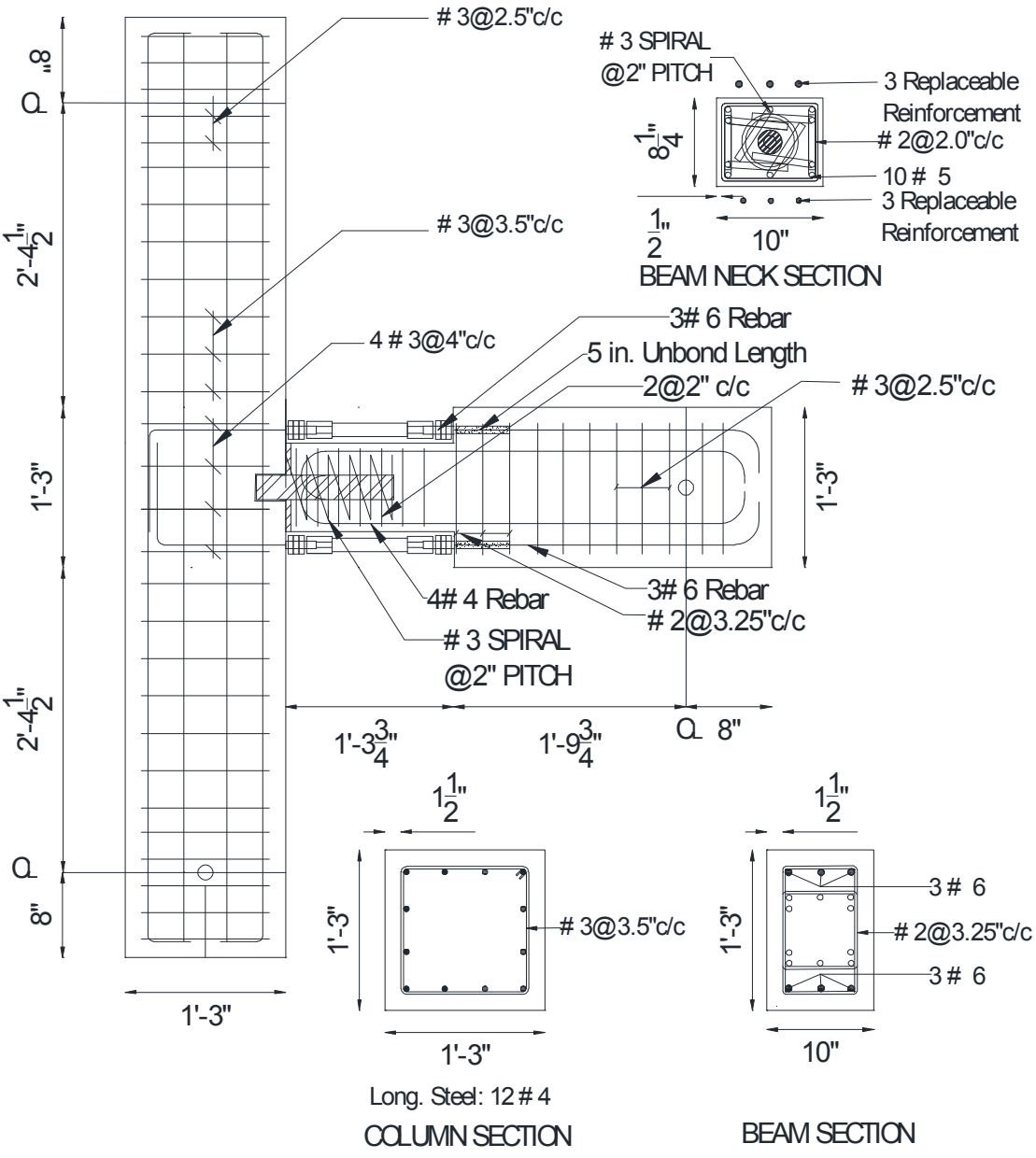

Figure 3-7. Detailing of Improved Precast Beam-Column Specimen, PBC2

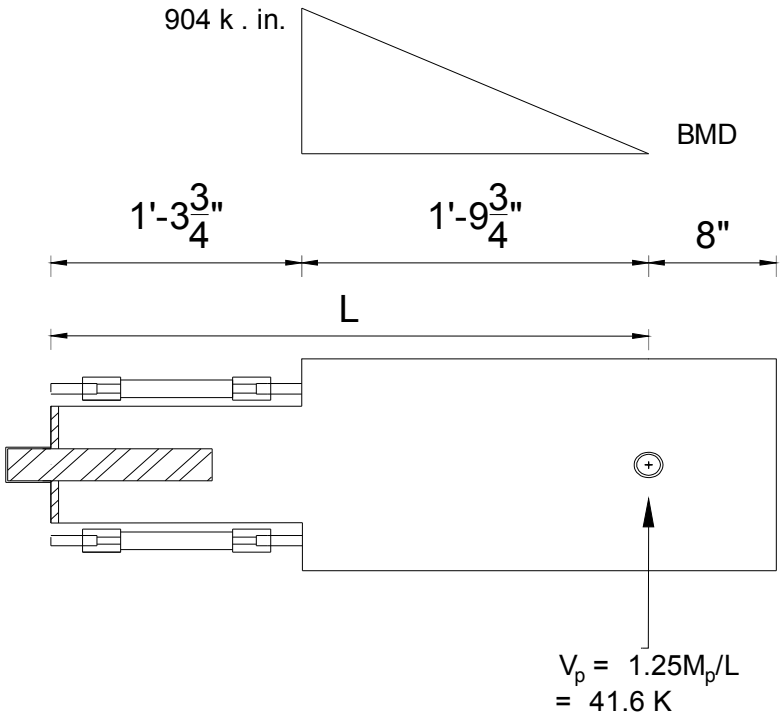

Figure 3-8. Plastic Moment Resisted by Beam Neck

3.4.2 Construction of Precast Beam-Column Specimens

This section discusses the construction of the two repairable precast beam-column specimens, PBC1 and PBC2. The construction of CIP specimen was discussed in detail in Tuhin (2016).

3.4.2.1 Construction of Pilot Precast Beam-Column Specimen, PBC1

The construction stages of PBC1 can be summarized as:

- Fabricating the dog-bone steel BRR (Fig. 3-9)
- Preparing the wood formwork (Fig. 3-10)
- Preparing steel cages and installing strain gauges (Fig. 3-11)
- Placement of steel cages into the wood formwork (Fig. 3-12)
- Pouring ready-mixed concrete (Fig. 3-13)

- Erecting and positioning precast column followed by installing the precast beam then installing BRR using headed bar couplers to complete the test specimen (Fig. 3-14)

a) Dog-bone Steel Bars b) Steel Tubes c) Assembled BRR

Figure 3-9. Fabrication of Dog-Bone Steel BRR

Figure 3-10. Construction of Wood Formwork for Precast Beam-Column Specimens

a) Strain Gauges on Longitudinal Reinforcement

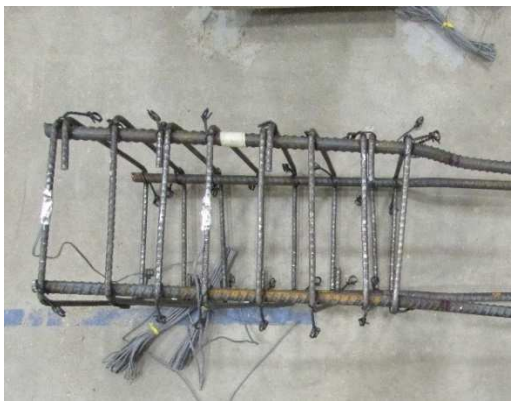

b) Strain Gauges on Transverse Reinforcement

Figure 3-11. Strain Gauge Installation on Precast Beam-Column Specimens

a) Beam Steel Cage

b) Column Steel Cage

Figure 3-12. Assembly of Steel Cages for Precast Beam-Column Specimens

Figure 3-13. Pouring Concrete for Precast Beam-Column Specimens

a) Column Installation

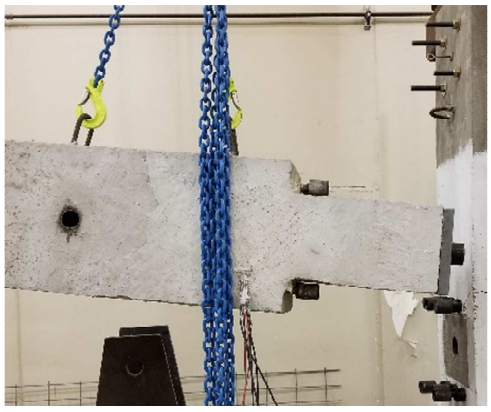

b) Beam Installation

Figure 3-14. Erecting and Positioning of PBC1 Elements

To form BRR, Gauge 14 ASTM A513 Grade 1026 carbon steel tubes were fixed on a wood formwork using steel straps. ASTM A706 Grade 60 reinforcing steel bars were machined down to different diameters (Fig. 3-15) then were passed through the pipes. The gap between the steel bar and the tube was filled with a non-shrink grout

(HP). The bottom of the tubes was sealed using duct tapes to prevent grout leakage. The main reinforcement in both beam and columns were connected to headed BRR using HRC couplers. Two different sizes of BRR were used as the top and bottom beam reinforcement. Number five (16 mm) headed reinforcing bars machined down to No. 4 (13 mm) with a fuse length of 5 in. (127 mm) were used as the top BRR. The bottom BRR incorporated No. 4 (13 mm) reinforcing bars machined to No. 3 (10 mm) with a 5 in. (127 mm) fuse length.

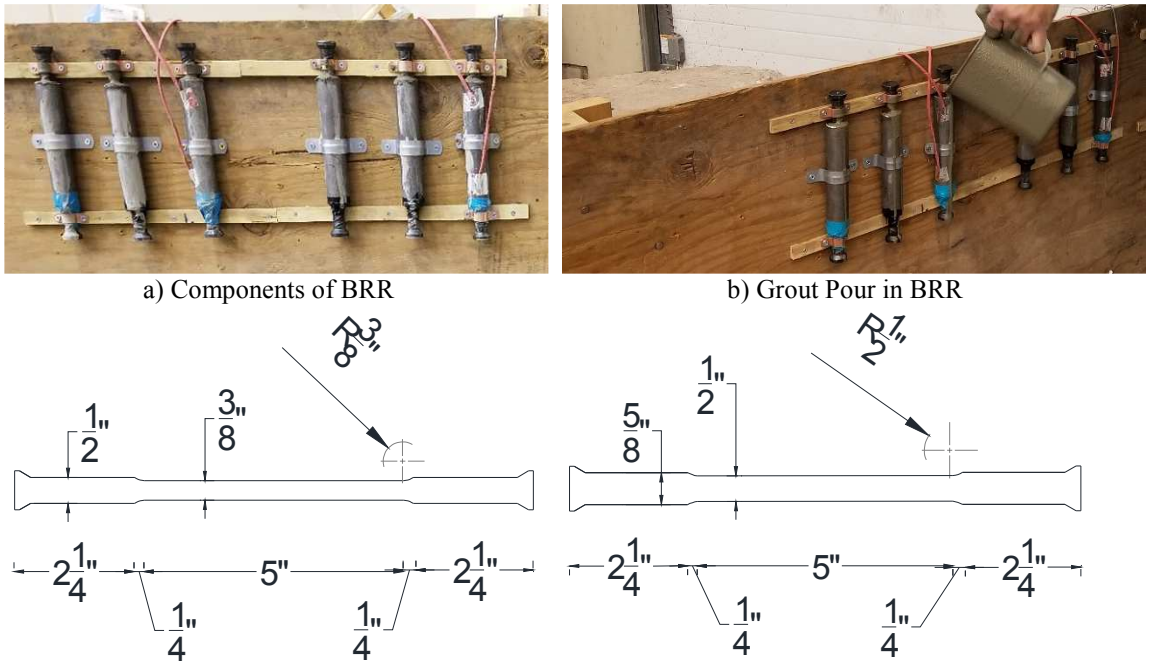

a) Components of BRR

b) Grout Pour in BRR

c) Dimension of No.4 BRR Bar

d) Dimension of No.5 BRR Bar

Figure 3-15. Dimensions of BRR Bars Used in PBC1 Specimen

A 2.5 in. (64 mm) inner diameter steel cup was placed into the column to accommodate the shear pipe-pin, which was embedded inside the beam with a distance of 12.75 in. (324 mm).

Different spacers were used to provide a clear cover of 1.5 in. (38 mm) for the column and the unreduced beam region, and a clear cover of 0.5 in. (13mm) for the neck region. A slump test was performed according to ASTM standard C143 (2012) before

pouring concrete (Fig. 3-16). The ready-mix concrete slump was 4.5 in. (114 mm). Sixteen 6- by 12-in (152- by 305-mm) standard concrete cylinders were collected for compressive strength testing according to ASTM C617-12 (2012). Twelve 2-in. (50-mm) cube grout samples were collected to measure the grout compressive strength according to ASTM C1019-16 (2012). After the cure of PBC1, the beam was disassembled from the column then the column was placed on the test setup. A 0.5-in. (127-mm) Grade 36 (250 MPa) steel plate was placed at the beam-column interface before the reassembly of the beam-column specimen.

Figure 3-16. Slump Test for PBC1 Specimen

3.4.2.2 Construction of Improved Precast Beam-Column Specimen, PBC2

The second precast specimen (PBC2) utilizes the same precast column from the PBC1 specimen. Only a new precast beam with improved detailing was constructed in this phase. At first, a wood formwork was constructed for the beam and then the steel

cage was assembled and positioned inside the formwork. The construction steps and arrangement of PBC2 beam were similar to those in PBC1 with the following exceptions: (1) 10 No. 5 (16 mm) reinforcing bars were placed inside the neck region, (2) the beam longitudinal bars were debonded from concrete using two wraps of duct tape with a length of 5 in. (127 mm) from where the beam depth changes. Figures 3-17 to 3-21 show different stages of the PBC2 specimen construction.

The slump for the ready-mix concrete in PBC2 was 3.5 in. (89 mm) (Fig. 3-21). Sixteen 6- by 12-in. (152- by 305-mm) standard concrete cylinders were collected for compressive strength testing according to ASTM C617-12 (2012). Twelve 2-in. (50-mm) cube grout samples were collected to measure the grout compressive strength according to ASTM C1019-16 (2012).

a) Steel BRR b) SMA BRR

Figure 3-17. Construction of BRR Used in PBC2 Specimen

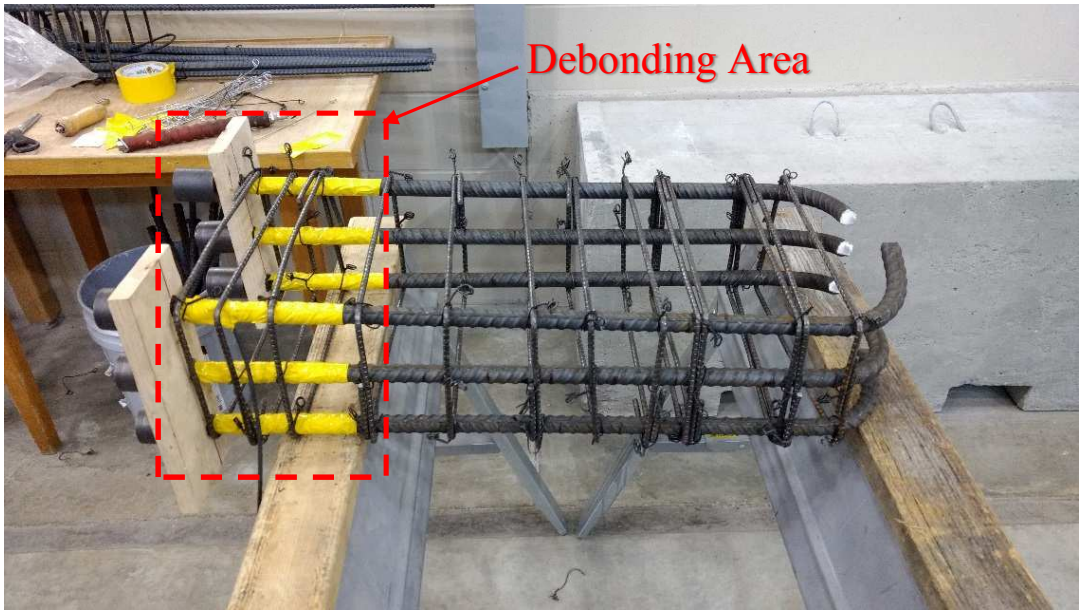

Figure 3-18. Debonding Beam Longitudinal Reinforcement in PBC2

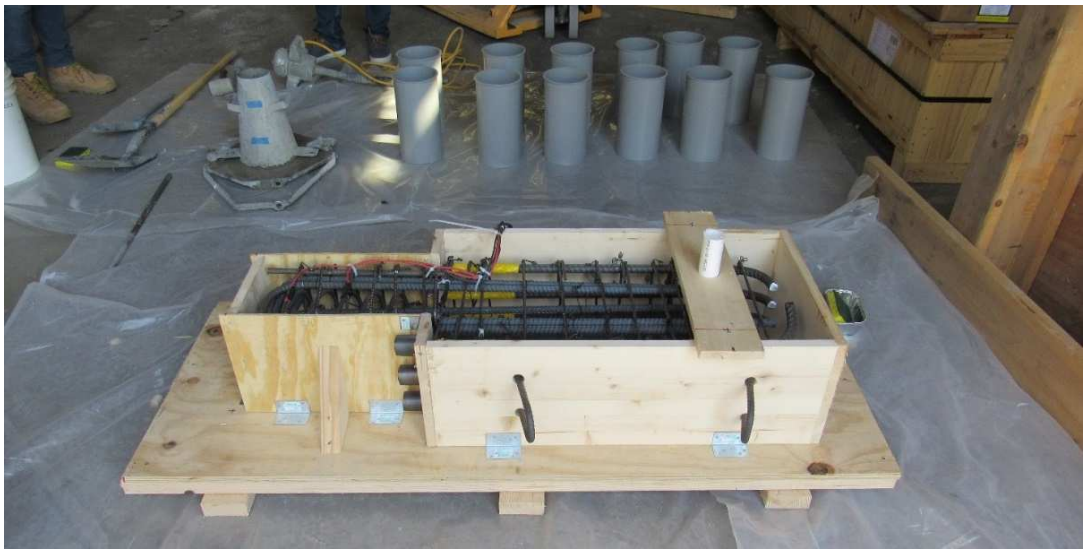

Figure 3-19. Construction of Steel Cage and Formwork for PBC

Figure 3-20. Beam for PBC2 after Concrete Curing

Figure 3-21. Slump Test for PBC2 Specimen

Two types of BRR (Fig. 3-22) were used in PBC2, dog-bone steel BRR for the first testing and SMA BRR for the repair and retesting. All steel BRR were constructed using No. 5 (16 mm) reinforcing bars. The top BRR reinforcing bars were machined down to No. 4 (13 mm) with a fuse length of 5 in. (127 mm) while the bottom bars were machined down to No. 3 (10 mm) with the same fuse length. The total length of steel BRR from head to head was 10 in. (254 mm) for all steel BRR. SMA BRR were constructed using 0.5-in. (127-mm) SMA bar with a total length of 9 in. (229 mm) head to head.

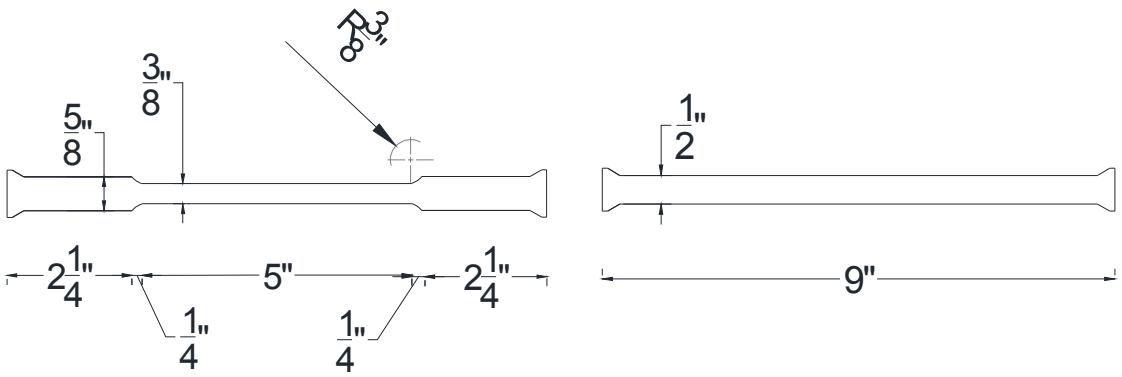

a) Dimension of Steel BRR Bar b) Dimension of SMA BRR Bar

Figure 3-22. Dimension of BRR Bars Used in PBC2 Specimen

To compensate for the length difference of the two types of BRR, two steel plates with two different thicknesses were used for the testing of each specimen. The length of the neck region was 0.5 in. (13 mm) shorter than that in PBC1 thus a 1-in. (25-mm) thick steel plate was used with dog-bone steel BRR. A 0.5 in. (13mm) steel plate was used with the SMA BRR in retesting. The other 0.5 in. (13mm) difference in length was compensated by using steel spacers inside the headed bar splices.

3.5 Test setup, Loading Protocol, and Instrumentation for Beam-Column Specimens

The test setup, instrumentation, and loading protocol used for all beam-column specimens are discussed in this section.

3.5.1 Test Setup for Beam-Column Specimens

Figure 3-23 shows the test setup used for CIP and precast specimens. To simulate the lateral displacements of the test beam-column specimen within a portal frame, the column was pinned at the base while the beam was supported by a roller at the end. The pinned support (the rocker) was fabricated using a heavy-duty steel shaft passing through vertically slotted steel chair and through steel pipe installed at the column base (Fig. 3-23b). The roller support was constructed using the same configuration for the rocker but

with the steel chair had a long horizontal slotted-hole to allow the beam to displace in its axial direction or the lateral direction of the frame (Fig. 3-23c). The vertical gap between the steel shaft and the chair was closed using a hand-tight bolt to prevent any uplift in the beam.

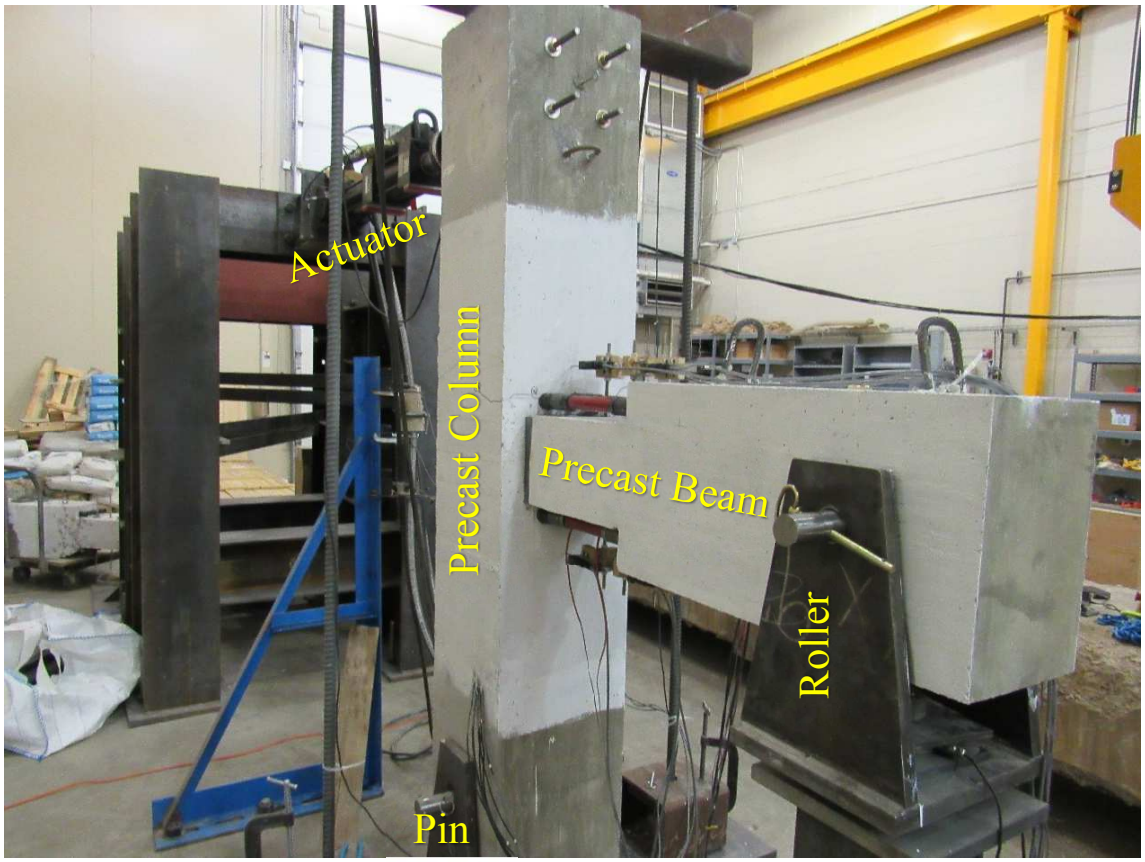

a) Complete test setup

b) Reaction Chair under Column

c) Reaction Chair under Beam

Figure 3-23. Photograph of Test Setup for PBC1 Specimen

More details of the test setup are shown in Figures 3-24 and 3-25. An axial load of 68 kips (302.5 kN) was applied to the top of the column using two post tensioning bars and two 100 kips (445 kN) hollow-core jacks. A 22-kip (98-kN) actuator with a ±5-in. (127-mm) stroke was used at the column tip to apply lateral displacements using a cyclic loading protocol.

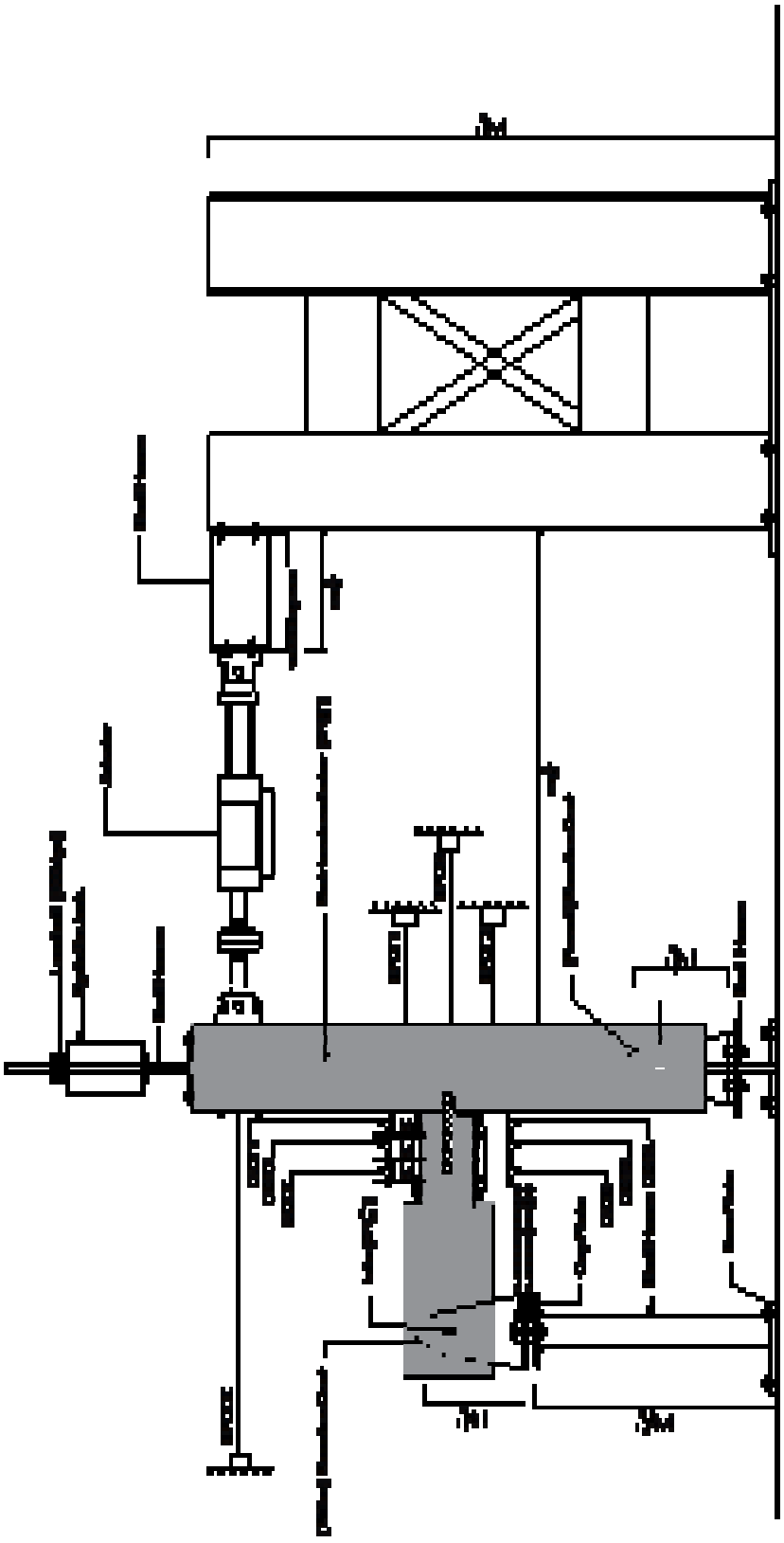

Figure 3-24. Test Setup for Precast Beam-Column Specimens

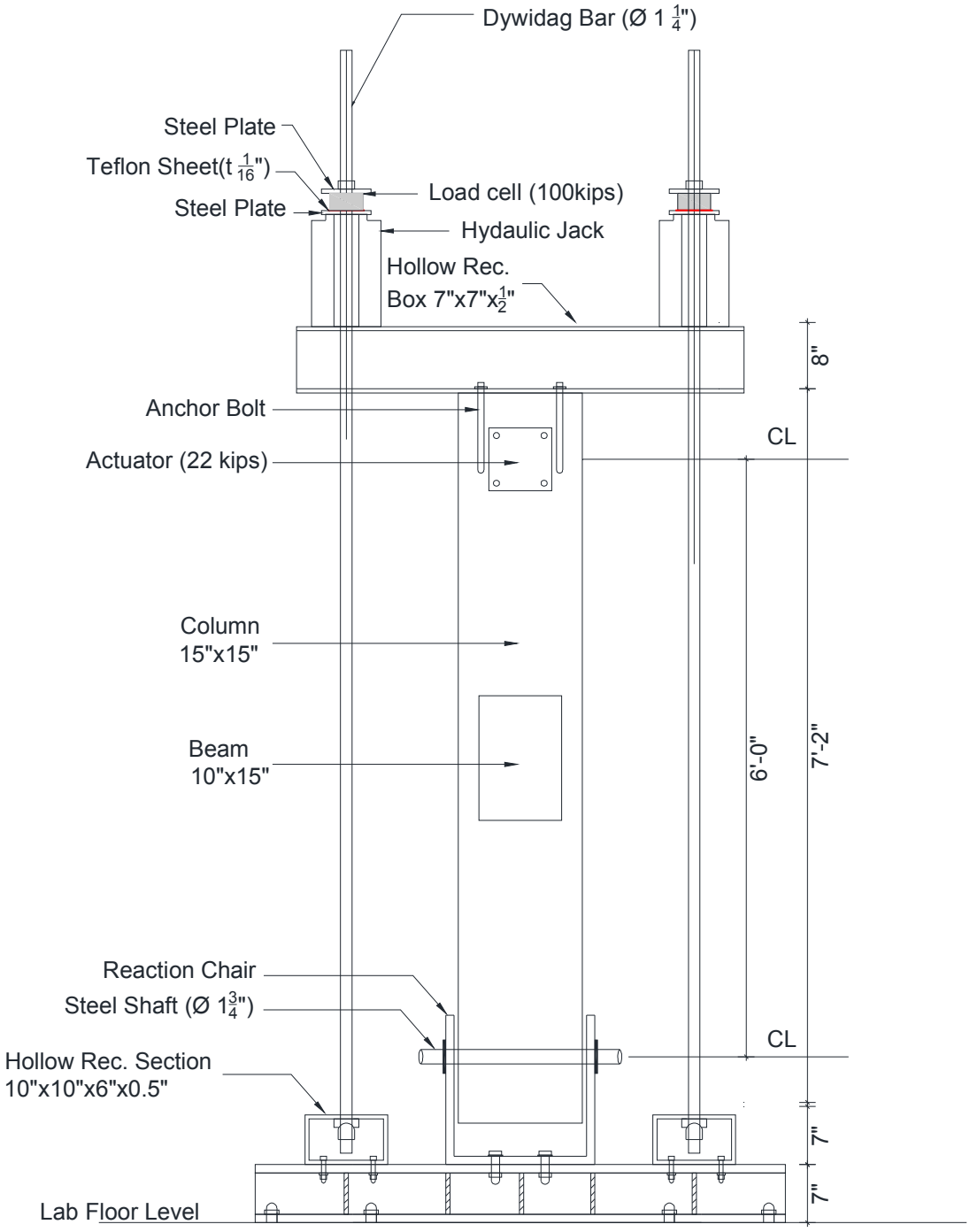

Figure 3-25. Axial Load Setup for Precast Beam-Column Specimens

3.5.2 Instrumentation of Beam-Column Specimens

Both precast beam-column specimens were tested with the same instrumentation plan. Eighteen strain gauges were utilized in the precast specimens to measure the strains at different locations (Fig. 3-26). Four strain gauges were installed on the top and the bottom longitudinal reinforcing steel bars of each precast beam (two per bar), four strain gauges were placed on one of the top and the bottom BRR (two per bar), four were installed on the longitudinal bars of the precast column, and six were installed on the transverse reinforcement of beam or column.

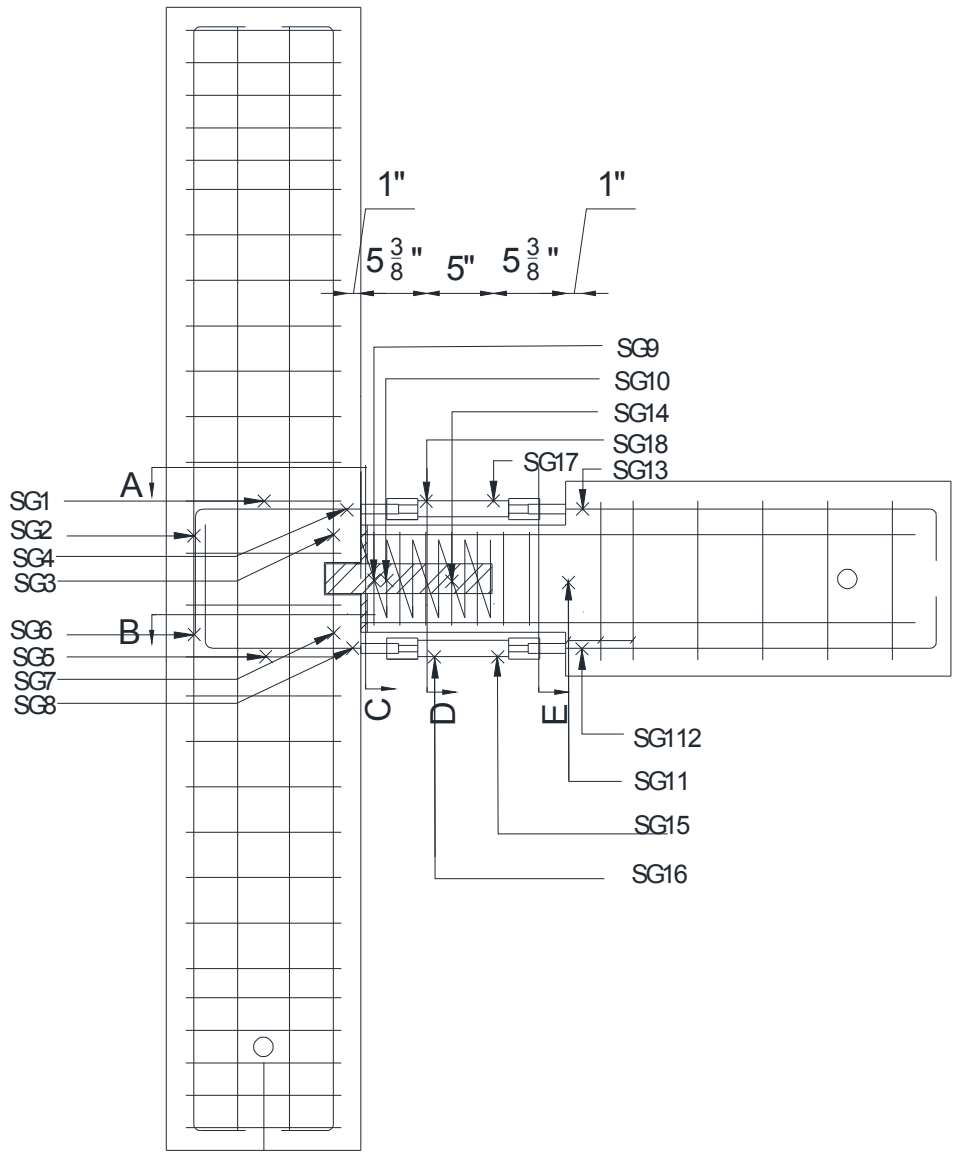

Figure 3-26. Strain Gauges Locations for Precast Beam-Column Specimens

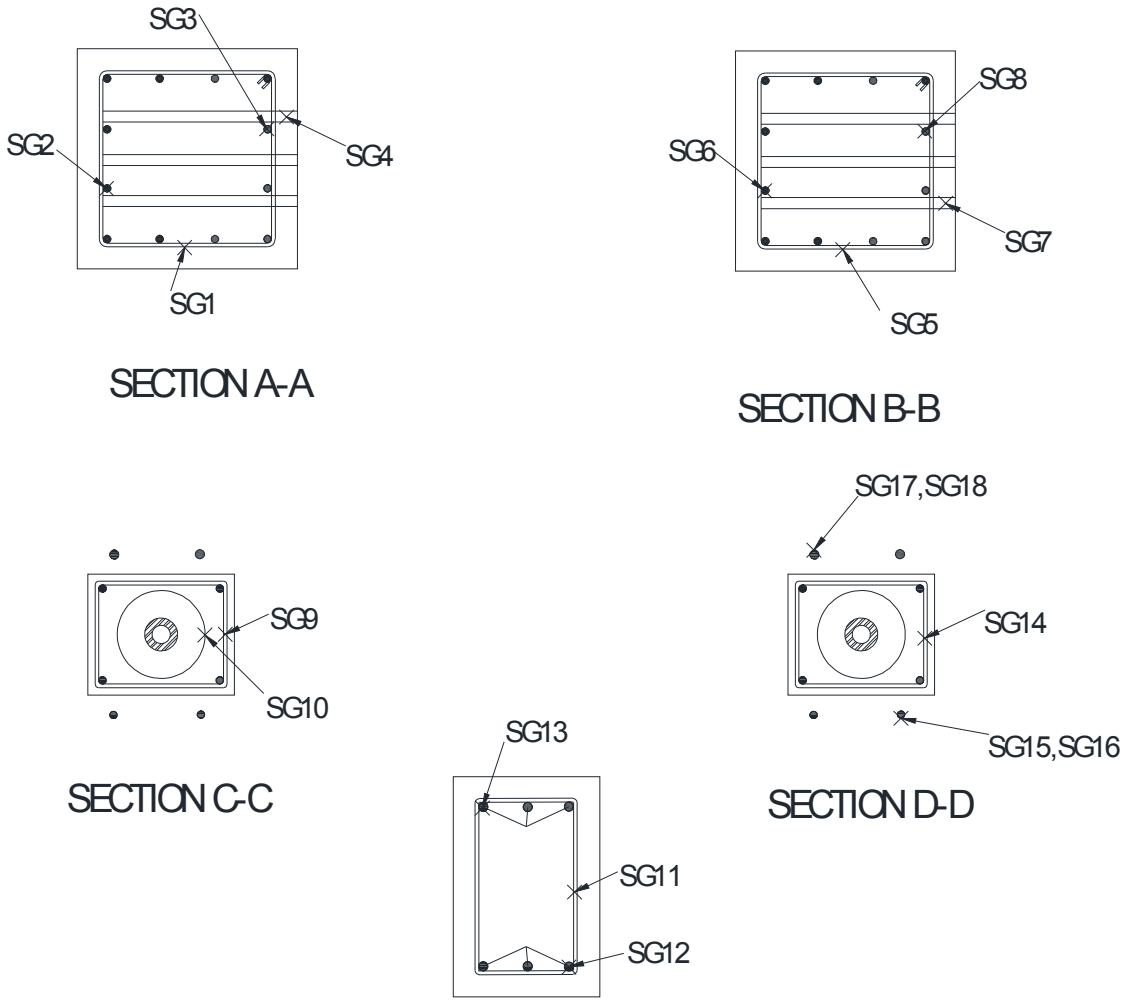

Figure 3-26. Continued

To measure the rotations and curvatures of the beam in the plastic hinge region, six linear variable displacement transformers (LVDT) were placed at the top and bottom of the beam (Fig. 3-27). Four string potentiometers (string POT) were used to measure lateral displacements of the specimen.

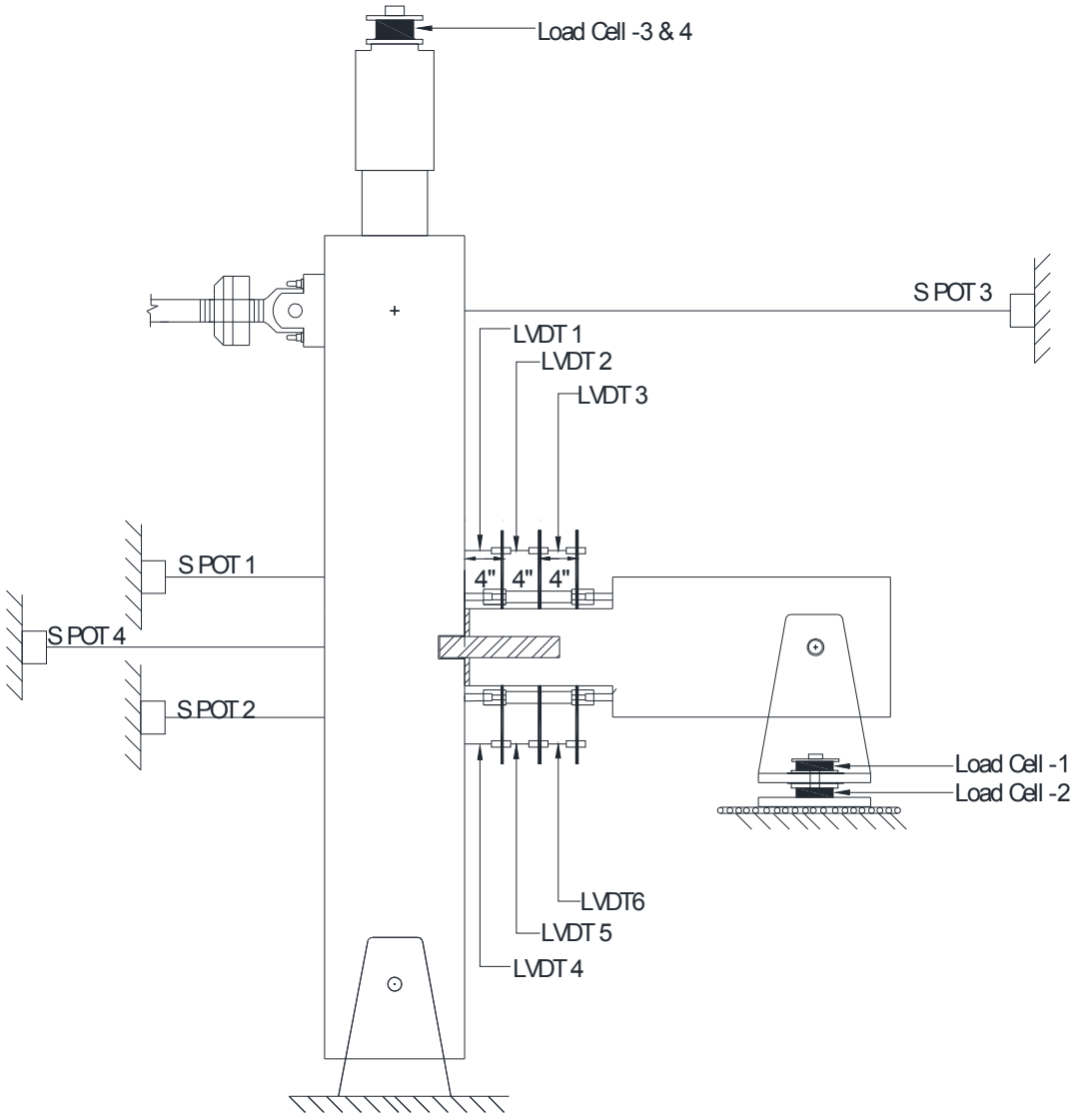

Figure 3-27. Instrumentation (String POT, LVDT, and Load Cell) of Precast Connections

A 22-kip (98-kN) actuator with a ±5-in. (127-mm) stroke was used at the column tip to apply lateral displacement using a cyclic loading protocol. Two 100-kip (445-kN) load cells were used to measure the axial load variations of the columns during the test. Furthermore, two 50-kip (222-kN) compressive load cells were installed at the ends of the beam to measure the beam reactions, each with be activated during push or pull.

3.5.3 Loading Protocol

A displacement-based loading protocol was utilized for testing of all beam-column specimens (Fig. 3-28). Target displacements was selected according to the ACI Simulated Seismic Loading Protocol (ACI 374.2R-13, 2013). Each target displacement was repeated twice per displacement amplitude. Two loading rates was used: a slow displacement rate of 0.03 in./sec (0.76 mm/sec) up to two times the expected yield displacement to capture the yield point, and a faster rate of 0.15 in./sec (3.8 mm/sec) at higher displacements.

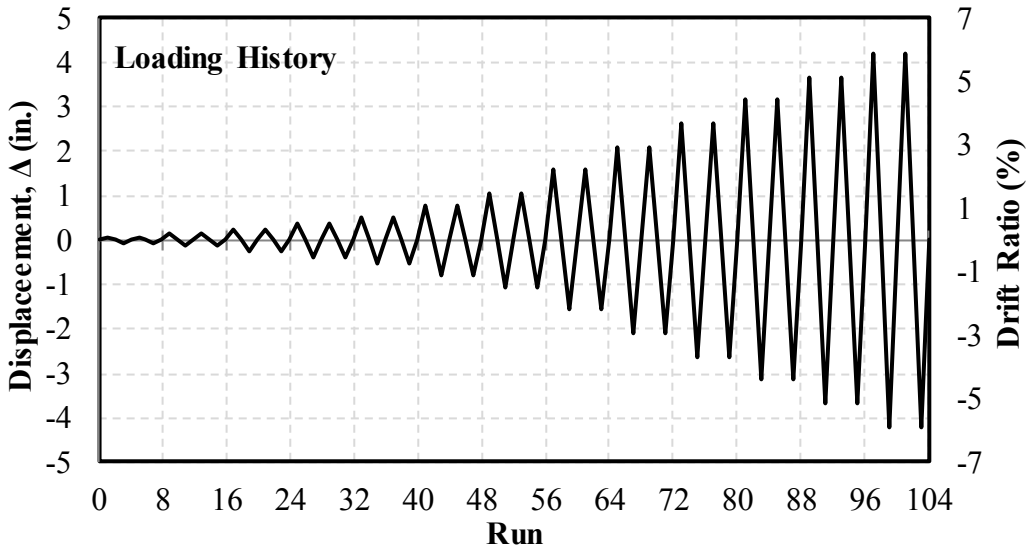

Figure 3-28. Cyclic loading protocol for Precast Beam-Column Specimens

3.6 Test Results

The experimental results of two precast beam-column specimens, PBC1 and PBC2 are presented first. At the end of the section, the seismic performance of the two precast specimens is compared with that of CIP.

3.6.1 Material Strength

Different materials were used in the construction of the precast beam-column specimens: conventional concrete, conventional reinforcing steel bars, NiTi SMA bars, non-shrink grout, and steel tubes. The measured or ASTM minimum strength values are listed herein for each material.

3.6.1.1 Conventional Concrete

Ready-mix conventional concrete was used to form all precast beams and columns. Table 3-3 presents the measured compressive concrete strength for different components of the beam-column test specimens according to ASTM Standard C39-12 (2012). At least three 6- by 12-in (152- by 305-mm) standard concrete cylinders were tested per target day and the average strength was report in the table.

Table 3-3. Measured Concrete Compressive Strength for Beam-Column Specimens

Specimen ID	Beam			Column		
	Age (Days)			Age (Days)		
	7	28	Test Day	7	28	Test Day
CIP	-	5110 psi (35.2 MPa)	5415 psi (37.3 MPa)	-	5110 psi (35.2 MPa)	5415 psi (37.3 MPa)
PBC1-D	3676 psi(25.4 MPa)	4775 psi (32.9 MPa)	4889 psi (33.7 MPa)	3676 psi (25.4 MPa)	4775 psi (32.9 MPa)	4889 psi (33.7 MPa)
PBC1-D-R	3676 psi (25.4 MPa)	4775 psi (32.9 MPa)	5136 psi (35.4 MPa)	3676 psi (25.4 MPa)	4775 psi (32.9 MPa)	5136 psi (35.4 MPa)
PBC2-D	4592 psi (31.7 MPa)	5202 psi (35.9 MPa)	5742 psi (39.6 MPa)	3676 psi (25.4 MPa)	4775 psi (32.9 MPa)	5800 psi (40.0 MPa)
PBC2-SMA	4592 psi (31.7 MPa)	5202 psi (35.9 MPa)	5410 psi (37.3 MPa)	3676 psi (25.4 MPa)	4775 psi (32.9 MPa)	5800 psi (40.0 MPa)

3.6.1.2 Reinforcing Steel Bars

Two types of reinforcing steel bars were used to construct the precast specimens, steel bars confirming to ASTM A706 and deformed steel wire confirming to ASTM A496. All bars were monotonically tested according to the ASTM E8 testing procedure. Table 3-4 presents a summary of the measured mechanical properties for each

reinforcement. The measured stress-strain relationships for these bars are shown in Fig. 3-29 to 3-35.

Table 3-4. Measured Mechanical Properties for Reinforcing Steel Bars

Mechanical property	Bar Size						
	No. 2 wire	No.3	No. 4	No. 5	No. 6	No. 4 (BRR)[a]	No. 5 (BRR)[b]
Grade	60	60	60	60	60	60	60
Yield Stress, f_y	54.0 ksi (372.3 MPa)	78.77 ksi (543.1 MPa)	70.43 ksi (458.5 MPa)	72.23 ksi (498 MPa)	69.185 ksi (477 MPa)	66.875 ksi (461 MPa)	70 ksi (482.6 MPa)
Ultimate Tensile Strength, f_u	107.2 ksi (739.1 MPa)	117.8 ksi (812.2 MPa)	107.19 ksi (739 MPa)	112.17 ksi (773.3 MPa)	93.52 ksi (644.7 MPa)	93.99 ksi (648 MPa)	98.59 ksi (679.7 MPa)
Strain at Peak Stress, ε_u	0.0563 in./in.	0.0659 in./in.	0.1 in./in.	0.0966 in./in.	0.13 in./in.	0.0775 in./in.	0.109 in./in.
Strain at fracture	0.146 in./in.	0.119 in./in.	0.1397 in./in.	0.135 in./in.	0.1979 in./in.	0.117 in./in.	0.18 in./in.

Note:
[a] No. 4 BRR was used in PBC1-D/PBC1-D-R at the bottom of precast beam.
[b] No. 5 BRR was used in PBC2-D at the top/bottom of precast beam and was used in PBC1-D/PBC1-D-R at the top of precast beam.

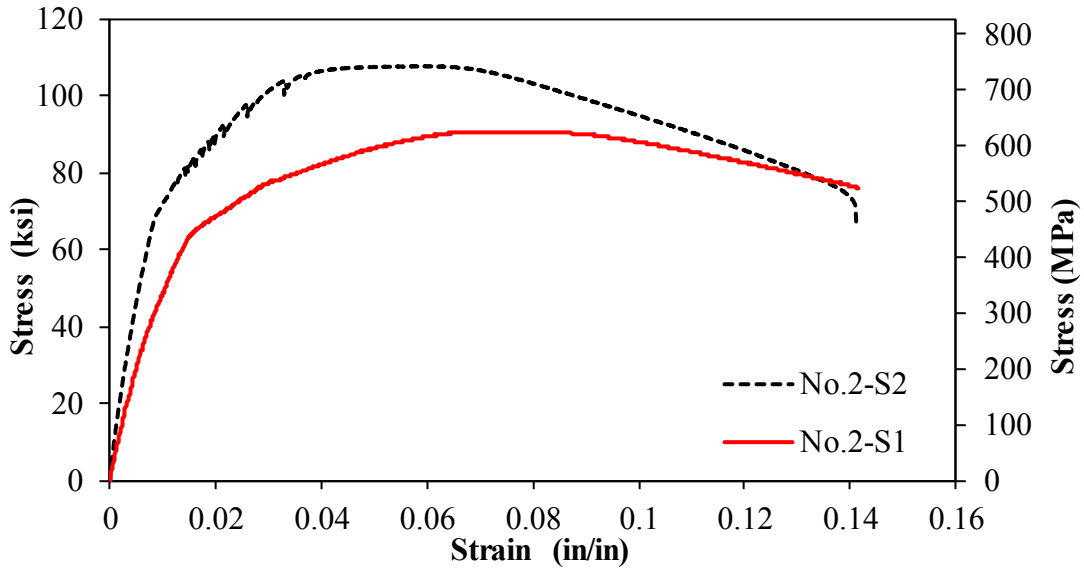

Figure 3-29. Measured Stress-Strain Relationship for No. 2 Deformed Wire Used as Beam Transverse Bars

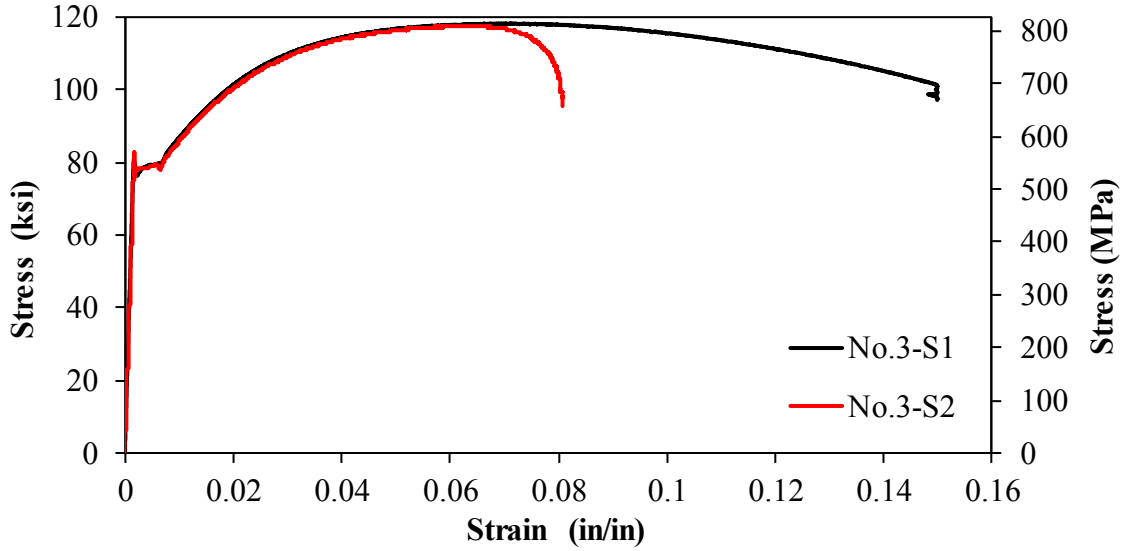

Figure 3-30. Measured Stress-Strain Relationship for No. 3 Reinforcing Steel Bar Used as Column Transverse Bars

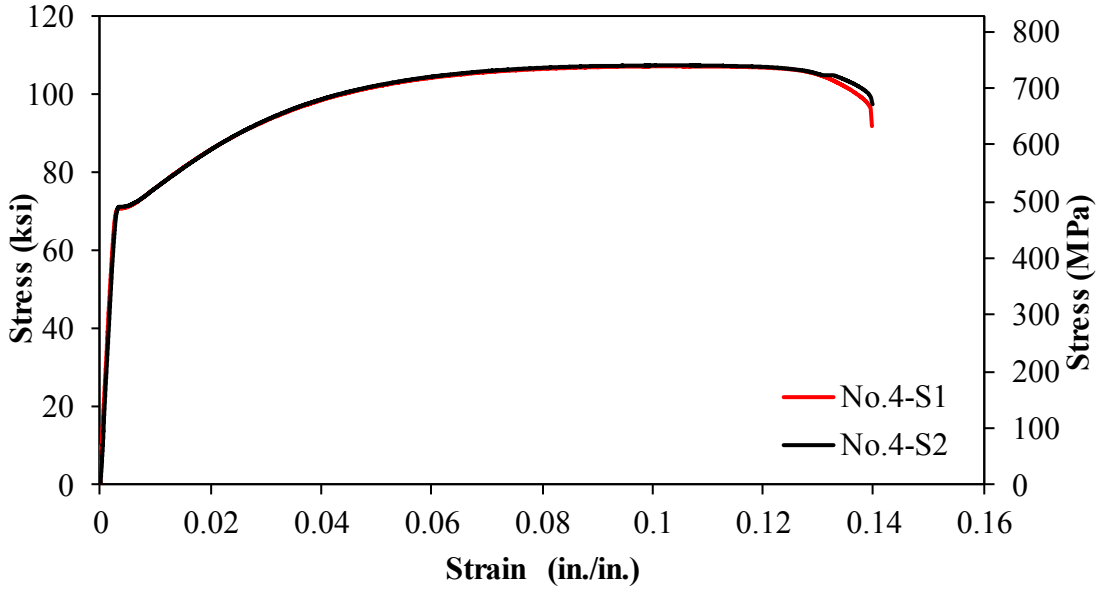

Figure 3-31. Measured Stress-Strain Relationship of No. 4 Reinforcing Steel Bar Used as Column Longitudinal Bars

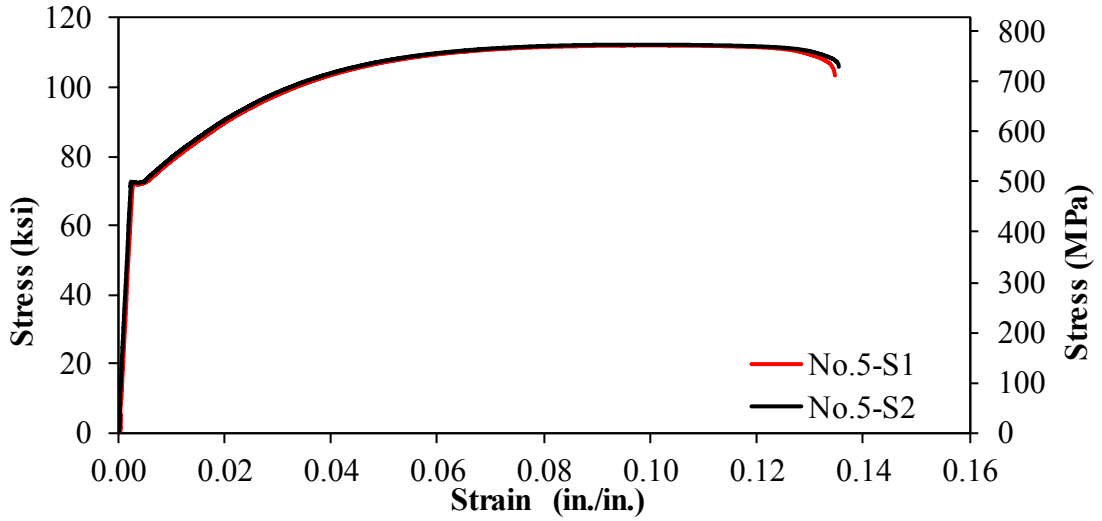

Figure 3-32. Measured Stress-Strain Relationship for No. 5 Reinforcing Steel Bar Used as Beam Longitudinal Bars

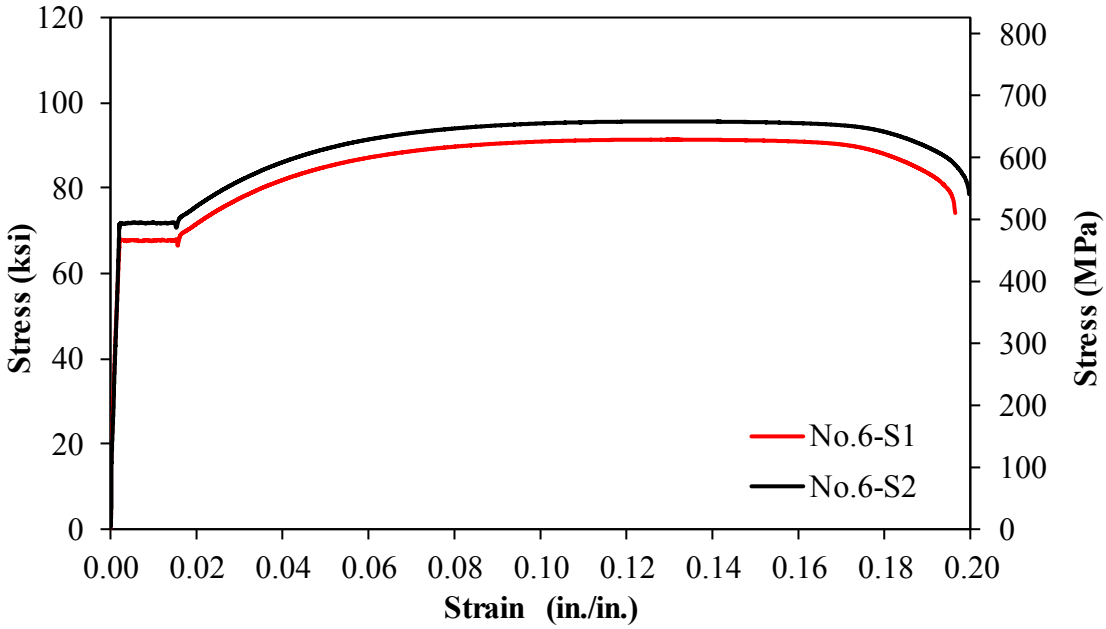

Figure 3-33. Measured Stress-Strain Relationship for No. 6 Reinforcing Steel Bar Used as Beam Longitudinal Bars

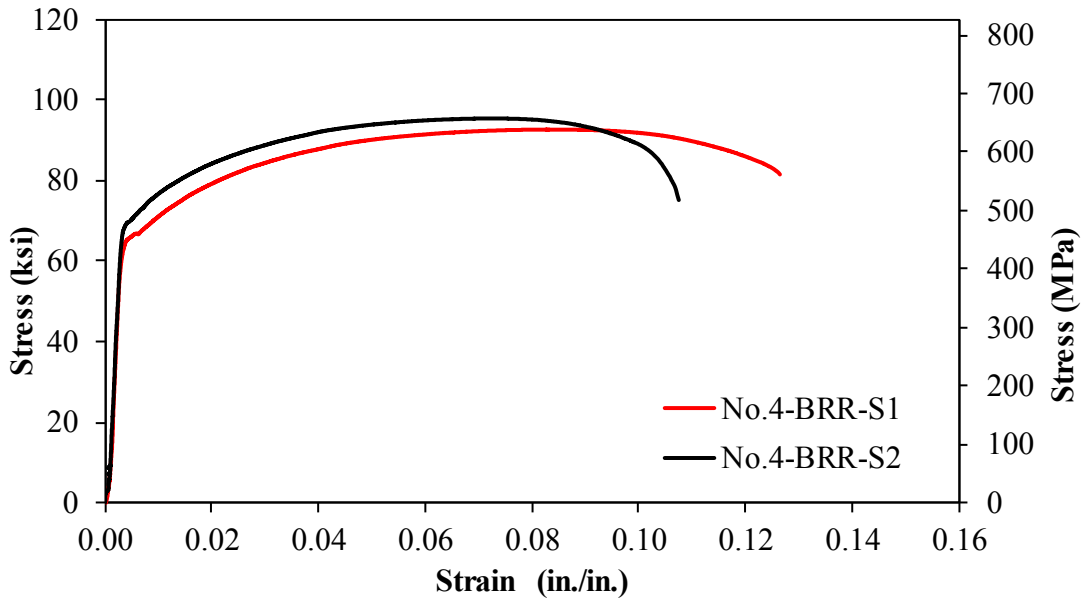

Figure 3-34. Measured Stress-Strain Relationship for No. 4 BRR Bar Used in PBC1-D/PBC1-D-R at the bottom of Precast Beam

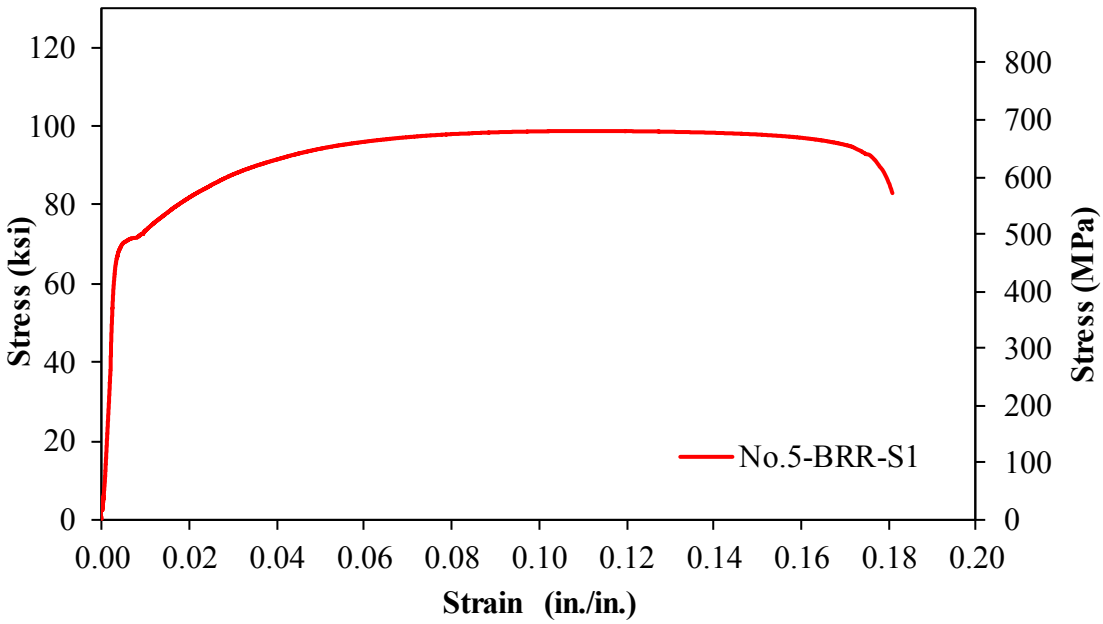

Figure 3-35. Measured Stress-Strain Relationship for No. 5 BRR Bar Used in PBC2-D at Top/Bottom of Precast Beam and Used in PBC1-D/PBC1-D-R at Bottom of Precast Beam

3.6.1.3 NiTi SMA Bars

NiTi SMA headed bars with a diameter of 0.5 in. (13 mm) were used to form SMA BRR, which were used in PBC2-SMA. The testing method and stress-strain

material model proposed by Tazarv and Saiidi (2014) for NiTi SMA reinforcing bars were used in the present study to obtain the mechanical properties of SMA bars used in BRR of PBC2-SMA. A summary of the measured mechanical properties for the NiTi SMA bars is presented in Table 3.5. Figure 3-36 shows the hysteretic behavior of NiTi SMA bar.

Table 3-5. Measured Mechanical Properties of SMA bars

Mechanical property	Value
Size	0.5 in. (13 mm)
Austenite Modulus, k_1 , ksi (MPa)	5362.5 (36973)
Post Yield Stiffness, k_2 , ksi (MPa)	180 (1241)
Austenite Yield Strength, f_y , ksi (MPa)	56.44 (389)
Lower Plateau Stress Factor, β	0.309
Secondary Post Yield Stiffness Ratio, α	N/A (Recommended value is 0.3)
Ultimate Strain, ε_u (in./in.)	0.0748

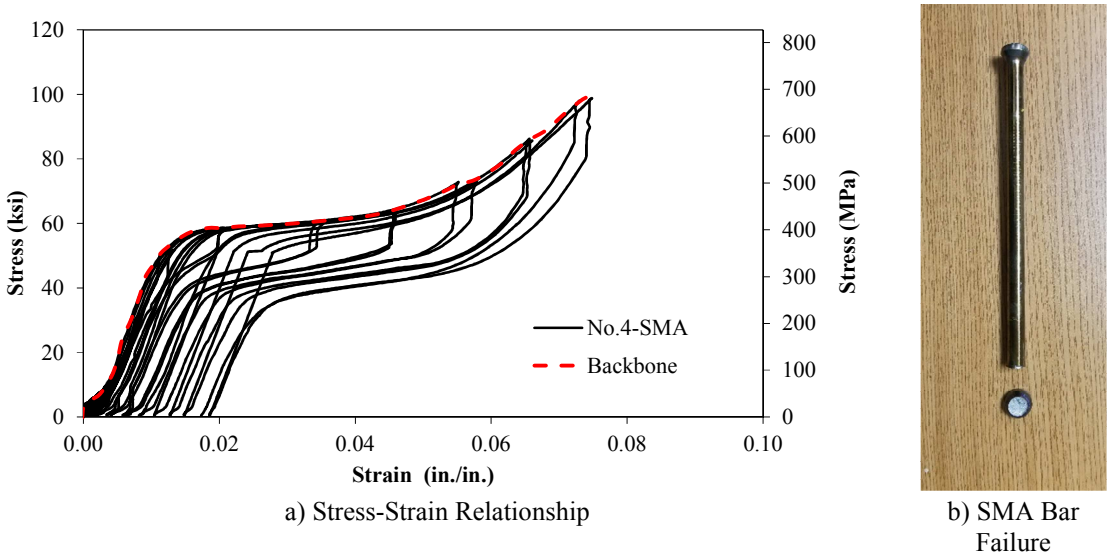

a) Stress-Strain Relationship

b) SMA Bar Failure

Figure 3-36. Measured Hysteretic Stress-Strain Relationship for No. 4 SMA Bar Used in PBC2-SMA at Top/Bottom of Precast Beam

3.6.1.4 Non-Shrink Grout

Conventional non-shrink fine-aggregate high-flow grout (1428 HP) was used to fill the gap between reinforcing bars and steel tubes in BRR. The measure grout

compressive strength are presented in Table 3-6. The reported strength was based on the average of at least three 2-in. (50-mm) cube grout samples tested according to ASTM Standard C39-12 (2012).

Table 3-6. Measure Compressive Strength of Non-Shrink Grout

Specimen ID	Age (Days)		
	1	7	Test Day
PBC1-D	3259 psi (22.5 MPa)	N/A	6226 psi (42.9 MPa)
PBC1-D-R	3259 psi (22.5 MPa)	N/A	6696 psi (46.2 MPa)
PBC2-D	1174 psi (8.1 MPa)	4552 psi (31.4 MPa)	6006 psi (41.4 MPa)
PBC2-SMA	1174 psi (8.1 MPa)	4552 psi (31.4 MPa)	6325 psi (43.6 MPa)

3.6.1.5 Steel Tubes

Steel tubes made of ASTM A513 Grade 1026 carbon steel were used to confine bars in BRR. Gauge 13 (2.3 mm) tubes with an outer diameter of 1.25 in. (32 mm) were used to form all BRR incorporated in precast beam-column specimens. Table 3-7 presents the required mechanical properties of the steel tubes according to the ASTM standard.

Table 3-7. Mechanical Properties of ASTM A513 Grade 1026 Steel

	Yield Strength	Ultimate Tensile Strength	Elongation (%)	Hardness (HRB)
Min	66,000 psi (35.2 MPa)	75,000 psi (35.2 MPa)	10.00	80.00
Max	73,546 psi (35.2 MPa)	86,524 psi (35.2 MPa)	20.00	91.00

3.6.2 PBC1 Results

This section presents the experimental results for PBC1-D and PBC1-D-R.

3.6.2.1 Force-Displacement Relationships for PBC1

3.6.2.1.1 PBC1-D

Figure 3-37 shows the measured lateral force-displacement relationship for PBC1-D. The force was obtained directly from the actuator reading and the displacement was measured from the string POT attached to column tip (SPOT 3). The drift ratio is defined as the column tip displacement to the column height. The lateral load carrying capacity in the push and pull directions was 6.14 kips (27.3 kN) and 11.23 kips (50 kN), respectively. The 83% higher lateral load carrying capacity in the pull direction of PBC1-D was due to 81% higher BRR steel area at the top of the beam than the bottom beam reinforcement. The bottom BRR bar yielded at a displacement of 1.05 in. (27 mm) corresponding to a lateral force of 4.31 kips (19.2 kN). The yield displacement and the yield force for top BRR bar (or in pull direction) were 1.05 in. (27 mm) and 6.63 kips (29.5kN), respectively. The test was stopped at 4.37% drift ratio to avoid excessive damage of the beam to perform the repair by replacing the BRR and to retest the specimen. The beam end reaction versus the column tip lateral displacement is shown in Fig. 3-38. The maximum beam reaction was 9.52 kips (42.3 kN) and 18.26 kips (81.2 kN) in the push and pull directions, respectively.

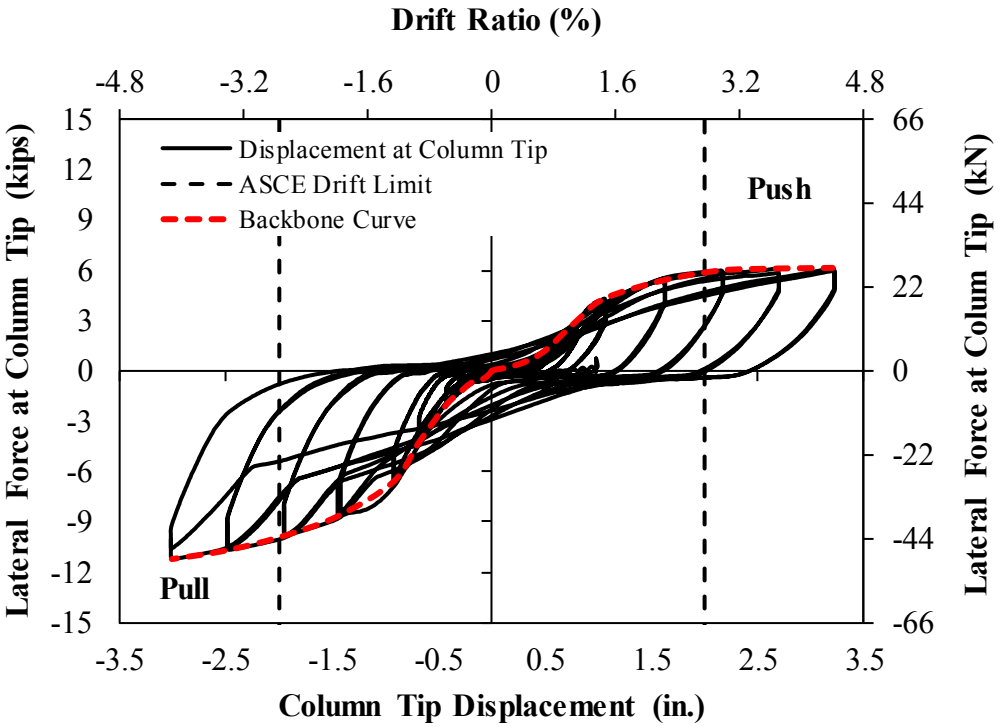

Figure 3-37. Measured Force-Displacement Relationship for PBC1-D

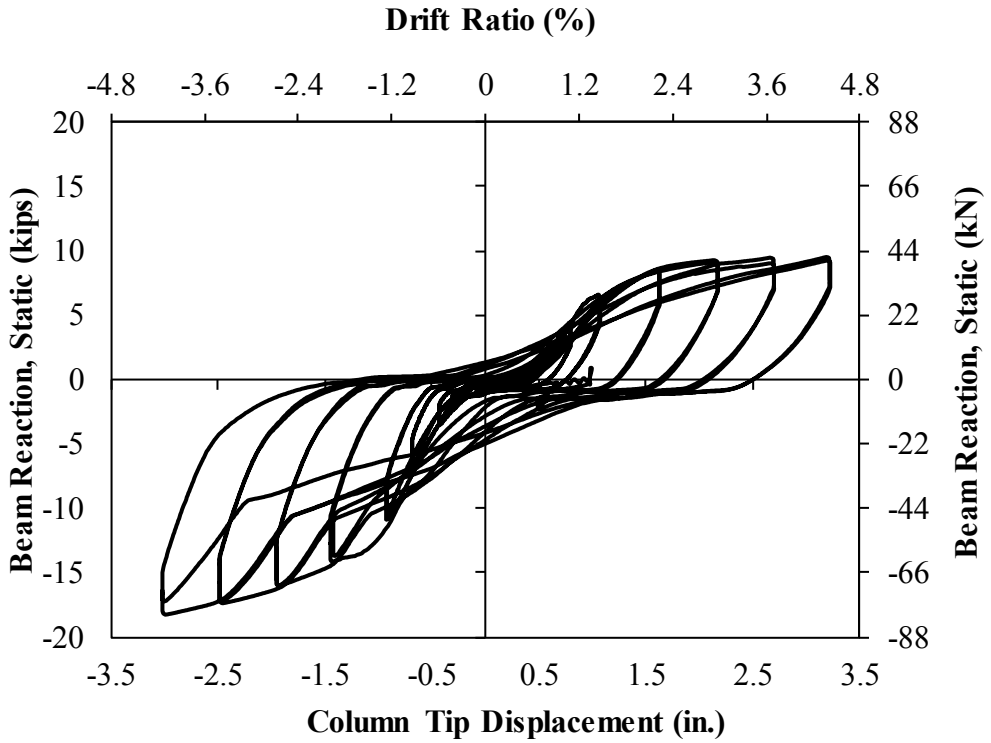

Figure 3-38. Measured Beam End Reaction for PBC1-D

3.6.2.1.2 PBC1-D-R

After testing PBC1-D, its BRR were replaced with the same size and type but new BRR to investigate the repair-by-replacement method proposed in the present study. Figure 3-39 shows the lateral force-displacement relationship for PBC1-D-R. The lateral load carrying capacity in the push and pull directions were 7.11 kips (31.6 kN) and 10.69 kips (47.6 kN), respectively. The bottom BRR bar yielded at a displacement of 1.05 in. (27 mm) corresponding to a lateral force of 5.02 kips (22.3 kN). The yield displacement and the yield force for top BRR bar (or in pull direction) were 1.57 in. (40 mm) and 7.56 kips (33.6 kN), respectively. The test was stopped at 4.37% drift ratio with no reinforcing fracture or core concrete failure.

The beam end reaction versus the column tip lateral displacement is shown in Fig. 3-40. The maximum beam reaction was 11.14 kips (49.6 kN) and 17.4 kips (77.4 kN) in the push and pull directions, respectively.

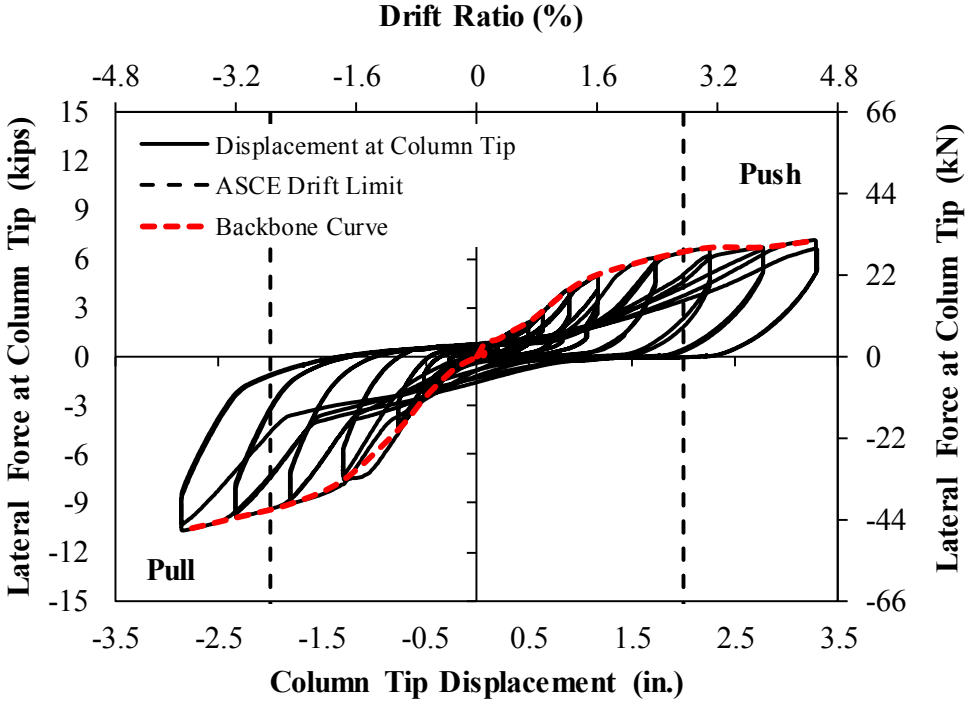

Figure 3-39. Measured Force-Displacement Relationship for PBC1-D-R

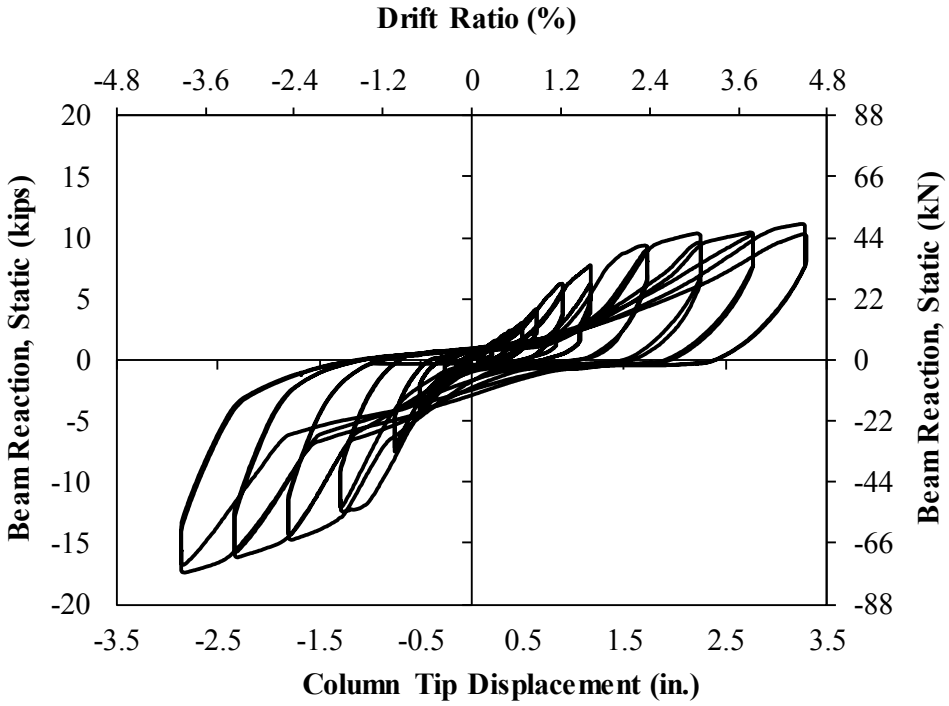

Figure 3-40. Measured Beam End Reaction for PBC1-D-R

3.6.2.2 Damage in PBC1

Damage and crack pattern were documented throughout the entire test for both PBC1-D and PBC1-D-R. Each precast specimen withstood 22 full cycles of loading without any failure. These tests were stopped at 4.37 % drift ratio, which was 20% higher than the CIP failure drift.

3.6.2.2.1 PBC1-D

Figure 3-41 shows the damage of PBC1-D at selected drift ratios. It can be seen that PBC-D had no damage in the plastic hinge region at 3.64% drift ratio (equivalent to six times the design level earthquake). The first crack was developed at 1.45% drift ratio where the beam depth changes. More flexural cracks were developed or widened in this region at higher drift ratios. Some cracks were developed as the 2.9% drift ratio cycle,

which are most likely due to the strain concentration in where No.6 longitudinal reinforcement entered into the precast beam (Fig. 3-41h). Concrete cover started to spall around the beam depth change region at a drift ratio of 4.37%. Only one crack was observed on the precast column at 2.91% drift ratio (Fig. 3.41g).

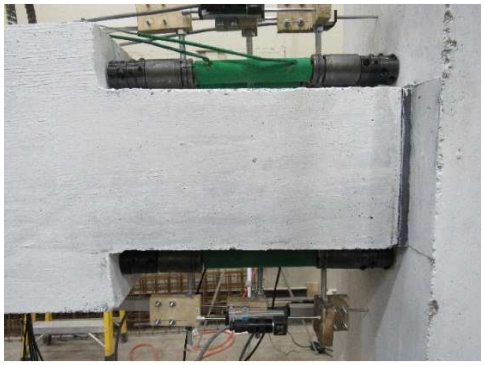

a) Drift Ratio 1.09% (east side)

b) Drift Ratio 1.09% (west side)

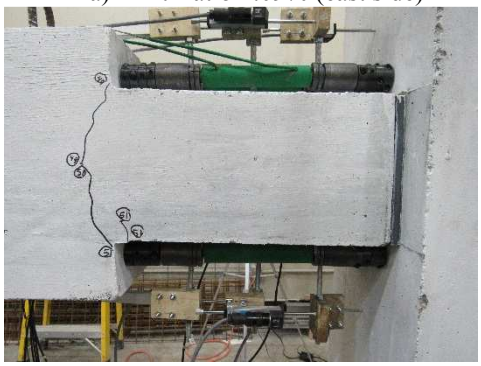

c) Drift Ratio 1.45% (east side)

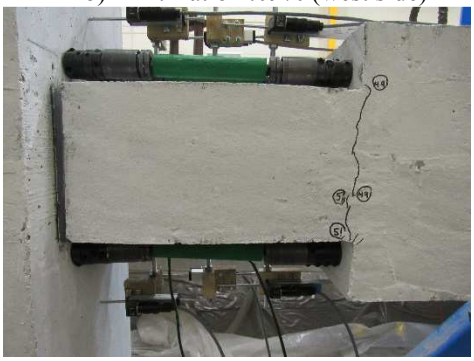

d) Drift Ratio 1.45% (west side)

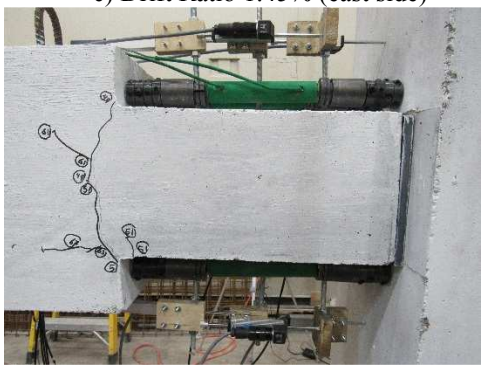

e) Drift Ratio 2.19% (east side)

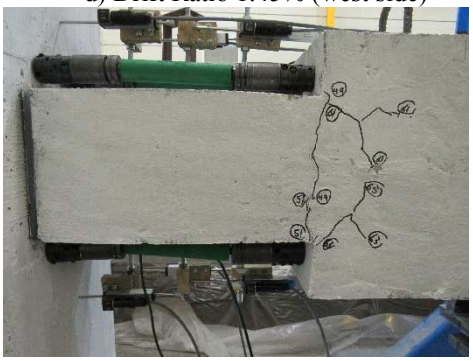

f) Drift Ratio 2.19% (west side)

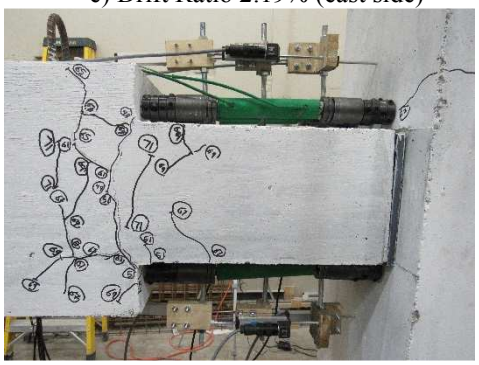

g) Drift Ratio 2.91% (east side)

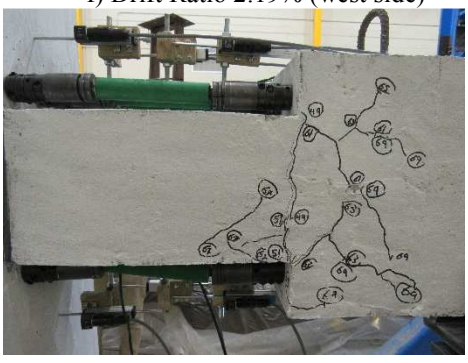

h) Drift Ratio 2.91% (west side)

Figure 3-41. Damage for PBC1-D at Selected Drift Ratios

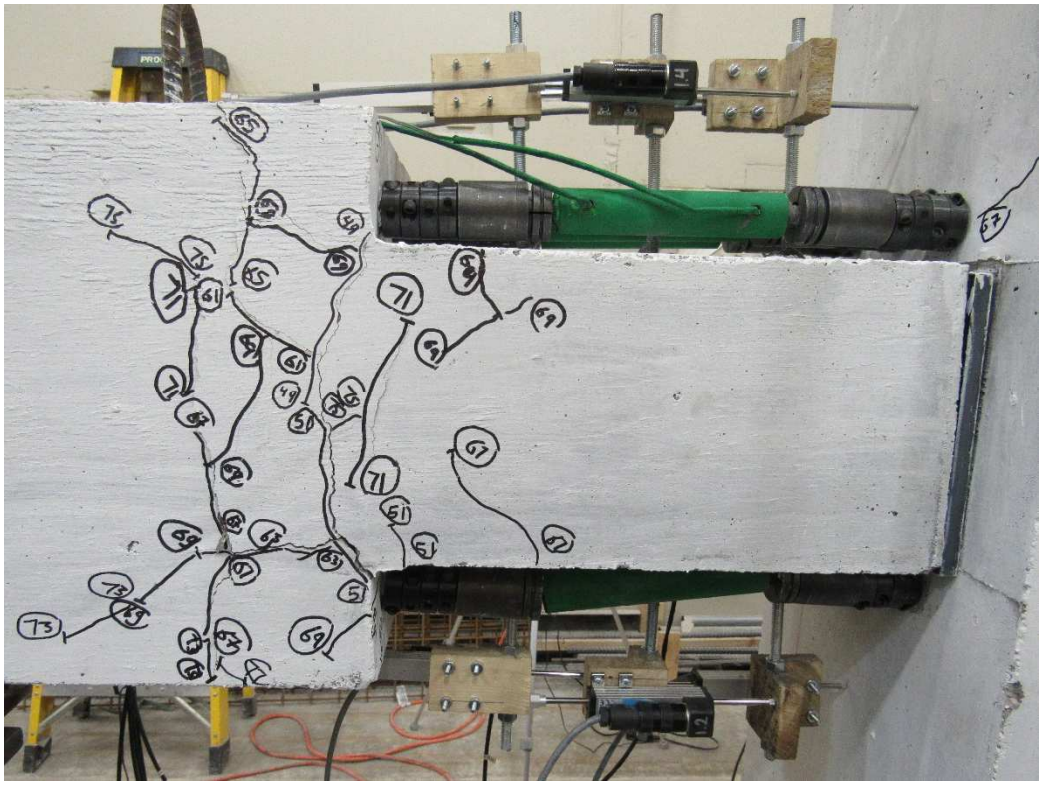

i) Drift Ratio 3.64% (east side)

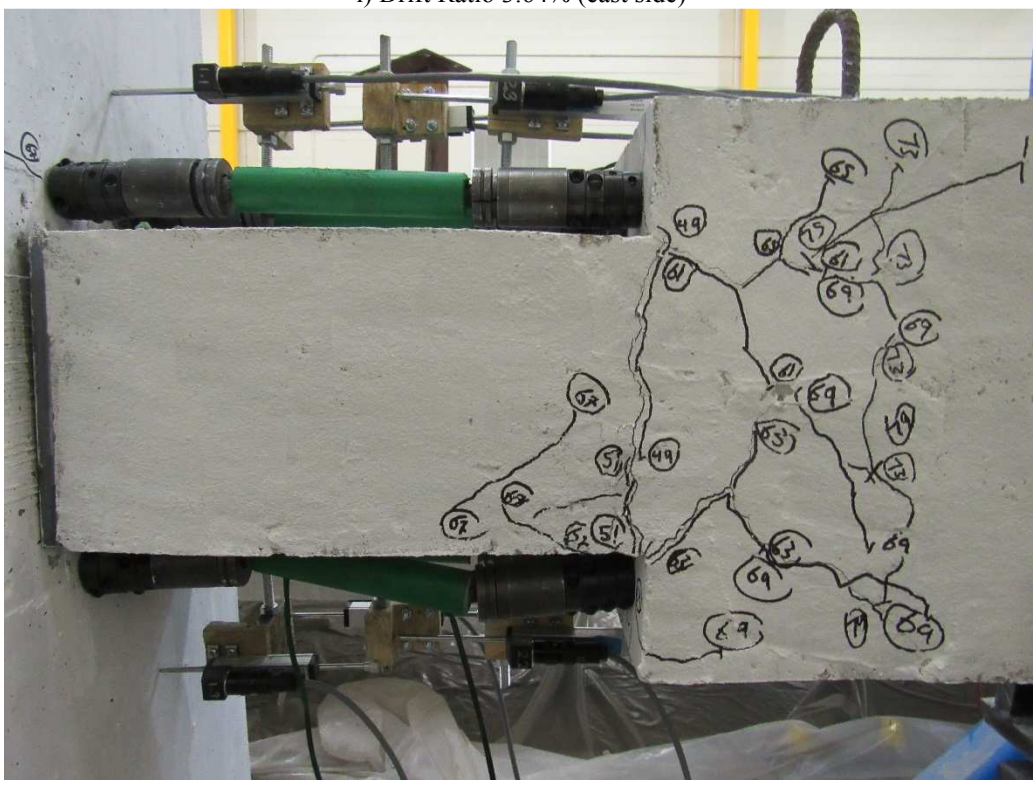

j) Drift Ratio 3.64% (west side)

Figure 3-41. Continued

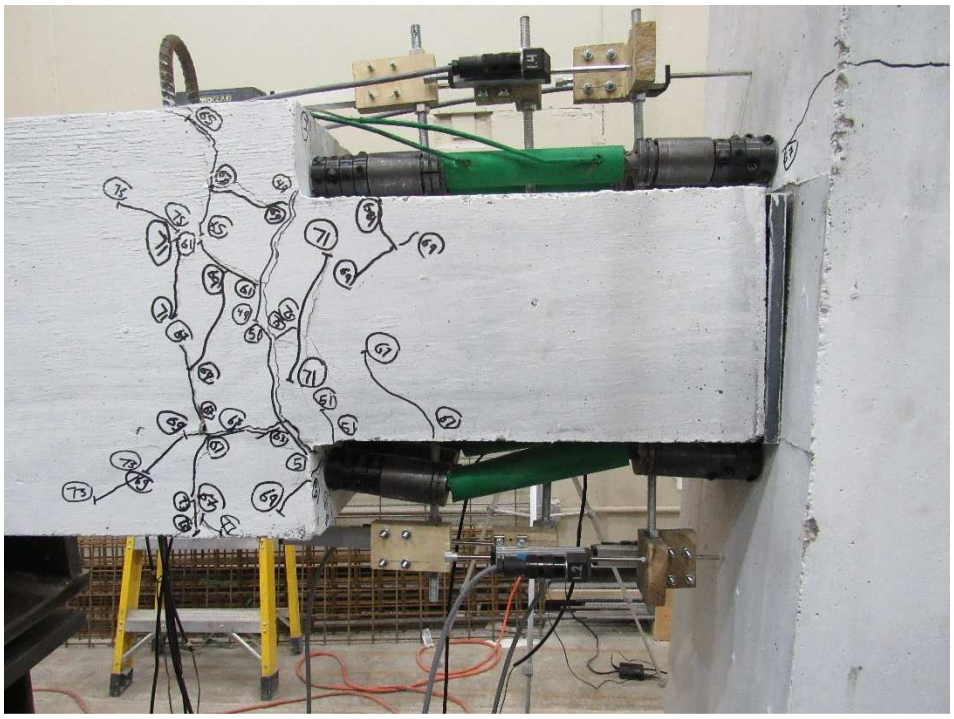

k) Drift Ratio 4.37% (east side)

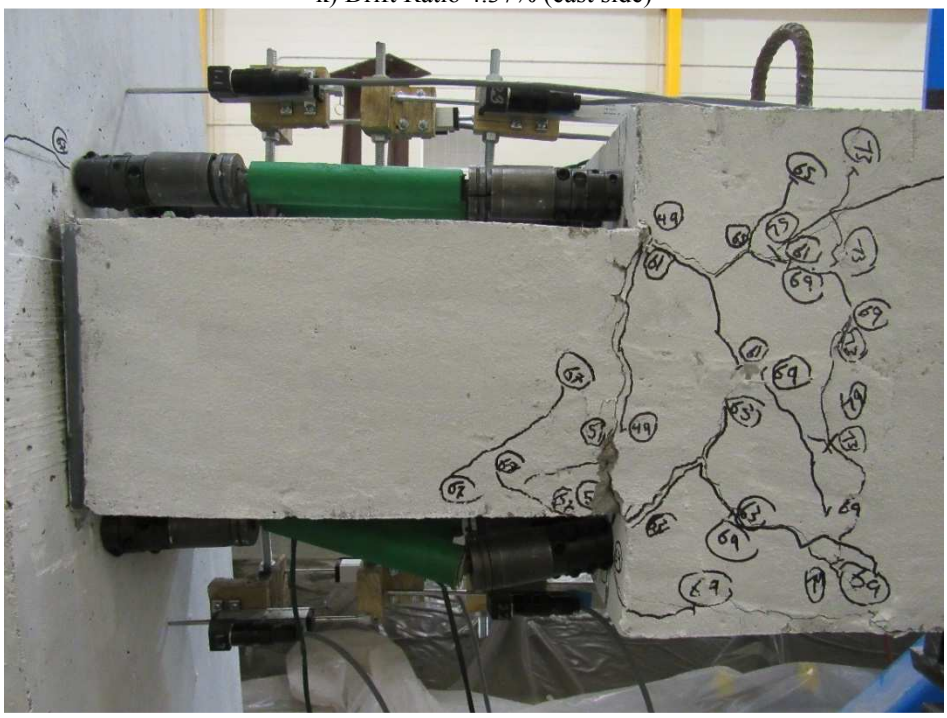

l) Drift Ratio 4.37% (west side)

Figure 3-41. Continued

3.6.2.2.2 PBC1-D-R

Figure 3-42 shows the damage of PBC1-D-R at selected drift ratios. It can be seen that PBC-D-R has not sustained any significant damage after the repair phase. A few cracks were observed at the early stages of the test due to the movement of the cracked concrete pieces. Only minor flexural cracks were developed at the end of the neck region after 2.19% drift ratio cycle. It is worth mentioning that the damage of the precast beam where the depth changes was only cosmetic since the force-displacement behavior of the precast specimen remained essentially the same before and after the repair (Fig 3-77). Figure 3-46 shows the ultimate damage of PBC1-D-R after two full cycles of 4.37% drift ratio.

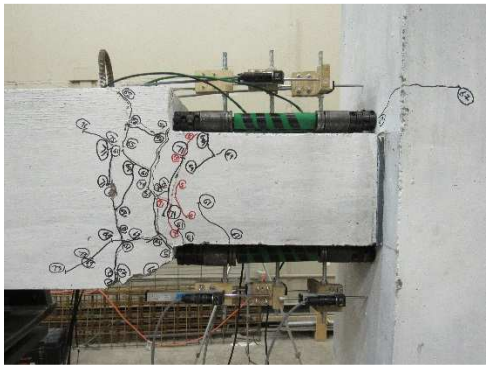

a) Drift Ratio 1.09% (east side)

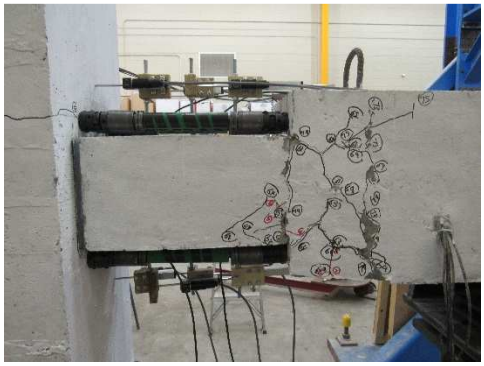

b) Drift Ratio 1.09% (west side)

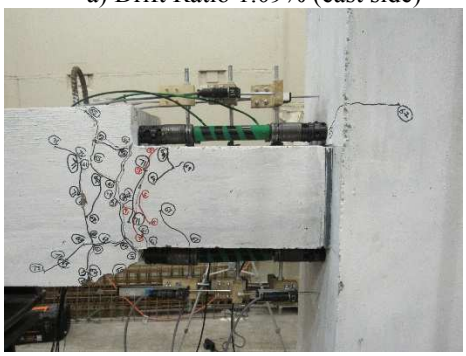

c) Drift Ratio 1.45% (east side)

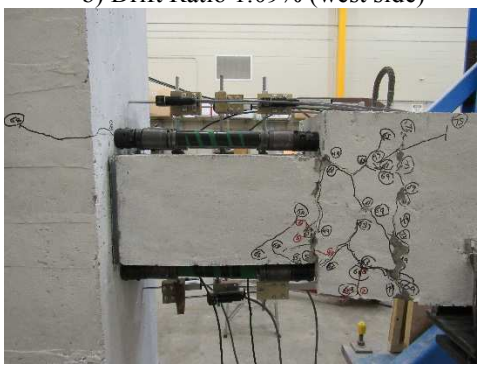

d) Drift Ratio 1.45% (west side)

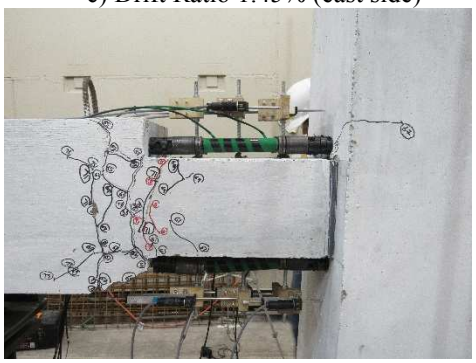

e) Drift Ratio 2.19% (east side)

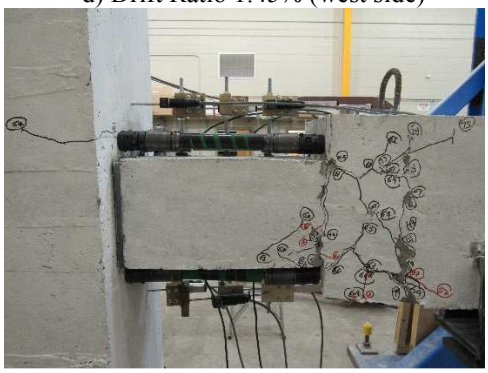

f) Drift Ratio 2.19% (west side)

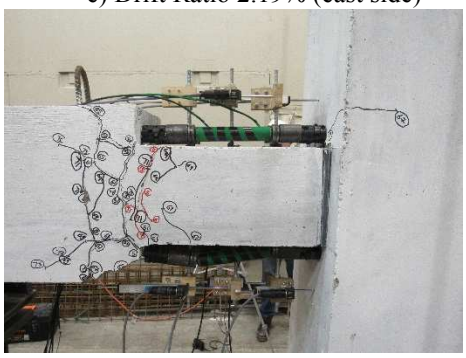

g) Drift Ratio 2.91% (east side)

h) Drift Ratio 2.91% (west side)

Figure 3-42. Damage for PBC1-D-R at Selected Drift Ratios

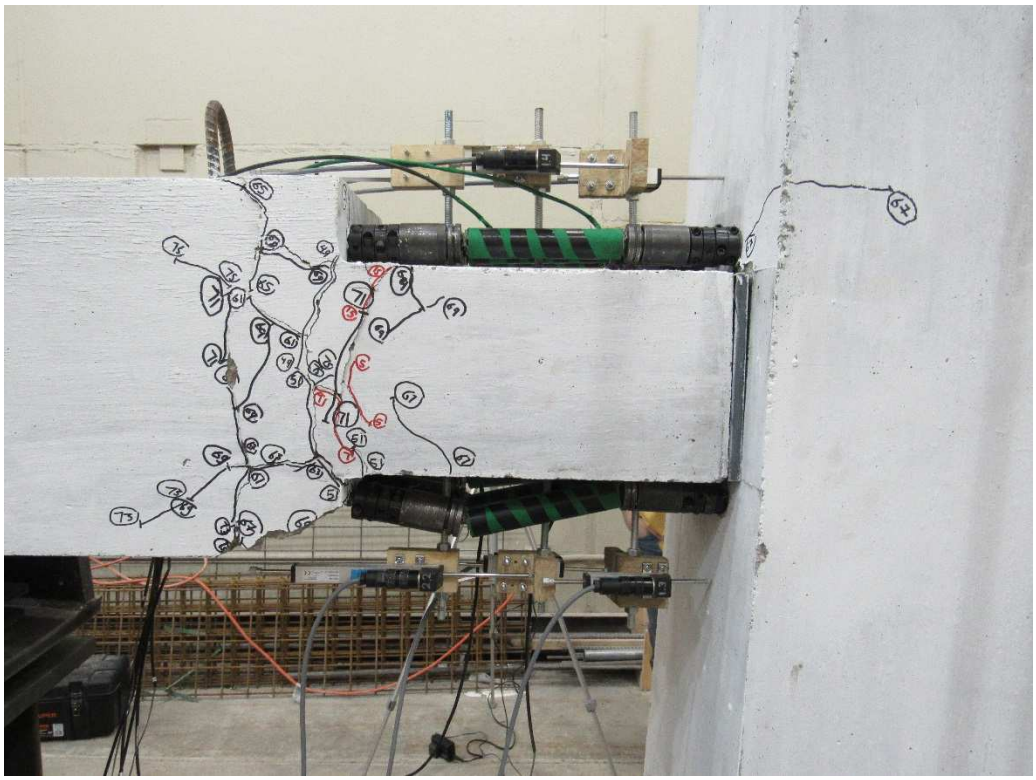

i) Drift Ratio 3.64% (east side)

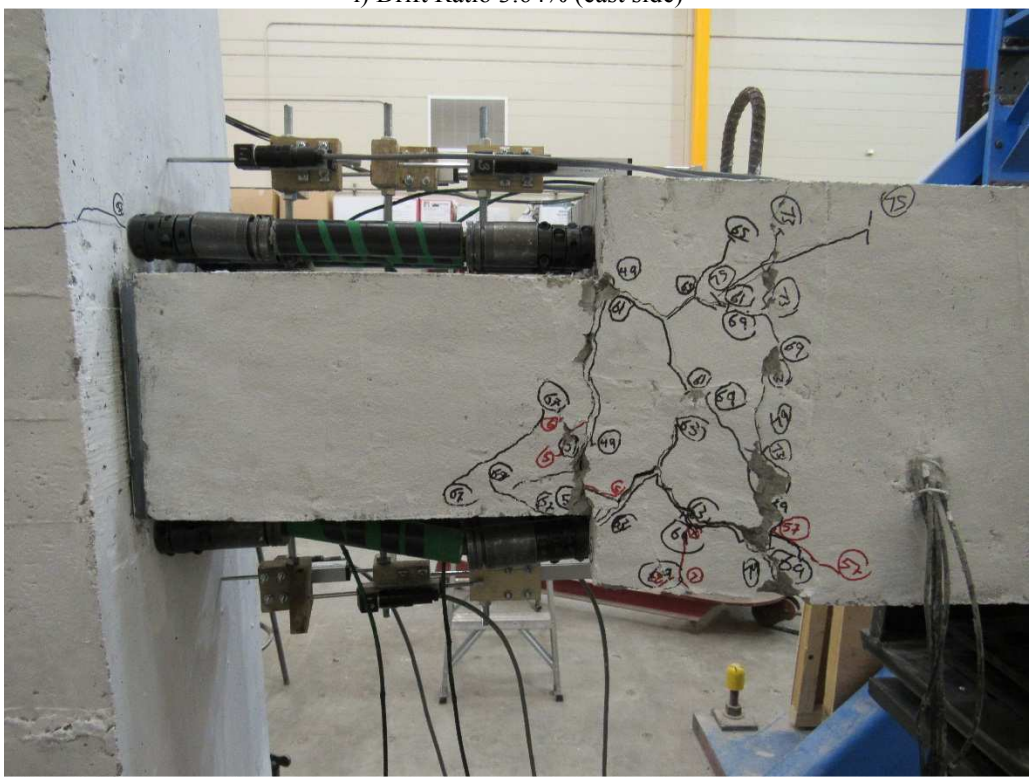

g) Drift Ratio 3.64% (west side)

Figure 3-42. Continued

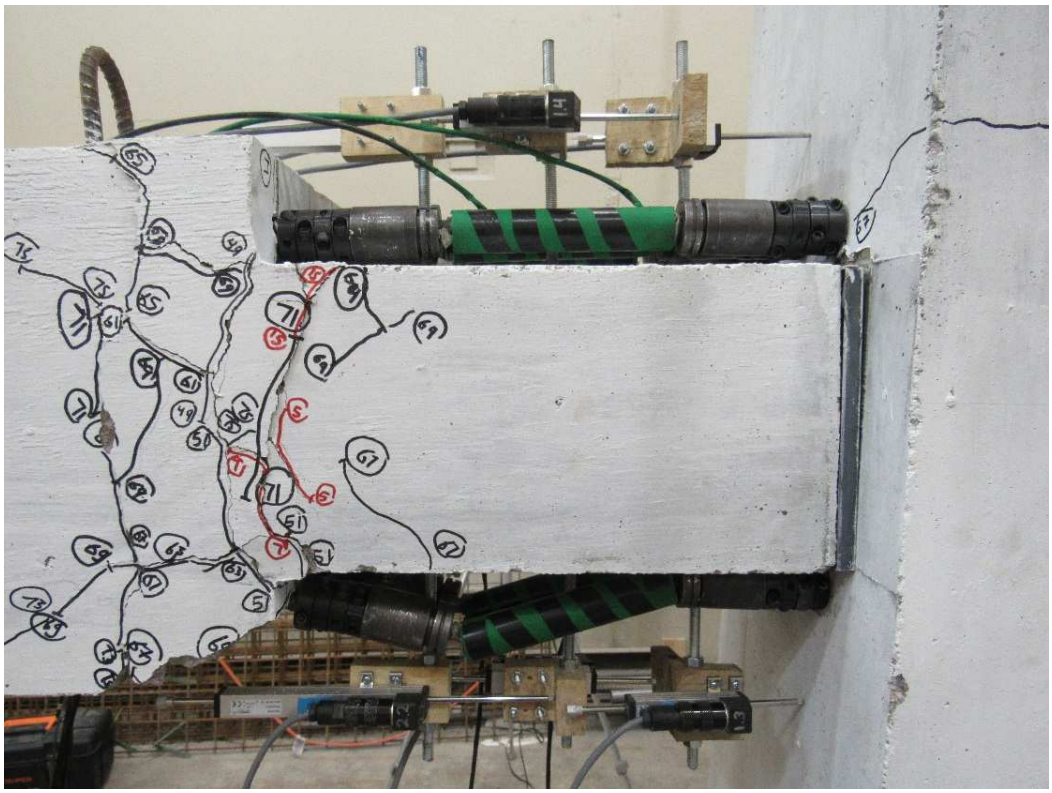

k) Drift Ratio 3.64% (east side)

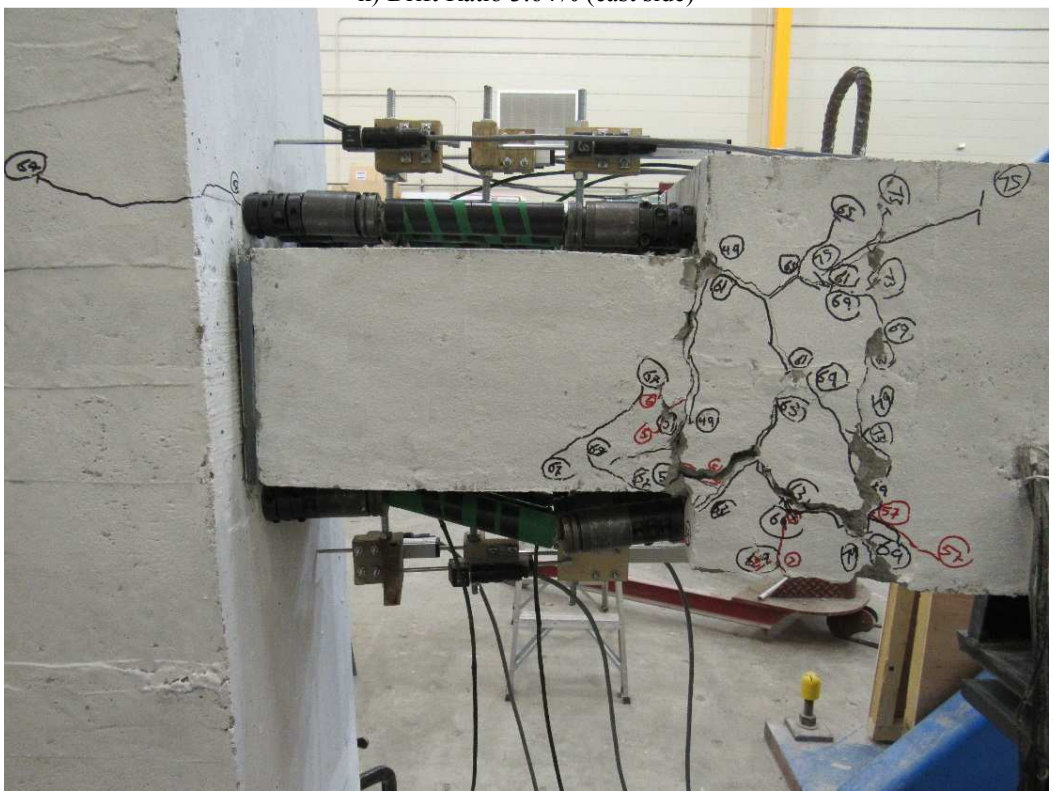

l) Drift Ratio 3.64% (west side)

Figure 3-42. Continued

3.6.2.3 Failure Mode of PBC1

As mentioned before, PBC1-D and PBC1-D-R withstood 22 full cycles of loading, the largest of which was at 4.37% drift ratio, without any signs of failure. The BRR in both tests were deformed in a Z-shape manner (Fig 3-43) during the cycles of 4.37% drift ratio but did not fail. If the test was continued, BRR would have been straightened and functional in tension. The precast beam concrete cover spalled where the beam depth changes. Nevertheless, this damage was not detrimental and was only cosmetic. It will be discussed in Sec. 3.6.4 that the force-displacement relationships for PBC1-D and PBC1-D-R were essentially the same before and after the repair while a structural damage would have degraded the strength and stiffness. The cosmetic damage at the end of the neck region can be mitigated by a better design and detailing, which is discussed under the next section for PBC2. It was initially assumed that the plastic moment will be fully resisted by BRR while a secondary moment, the product of the vertical reaction at the pipe-pin connection and the neck length, should be included in the design of the neck. A minimal longitudinal reinforcement was provided in the neck region of the precast PBC1 beam while more reinforcement was needed to avoid neck cracking. PBC2 was designed to prevent this cosmetic damage.

a) PBC1-D b) PBC1-D-R

Figure 3-43. Z-Shape Deformation of BRR in PBC1

3.6.2.4 Residual Displacements of PBC1

Figures 3.44 and 3.45 show the peak drifts versus the residual drifts for PBC1-D and PBC1-D-R, respectively. The residual displacement was calculated as the displacement at zero force in the unloading branch of the first cycle per drift level. It can be seen that the residual displacements of PBC1-D were slightly higher than those in PBC1-D-R.

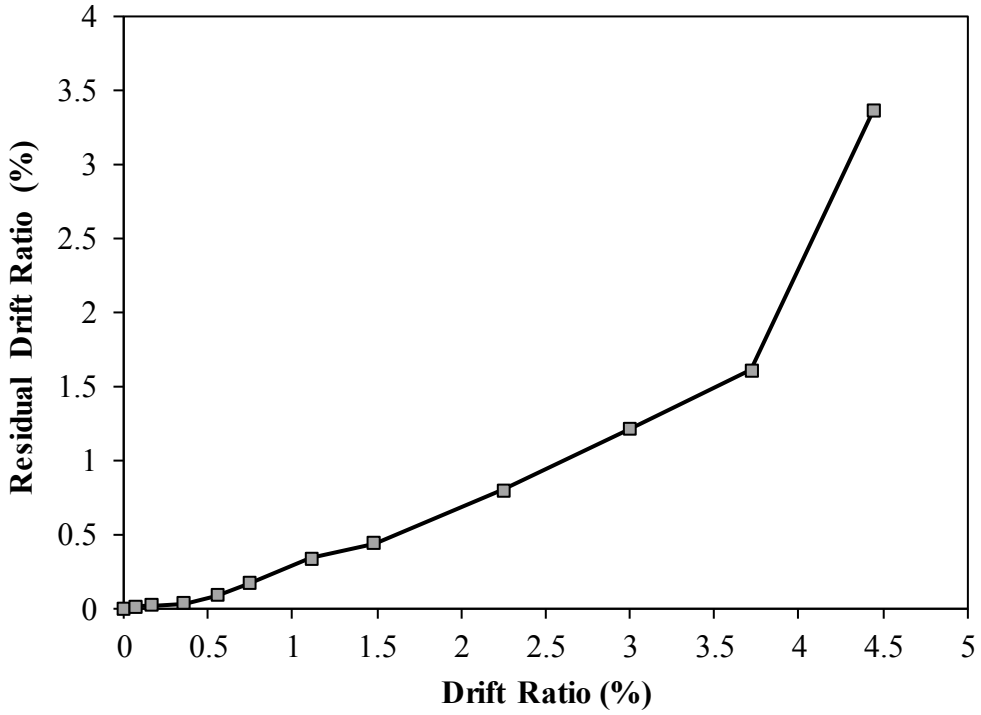

Figure 3-44. Residual Drifts for RBC1-D

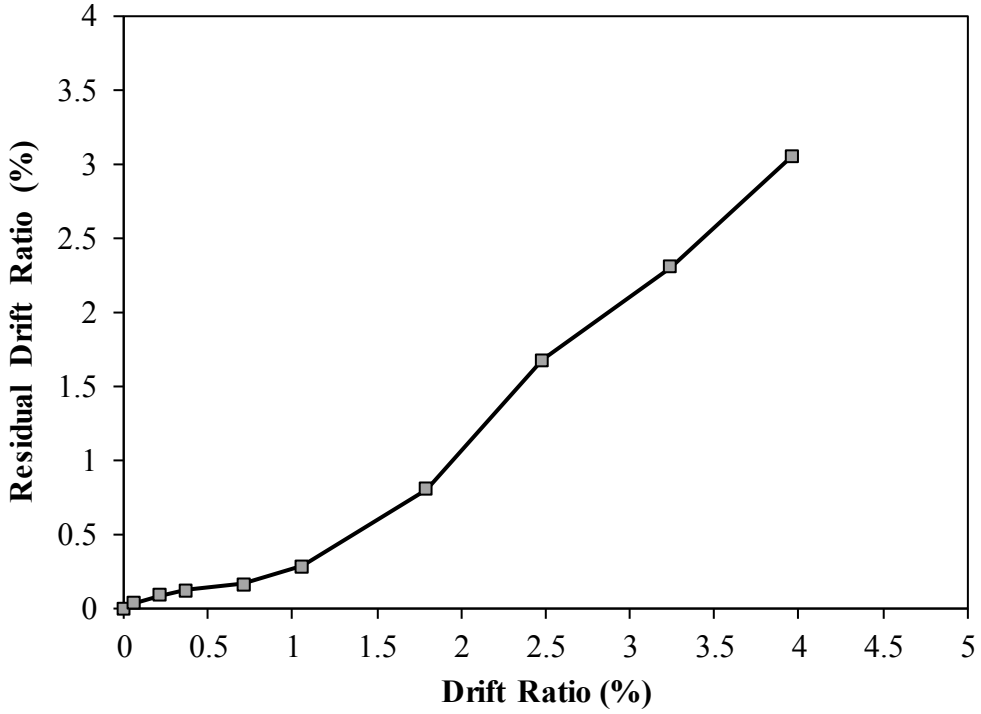

Figure 3-45. Residual Drifts for RBC1-D-R

3.6.2.5 Strain profiles for Beam of PBC1

The strain for both longitudinal and transverse reinforcement were measured using strain gauges installed at different locations within the precast specimens. Figure 3-46 and 3-47 show the strain profiles for the beam top and bottom reinforcement in PBC1-D and PBC1-D-R, respectively. The data was presented up to the displacement where the measured strains were valid. The BRR in beam yielded at 1.45% drift ratio. Furthermore, it can be seen that the strain is well distributed in the plastic hinge area. Further, the column reinforcement did not yield even at the peak displacement. The beam transverse reinforcement also did not yield. It can be concluded that the proposed detailing was compatible with the "strong-column weak-beam" design method to achieve large displacements.

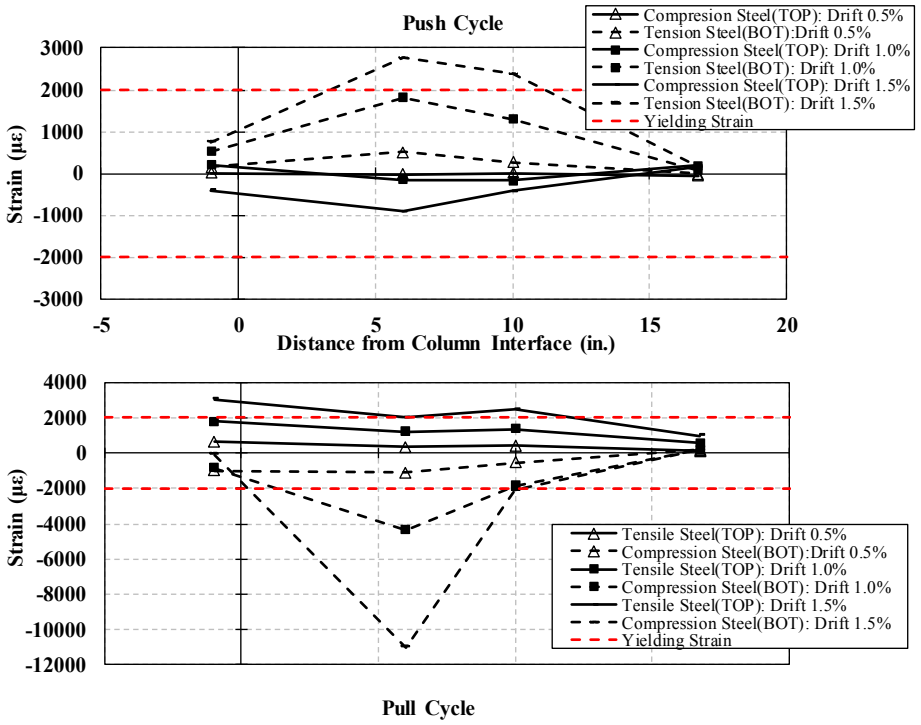

Figure 3-46. Strain Profiles for Beam Longitudinal Reinforcement in RBC1-D

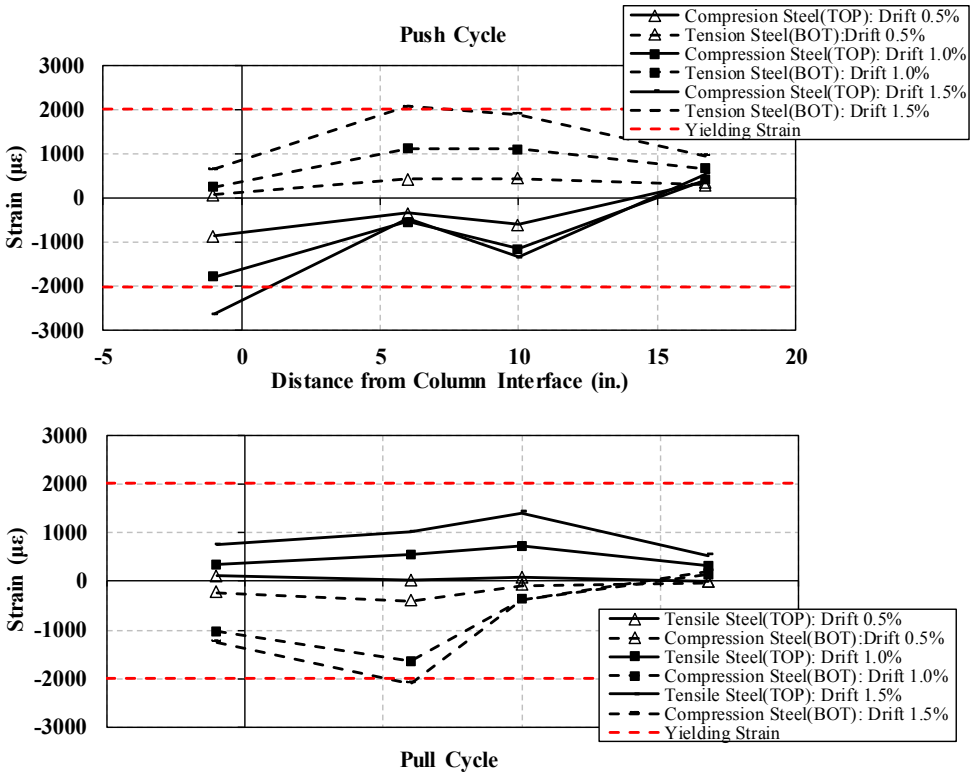

Figure 3-47. Strain Profile for Beam Longitudinal Reinforcement of RBC-D-R

3.6.2.6 Plastic Hinge Rotations and Curvatures for PBC1

Rotations were measured in the plastic hinge region of the precast beam for PBC1. Figures 3-48 and 3-49 show beam rotations at different drift ratios for PBC1-D and PBC1-D-R, respectively. As a general trend, the beam rotation was maximum at the column face due to the rocking of the beam.

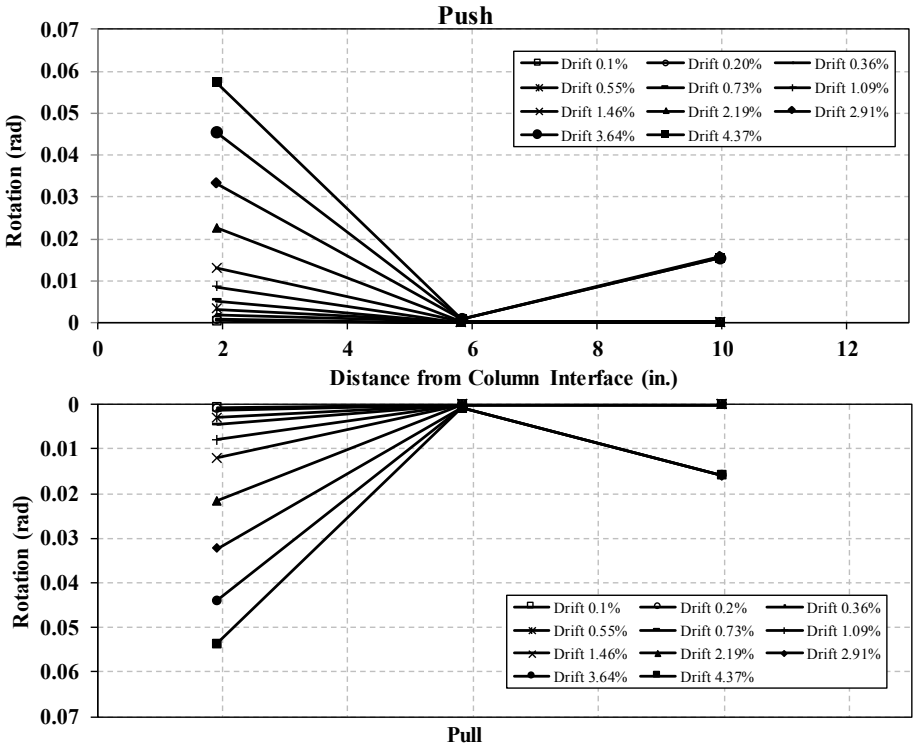

Figure 3-48. Plastic Hinge Rotations for PBC1-D

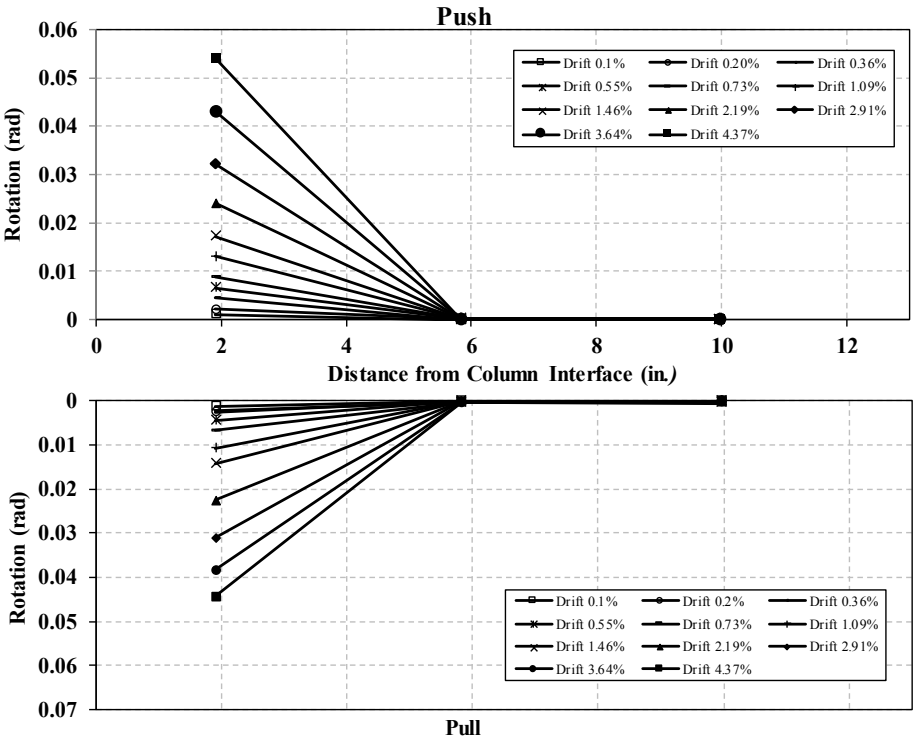

Figure 3-49. Plastic Hinge Rotations for PBC1-D-R

Plastic curvatures were measured at three different locations within the beam. Figures 4-50 and 3-51 show the measured curvatures for PBC1-D and PBC1-D-R, respectively. Similar to the beam rotations, the curvatures were maximum at the beam-column interface.

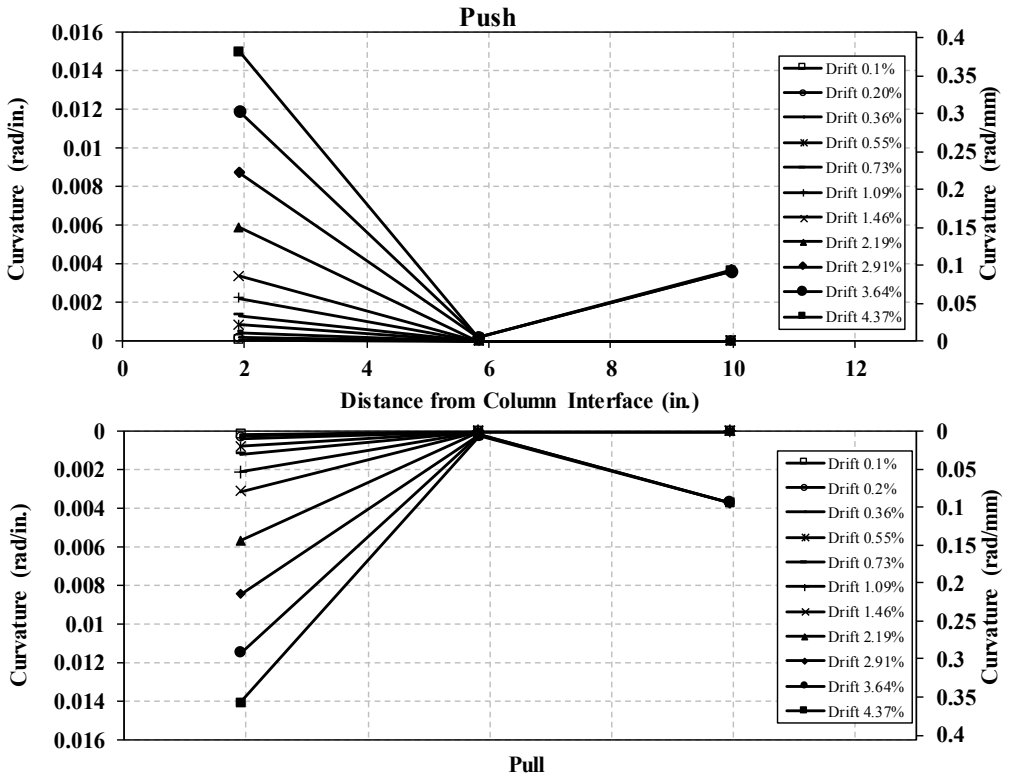

Figure 3-50. Plastic Hinge Curvature for PBC1-D

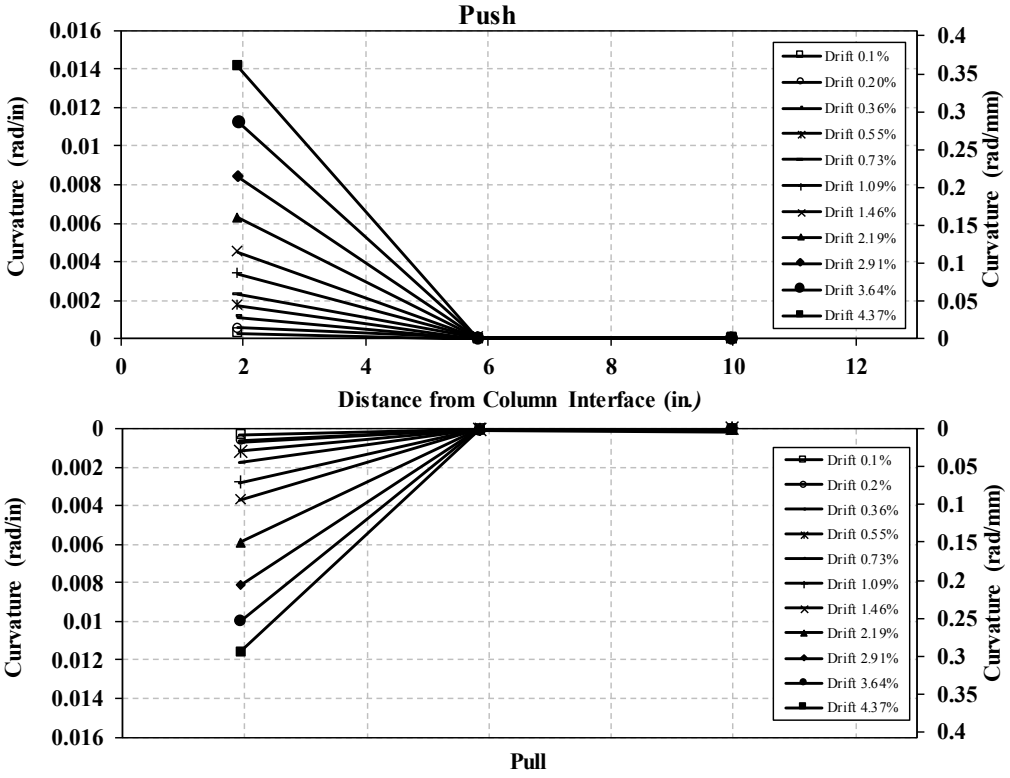

Figure 3-51. Plastic Hinge Curvature for PBC1-D-R

3.6.3 PBC2 Results

The testing of the pilot precast specimen, PBC1, showed that the precast beam detailing was not sufficient to prevent cosmetic damage where the beam depth changed. Therefore, another precast beam was designed and constructed to minimize the beam damage. PBC2 specimen consisted of this new precast beam and the same precast column used in PBC1. This section discusses the experimental findings of PBC2 including initial test with steel BRR, PBC2-D, and retest after repair with SMA BRR, PBC2-SMA.

3.6.3.1 Force-Displacement Relationships for PBC2

3.6.3.1.1 PBC2-D

Figure 3-52 shows the measured lateral force-displacement relationship for PBC2-D. The lateral load carrying capacity in the push and pull directions was 6.85 kips (30.5 kN) and 11.5 kips (51.2 kN), respectively. The bottom BRR bar yielded at a displacement of 0.787 in. (20 mm) corresponding to a lateral force of 3.87 kips (17.2 kN). The yield displacement and the yield force for top BRR bar (or in pull direction) were 1.57 in. (40 mm) and 8.44 kips (37.5 kN), respectively. The test was stopped at 3.64% drift ratio to perform the repair by replacing the BRR and to retest the specimen.

The beam end reaction versus the column tip lateral displacement is shown in Fig. 3-53. The maximum beam reaction was 10.69 kips (47.6 kN) and 18.7 kips (83.2 kN) in the push and pull directions, respectively.

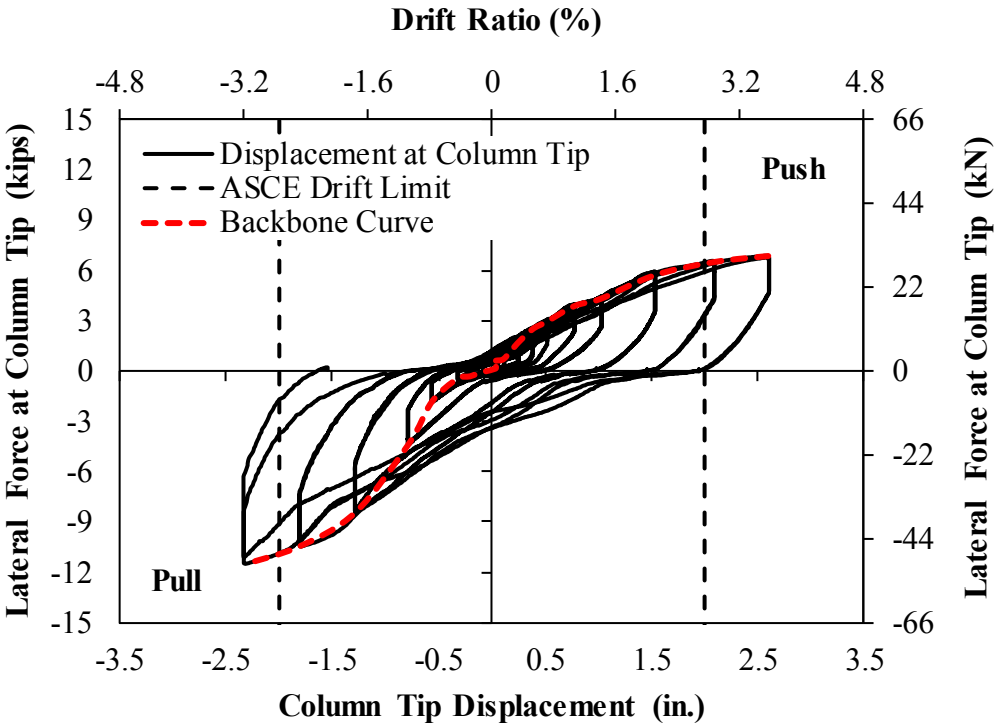

Figure 3-52. Measured Force-Displacement Relationship for PBC2-D

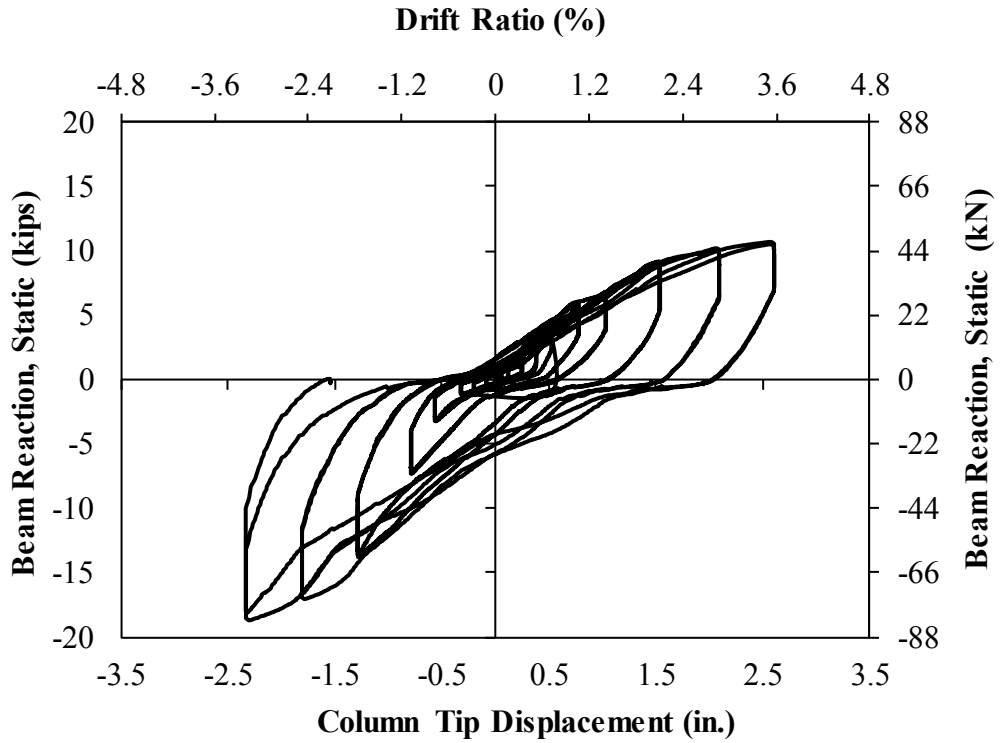

Figure 3-53. Measured Beam End Reaction for PBC2-D-R

3.6.3.1.2 PBC2-SMA

After testing PBC2-D, its BRR were replaced with new SMA BRR to investigate the repair-by-replacement method proposed in the present study. Figure 3-54 shows the lateral force-displacement relationship for PBC2-SMA. The lateral load carrying capacity in the push and pull directions was 9.56 kips (42.5 kN) and 7.67 kips (34.1 kN), respectively. The bottom BRR bar exceeded the SMA yield (or elastic austenite phase) at a displacement of 2.1 in. (53 mm) corresponding to a lateral force of 6.48 kips (28.8 kN). The yield displacement and the yield force for top BRR bar (or in pull direction) were 2.1 in. (53 mm) and 10.46 kips (46.5 kN), respectively. The specimen was displaced laterally to the failure point (8% drift ratio) in push direction only due to the stroke limitation in the other direction.

The beam end reaction versus the column tip lateral displacement is shown in Fig. 3-55. The maximum beam reaction was 10.95 kips (48.7 kN) and 9.73 kips (43.3 kN) in the push and pull directions, respectively.

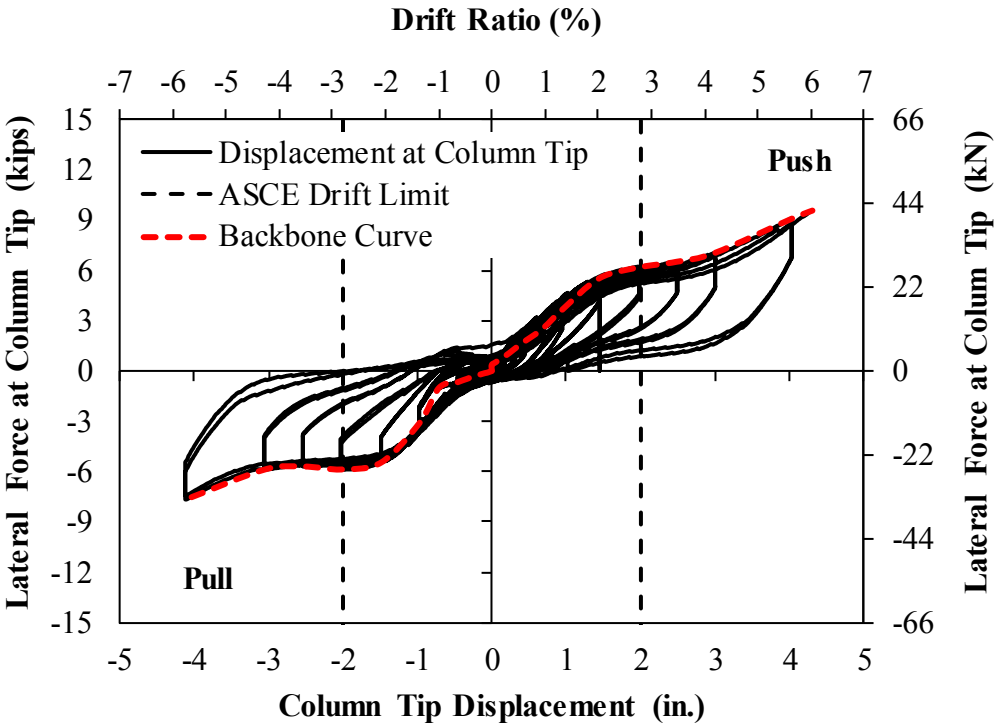

Figure 3-54. Measured Force-Displacement Relationship for PBC2-SMA

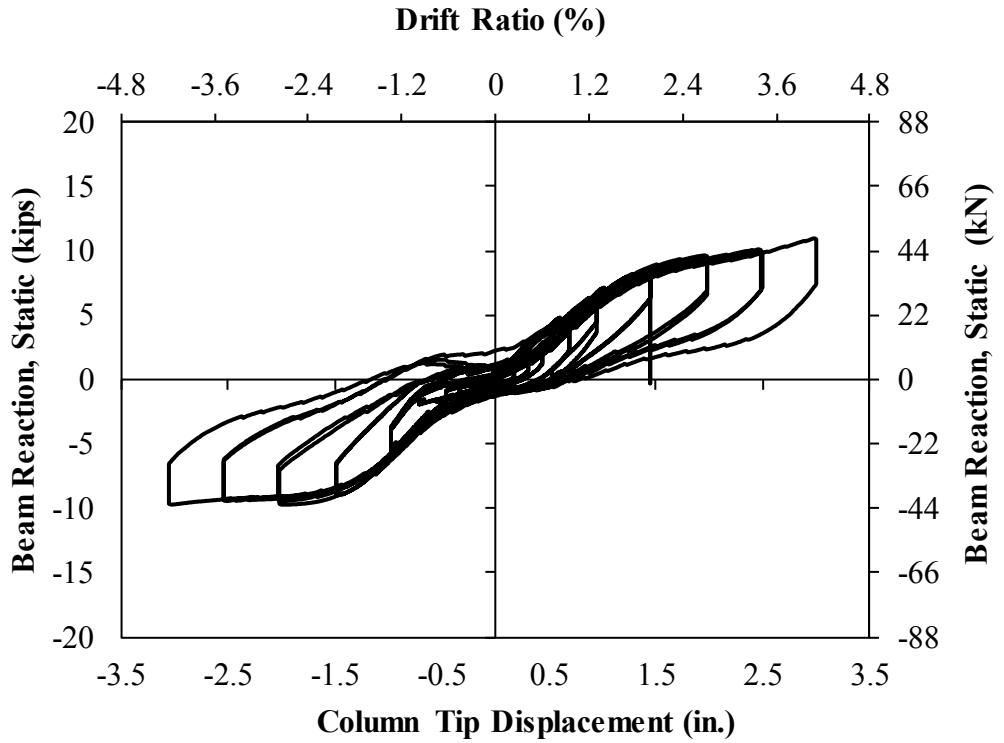

Figure 3-55. Measured Beam End Reaction for PBC2-SMA

3.6.3.2 Damage in PBC2

Damage and crack pattern were documented throughout the entire test for both PBC2-D and PBC2-SMA. PBC2-D specimen withstood 20 full cycles of loading without any failure. PBC2-SMA specimen withstood 24 full cycles of loading before exhibiting SMA BRR failure.

3.6.3.2.1 PBC2-D

Figure 3-56 shows the damage of PBC2-D at selected drift ratios. It can be seen that PBC2-D had no damage in the plastic hinge region at 3.64% drift ratio (equivalent to six times the design level earthquake). The first crack was developed at 1.45% drift ratio where the beam depth changes. The initial crack was extended in this region at higher drift ratios. No cracks long the length of the beam longitudinal bars was observed during this test. Overall, the specimen exhibited minimal damage after 20 full cycles thus the improved detailing was successful.

a) Drift Ratio 1.09% (east side)

b) Drift Ratio 1.09% (west side)

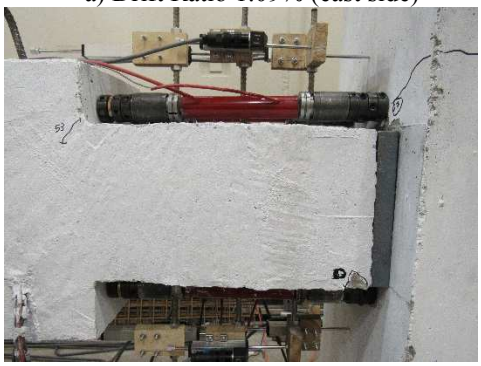

c) Drift Ratio 1.45% (east side)

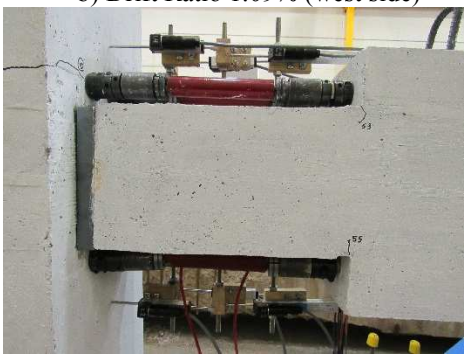

d) Drift Ratio 1.45% (west side)

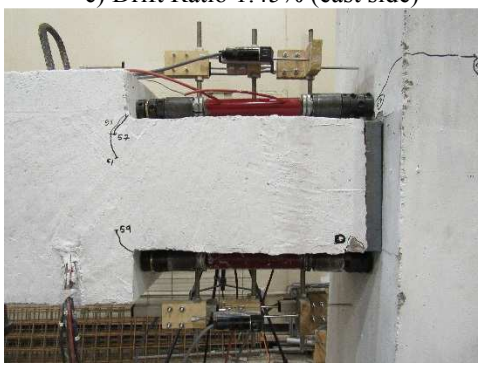

e) Drift Ratio 2.19% (east side)

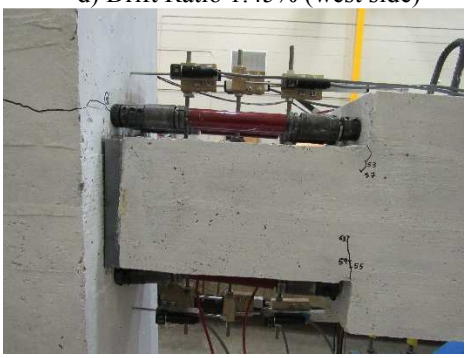

f) Drift Ratio 2.19% (west side)

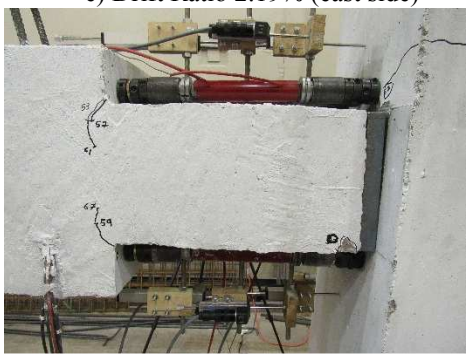

g) Drift Ratio 2.91% (east side)

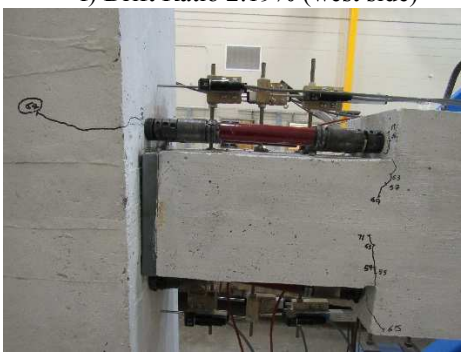

h) Drift Ratio 2.91% (west side)

Figure 3-56. Damage for PBC2-D at Selected Drift Ratios

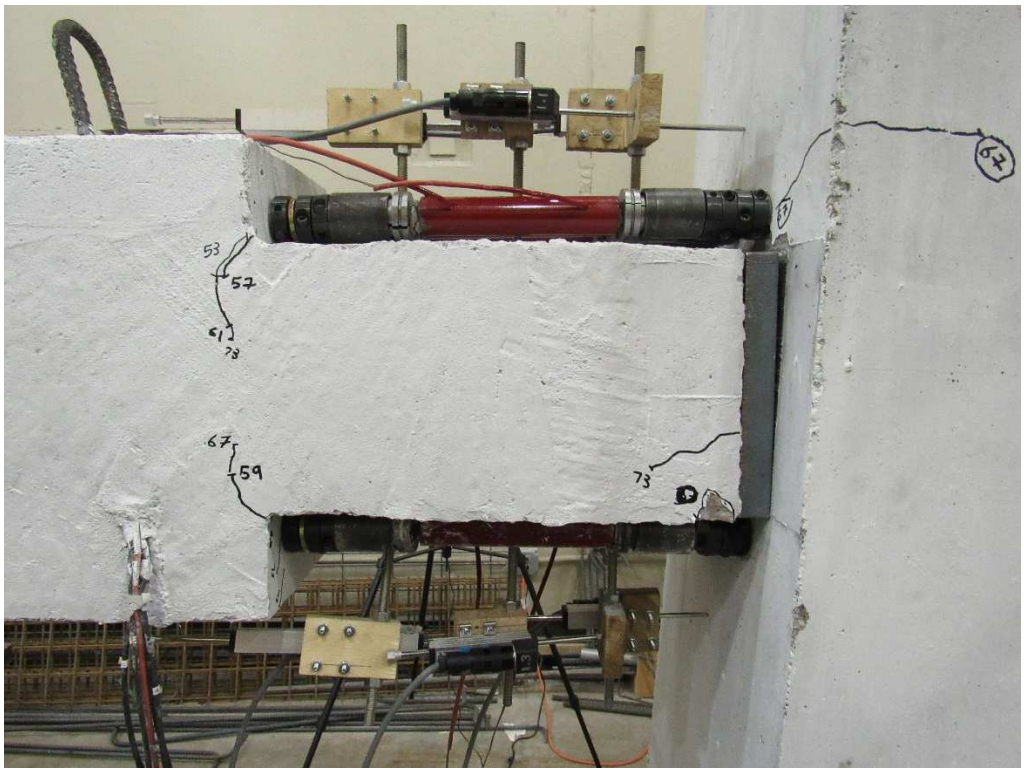

i) Drift Ratio 3.64% (east side)

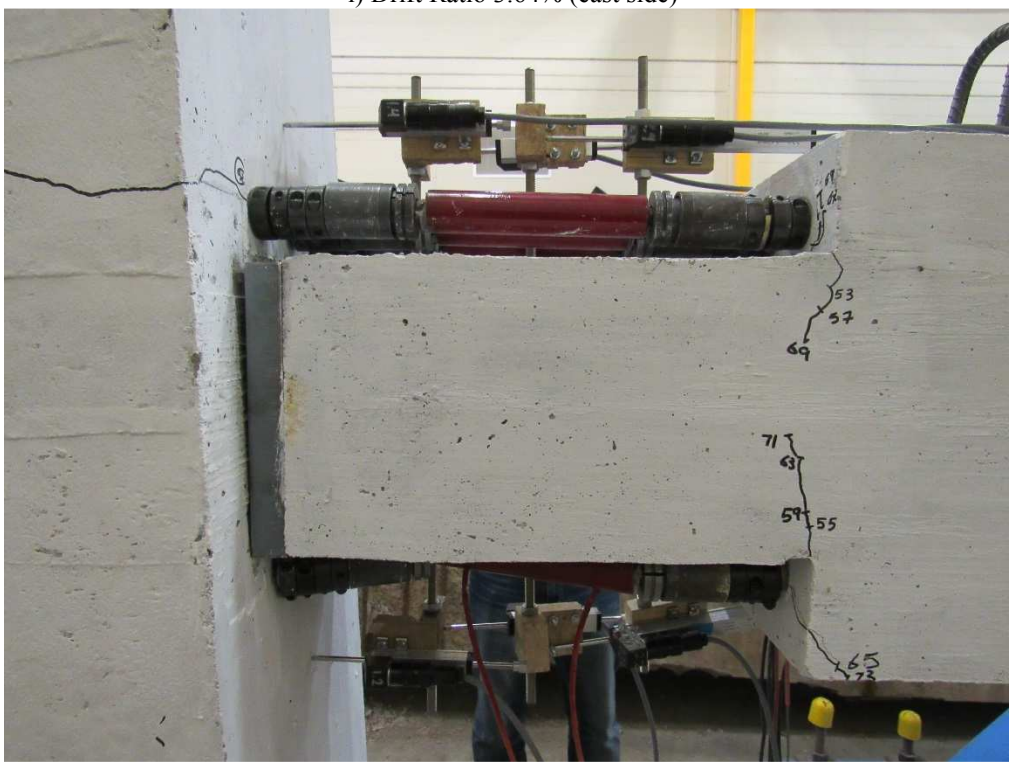

g) Drift Ratio 3.64% (west side)

Figure 3-56. Continued

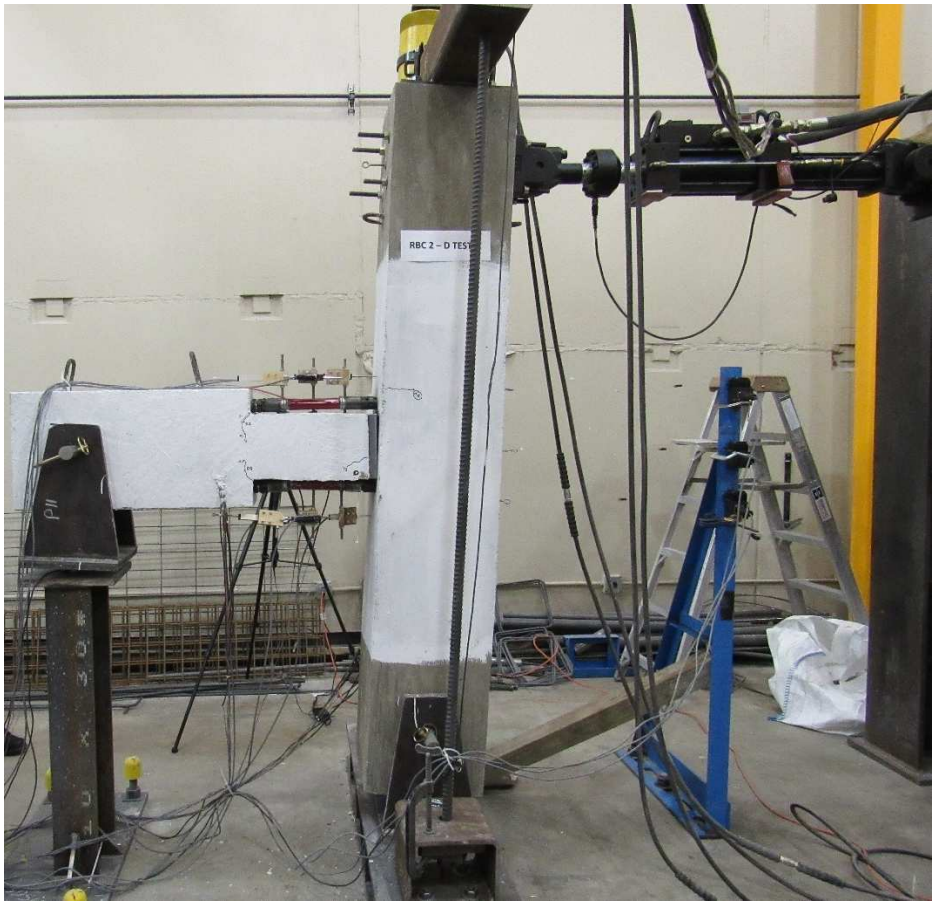

k) Drift Ratio 3.64% (full view)

Figure 3-56. Continued

3.6.3.1 PBC2-SMA

Figure 3-57 shows the damage of PBC2-SMA at selected drift ratio. It can be seen that PBC2-SMA had no damage beyond a few minor cracks in the first round of testing and event even at 8% drift ratio (equivalent to 14 times the design level earthquake). Figure 3-57o shows the damage of PBC2-SMA 8% drift ratio where SMA BRR fractured at the head.

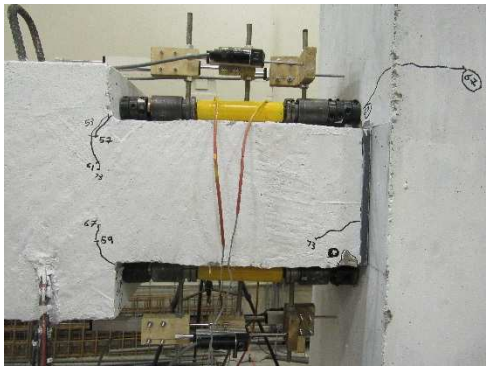

a) Drift Ratio 1.09% (east side)

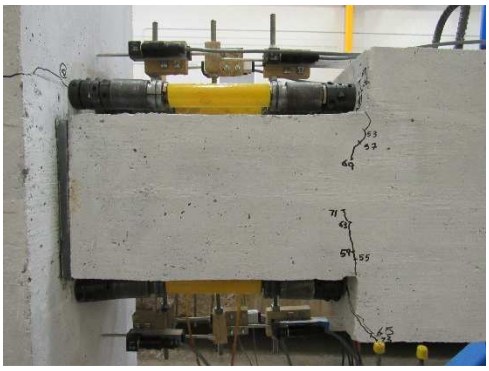

b) Drift Ratio 1.09% (west side)

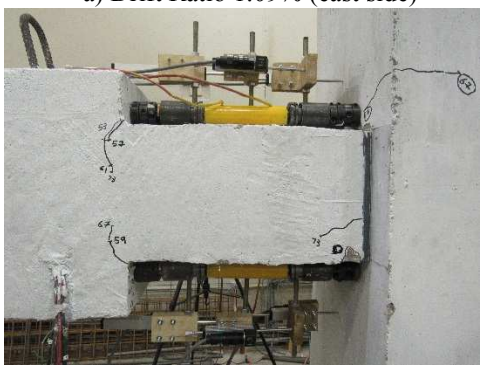

c) Drift Ratio 1.45% (east side)

d) Drift Ratio 1.45% (west side)

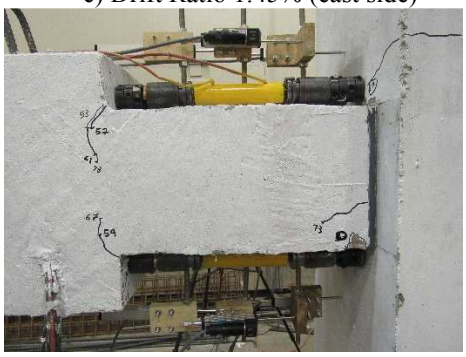

e) Drift Ratio 2.19% (east side)

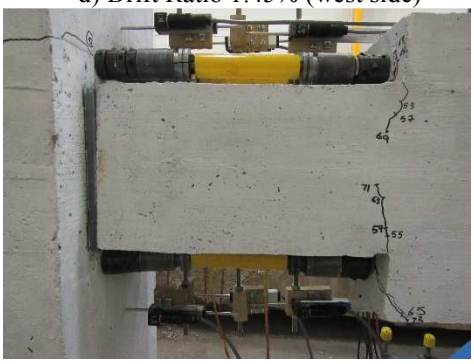

f) Drift Ratio 2.19% (west side)

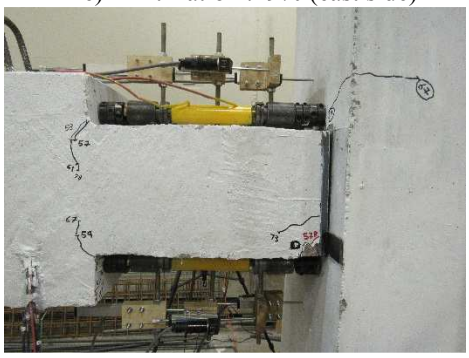

g) Drift Ratio 2.91% (east side)

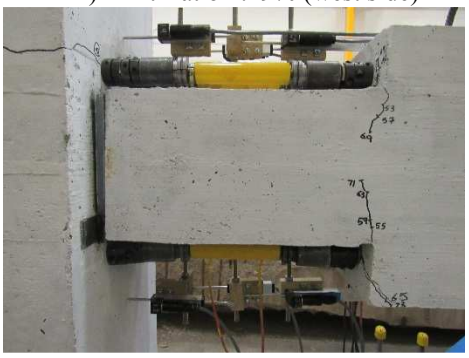

h) Drift Ratio 2.91% (west side)

Figure 3-57. Damage for PBC2-SMA at Selected Drift Ratios

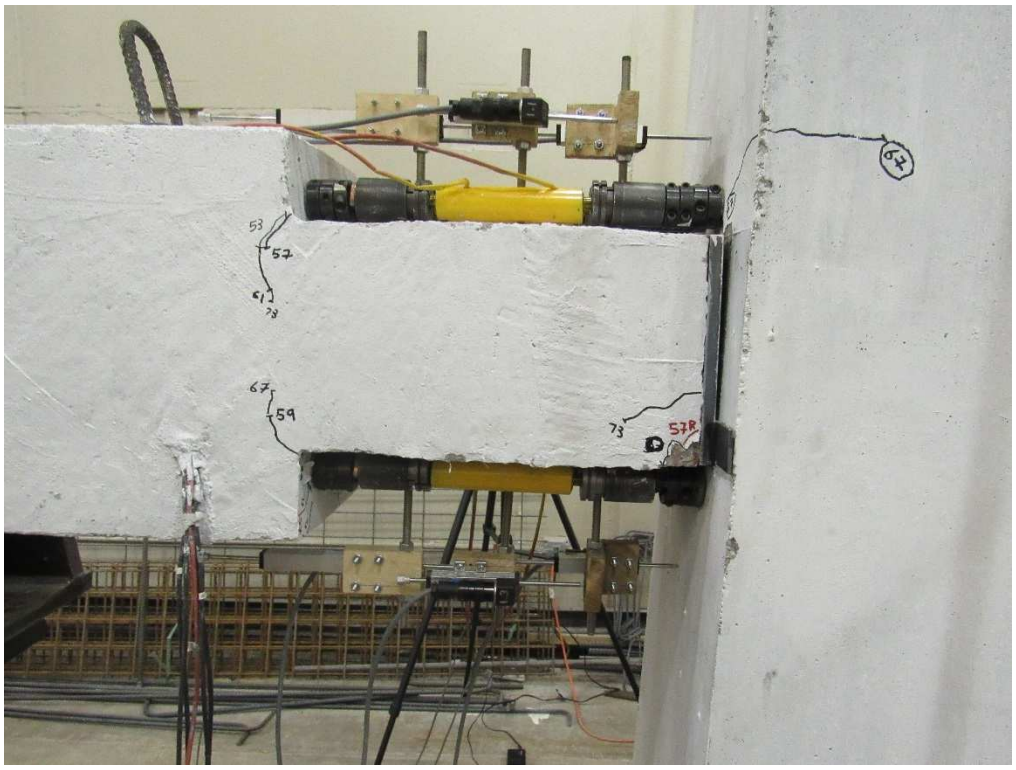

i) Drift Ratio 3.64% (east side)

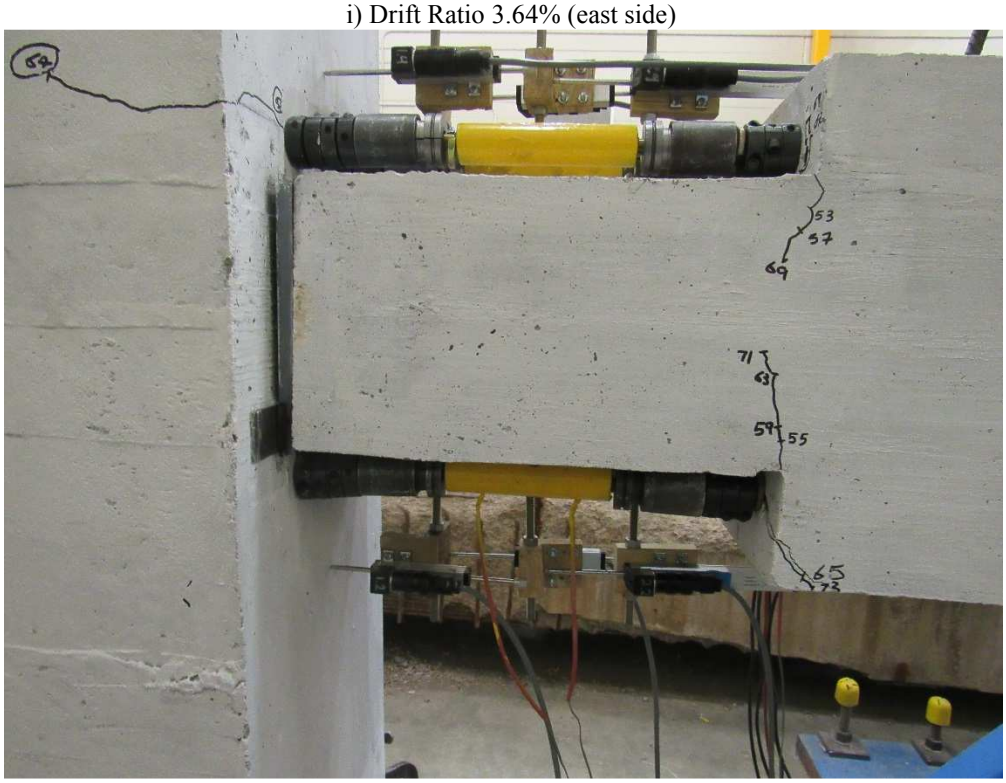

g) Drift Ratio 3.64% (west side)

Figure 3-57. Continued

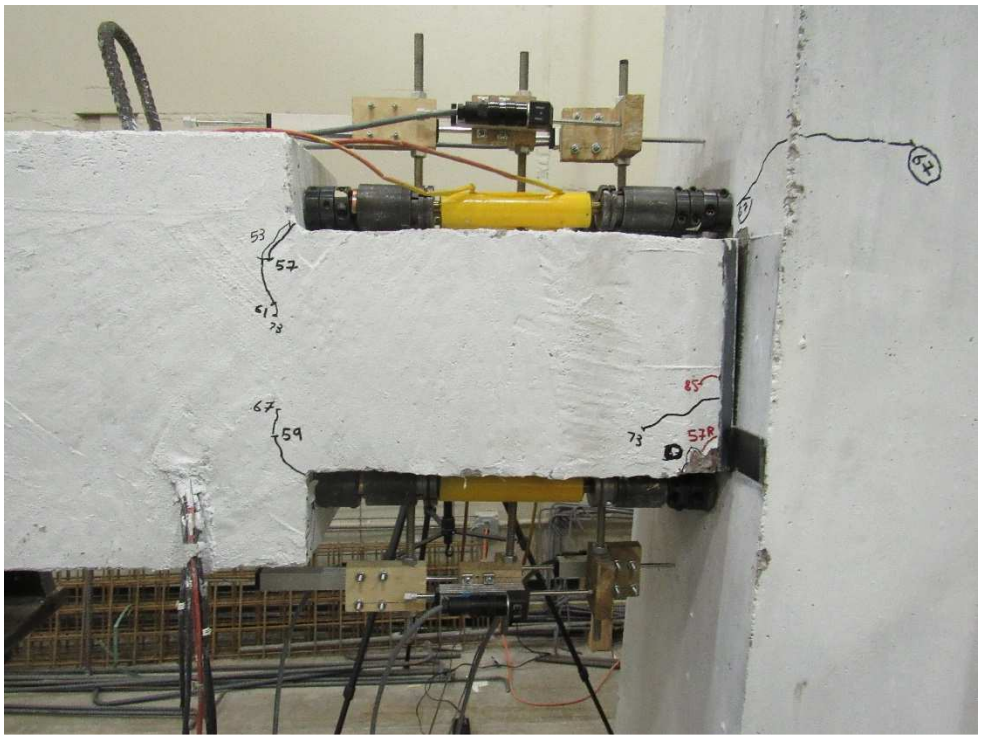

k) Drift Ratio 4.37% (east side)

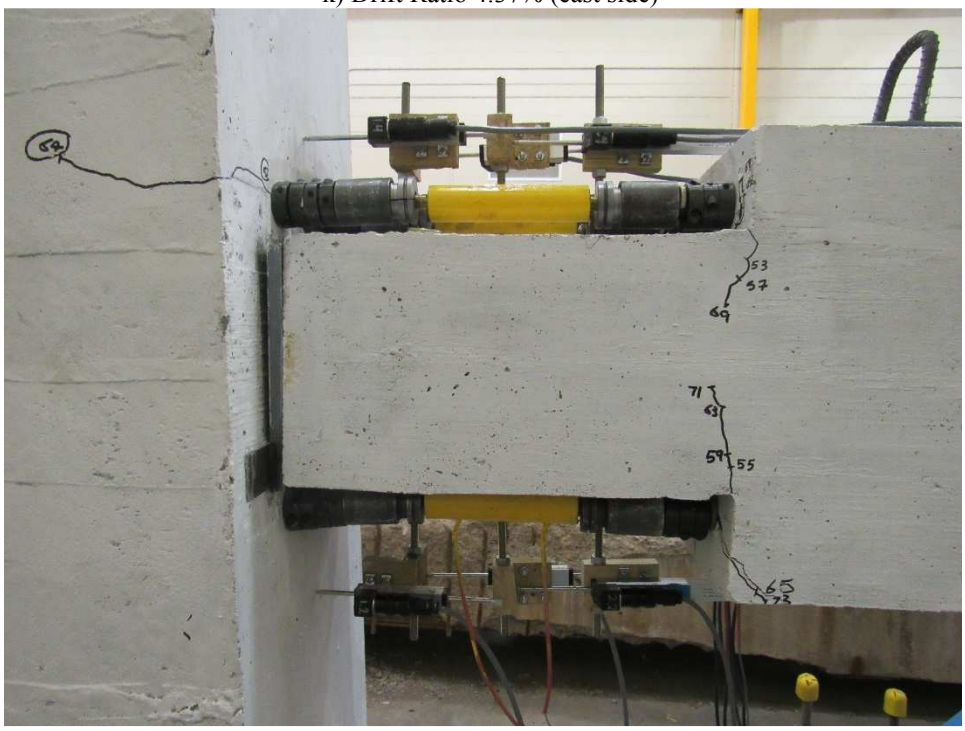

l) Drift ratio 4.37% (west side)

Figure 3-57. Continued

m) Drift Ratio 5.83 % (east side)

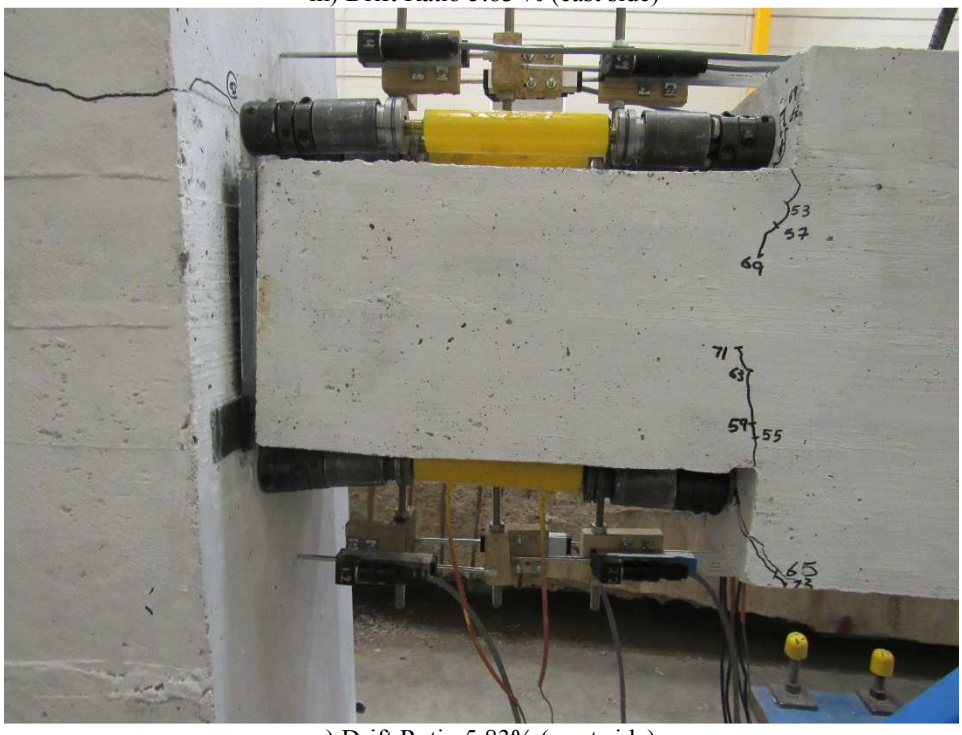

n) Drift Ratio 5.83% (west side)

Figure 3-57. Continued

o) Drift Ratio 5.83% (full view)

Figure 3-57. Continued

3.6.3.3 Failure Mode of PBC2

As mentioned before, PBC2-D and PBC2-SMA respectively withstood 20 and 24 full cycles of loading, the largest of which was at 8% drift ratio, without any signs of failure. The steel BRR in PBC2-D were deformed in a Z-shape manner (Fig 3-58a) during the cycles of 3.64% drift ratio but did not fail. If the test was continued, BRR would have been straightened and functional in tension. PBC2-SMA did not show any sign of failure until rupture at 8% drift ratio. No concrete spalling was observed in both tests.

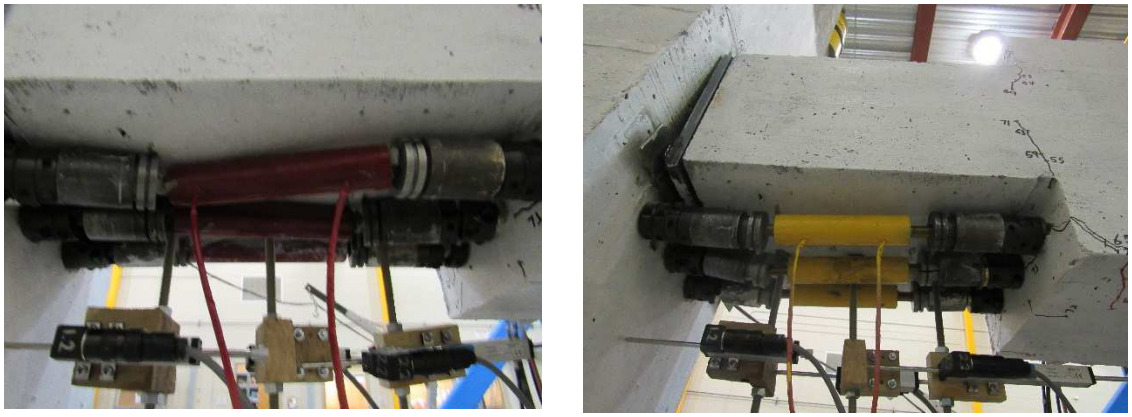

a) Z-Shape Damage for PBC2-D b) Damage for PBC2-SMA

Figure 3-58. Replaceable Reinforcement Damage Sustained by PBC2 Specimen

3.6.3.4 Residual Displacements of PBC2

Figures 3-59 and 3-60 show the peak drifts versus the residual drifts for PBC2-D and PBC-SMA, respectively. The residual displacement was calculated as the displacement at zero force in the unloading branch of the first cycle per drift level. It can be seen that the residual displacements of PBC2-D were higher than those in PBC2-SMA due to low residual strains in SMA bars.

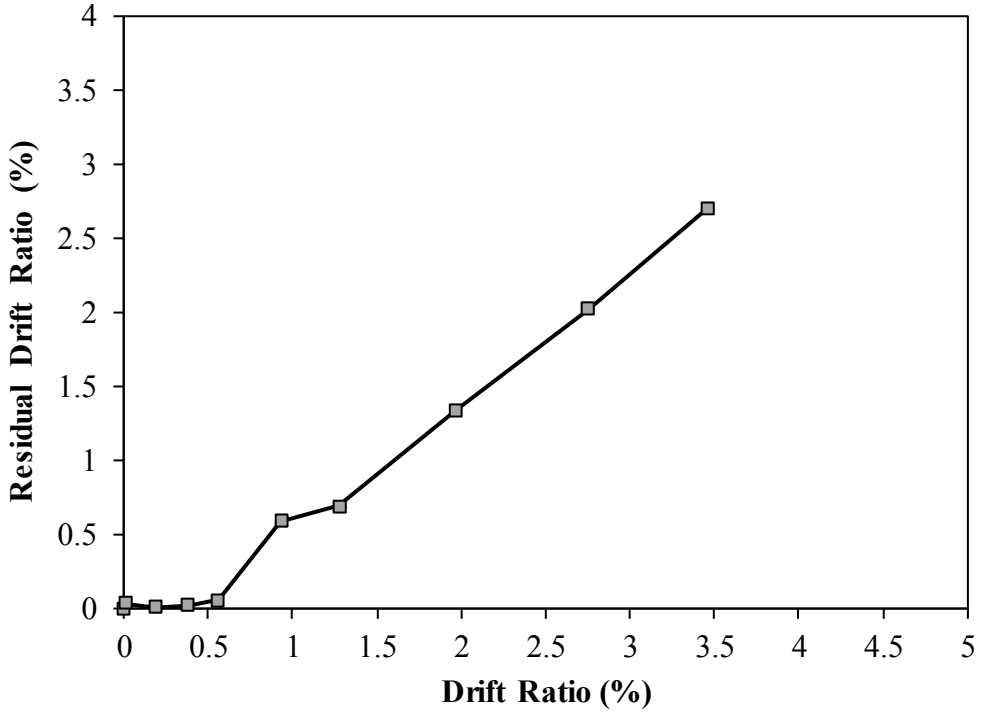

Figure 3-59. Residual Drifts for RBC2-D

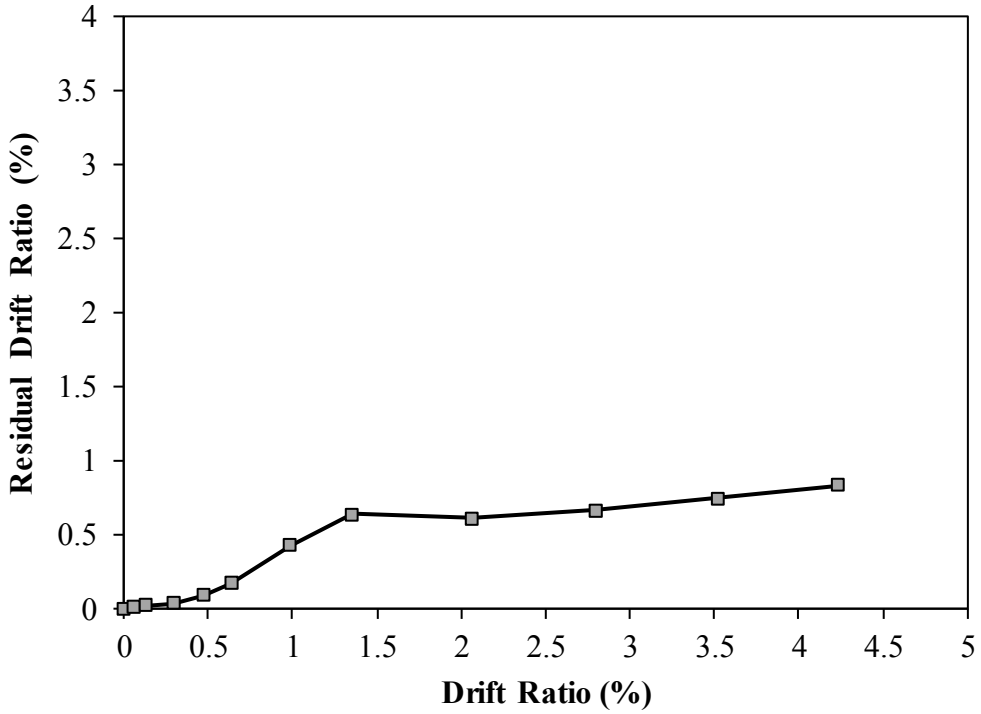

Figure 3-60. Residual Drifts for RBC2-SMA

3.6.3.5 Strain profiles for Beams of PBC2

The strain for both longitudinal and transverse reinforcement were measured using strain gauges installed at different locations. Figure 3-61 and 3-62 show the strain profiles for the beam top and bottom reinforcement in PBC2-D and PBC2-SMA, respectively. The data was presented up to the displacement where the measured strains were valid. The steel BRR in beam yielded at 1.09% drift ratio while the SMA BRR yielded at 2.91% drift ratio. Furthermore, it can be seen that the strain is well distributed in the plastic hinge area. Further, the column reinforcement did not yield even at the peak displacement. The beam transverse reinforcement also did not yield. It can be concluded that the proposed detailing was compatible with the "strong-column weak-beam" design method to achieve large displacements.

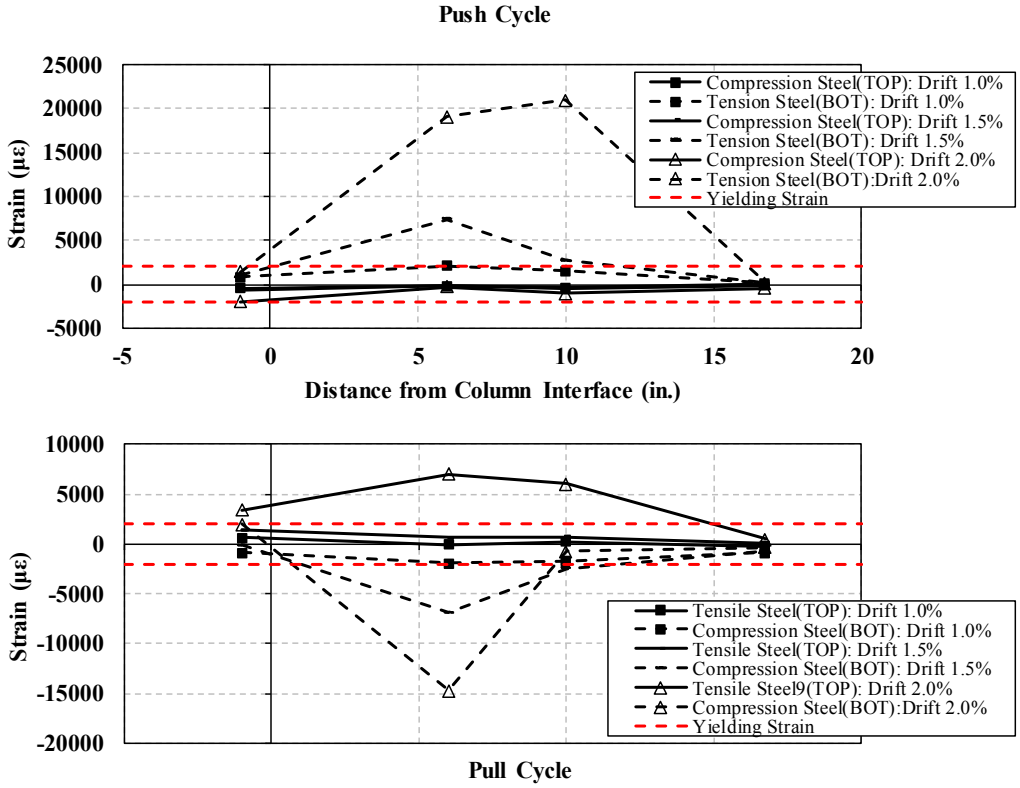

Figure 3-61. Strain Profiles for Beam Longitudinal Reinforcement in RBC2-D

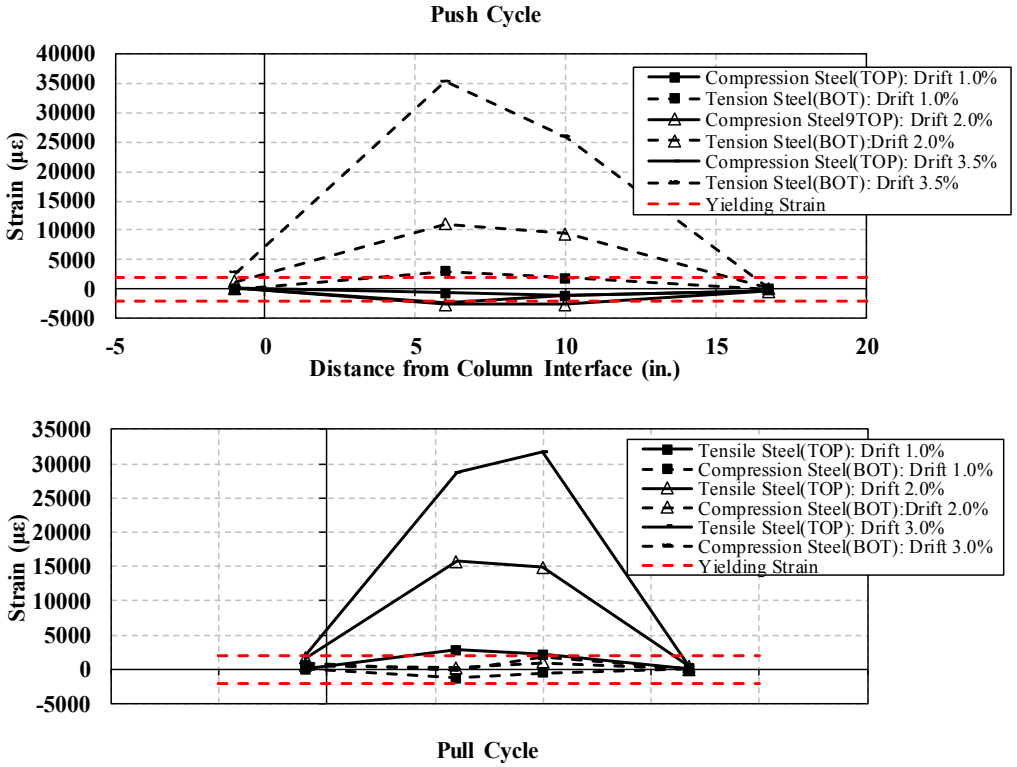

Figure 3-62. Strain Profiles for Beam Longitudinal Reinforcement in RBC2-SMA

3.6.3.6 Plastic Hinge Rotations and Curvatures for PBC2

Rotations were measured in the plastic hinge region of the precast beam for PBC2. Figures 3-63 and 3-64 show beam rotations at different drift ratios for PBC2-D and PBC2-SMA, respectively. As a general trend, the beam rotation was maximum at the column face due to the rocking of the beam.

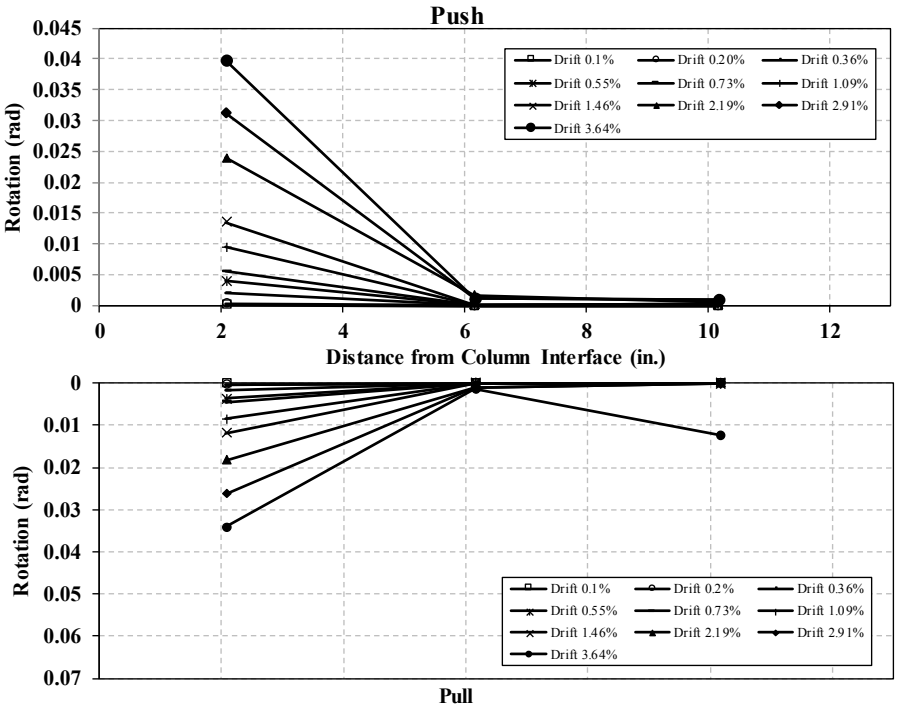

Figure 3-63. Plastic Hinge Rotations for PBC2-D

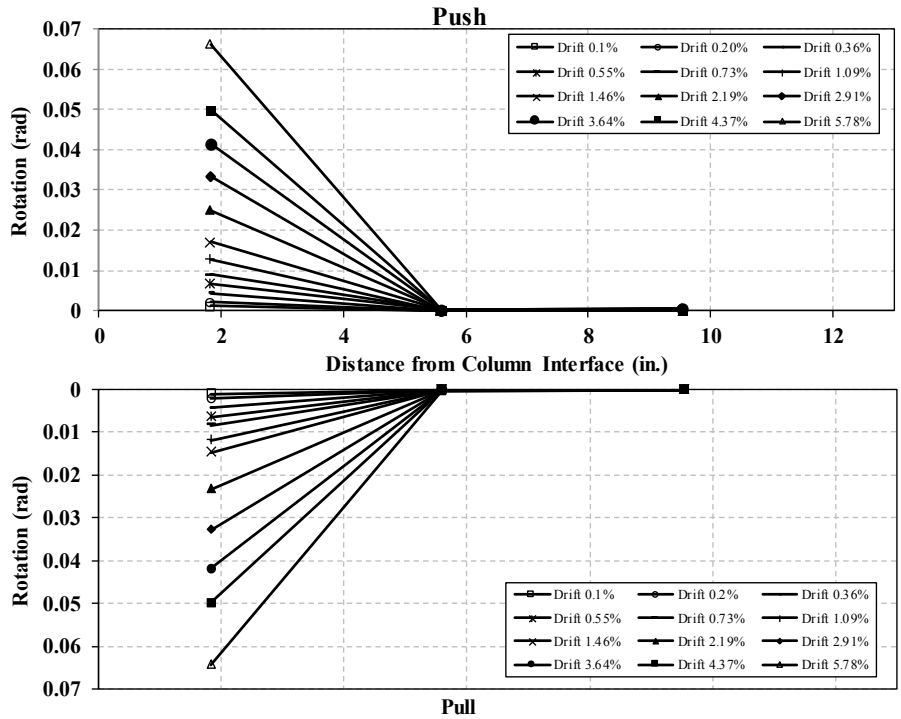

Figure 3-64. Plastic Hinge Rotations for PBC2-SMA

Plastic curvatures were measured at three different locations within the beam. Figures 4-65 and 3-66 show the measured curvatures for PBC2-D and PBC2-SMA, respectively. Similar to the beam rotations, the curvatures were maximum at the beam-column interface.

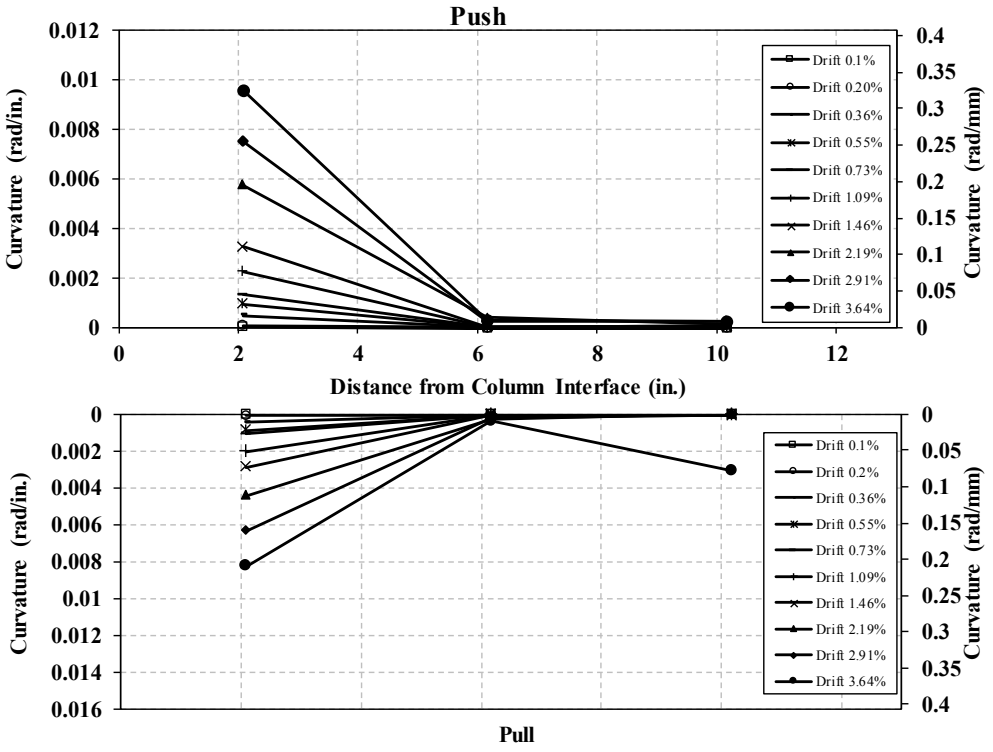

Figure 3-65. Plastic Hinge Curvatures for PBC2-D

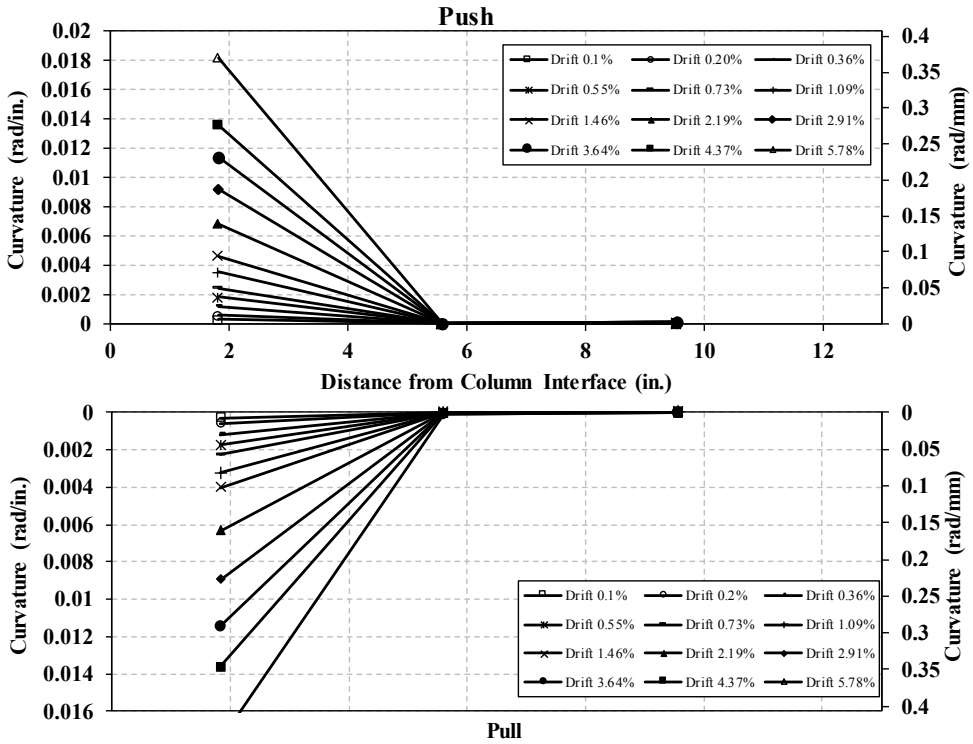

Figure 3-66. Plastic Hinge Curvatures for PBC2-SMA

3.6.4 Seismic Performance of Cast-in-Place and Precast Specimens

In this section, the seismic performance of all precast specimens is compared to that of the reference cast-in-place specimen (CIP) tested by Tuhin (2016).

3.6.4.1 Force-Displacement Relationships for All Beam-Column Specimens

Figure 3-67 shows the lateral force-displacement relationships for CIP and all precast specimens. Figure 3-68 shows the lateral force- displacement hysteresis for all beam-column specimens. Table 3-8 presents a summary of the test results. The lateral load resistance for PBC1-D, PBC1-D-R, PBC2-D, and PBC2-SMA, where the tests were stopped, was 11.23 kips (50 kN), 10.69 kips (47.6 kN), 11.5 kips (51.2 kN), and 9.56 kips (42.5 kN), respectively. CIP showed the highest lateral load resistance at 3.64% drift ratio (where it failed), which was 12.62 kips (56.1 kN). The higher lateral force capacity

in CIP up this drift limit was due to a higher beam reinforcement ratio and a higher beam depth at the beam-column interface. Nevertheless, the precast specimens could provide similar lateral load resistance using a large size reinforcement. PBC2-SMA showed the highest lateral load capacity among all other in the pull direction specimens. However, due to an initial gap between the steel plate and the column, its lateral load resistance was the lowest in all specimens. The gap was filled with a steel spacer later in the test at 2.9% drift ratio in the pull direction (Fig. 3-57g).

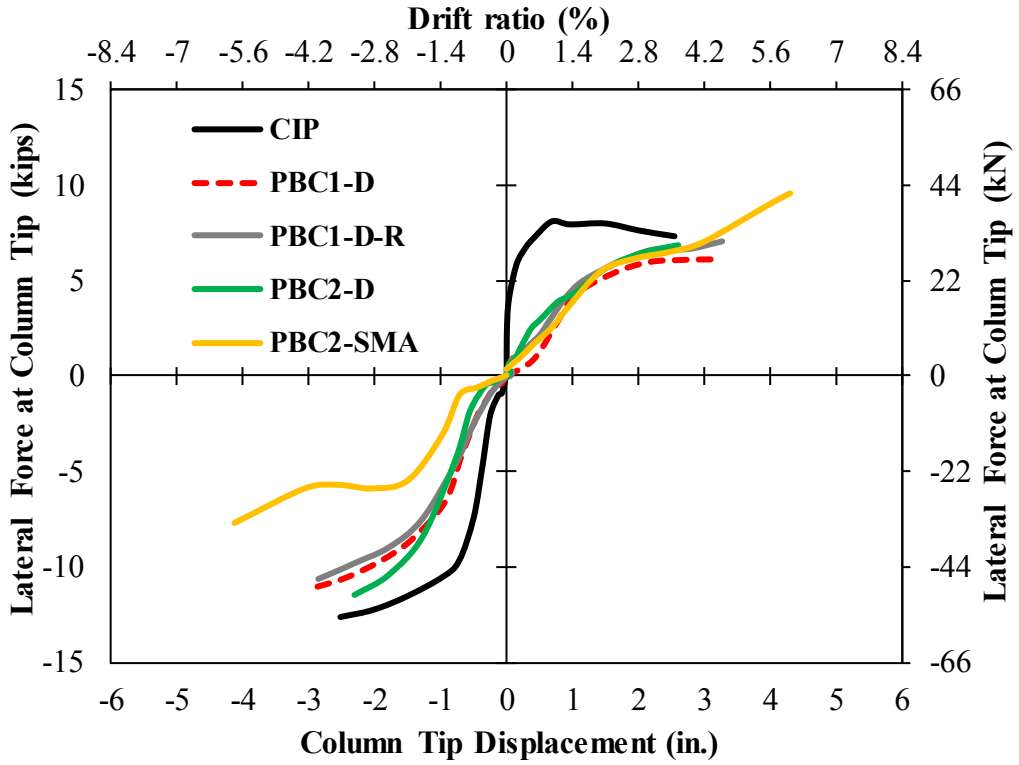

Figure 3-67. Measured Force-Displacement Relationships of all Beam-Column Specimens

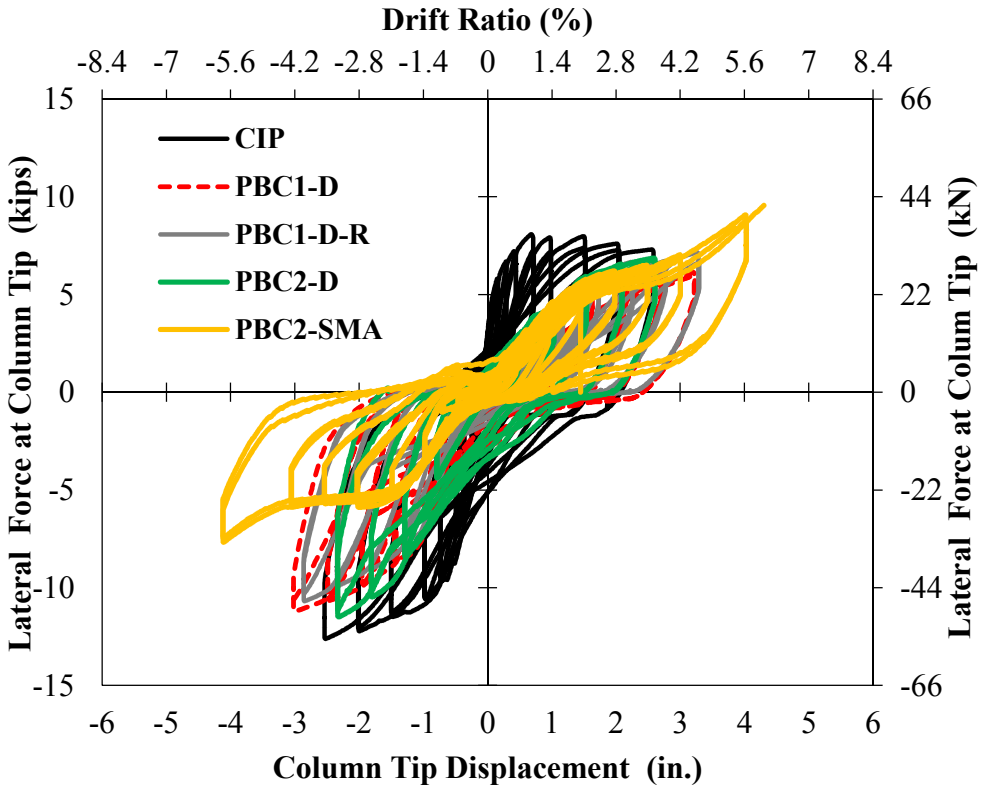

Figure 3-68. Stress-strain Hysteretic Relationship of all Beam-Column Specimens

Table 3-8. Summary of Test Results for Half-Scale Beam-Column Specimens

Specimen ID	Initial Stiffness, kip/in (kN/m)	Yield Drift Ratio (%)	Yield Force, kips (kN)	Ultimate Drift Ratio (%)	Ultimate Force, kips (kN)	Mode of Failure
CIP	24.83 (4348)	0.18	5.63 (25)	3.64	12.62 (56.1)	Beam Bar Fracture
PBC1-D	5.64 (988)	1.46	4.31 (19.2)	Stopped at 4.37	11.23 (50)	Did not fail
PBC1-D-R	4.54 (795)	1.46	5.02 (22.3)	Stopped at 4.37	10.69 (47.6)	Did not fail
PBC2-D	6.52 (1142)	1.09	3.87 (17.2)	Stopped at 3.64	11.5 (51.2)	Did not fail
PBC2-SMA	3.7 (648)	2.91	6.48 (28.8)	8	9.56 (42.5)	SMA BRR fracture

Note: Column Height: 72 in. (YY mm); Beam Length: 45 in. (1143 mm);

Although the precast specimens had lower initial stiffness compared to CIP, it exhibited significantly higher drift capacity with no reinforcement fracture. The lower initial stiffness of the precast specimens could be due to the nature of the proposed connection and the vertical gap between the steel pipe and the steel socket (cup) at the

beam end. CIP failed at 3.64% drift ratio by beam longitudinal reinforcement fracture while all precast specimens withstood the same drift ratio without any signs of failure. Only PBC2-SMA was pushed to failure at 8% drift ratio, which was 2.2 times higher than the CIP drift capacity. This finding indicates that the displacement capacity of a precast building incorporating the proposed connections can be significantly higher than that for a corresponding conventional cast-in-place building.

3.6.4.2 Damage for All Beam-Column Specimens

Figure 3-69 shows the damage of all precast and CIP specimens at 3.64% drift ratio equivalent to six times the design level earthquake, where CIP failed. It can be seen that precast specimens had no damage in the plastic hinge region while the CIP specimen failed by beam reinforcement fracture. The improved beam detailing in PBC2 was successful in minimizing the beam damage where the depth changed. For example, PBC2-SMA had two hairline cracks at 8% drift ratio (equivalent to 13.5 times the design level earthquake) where SMA bar rapture. Overall, the damage of precast components of the proposed detailing is expected to be insignificant even under extreme earthquakes. However, BRR may yield or fracture, which can be simply replaced after the earthquake to complete the repair.

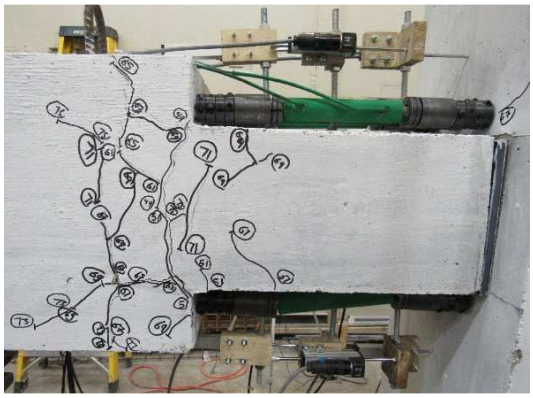

a) Damage of PBC1-D

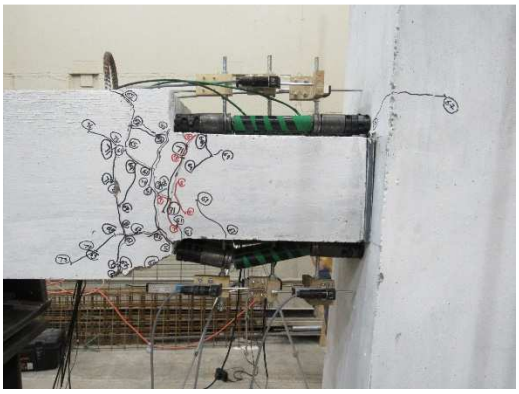

b) Damage of PBC1-D-R

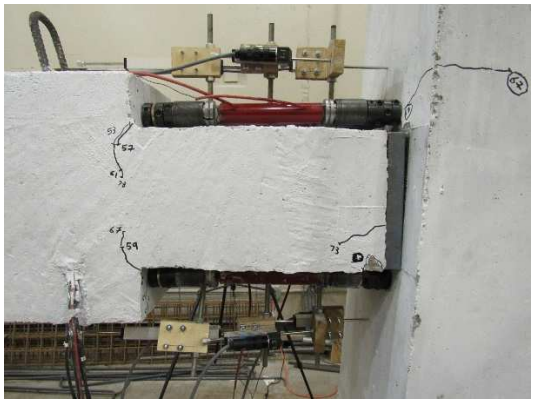

c) Damage of PBC2-D

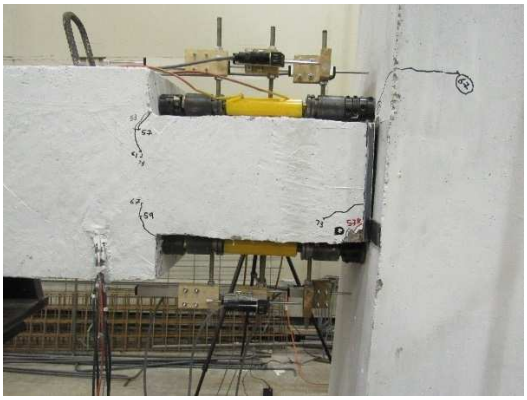

d) Damage of PBC2-SMA

e) Damage of CIP Specimen

Figure 3-69. Damage of All Beam-Column Specimens at 3.64% Drift Ratio

3.6.4.3 Failure Mode for All Beam-Column Specimens

Table 3-8 presents the failure mode of all specimens. CIP and PBC2-SMA failed by bar fracture at 3.64 and 8% drift ratios, respectively. However, the test in other

precast specimens were stopped beyond the failure of CIP to perform the repair by bar replacement. Overall, the proposed detailing will increase the displacement capacity of precast buildings, will prevent concrete damage, and will eliminate building total replacement.

3.6.4.4 Residual Displacements for All Beam-Column Specimens

Figure 3-70 shows the peak drift ratios versus the residual drift ratios for all precast and CIP specimens. It can be seen that all precast specimens showed lower residual displacements than those in CIP for all corresponding drift ratios. The precast specimen reinforced with SMA BRR showed the lowest residual drifts, less than 1%, among all other specimens indicating that SMA BRR can bring back the structure to its original position even under severe earthquake with the need of BRR replacement.

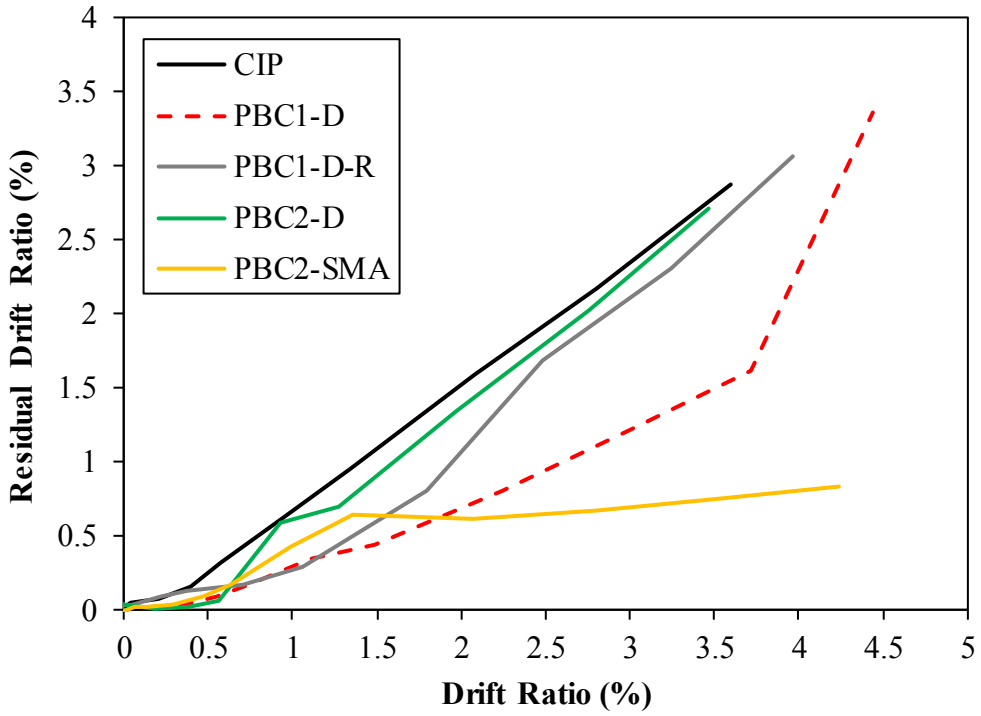

Figure 3-70. Residual Drifts for All Beam-Column Specimens

3.7 Summary and Conclusions

An innovative moment-resisting connection was developed for precast buildings in which the damage is limited to exposed reinforcement, and these reinforcement can be replaced. A proof-testing was performed to investigate the feasibility and seismic performance of the proposed precast connection. Two repairable precast specimens and one reference cast-in place beam column specimen were constructed and tested. Each precast specimen was tested twice to exercise the repair by bar replacement method. Each precast specimen was repaired after the first round of testing by simply replacing its buckling restrained reinforcement, BRR, and was retested under the same loading protocol. The following conclusions can be drawn from the experimental study:

1) No damage was observed in the plastic hinge regions of the precast specimens. The improved precast beam had insignificant concrete damage even at 13.5 times the design level earthquake.

2) The displacement capacity of all precast specimens was higher than that in CIP.

3) The lateral load carrying resistance of the precast specimens were lower than that in CIP at the same drift ratios due to lower reinforcement ratio and reduce beam depth at the neck region.

4) The initial stiffness of the precast specimens were lower than that in CIP at the same drift ratios due to the vertical gap between the steel pipe and the steel socket (cup) at the beam-column interface.

5) All precast specimens showed lower residual displacements than those in CIP. The residual drift ratio for SMA reinforced precast specimen was less than 1%,

which is insignificant. SMA will be able to bring back the building to its original shape.

6) The repair by replacement method was practiced twice in the present study for the proposed detailing. The results confirm that this method is viable repair option for buildings. Building total replacement is prevented using the proposed method. Precast buildings can withstand severe earthquakes with minimal damage and ability to be repaired afterward by replacing the damaged reinforcement. This will prevent total replacement of the building.

Overall, the proposed detailing can significantly increase the displacement capacity of a precast building incorporating the proposed detailing compared to a corresponding cast-in-place building. The concrete damage will be insignificant in precast members which will prevent component repair or replacement. The precast building can be repaired by simply replacing the exposed BRR after a severe event. The building total replacement is eliminated used the proposed method.

3.8 References

1. Zaghi, A., and Saiidi, M.S. (2010). "Seismic Design of pipe pin connections in Concrete Bridges," Center for Civil Engineering Earthquake Research, University of Nevada, Reno, Nevada. CCEER Report No. 10-01.
2. ASCE Standard (2010). "Minimum Design Loads for Buildings and Other Structures," American Society of Civil Engineers (ASCE), 1801 Alexander Bell Drive, Reston, Virginia 20191.

3. American Concrete Institute (ACI) Committee 318 (2014). “Building Code Requirements for Structural Concrete and Commentary,” ACI 318-14, ACI, Farmington Hills, MI.
4. Tuhin, I.A. (2016). “Application of New Materials and Innovative Detailing for Reinforced Concrete Structures,” MSc thesis, South Dakota State University, Brookings, SD.
5. Krawinkler, Helmut, and Piotr, D. M. (1982). "Similitude Requirements for Dynamic Models," Special Publication, 73, pp. 1-22.
6. Mander, J., Priestley, M., & Park, R. (1988). "Observed stress-strain behavior of confined concrete," Journal of structural engineering, 114(8), 1827-1849.
7. American Concrete Institute (ACI) Committee 374 (2013). “Guide for Testing Reinforced Concrete Structural Elements Under Slowly Applied Simulated Seismic Loads,” ACI 374.2R-13, ACI, Farmington Hills, MI.
8. AISC (2011). “Specification for Structural Steel Buildings,” American Institute of Steel Construction, Inc., One East Wacker Drive, Suite 700, Chicago, Illinois 60601-1802.
9. ASTM Standard C39-12 (2012). "Standard Test Method for Compressive Strength of Cylinder Concrete Specimens," ASTM International, West Conshohocken, PA.
10. ASTM Standard C143 (2012). "Standard Test Method for Slump of Hydraulic-Cement Concrete," ASTM International, West Conshohocken, PA. doi:10.1520/C0143_C0143M-12.

11. ASTM Standard C617-12 (2012). “Standard Practice for Capping Cylindrical Concrete Specimens,” ASTM International, West Conshohocken, PA.
12. ASTM Standard A706/A706M-09b (2009). “Standard Specification for Low-Alloy Steel Deformed and Plain Bars for Concrete Reinforcement,” ASTM International, West Conshohocken, PA.
13. ASTM Standard E8/E8M-11 (2011). “Standard Test Methods for Tension Testing of Metallic Materials,” ASTM International, West Conshohocken, PA.
14. ASTM Standard A-496 (2007), “Standard Specification for Steel Wire, Deformed, for Concrete Reinforcement,” ASTM International, West Conshohocken, PA.
15. ASTM International. A370-12 (2012). “Standard Test Methods and Definitions for Mechanical Testing of Steel Products,” ASTM International, West Conshohocken, PA. DOI: 10.1520/A0370-12a.

Chapter 4: Repairable Reinforced Concrete Frames - Analytical Investigations

4.1 Introduction

The seismic performance of precast buildings incorporating the proposed connection detailing presented in the previous chapter is analytically investigated. First, modeling methods and the analytical results for all beam-column test specimens (Ch. 3) are discussed. The calculated and measured responses are compared to comment on the accuracy of the proposed modeling method. Then, using the verified model, a comprehensive analytical study including pushover and nonlinear response history analyses was performed to investigate the seismic performance of three-, six-, and nine-story precast and cast-in-place (CIP) buildings. Finally, a summary of the analytical findings is presented.

4.2 Post-Test Analysis of Beam-Column Specimens

4.2.1 Modeling Methods for Precast Beam-Column Specimens

A three-dimensional fiber-section finite element model was developed to investigate the performance of PBC1 and PBC2 specimens (Fig. 4-1). OpenSees (2016) was used for modeling. The Beam model can be generally divided into two submodules. The first module represents the beam neck where yielding and damage of replaceable reinforcement are allowed. The second module is the original beam section. The column

was modeled as two elements, one starting from the base pin to the mid-height of the column (where the column meets the beam) and another element from the column mid-height to where the load is applied. A "forceBeamColumn" element with five integration points was used to model the column and the beam elements in both modules.

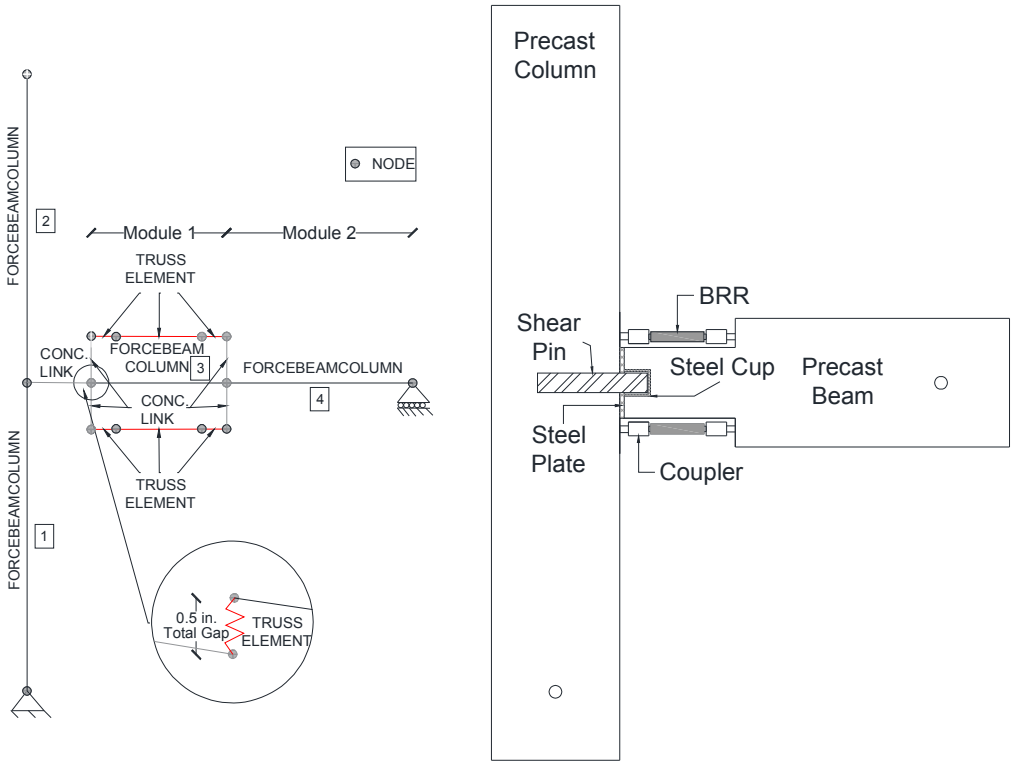

Figure 4-1. Precast Beam-Column Analytical Model

A "gap" element was assigned at the beam-column interface to simulate the gap between the shear pin and the steel cup. "ElasticPPGap" material was used to model the gap properties. The shear pin was modeled using "Steel02" uniaxial material. The stiffness of the shear pin and the gap were combined using a "Series" material and then assigned to a truss element in the vertical direction. A uniaxial material model, "ReinforcingSteel", was used to simulate all reinforcing steel bars. A "SelfCentering"

material model was used in PBC2 to simulate the SMA BRR. The concrete cover and core were modeled using "Concrete01" material model. Figure 4-2 shows the stress strain material models used in simulating the precast beam-column specimens.

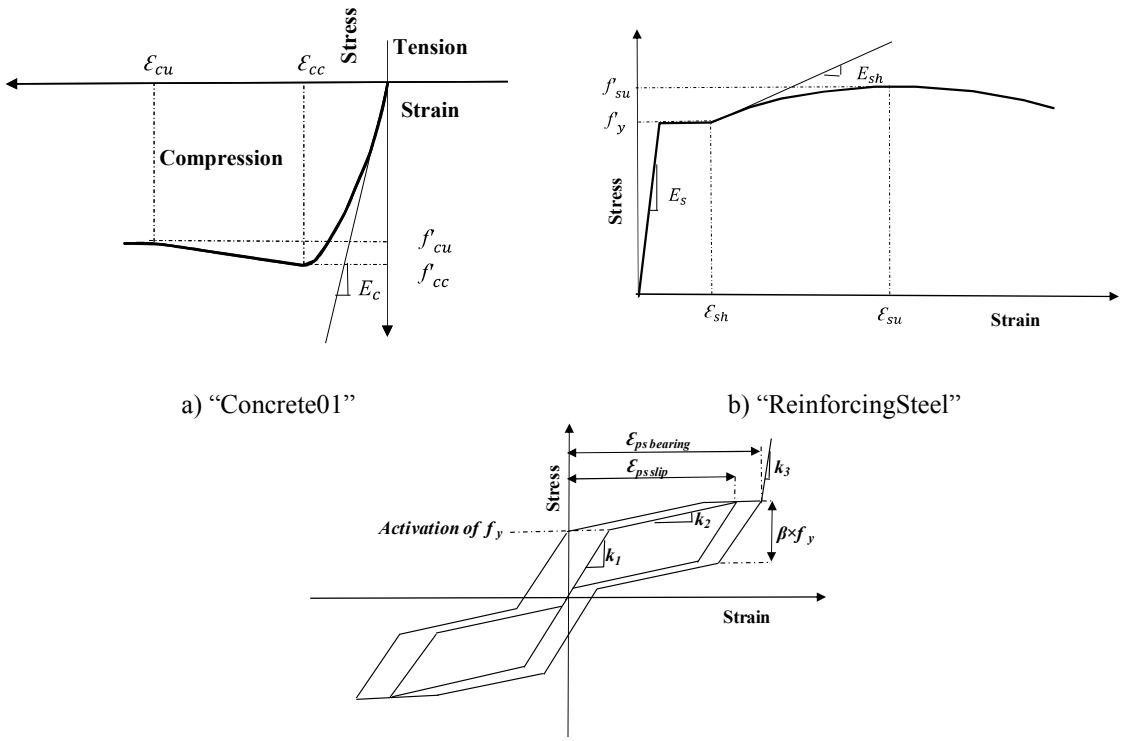

a) "Concrete01" b) "ReinforcingSteel"

b) "SelfCentering"

Figure 4-2. Stress-Strain Material Models Used in Simulation of Precast Beam-Column Specimens

The replaceable reinforcement (buckling restrained reinforcement) between the two couplers, which can be either steel BRR or SMA BRR, was modeled using truss elements. The exposed beam or column reinforcement beyond BRR were also modeled using truss element. Finally, the exposed reinforcement was connected to the beam and column elements using vertical elastic elements with elastic properties the same as those of the confined concrete.

The measured mechanical properties of concrete, steel bars, and SMA bars were used in the analysis (Chapter 3). Table 4-1 and 4-2 present the parameters used in the modelling of different fibers used in PBC1 and PBC2, respectively.

Table 4-1. Fibers Used in PBC1 Analytical Model

Longitudinal Steel Fibers	
Buckling Restrained Reinforcement, BRR	Beam & Column
Type: ReinforcingSteel Bar Size: No. 5 BRR at Top Layer (Machined down to No. 4) f_y = 70 *ksi* (482.63 *MPa*) f_{su} = 98.59 *ksi* (679.75 *MPa*) E_s = 29000 *ksi* (200000 *MPa*) ε_{sh} = 0.005 *in./in.* ε_{su} = 0.109 *in./in.*	Type: ReinforcingSteel Bar Size: No. 4 as Column and Beam Long. Bar f_y = 70.43 *ksi* (485.59 *MPa*) f_{su} = 107.19 *ksi* (739.0 *MPa*) E_s = 29000 *ksi* (200000 *MPa*) ε_{sh} = 0.005 *in./in.* ε_{su} = 0.1 *in./in.*
Type: ReinforcingSteel Bar Size: No. 4 BRR at Bottom Layer (Machined down to No. 3) f_y = 66.875 *ksi* (641.0 *MPa*) f_{su} = 93.99 *ksi* (648.0 *MPa*) E_s = 29000 *ksi* (200000 *MPa*) ε_{sh} = 0.005 *in./in.* ε_{su} = 0.0775 *in./in.*	Type: ReinforcingSteel Bar Size: No. 6 as Beam Long. Bar f_y = 69.18 *ksi* (477.0 *MPa*) f_{su} = 93.52 *ksi* (644.8 *MPa*) E_s = 29000 *ksi* (200000 *MPa*) ε_{sh} = 0.005 *in./in.* ε_{su} = 0.13 *in./in.*
Unconfined Concrete Fibers	
Column	Beam
Type: Concrete01 f'_{cc} = -4888 *psi* (33.7 *MPa*) ε_{cc} = -0.002 *in./in.* ε_{cu} = -0.005 *in./in.*	Type: Concrete01 f'_{cc} = -4888 *psi* (33.7 *MPa*) ε_{cc} = -0.002 *in./in.* ε_{cu} = -0.005 *in./in.*
Confined concrete Fibers (Mander's Model)	
Column	Beam
Type: Concrete01 f'_{cc} = -5590 *psi* (38.5 *MPa*) ε_{cc} = -0.0044 *in./in.* f'_{cu} = -3660 *psi* (25.2 *MPa*) ε_{cu} = -0.0209 *in./in.*	Type: Concrete01 f'_{cc} = -5270 *psi* (36.3 *MPa*) ε_{cc} = -0.0037 *in./in.* f'_{cu} = -3010 *psi* (20.8 *MPa*) ε_{cu} = -0.0174 *in./in.*
	Neck
	Type: Concrete01 f'_{cc} = -9230 *psi* (63.6 *MPa*) ε_{cc} = -0.015 *in./in.* f'_{cu} = -8820 *psi* (60.8 *MPa*) ε_{cu} = -0.03 *in./in.*
Gap Properties	
Type: ElasticPPGap as Gap Element Gap in Tension = 0.25 *in*. (6 *mm*) Gap in Comp. = 0.25 *in*. (6 *mm*)	Type: Steel02 as Shear Pin f_y = 50 *ksi* (345 *MPa*) E_s = 29000 *ksi* (200000 *MPa*)

Table 4-2. Fibers Used in PBC2 Analytical Model

Longitudinal Steel Fibers	
Buckling Restrained Reinforcement BRR	Beam & Column
Type: ReinforcingSteel Bar Size: No. 5 BRR at Top Layer (Machined down to No. 4) and at Bottom Layer (Machined down to No. 3) f_y = 70 *ksi* (482.63 *MPa*) f_{su} = 98.59 *ksi* (679.75 *MPa*) E_s = 29000 *ksi* (200000 *MPa*) ε_{sh} = 0.005 *in./in.* ε_{su} = 0.18 *in./in.*	Type: ReinforcingSteel Bar Size: No. 4 as Column Long. Bar f_y = 70.43 *ksi* (485.59 *MPa*) f_{su} = 107.19 *ksi* (739.0 *MPa*) E_s = 29000 *ksi* (200000 *MPa*) ε_{sh} = 0.005 *in./in.* ε_{su} = 0.1 *in./in.*
Type: SelfCentering Bar Size: No. 4 BRR SMA at Top and Bottom Layers k_1 = 5362.5 *ksi* (36972.8 *MPa*) k_2 = 180 *ksi* (1241.0 *MPa*) $k_3 = \alpha \times k_1$ f_y = 56.44 *ksi* (389.1 *MPa*) β = 0.35 α = 0.3 (Suggested) $\varepsilon_{ps\ slip}$ = 0.055 *in./in.* $\varepsilon_{ps\ \mathrm{bear}}$ = 0.055 *in./in.*	Type: ReinforcingSteel Bar Size: No. 5 as Beam Long. Bar f_y = 72.23 *ksi* (498.0 *MPa*) f_{su} = 112.17 *ksi* (779.4 *MPa*) E_s = 29000 *ksi* (200000 *MPa*) ε_{sh} = 0.005 *in./in.* ε_{su} = 0.0966 *in./in.* Type: ReinforcingSteel Bar Size: No. 6 as Beam Long. Bar f_y = 69.18 *ksi* (477.0 *MPa*) f_{su} = 93.52 *ksi* (644.8 *MPa*) E_s = 29000 *ksi* (200000 *MPa*) ε_{sh} = 0.005 *in./in.* ε_{su} = 0.13 *in./in.*
Unconfined Concrete Fibers	
Column	Beam
Type: Concrete01 f'_{cc} = -5800 *psi* (40.0 *MPa*) ε_{cc} = -0.002 *in./in.* ε_{cu} = -0.005 *in./in.*	Type: Concrete01 f'_{cc} = -5742 *psi* (39.6 *MPa*) ε_{cc} = -0.002 *in./in.* ε_{cu} = -0.005 *in./in.*
Confined concrete Fibers (Mander's model)	
Column	Beam
Type: Concrete01 f'_{cc} = -7290 *psi* (50.3 *MPa*) ε_{cc} = -0.00453 *in./in.* f'_{cu} = -5830 *psi* (40.2 *MPa*) ε_{cu} = -0.01198 *in./in.*	Type: Concrete01 f'_{cc} = -6600 *psi* (45.5 *MPa*) ε_{cc} = -0.00337 *in./in.* f'_{cu} = -5280 *psi* (36.4 *MPa*) ε_{cu} = -0.00746 *in./in.*
	Neck
	Type: Concrete01 f'_{cc} = -9740 *psi* (67.2 *MPa*) ε_{cc} = -0.0146 *in./in.* f'_{cu} = -9330 *psi* (64.3 *MPa*) ε_{cu} = -0.0309 *in./in.*
Gap Properties	
Type: ElasticPPGap as Gap Element Gap in Tension = 0.25 *in*. (6 *mm*) Gap in Comp. = 0.25 *in*. (6 *mm*)	Type: Steel02 as Shear Pin f_y = 50 *ksi* (345 *MPa*) E_s = 29000 *ksi* (200000 *MPa*)

Fiber sections with 50 segments in both directions were used to model the confined concrete for all element. The unconfined concrete was modeled with 20 segments in both directions. The column models were pinned at the bottom and the beams were modeled as a roller at the free end. The column axial load of 68 kips (302.5 kN) was applied to the top node of the column. The $P-\Delta$ effect was included in all analysis. The lateral load was applied at the top node of the column using displacement control method.

4.2.2 Force-Displacement Relationships

Force-displacement analyzes were performed for both precast specimen, PBC1 and PBC2 and the calculated results were compared with those measured in chapter three to validate the accuracy of the modeling method. The analytical force-displacement relationship of each test is presented herein.

4.2.2.1 PBC1-D

Figure 4-3 shows the calculated and measured envelope force-displacement relationships for PBC1-D. Figure 4-4 shows the calculated and measured hysteretic force-displacement relationships for PBC1-D. It can be seen that the calculated push initial stiffness and the maximum push force were overestimated. For example, the calculated initial stiffness and calculated force in the push direction were 49% and 22% higher than those measured in the test, respectively. However, the calculated pull initial stiffness was the same as that measured in the test. The maximum calculated pull force was underestimated by 13%. Overall, a good agreement between the measured and calculated force-displacement behavior was observed using the proposed modeling methods.

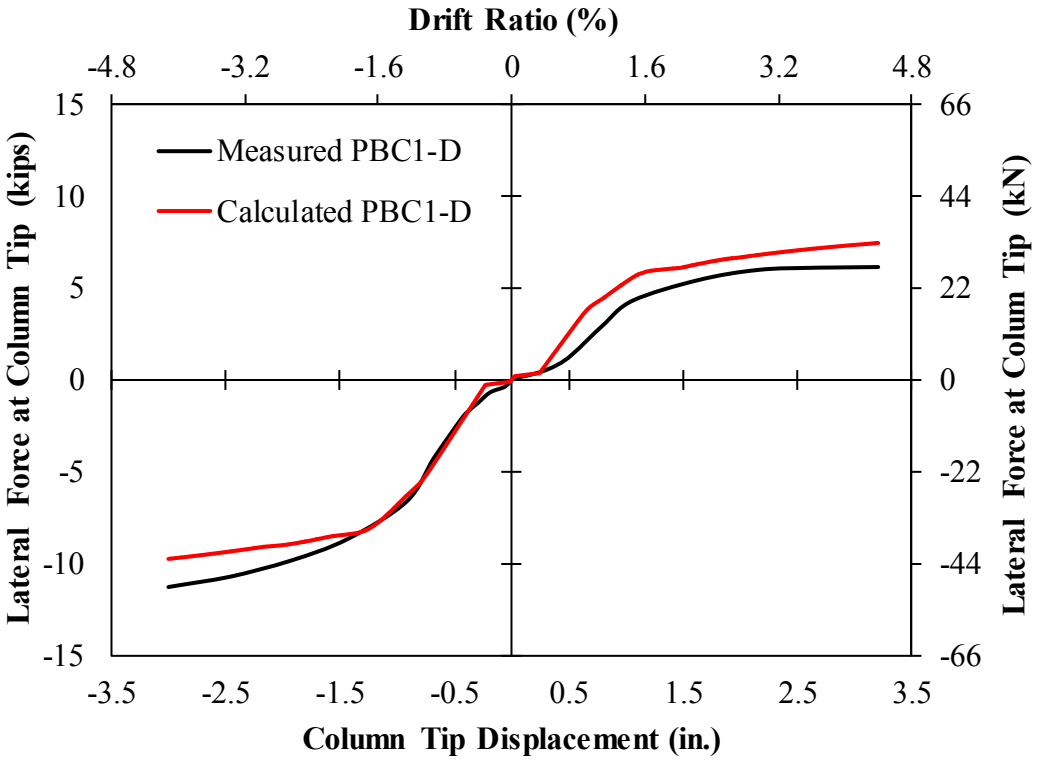

Figure 4-3. Calculated and Measured Force-Displacement Envelopes for PBC1-D

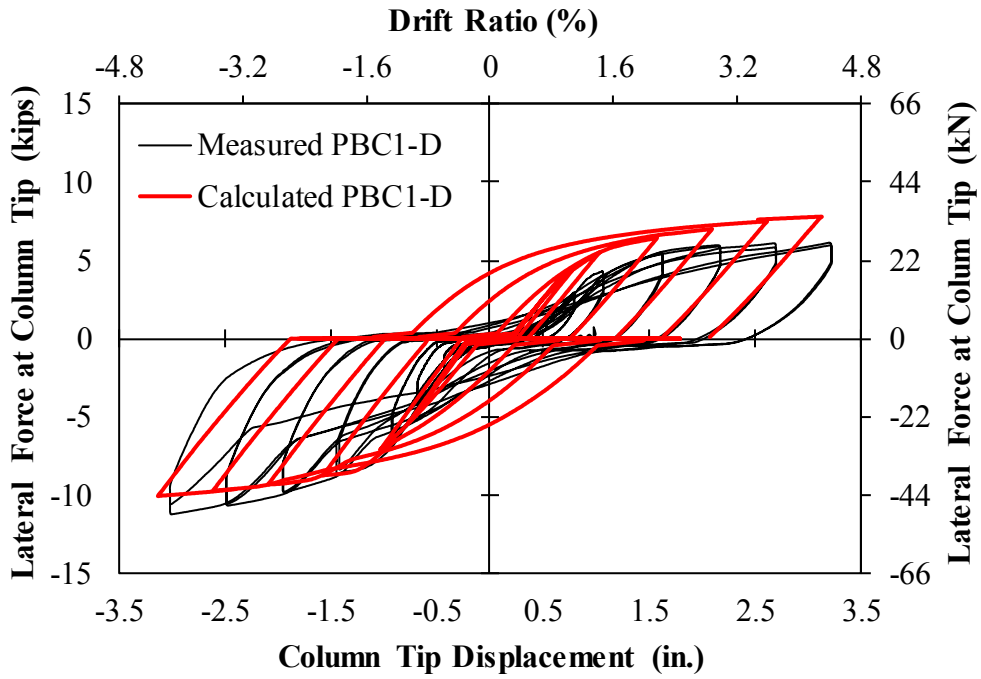

Figure 4-4. Calculated and Measured Force-Displacement Hysteresis for PBC2-D

4.2.2.2 PBC2-D

Figure 4-5 shows the calculated and measured envelope force-displacement relationships for PBC2-D. Figure 4-6 shows the calculated and measured hysteretic force-displacement relationships for PBC2-D. It can be seen that the calculated push initial stiffness and the maximum push force were overestimated. For example, the calculated initial stiffness and calculated force in the push direction were 80% and 18% higher than those measured in the test, respectively. However, the calculated pull initial stiffness was the same as that measured in the test. The maximum calculated pull force was underestimated by 14%. Overall, a good agreement between the measured and calculated force-displacement behavior was observed using the proposed modeling methods.

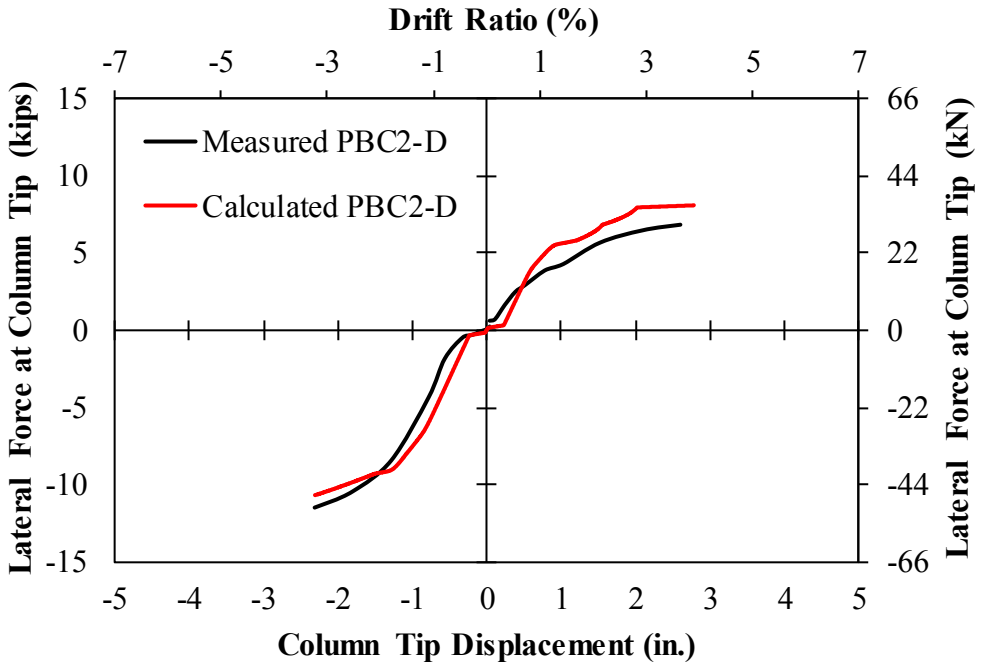

Figure 4-5. Calculated and Measured Force-Displacement Envelopes for PBC2-D

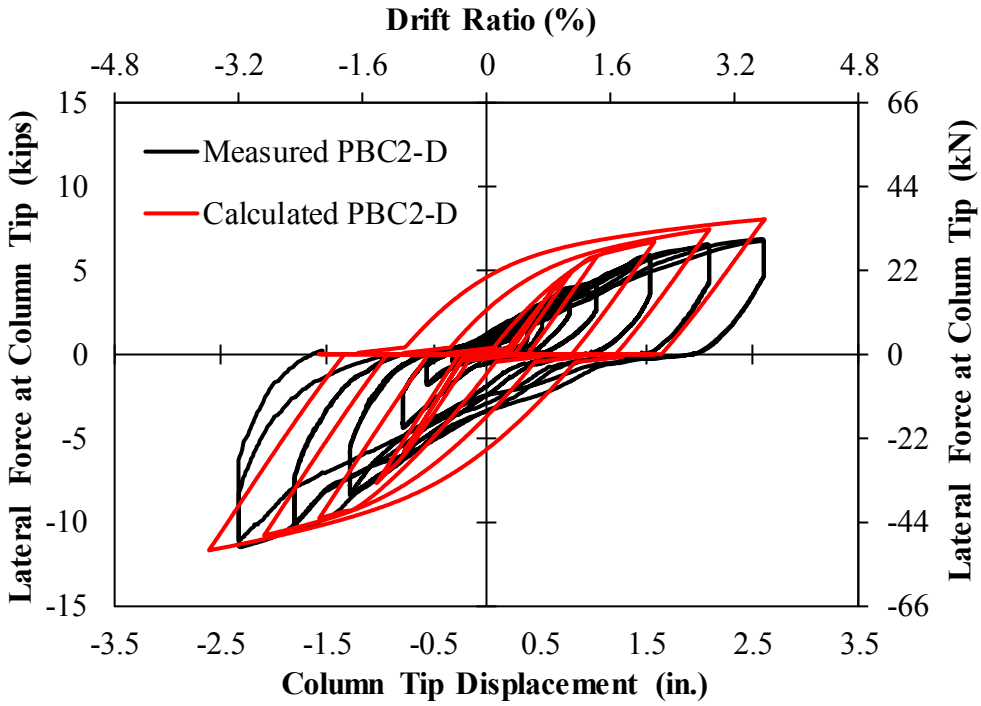

Figure 4-6. Calculated and Measured Force-Displacement Hysteresis for PBC2-D

4.2.2.3 PBC2-SMA

Figure 4-7 shows the calculated and measured envelope force-displacement relationships for PBC2-SMA. Figure 4-8 shows the calculated and measured hysteretic force-displacement relationships for PBC2-SMA. It can be seen that the calculated push initial stiffness and the maximum push force were overestimated. For example, the calculated initial stiffness and calculated force in the push direction were 61% and 7% higher than those measured in the test, respectively. The calculated pull initial stiffness was the same as that measured in the test. The calculated pull initial stiffness and the maximum calculated pull force was overestimated by 6% and 5%, respectively. Overall, a good agreement between the measured and calculated force-displacement behavior was observed using the proposed modeling methods.

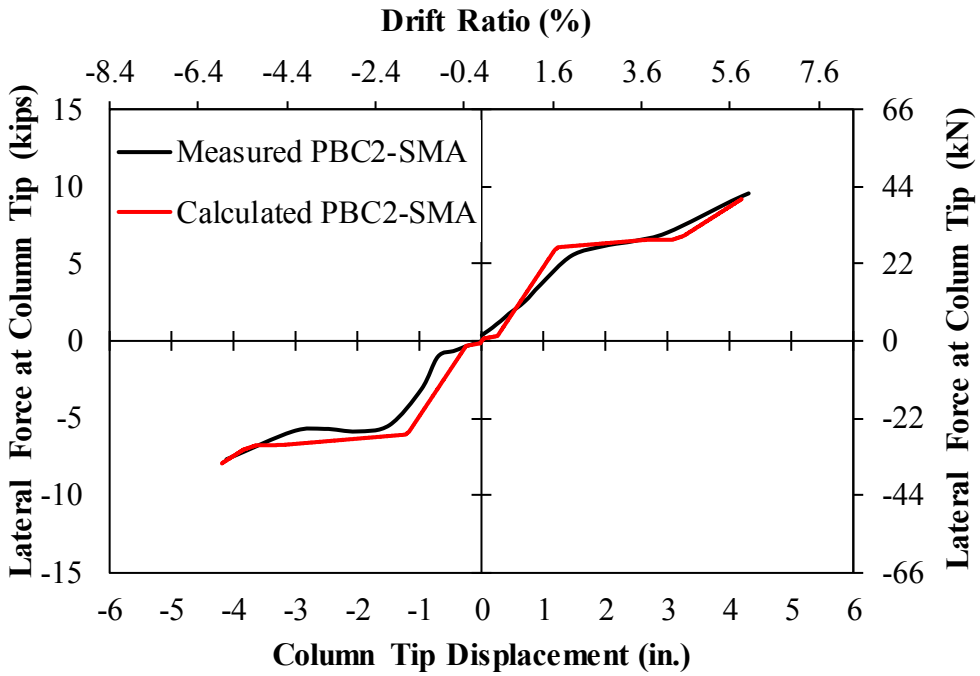

Figure 4-7. Calculated and Measured Force-Displacement Envelopes for PBC2-SMA

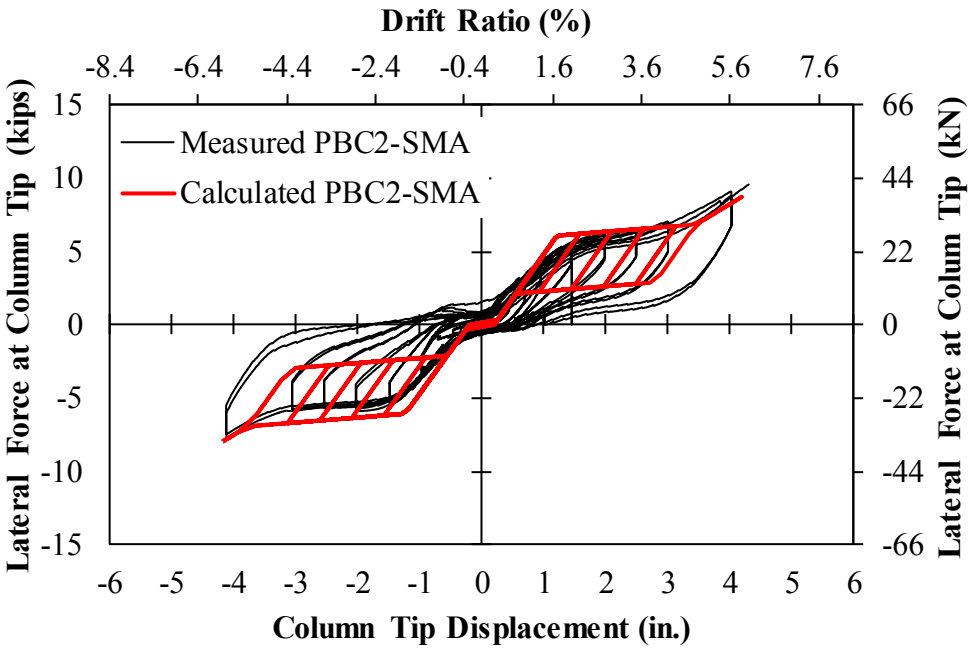

Figure 4-8. Calculated and Measured Force-Displacement Hysteresis for PBC2-SMA

4.3 Analytical Study on Building Frames

A comprehensive analytical study including pushover and nonlinear response history analyses was performed to investigate the seismic performance of three-, six-, and nine-story precast and cast-in-place (CIP) frames. First, conventional RC building frames were designed, by Al Hashib (2017), for Los Angeles, CA as special moment-resisting frames SMRF to account for extreme seismic events into the design. Then the proposed detailing was used to make the frames precast. The proposed repairable connection model was verified in Sec. 4.2 and then used to make the precast frame models. The modeling methods and the analytical results are discussed herein.

4.3.1 Design of Cast-in-Place RC Building Frames

The design of conventional RC building frames was performed by Al Hashib (2017). All SMRF were designed based on ACI-318-14 (2014). Design loads (wind, seismic, gravity, etc.) and combinations were according to the requirements of ASCE 7-10 (2010). The building was assumed to be an office with a Seismic Importance Factor (I_e) of 1 and a Risk Category of II. The soil category was considered as type D site class. The building was assumed be located in Los Angeles, CA.

Only an interior frame of the building was considered in this analytical study to better investigate the seismic performance of the cast-in-place and precast frames (Fig. 4-9). All frames had four spans of 20 ft. and a story height of 12 ft.

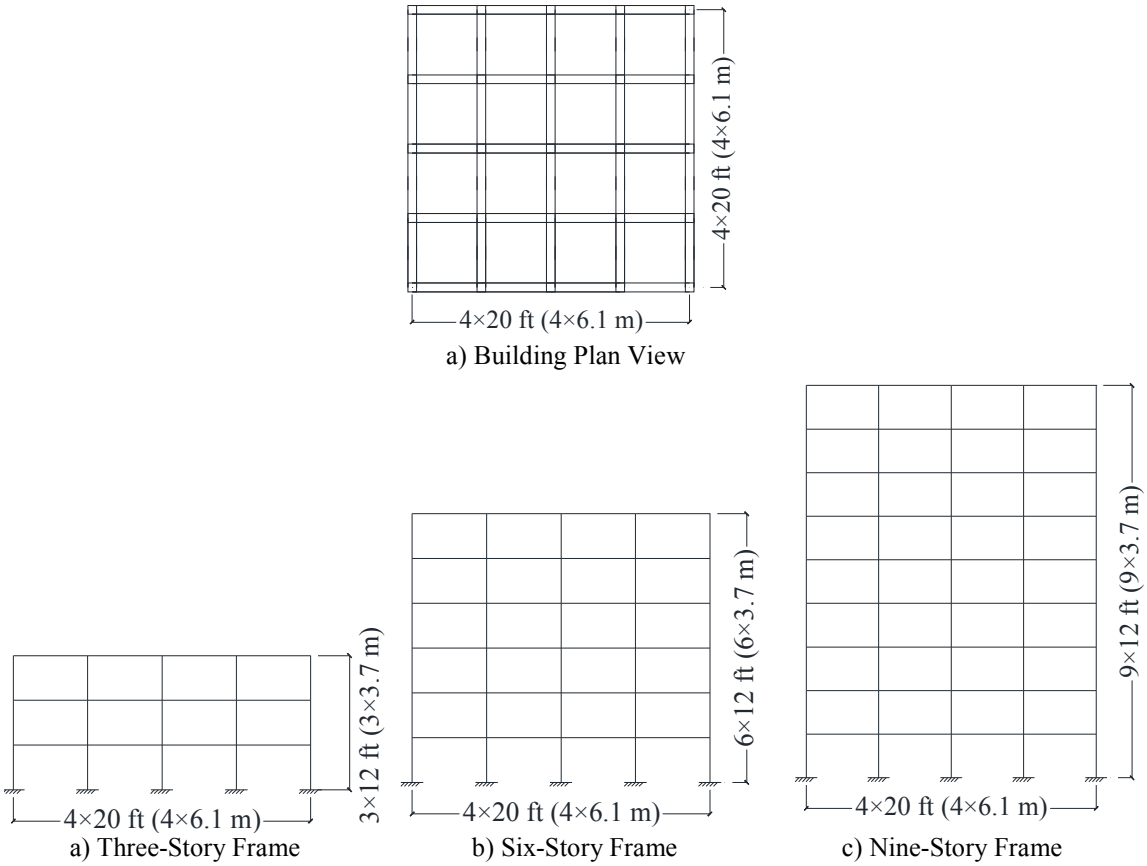

Figure 4.9- Building Frames for Analytical Studies

The concrete compressive strength was taken as 5000 psi and all reinforcing steel bars were ASTM A706 Grade 60. The beams and columns were chosen in a way that each three stories had identical beam and column sections. This was done to minimize the section variations in analysis. The concrete cover was 2 in. (51 mm) and 1.5 in. (38 mm) for all columns and beams, respectively. All SMRFs were designed following the "strong column – weak beam" philosophy and thus, columns were at least 25% stronger than beams in flexure. Seismic detailing of all frames was based on the ACI seismic requirements. More information regarding the design of conventional frames can be found in Al Hashib (2017).

Figure 4-10 and 4-11 show the detailing of the three-story SMRF. The member geometry and reinforcement are listed in Table 4-3. Two identical column sections but with different transverse reinforcement were assigned to each column: C1 for the columns plastic hinge regions and C2 elsewhere.

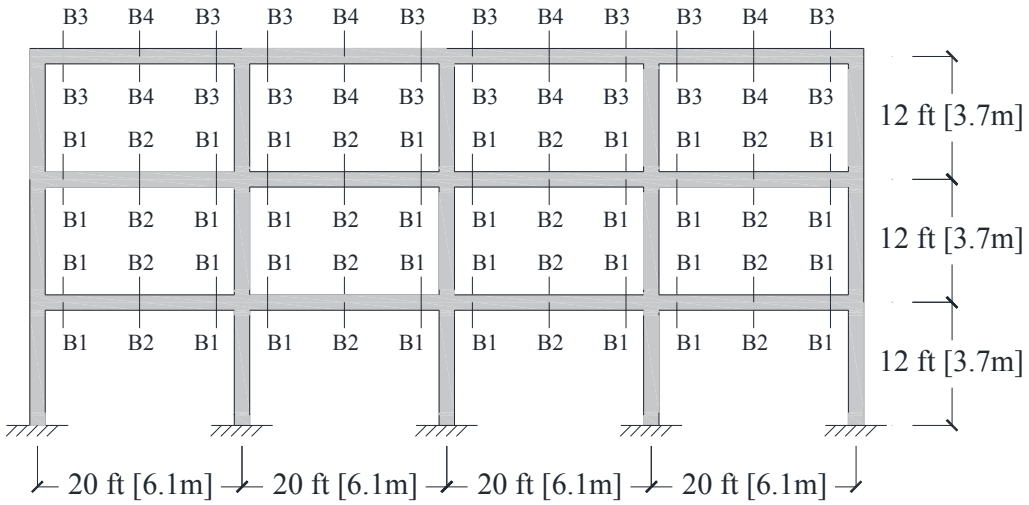

Figure 4-10. Three-Story Special Moment-Resisting Frame

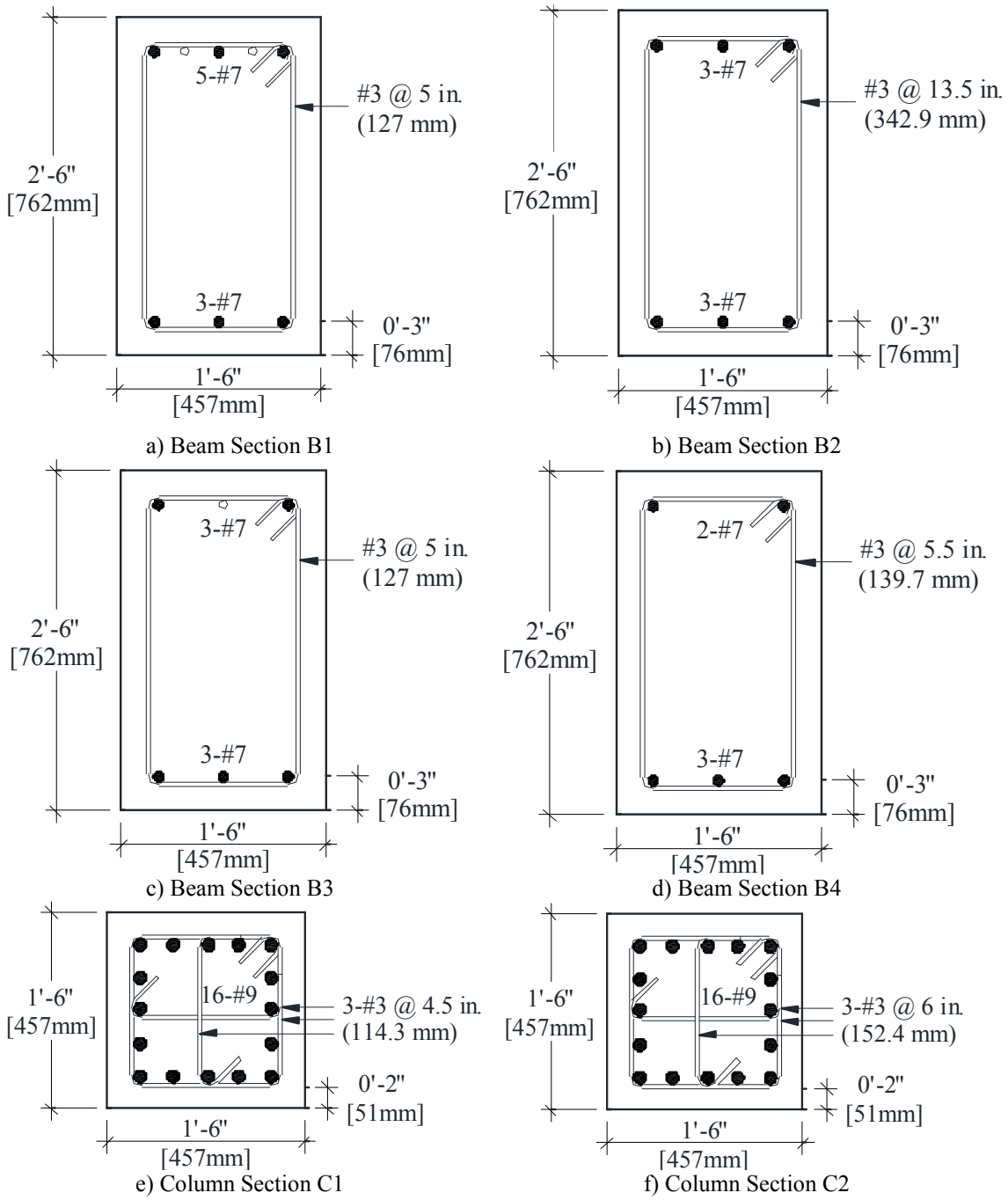

Figure 4-11. Section Details for Three-Story Special Moment-Resisting Frame

Table 4-3. Design Summary for Three-Story Special Moment-Resisting Frame

Member	Story	Section	Size (in.)	Longitudinal Reinforcement	Transverse Reinforcement
Beam	1 & 2	B1 (end)	18 × 30	Top 5 No. 7 Bottom 3 No. 7	No. 3 @ 5 in.
		B2 (middle)	18 × 30	Top 3 No. 7 Bottom 3 No. 7	No. 3 @ 13.5 in.
	3	B3 (end)	18 × 30	Top 3 No. 7 Bottom 3 No. 7	No. 3 @ 5 in.
		B4 (middle)	18 × 30	Top 2 No. 7 Bottom 3 No. 7	No. 3 @ 13.5 in.
Column	1 to 3	C1 (ends)	18 × 18	16 No. 9	3 No. 3 @ 4.5 in.
		C2 (middle)	18 × 18	16 No. 9	3 No. 3 @ 6 in.

Note: 1 in. = 25.4 mm, Bar No. 3 = No. 10 mm, Bar No. 7 = No. 22 mm, Bar No. 9 = No. 29 mm

Figure 4-12 and 4-13 show the detailing of the six-story SMRF. The member geometry and reinforcement are listed in Table 4-4. Two identical column sections but with different transverse reinforcement were assigned to each column.

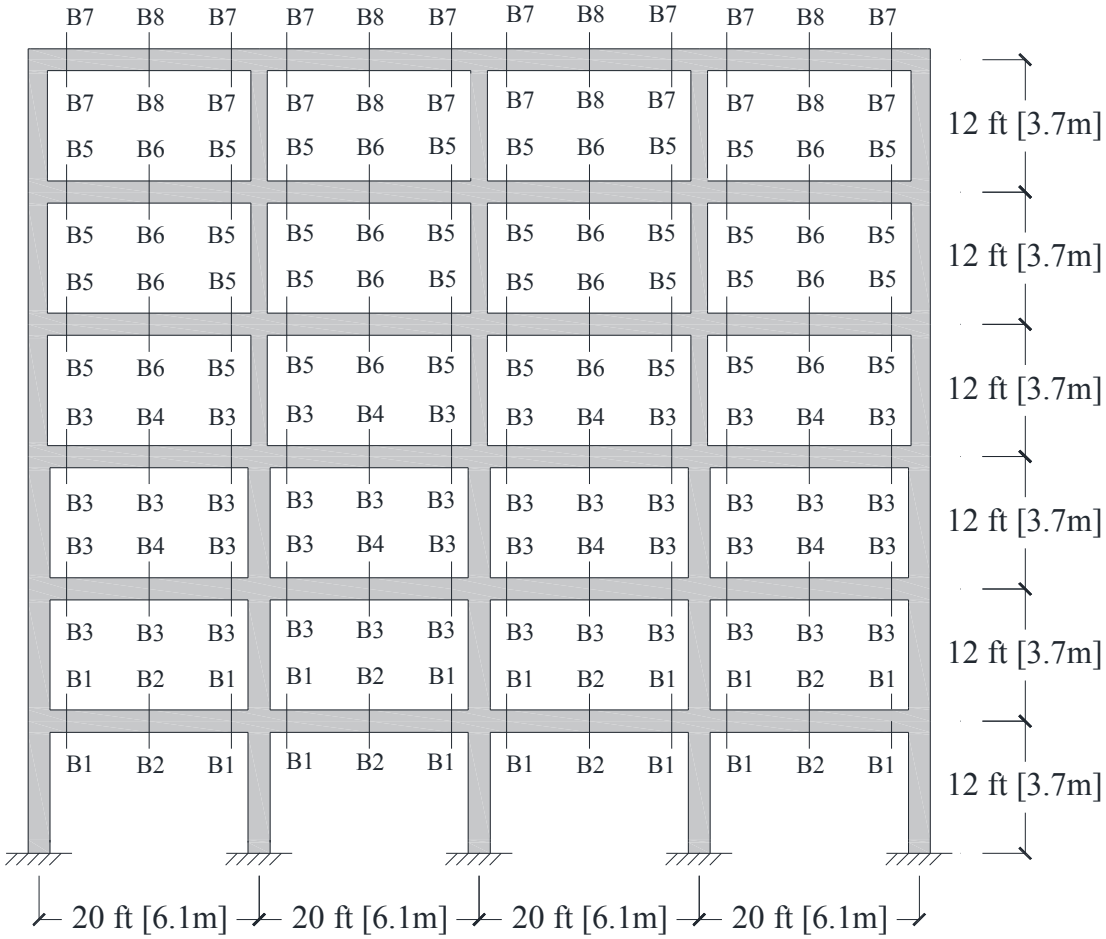

Figure 4-12. Six-Story Special Moment-Resisting Frame

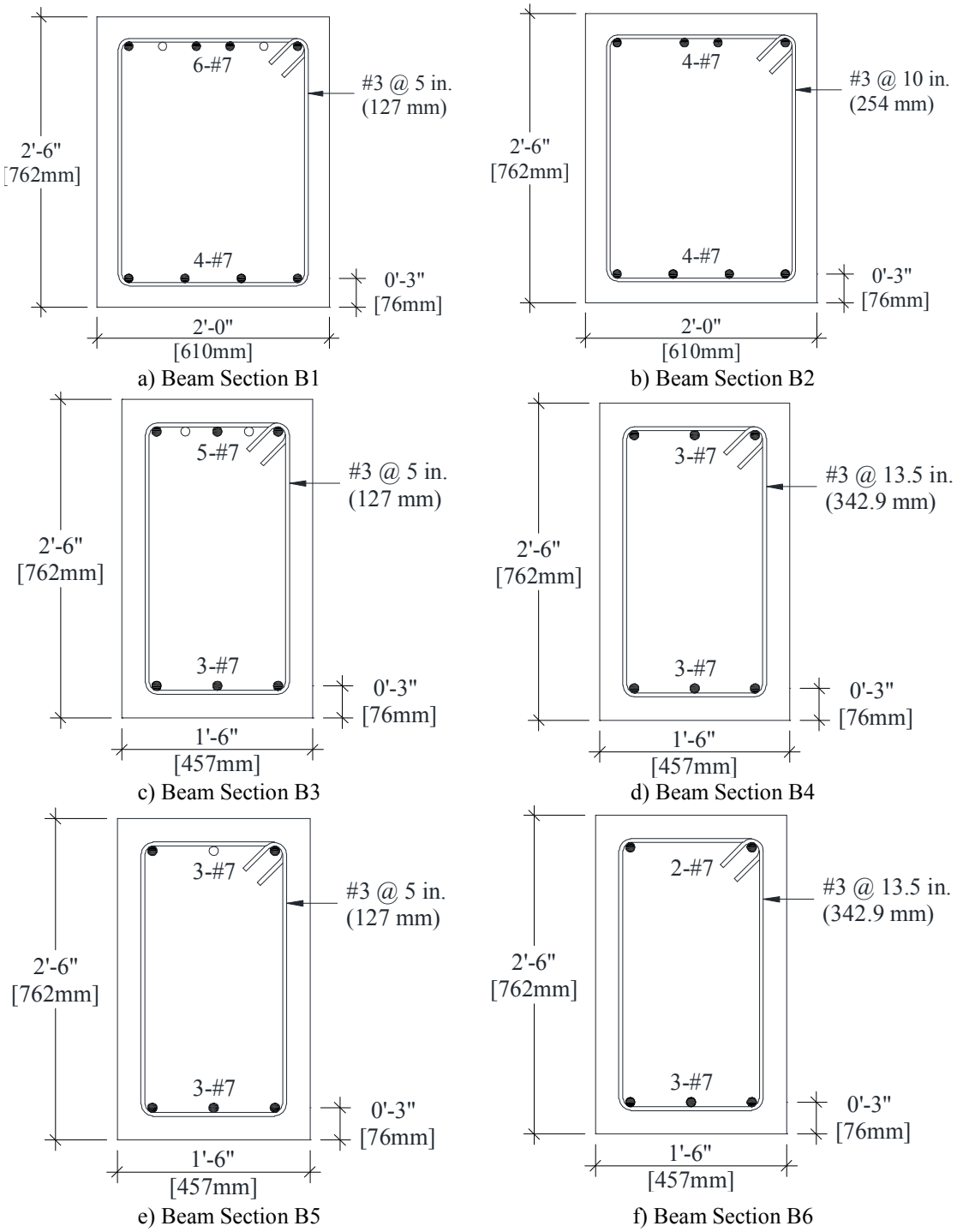

Figure 4-13. Section Details for Six-Story Special Moment-Resisting Frame

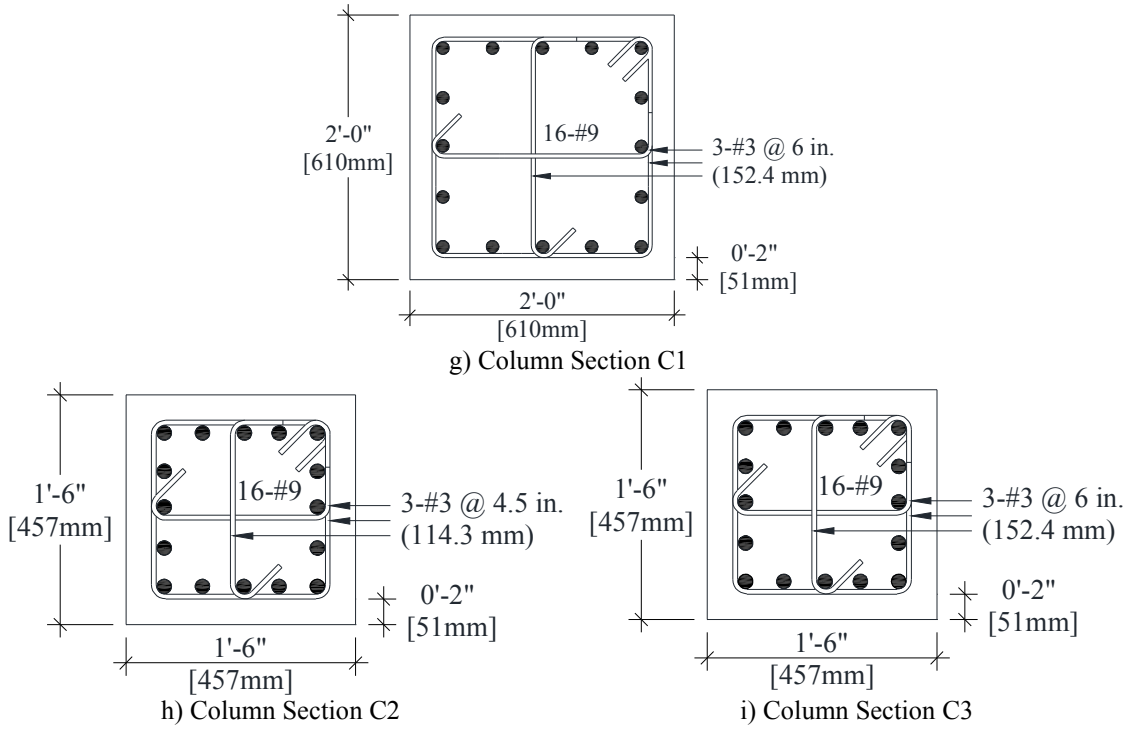

Figure 4-13. Section Details for Six-Story Special Moment-Resisting Frame (Continued)

Table 4-4. Design Summary for Six-Story Special Moment-Resisting Frame

Member	Story	Section	Size (in.)	Longitudinal Reinforcement	Transverse Reinforcement
Beam	1 to 3	B1 (end)	24 × 30	Top 6 No. 7 Bottom 4 No. 7	No. 3 @ 5 in.
		B2 (middle)	24 × 30	Top 4 No. 7 Bottom 4 No. 7	No. 3 @ 10 in.
	4 & 5	B3 (end)	18 × 30	Top 5 No. 7 Bottom 3 No. 7	No. 3 @ 5 in.
		B4 (middle)	18 × 30	Top 3 No. 7 Bottom 3 No. 7	No. 3 @ 13.5 in.
	6	B5 (end)	18 × 30	Top 3 No. 7 Bottom 3 No. 7	No. 3 @ 5 in.
		B6 (middle)	18 × 30	Top 2 No. 7 Bottom 3 No. 7	No. 3 @ 13.5 in.
Column	1 to 3	C1	24 × 24	16 No. 9	3 No. 3 @ 6 in.
	4 to 6	C2 (end)	18 × 18	16 No. 9	3 No. 3 @ 4.5 in.
		C3 (middle)	18 × 18	16 No. 9	3 No. 3 @ 6 in.

Note: 1 in. = 25.4 mm, Bar No. 3 = No. 10 mm, Bar No. 7 = No. 22 mm, Bar No. 9 = No. 29 mm

Figure 4-14 and 4-15 show the detailing of the nine-story SMRF. The member geometry and reinforcement are listed in Table 4-5. Two identical column sections but with different transverse reinforcement were assigned to each column.

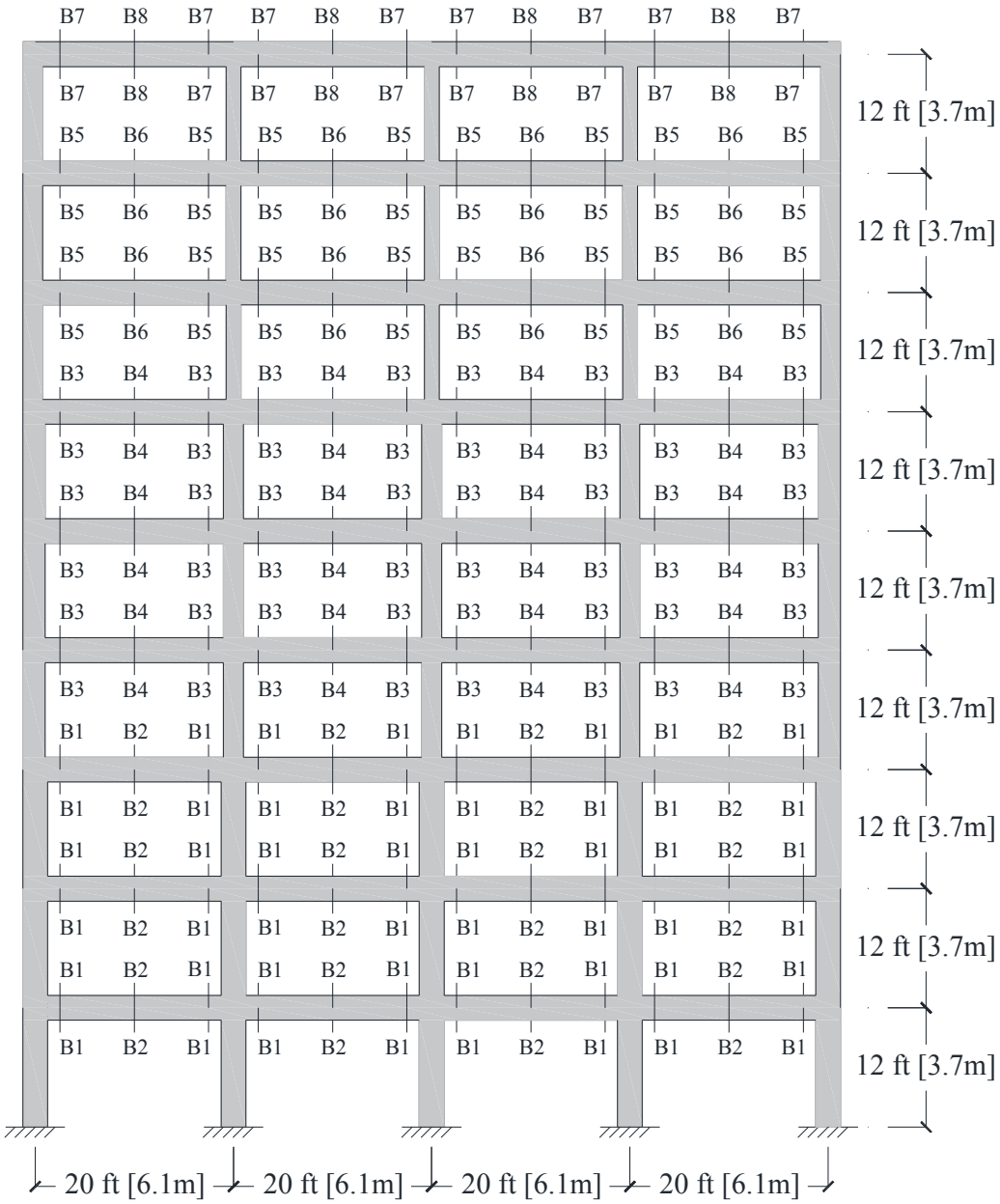

Figure 4-14. Nine-Story Special Moment-Resisting Frame

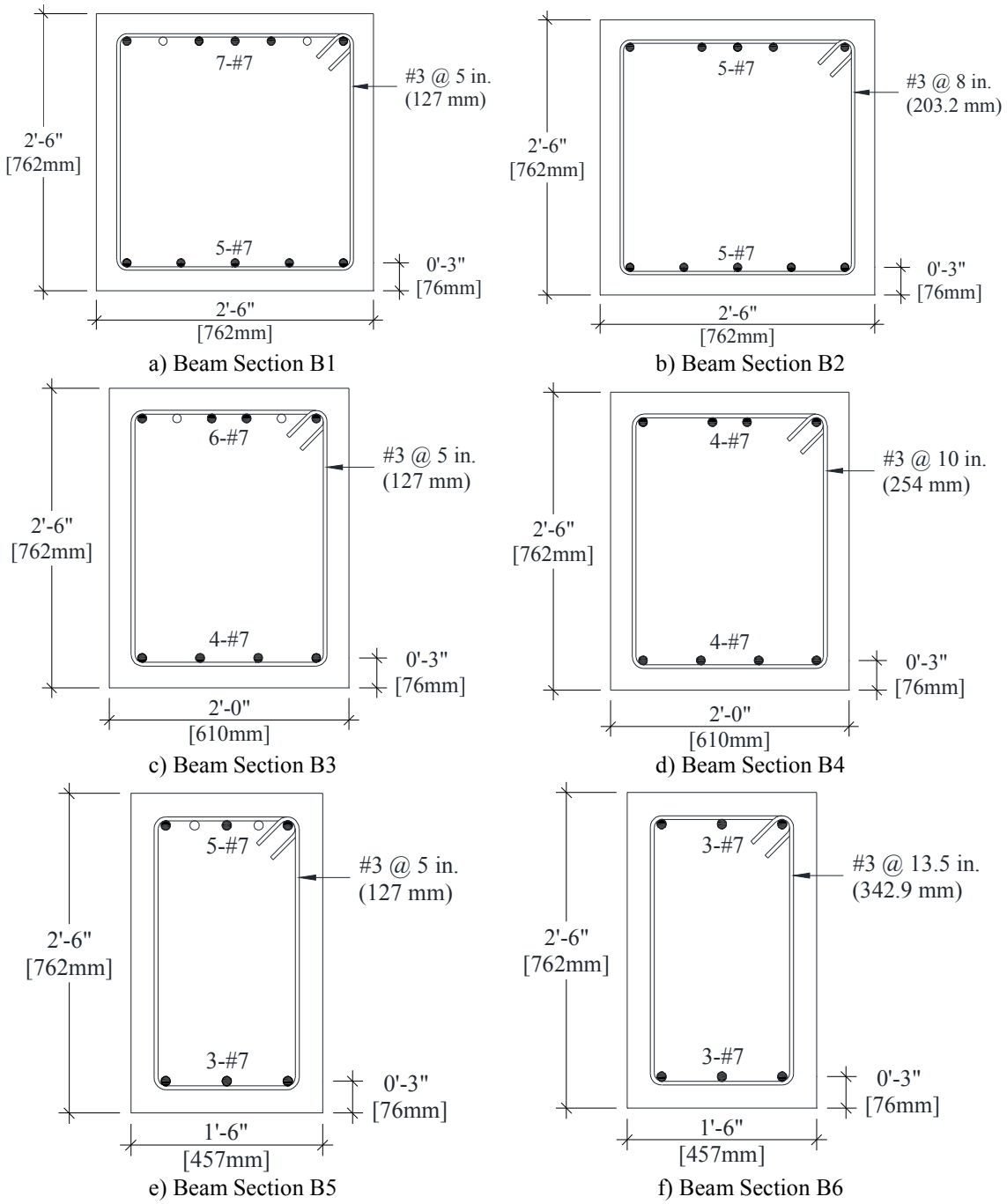

Figure 4-15. Section Details for Nine-Story Special Moment-Resisting Frame

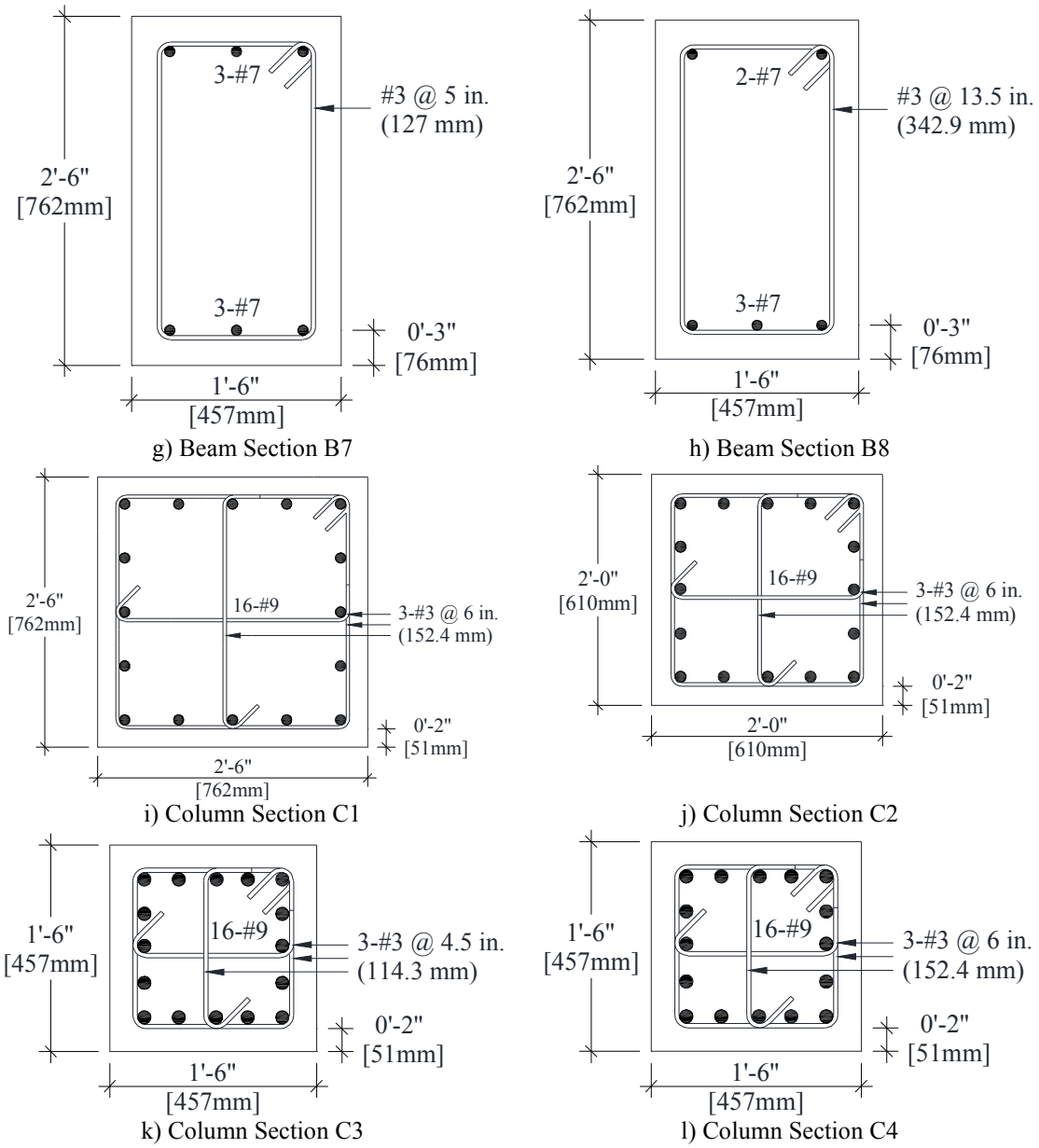

Figure 4-15. Section Details for Nine-Story Special Moment-Resisting Frame (Continued)

Table 4-5. Design Summary for Nine-Story Special Moment-Resisting Frame

Member	Story	Section	Size (in.)	Longitudinal Reinforcement	Transverse Reinforcement
Beam	1 to 3	B1 (end)	30 × 30	Top 7 No. 7 Bottom 5 No. 7	No. 3 @ 5 in.
		B2 (middle)	30 × 30	Top 5 No. 7 Bottom 5 No. 7	No. 3 @ 8 in.
	4 to 6	B3 (end)	24 × 30	Top 6 No. 7 Bottom 4 No. 7	No. 3 @ 5 in.
		B4 (middle)	24 × 30	Top 4 No. 7 Bottom 4 No. 7	No. 3 @ 10 in.
	7 & 8	B5 (end)	18 × 30	Top 5 No. 7 Bottom 3 No. 7	No. 3 @ 5 in.
		B6 (middle)	18 × 30	Top 3 No. 7 Bottom 3 No. 7	No. 3 @ 13.5 in.
	9	B7 (end)	18 × 30	Top 3 No. 7 Bottom 3 No. 7	No. 3 @ 5 in.
		B8 (middle)	18 × 30	Top 2 No. 7 Bottom 3 No. 7	No. 3 @ 13.5 in.
Column	1 to 3	C1	30 × 30	16 No. 9	3 No. 3 @ 6 in.
	4 to 6	C2	24 × 24	16 No. 9	3 No. 3 @ 6 in.
	7 to 9	C3 (end)	18 × 18	16 No. 9	3 No. 3 @ 4.5 in.
		C4 (middle)	18 × 18	16 No. 9	3 No. 3 @ 6 in.

Note: 1 in. = 25.4 mm, Bar No. 3 = No. 10 mm, Bar No. 7 = No. 22 mm, Bar No. 9 = No. 29 mm

4.3.2 Modeling Methods for Conventional Cast-in-Place RC Frames

OpenSees (2016) was used for the analysis all frames. A three-dimensional fiber-section model was developed for RC frames in which the "forceBeamColumn" elements with seven integration points were used to model beams and columns. Table 4-6 summarizes the modeling methods for CIP frames.

One challenge of using fiber-section models for nonlinear analysis of buildings is how to determine the building failure point. Failure of one fiber (core concrete or steel bar) in one or more sections does not necessarily results in the failure of the building. Furthermore, monitoring thousands of fibers in the plastic hinge regions of beams and columns are tedious. To address this challenge, it was decided to use only fiber models that show abrupt loss of strength in the stress-strain relationship when the strain reaches the ultimate strain. Therefore, the concrete cover and core were modeled using

"Concrete04" material models, respectively. In OpenSees, "Concrete04" is a uniaxial material model that includes tensile properties of concrete and exhibit zero residual strength, which can be used to identify the failure mode due to core concrete failure. A uniaxial material, "ReinforcingSteel", was used to simulate the reinforcement in the column mid-section.Since "ReinforcingSteel" does not show a sudden drop in the strength at the ultimate strain, another material model, "Pinching04", was utilized (Fig. 4-16) to simulate the steel fibers in the plastic hinge regions of beams and columns to determine the frame ultimate displacement using the force-displacement relationship not the failure of a few fibers. Al Hashib (2017) used the same method to determine the displacement capacity of RC frames.

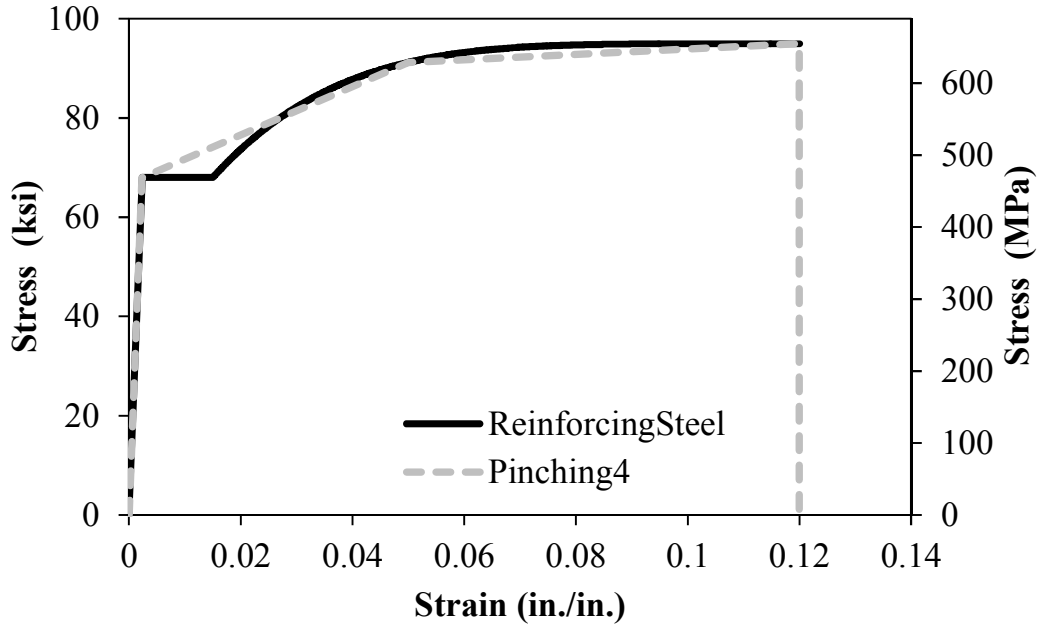

Figure 4-16. Stress-Strain Relationships for "ReinforcingSteel" and "Pinching4" Material Models

Fiber sections consisting of 30 segments and 10 segments in both directions were used to model the confined and unconfined concrete, respectively. Mander's model (Mander et al., 1988) was utilized to calculate properties of the confined concrete. Table

4-7, 4-8, and 4-9 present the properties for core concrete fibers used in three-, six-, and nine-story frames, respectively. All pushover analysis was carried out by applying displacements at the roof level.

Table 4-6. Modeling Methods for CIP Frames

General Remarks	
Three Dimensions with six Degrees of freedom per node. Supports are fixed. Element type: *forcebeamcolumn* with 7 integration points Gravity load and P-Δ effects were considered.	Sectional Properties: Fiber Section, Core Concrete Discretization: 30 by 30, Cover Concrete Discretization: 10 by 10. Element in the middle of the beam or column has less transverse reinforcement. Masses were assigned at each Beam-Column intersection node
Concrete Fibers	
Unconfined Concrete (cover)	Confined Concrete (core)
Type: Concrete04 f'_{cc} = -5 ksi (34.47 MPa) $\mathcal{E}_{cc}$ = -0.002 in./in. f'_{cu} = 0.0 ksi (0.0 MPa) $\mathcal{E}_{cu}$ = -0.005 in./in. E_c = 4030.51 ksi (27789.39 MPa)	Type: Concrete04 f'_{cc}, ε_{cc}, f'_{cu} and ε_{cu} transverse reinforcement according to Mander's model.
Steel Fibers	
General Long. Reinforcement	Long. Reinforcement at Plastic Hinges
Type: ReinforcingSteel f_y = 68 ksi (468.84 MPa) f_{su} = 95 ksi (655 MPa) E_s = 29000 ksi (199947.96 MPa) E_{sh} = 1247 ksi (8597.76 MPa) $\mathcal{E}_{sh}$ = 0.015 in./in. $\mathcal{E}_{su}$ = 0.12 in./in.	Type: Pinching4 f_1 = 68 ksi (468.84 MPa) f_2 = 91.22 ksi (628.94 MPa) f_3 = 95 ksi (655 MPa) f_4 = 0.5 ksi (3.45 MPa) $\mathcal{E}_1$ = 0.0023 in./in. $\mathcal{E}_2$ = 0.05 in./in. $\mathcal{E}_3$ = 0.11 in./in. $\mathcal{E}_4$ =0.12 in./in.

Table 4-7. Properties of Core Concrete Fibers in Three-Story Special MRF

Beams	
B1 & B3	B2 & B4
f'_{cc} = -5.95 ksi (41.02 MPa) $\mathcal{E}_{cc}$ = -0.0039 in./in. f'_{cu} = -4.0365 ksi (27.83 MPa) $\mathcal{E}_{cu}$ = -0.0143 in./in.	f'_{cc} = -5.25 ksi (36.2 MPa) $\mathcal{E}_{cc}$ = -0.0025 in./in. f'_{cu} = -2.7229 ksi (18.77 MPa) $\mathcal{E}_{cu}$ = -0.0083 in./in.
Columns	
C1	C2
f'_{cc} = -6.925 ksi (47.75 MPa) $\mathcal{E}_{cc}$ = -0.0059 in./in. f'_{cu} = -5.208 ksi (35.91 MPa) $\mathcal{E}_{cu}$ = -0.0234 in./in.	f'_{cc} = -6.325 ksi (43.61 MPa) $\mathcal{E}_{cc}$ = -0.0047 in./in. f'_{cu} = -4.308 ksi (29.7 MPa) $\mathcal{E}_{cu}$ = -0.0199 in./in.

Table 4-8. Properties of Core Concrete Fibers in Six-Story Special MRF

Beams		
B1	B2	B3 & B5
f'_{cc} = -5.7 ksi (39.3 MPa) ε_{cc} = -0.0034 in./in. f'_{cu} = -3.6006 ksi (24.83 MPa) ε_{cu} = -0.0124 in./in.	f'_{cc} = -5.25 ksi (36.2 MPa) ε_{cc} = -0.0025 in./in. f'_{cu} = -2.6498 ksi (18.27 MPa) ε_{cu} = -0.0086 in./in.	f'_{cc} = -5.7 ksi (39.3 MPa) ε_{cc} = -0.0034 in./in. f'_{cu} = -3.2455 ksi (22.38 MPa) ε_{cu} = -0.0147 in./in.
B4 & B6		
f'_{cc} = -5.25 ksi (36.2 MPa) ε_{cc} = -0.0025 in./in. f'_{cu} = -2.7229 ksi (18.77 MPa) ε_{cu} = -0.0083 in./in.		
Columns		
C1	C2	C3
f'_{cc} = -5.95 ksi (41.02 MPa) ε_{cc} = -0.0039 in./in. f'_{cu} = -3.8856 ksi (26.79 MPa) ε_{cu} = -0.0154 in./in.	f'_{cc} = -6.925 ksi (47.75 MPa) ε_{cc} = -0.0059 in./in. f'_{cu} = -5.208 ksi (35.91 MPa) ε_{cu} = -0.0234 in./in.	f'_{cc} = -6.325 ksi (43.61 MPa) ε_{cc} = -0.0047 in./in. f'_{cu} = -4.308 ksi (29.7 MPa) ε_{cu} = -0.0199 in./in.

Table 4-9. Properties of Core Concrete Fibers in Nine-Story Special MRF

Beams		
B1	B2	B3
f'_{cc} = -5.625 ksi (38.78 MPa) ε_{cc} = -0.0033 in./in. f'_{cu} = -3.5516 ksi (24.49 MPa) ε_{cu} = -0.0113 in./in.	f'_{cc} = -5.4 ksi (23.44 MPa) ε_{cc} = -0.0028 in./in. f'_{cu} = -3.2929 ksi (22.71 MPa) ε_{cu} = -0.0088 in./in.	f'_{cc} = -5.7 ksi (39.3 MPa) ε_{cc} = -0.0034 in./in. f'_{cu} = -3.6006 ksi (24.83 MPa) ε_{cu} = -0.0124 in./in.
B4	B5 & B7	B6 & B8
f'_{cc} = -5.25 ksi (36.2 MPa) ε_{cc} = -0.0025 in./in. f'_{cu} = -2.6498 ksi (18.27 MPa) ε_{cu} = -0.0086 in./in.	f'_{cc} = -5.7 ksi (39.3 MPa) ε_{cc} = -0.0034 in./in. f'_{cu} = -3.2455 ksi (22.38 MPa) ε_{cu} = -0.0147 in./in.	f'_{cc} = -5.25 ksi (36.2 MPa) ε_{cc} = -0.0025 in./in. f'_{cu} = -2.7229 ksi (18.77 MPa) ε_{cu} = -0.0083 in./in.
Columns		
C1	C2	C3
f'_{cc} = -5.75 ksi (39.64 MPa) ε_{cc} = -0.0035 in./in. f'_{cu} = -3.6728 ksi (25.32 MPa) ε_{cu} = -0.0129 in./in.	f'_{cc} = -5.95 ksi (41.02 MPa) ε_{cc} = -0.0039 in./in. f'_{cu} = -3.8856 ksi (26.79 MPa) ε_{cu} = -0.0154 in./in.	f'_{cc} = -6.925 ksi (47.75 MPa) ε_{cc} = -0.0059 in./in. f'_{cu} = -5.208 ksi (35.91 MPa) ε_{cu} = -0.0234 in./in.
C4		
f'_{cc} = -6.325 ksi (43.61 MPa) ε_{cc} = -0.0047 in./in. f'_{cu} = -4.308 ksi (29.7 MPa) ε_{cu} = -0.0199 in./in.		

4.3.3 Modeling Methods for Repairable Precast Frames

Figure 4-17 shows the three-, six-, and nine-story repairable precast frames. These precast frames were detailed with the same beam and column geometries and reinforcement used in the conventional cast-in-place frames (Sec. 4.3.1) but incorporating

the proposed joint detailing to investigate the seismic performance of the novel precast frames. Appendix B presents design and construction guidelines for repairable precast connections.

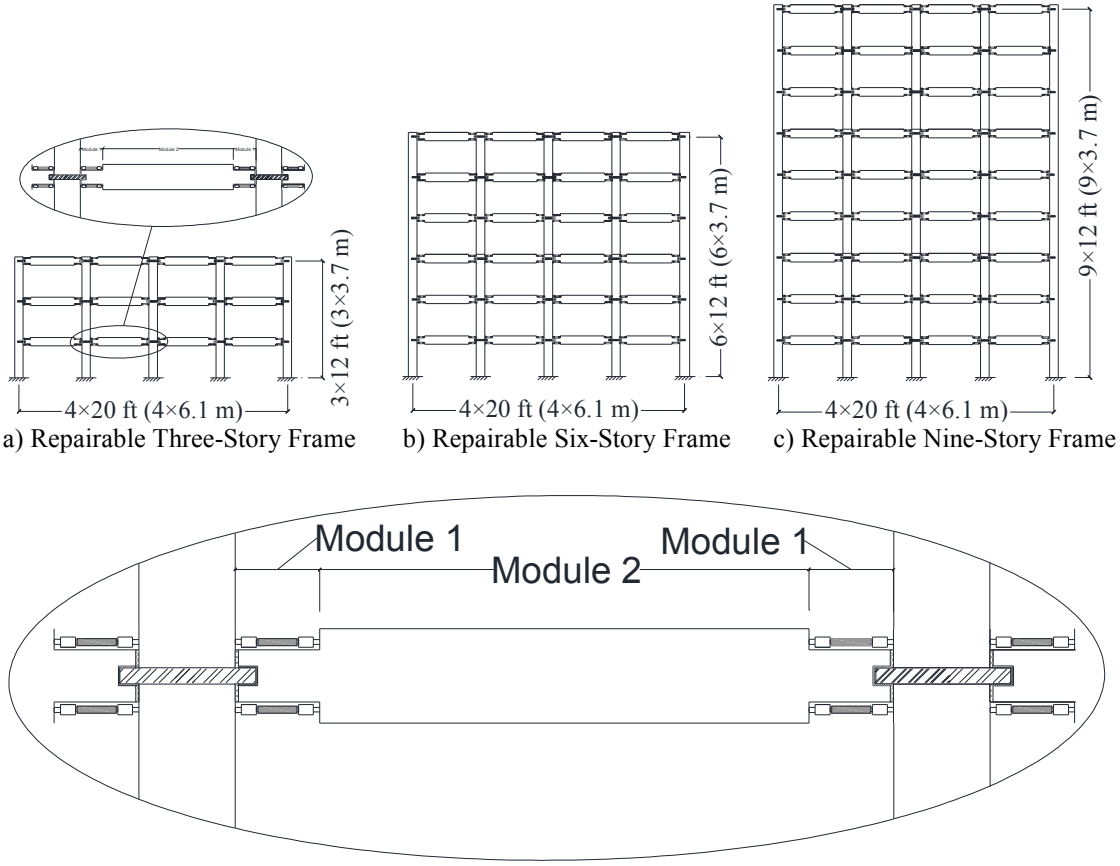

a) Repairable Three-Story Frame b) Repairable Six-Story Frame c) Repairable Nine-Story Frame

d) Interior Precast Beam

Figure 4-17. Repairable Precast Frames for Analytical Studies

Similar to the conventional frames, OpenSees (2016) was used for the analysis of precast frames. A three-dimensional fiber-section model was utilized for all precast frames. The beam-column joint model suggested in Sec 4.2.1 was utilized at each beam-column joint within the precast frames with some modifications (Fig. 4-17d). Both shear-pin capacity and concrete link strength was increased (in the beam-column connection model) to accommodate the increase of shear force and precast element geometries. The shear-pin is now inserted in the precast column instead of the beam for

better constructability and to facilitate the assembly of precast element during construction (see Appendix B). Each beam analytical model is divided into three sub-modules (Fig. 4-17d) to accommodate the beam neck model discussed in Sec. 4.2.1 within the internal joints. The beam end modules represent the beam necks located at the two ends of each beam. The third module consists of the beam original sections used in CIP and is located between the two end modules. A "forceBeamColumn" element with five integration points was used to model all beam elements. The column was modeled as a "forceBeamColumn" element with seven integration points.

The concrete cover and core were modeled using "Concrete04" material model. A uniaxial material, "ReinforcingSteel", was used to simulate the column reinforcement behavior. "Pinching04" was utilized to model BRR steel bars. The two material models will allow determination of the frames ultimate displacements as discussed in Sec. 4.3.2

Table 4-10 presents the general modeling parameters. Fiber sections consisting of 30 segments and 10 segments in both directions were used to model the confined and unconfined concrete, respectively. Mander's model (Mander et al., 1988) was utilized to calculate properties of the confined concrete. All pushover analysis was carried out by applying displacements at the roof level.

Table 4-10. Modeling Methods for Repairable Precast Frames

General Remarks	
Three Dimensions with six Degrees of freedom per node. Supports are fixed. Element type: *forcebeamcolumn* with seven integration points Gravity load and P-Δ effects were considered, Beams between columns consist of five elements; a middle element, two elements for beam necks, and two rigid elements representing the Beam-Column joint regions.	Sectional Properties: Fiber Section, Core Concrete Discretization: 30 by 30, Cover Concrete Discretization: 10 by 10. Element in the middle of the beam or column has less transverse reinforcement. The Beam-Column joint region is rigid. "elasticBeamColumn" elements with large moment of inertia were used in joint region. Truss elements were used to model all BRR Masses were assigned at each Beam-Column intersection node
Concrete Fibers	
Unconfined Concrete (cover)	Confined Concrete (core)
Type: Concrete04 f'_{cc} = - 5 ksi (34.47 MPa) ε_{cc} = -0.002 in./in. f'_{cu} = 0.0 ksi (0.0 MPa) ε_{cu} = -0.005 in./in. E_c = 4030.51 ksi (27789.39 MPa)	Type: Concrete04 f'_{cc}, ε_{cc}, f'_{cu} and ε_{cu} transverse reinforcement according to Mander's model.
Steel Fibers	
General Long. Reinforcement	Buckling Restrained Reinforcement (BRR)
Type: ReinforcingSteel f_y = 68 ksi (468.84 MPa) f_{su} = 95 ksi (655 MPa) E_s = 29000 ksi (199947.96 MPa) E_{sh} = 1247 ksi (8597.76 MPa) ε_{sh} = 0.015 in./in. ε_{su} = 0.12 in./in.	Type: Pinching4 f_1 = 68 ksi (468.84 MPa) f_2 = 91.22 ksi (628.94 MPa) f_3 = 95 ksi (655 MPa) f_4 = 0.5 ksi (3.45 MPa) ε_1 = 0.0023 in./in. ε_2 = 0.05 in./in. ε_3 = 0.11 in./in. ε_4 =0.12 in./in.

4.3.4 Pushover Analysis of Building Frames

Pushover analyses were carried out on precast and CIP frames to investigate their seismic performance. A summary of the analyses and findings is presented herein.

4.3.4.1 Building Frame Pushover Analysis Parameters

A total of 12 pushover analyzes were performed on precast and CIP frames. Of which, three analyzes were conducted on three-, six-, and nine-story CIP frames to serve

as the reference models, and nine analyzes were performed on three repairable precast frames with three BRR fuse lengths per frame. The BRR fuse length is expected to be a critical design parameter to control the displacement capacity of precast frames using the proposed detailing. Three different BRR fuse lengths used in each precast frame were 7.5 (191), 15 (381), and 22.5 in. (572 mm) corresponding to 25%, 50%, and 75% of the beam height (BH), respectively. The neck region length was assumed to be 15 in. (381 mm) larger than the BRR fuse length to include all components of the precast joint such as couplers and BRR.

4.3.4.2 Building Frame Pushover Analysis Results

Figures 4-19 to 4-20 show the pushover relationships for three-, six-, and nine-story precast and CIP frames, and Table 4-11 presents a summary of the pushover analyses. Note all CIP frames are SMRFs. It can be seen that all novel precast frames have significantly higher displacement capacities compared to those in CIP for all cases. For example, the displacement capacity of the nine-story precast frame with 15-in. (381-mm) BRR fuse length (or 0.5BH) was 2.4 times higher than the corresponding CIP frame (Fig. 4-20). Furthermore, the pushover analysis shows that a longer BRR fuse length results in a higher displacement capacity for the precast frame. The minimum practical BRR fuse length (0.25BH) ensures achieving the same or higher displacement capacity for all precast frames compared to their corresponding CIP frames.

Pushover analyses showed that the initial stiffness of the proposed precast buildings is 42.4% lower than that in CIP, on average. The initial stiffness of nine-story precast frame with 15 in. (381 mm) BRR fuse length (or 0.5BH) was 44.8% lower than the corresponding CIP initial stiffness. It also can be concluded that longer BRR fuse

lengths results in lower initial stiffness for precast frames. The effect of lower stiffness is mainly on the seismic demands. Nonlinear dynamic analyses were preformed to quantify the change in demands, which are presented in the following section.

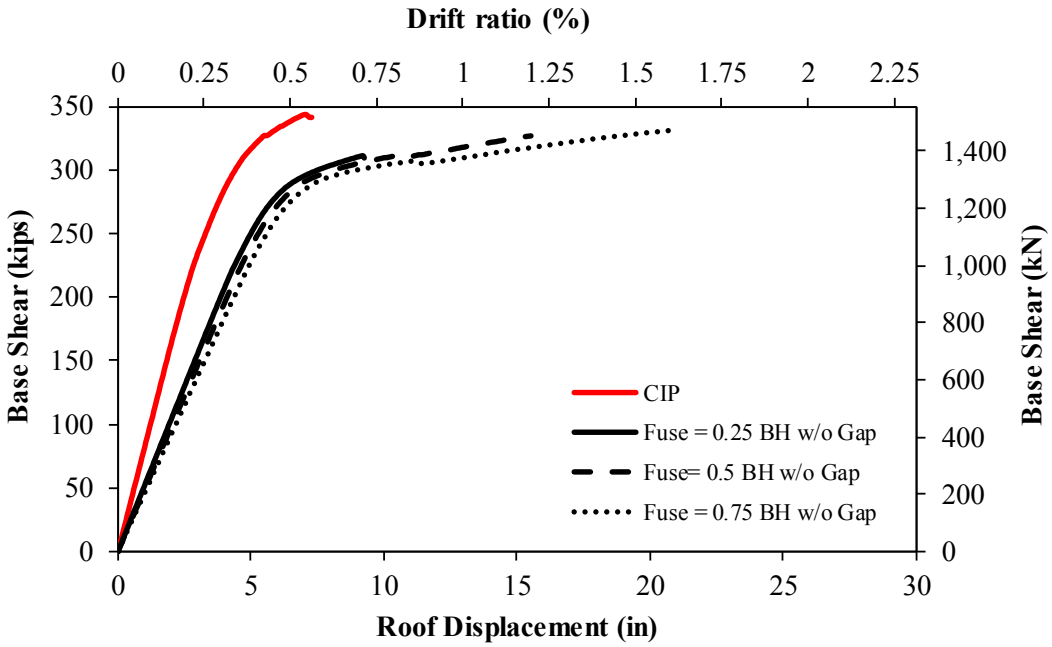

Figure 4-18. Pushover Response for Three-Story Precast and CIP Frames

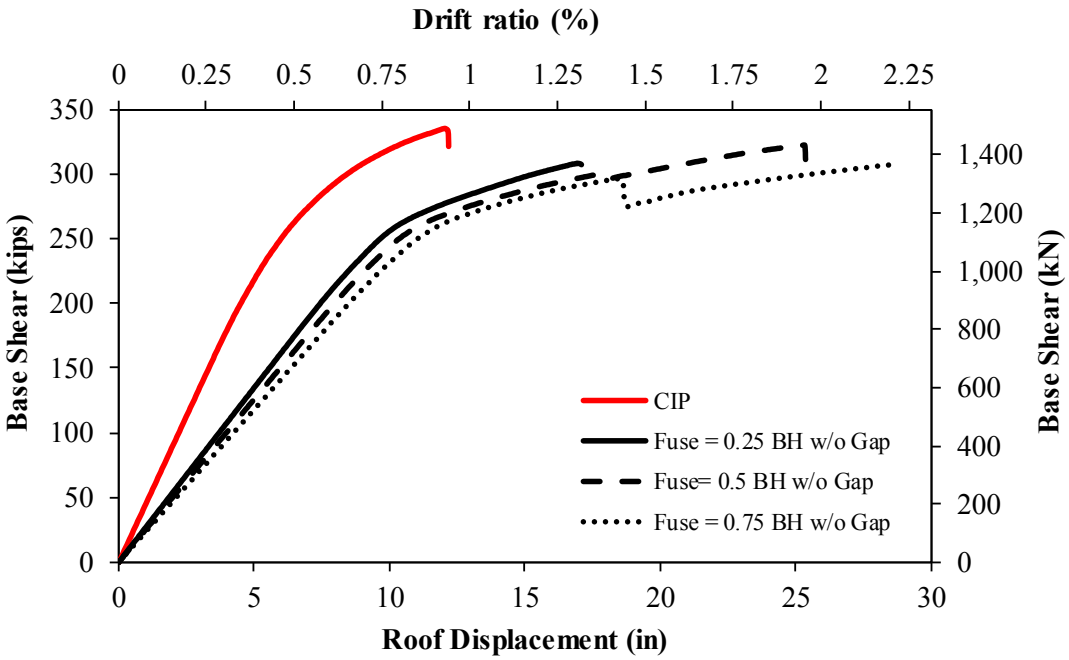

Figure 4-19. Pushover Response for Six-Story Precast and CIP Frames

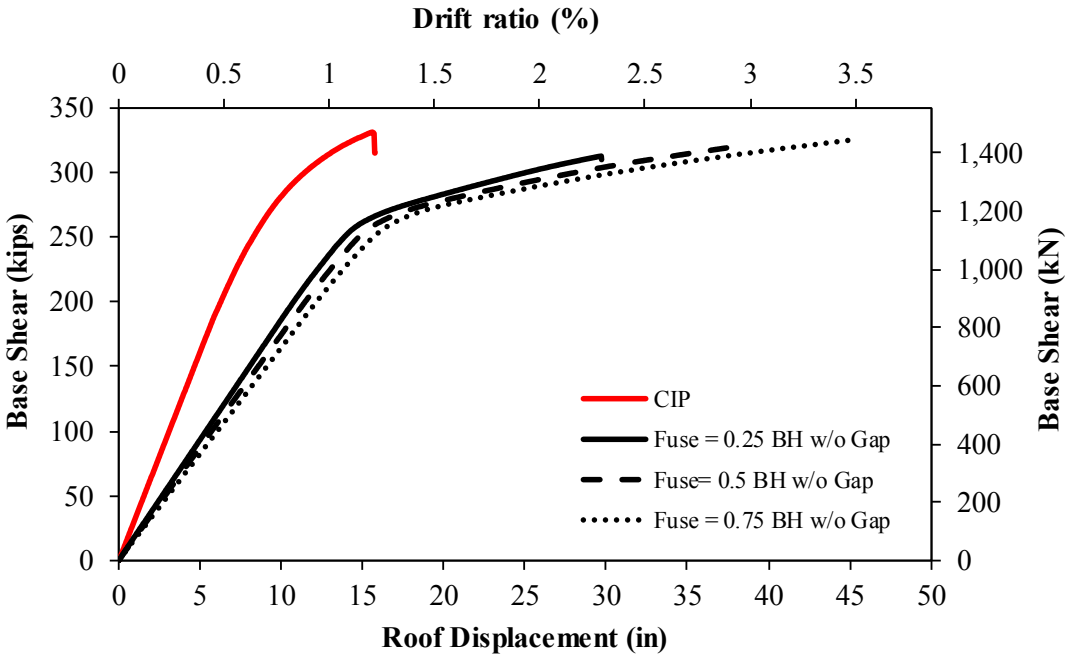

Figure 4-20. Pushover Response for Nine-Story Precast and CIP Frames

Table 4-11. Summary of Pushover Analysis for CIP and Repairable Frames

Number of Story	Frame Type	Parameters	
		Ultimate disp., in. (Change w.r.t CIP)	Stiffness (kip/in.) (Change w.r.t CIP)
Three Story	CIP	7.3	80.54
	Repairable Frame w/ 0.25 BH Fuse Length	9.27 (27.0%)	51.69 (-35.8%)
	Repairable Frame w/ 0.5 BH Fuse Length	15.5 (112.3%)	48.82 (-39.4%)
	Repairable Frame w/ 0.75 BH Fuse Length	20.8 (184.9%)	46.00 (-42.9%)
Six Story	CIP	12.23	44.1
	Repairable Frame w/ 0.25 BH Fuse Length	17.13 (40.1%)	26.76 (-39.3%)
	Repairable Frame w/ 0.5 BH Fuse Length	25.4 (107.7%)	25.12 (-43.0%)
	Repairable Frame w/ 0.75 BH Fuse Length	28.55 (133.4%)	23.54 (-46.6%)
Nine Story	CIP	15.85	31.62
	Repairable Frame w/ 0.25 BH Fuse Length	29.78 (87.9%)	18.52 (-41.4%)
	Repairable Frame w/ 0.5 BH Fuse Length	37.85 (138.8%)	17.45 (-44.8%)
	Repairable Frame w/ 0.75 BH Fuse Length	45.53 (187.3%)	16.37 (-48.2%)

Note: 1 in. = 25.1 mm; 1 kip = 4.448 kN

4.3.5 Dynamic Analysis of Building Frames

Nonlinear dynamic response history analyses were carried out on three-, six- and nine-story precast and CIP frames to investigate their dynamic behavior. Each frame was analyzed under ten near-field ground motions. The dynamic analysis parameters and findings are discussed herein.

4.3.5.1 Building Frame Dynamic Analysis Parameters

Sixty nonlinear dynamic response history analyzes were carried out on a total of six precast and CIP frames to investigate the dynamic behavior of the proposed precast buildings. Three-, six- and nine-story frames were included in the analysis. Precast frames had the minimal BRR fuse length of 7.5 in. (190 mm, 25% of the beam depth), which will result in the lowest displacement capacities for the frames. This was done to comment on the displacement capacity/demand ratio for the lowest ductile precast

frames. Each frame was analyzed under ten near-field ground motions (Table 4-12) selected by Somerville et al. (1997).

Table 4-12. Details of Near-Field Ground Motions Derived from Historical Acceleration Records

Earthquake ID	Record	Earthquake Magnitude	Distance (km)
EQ1	Tabas, 1978	7.4	1.2
EQ2	Loma Prieta, 1989, Los Gatos	7	3.5
EQ3	Loma Prieta, 1989, Lex. Dam	7	6.3
EQ4	C. Mendocino, 1992, Petrolia	7.1	8.5
EQ5	Erzincan, 1992	6.7	2
EQ6	Landers, 1992	7.3	1.1
EQ7	Nothridge, 1994, Rinaldi	6.7	7.5
EQ8	Nothridge, 1994, Olive View	6.7	6.4
EQ9	Kobe, 1995	6.9	3.4
EQ10	Kobe, 1995, Takatori	6.9	4.3

It is worth mentioning that in the dynamic analysis “Concrete01” model was used instead of “Concrete04” model for concrete fibers, and ”Pinching04” model was replaced with “ReinforcingSteel” model for steel fibers to improve stability of the nonlinear analyses. Nonlinear demands were the focus of the dynamic study thus these modeling method changes will not affect the seismic performance as long as the frame displacement demand is less than the frame displacement capacity obtained from the pushover analysis. A 5% damping ratio was utilized in the all dynamic analyses.

4.3.5.2 Building Frame Dynamic Analysis Results

4.3.5.2.1 Three-Story Frames

Figures 4-210 and 4-22 respectively show the dynamic response of CIP and repairable precast three-story frames under ten near-field ground motions. Table 4-13

presents the summary of the dynamic analysis. The analysis shows that the repairable precast frame can withstand severe earthquakes with at least a 30% reserved displacement capacity. Another finding is that the repairable three-story frame experienced 23% higher displacement demands on average compared to those in the CIP frame, which is due to a lower initial stiffness for the precast frame.

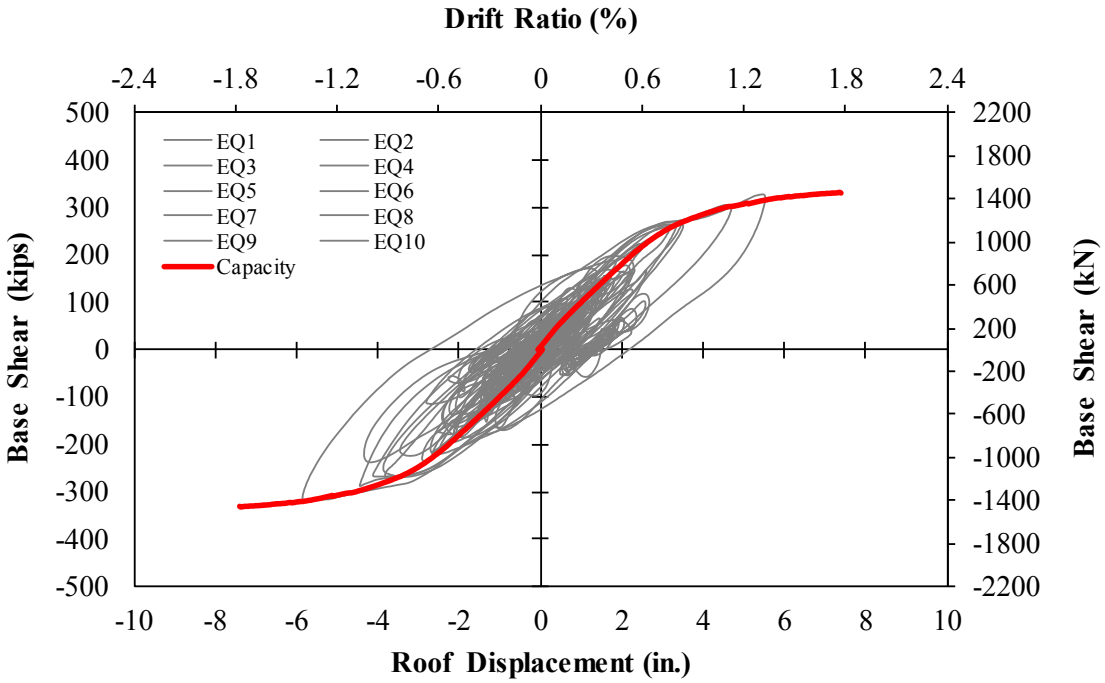

Figure 4-21. Dynamic Response of Three-Story SMRF CIP Frame under 10 Ground Motions

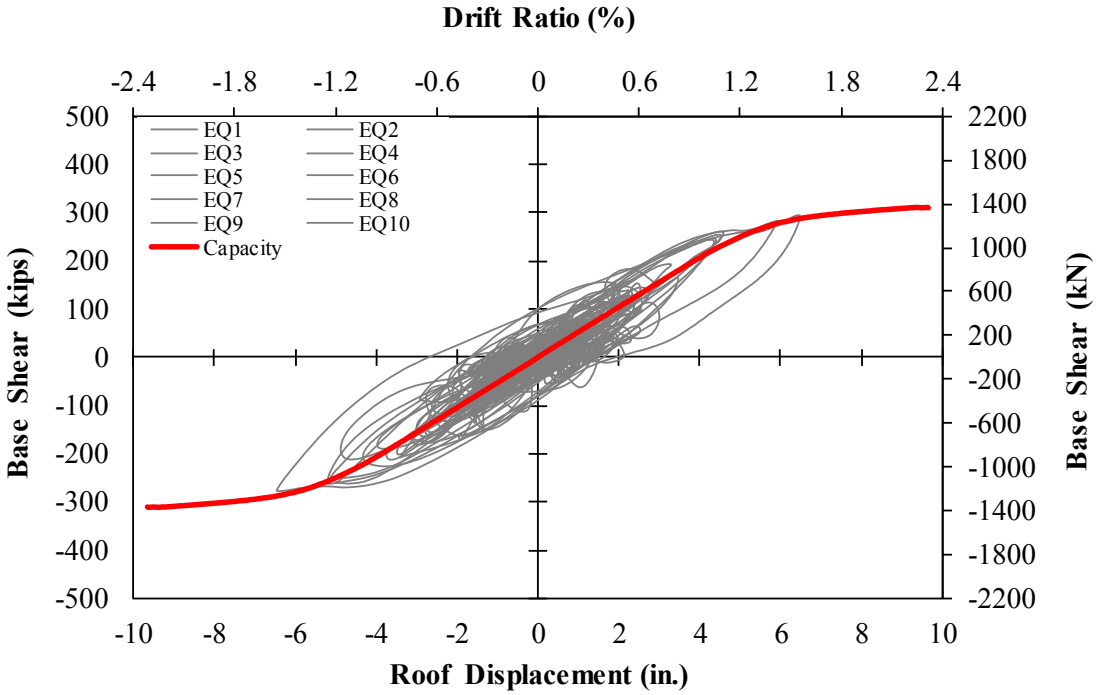

Figure 4-22. Dynamic Response of Three-Story Repairable Precast Frame under 10 Ground Motions

Table 4-13. Summary of Dynamic Analysis for Three-Story CIP and Repairable Frames

Parameter	CIP		Repairable	
	Peak Roof Displacement (Drift)	Peak Base Shear (kips)	Peak Roof Displacement (Drift)	Peak Base Shear (kips)
Capacity	7.30 in. (1.69%)	331.72	9.27 in. (2.15%)	310.875
Demand-EQ1	2.38 in. (0.55%)	197.26	2.75 in. (0.64%)	150.65
Demand-EQ2	4.44 in. (1.03%)	268.33	5.21 in. (1.21%)	254.03
Demand-EQ3	4.70 in. (1.09%)	305.74	5.94 in. (1.37%)	283.05
Demand-EQ4	4.11 in. (0.95%)	223.42	4.90 in. (1.13%)	193.39
Demand-EQ5	2.66 in. (0.62%)	95.82	3.48 in. (0.81%)	82.69
Demand-EQ6	1.45 in. (0.24%)	87	1.83 in. (0.42%)	81.59
Demand-EQ7	5.53 in. (1.28%)	327.49	6.48 in. (1.5%)	295
emand-EQ8	2.20 in. (0.51%)	177.78	3.00 in. (0.70%)	183
Demand-EQ9	5.84 in. (1.35%)	264.36	6.45 in. (1.49%)	243.98
Demand-EQ10	3.82 in. (0.88%)	263.97	5.02 in. (1.16%)	261.02

Note: 1 in. = 2.54 cm, 1 kip = 4.448 kN

Figures 4-23 and 4-24 respectively show the peak drift demands and the residual drifts for both CIP and precast three-story frames under 10 ground motions. It can be seen that the peak drift demands for repairable precast frame are always higher than those in CIP frame due to their lower initial stiffness of repairable frame. However, the

residual drifts for repairable precast frame were slightly lower than those in CIP but all residual drifts were insignificant.

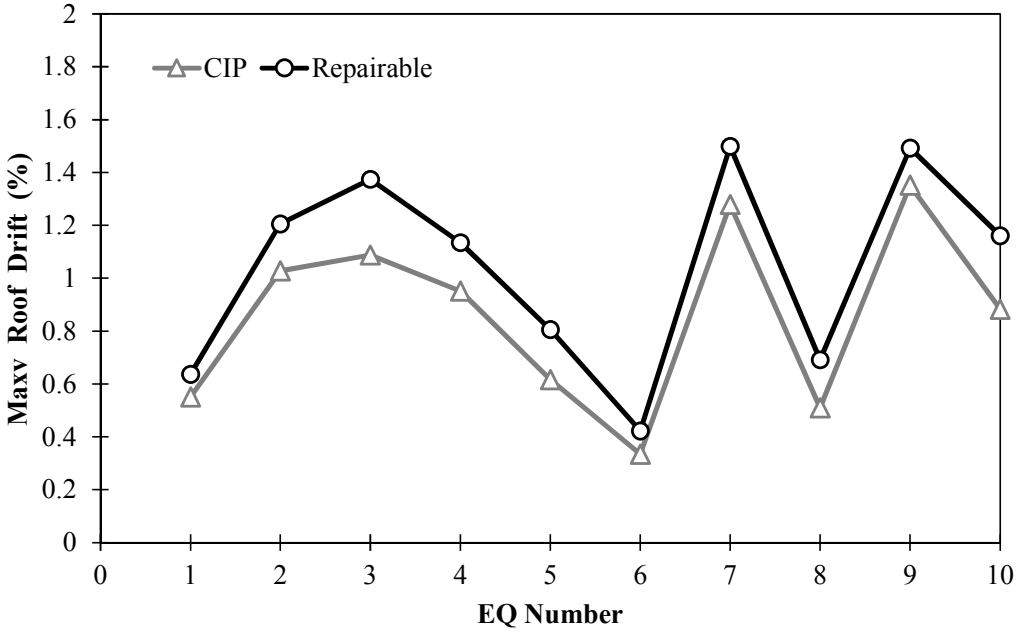

Figure 4-23. Peak Drift Demands for Three-Story Frames under 10 Ground Motions

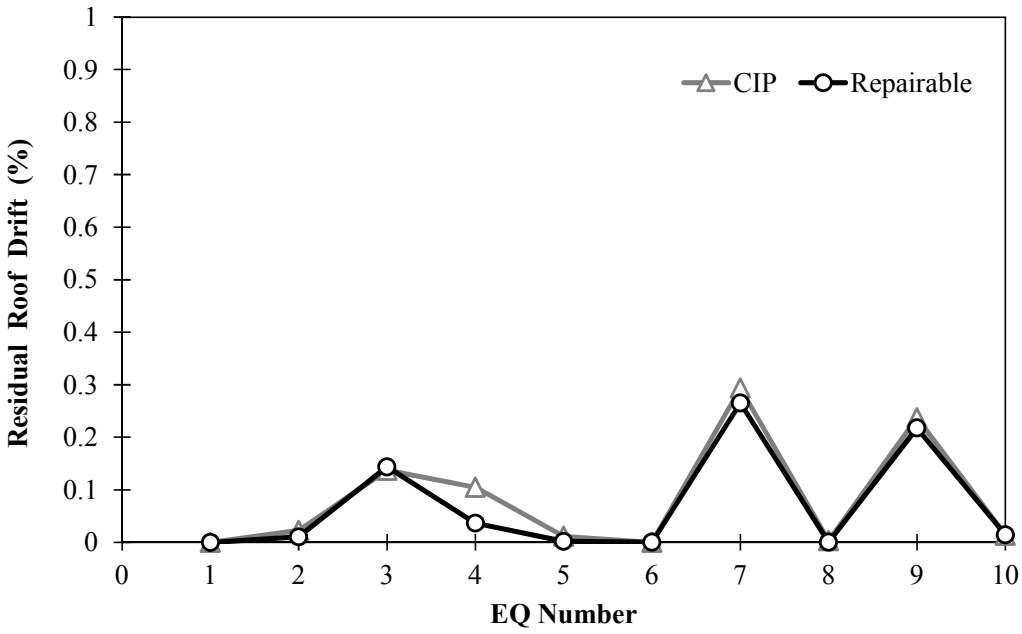

Figure 4-24. Residual Drifts for Three-Story Frames under 10 Ground Motions

The story drift demands for the three-story CIP and repairable precast frames are shown in Fig. 4-25 for ten near-field ground motions. The ASCE allowable drift demand is also included in the figures to better comparison. It can be seen that the repairable precast frame usually exhibit higher story drift demands than those in the CIP frame under the same ground motion. Nevertheless, the story drift demands for the three-story precast frame was always within the ASCE limit indicating that this frame is sufficient even without increasing the neck depth or the BRR sizes. Therefore, the lower initial stiffness for the three-story precast frame does not adversely affect the design and the precast does not require larger sections to increase the stiffness.

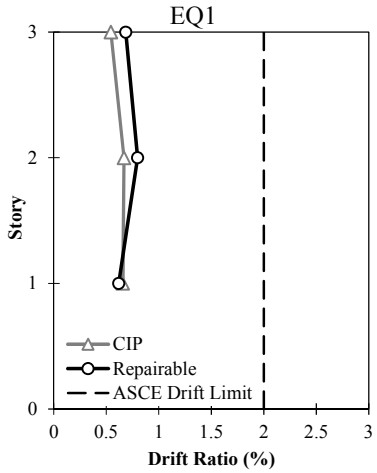

a) Story Drift Demands under EQ1

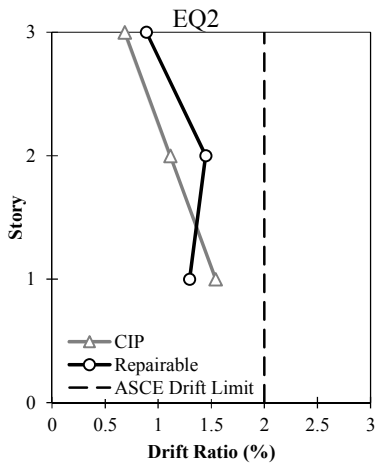

b) Story Drift Demands under EQ2

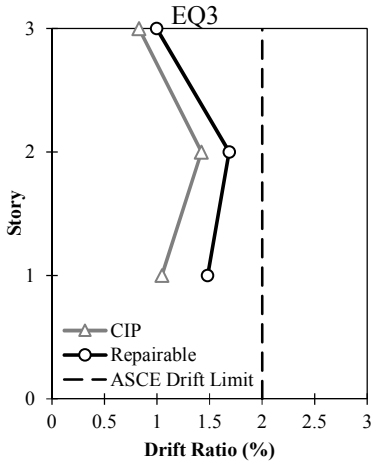

c) Story Drift Demands under EQ3

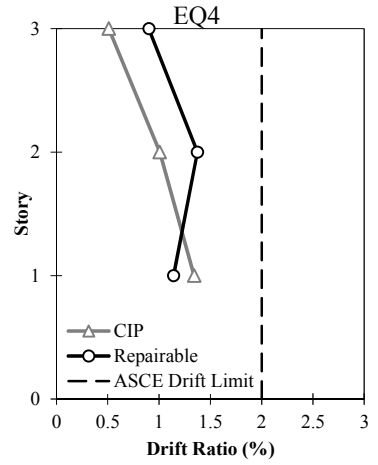

d) Story Drift Demands under EQ4

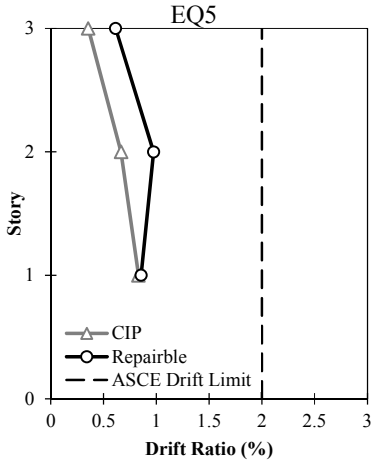

e) Story Drift Demands under EQ5

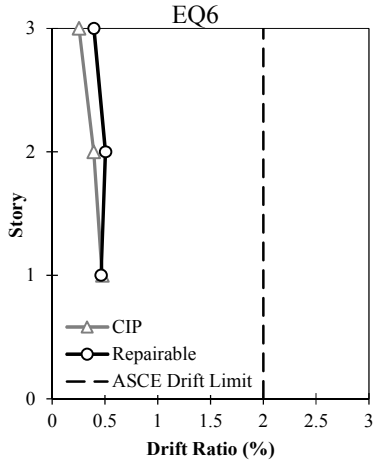

f) Story Drift Demands under EQ6

Figure 4-24. Story Drift Demands for Three-Story Frames

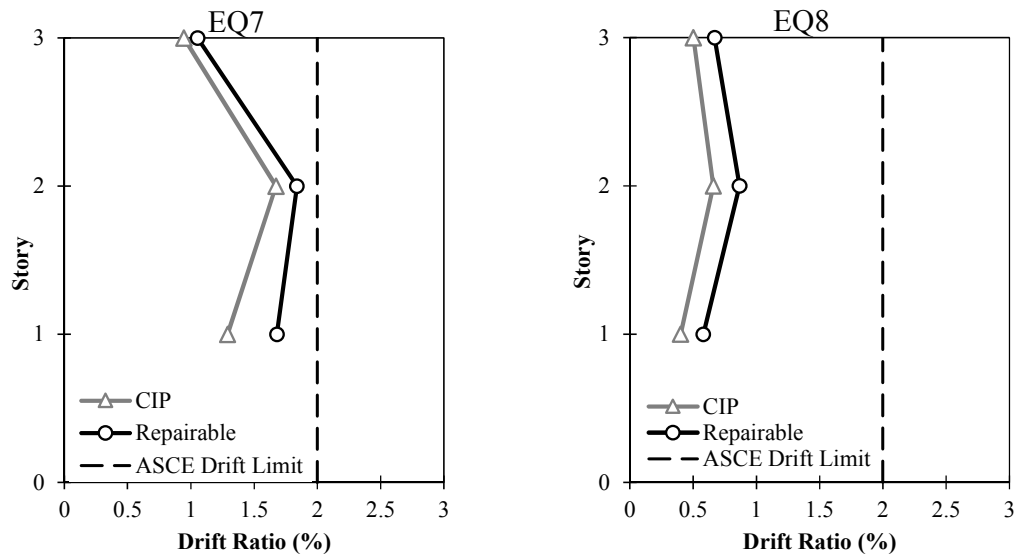

a) Story Drift Demands under EQ7

b) Story Drift Demands under EQ8

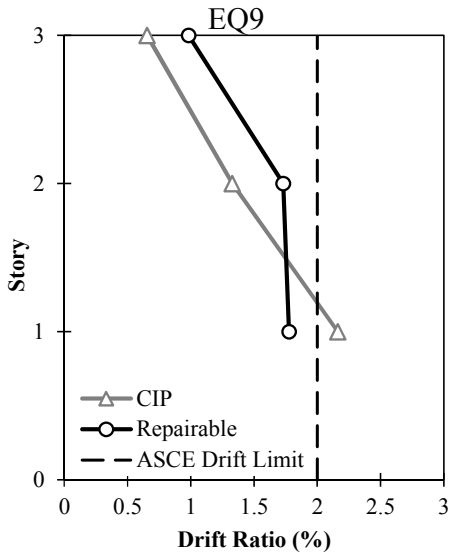

c) Story Drift Demands under EQ9

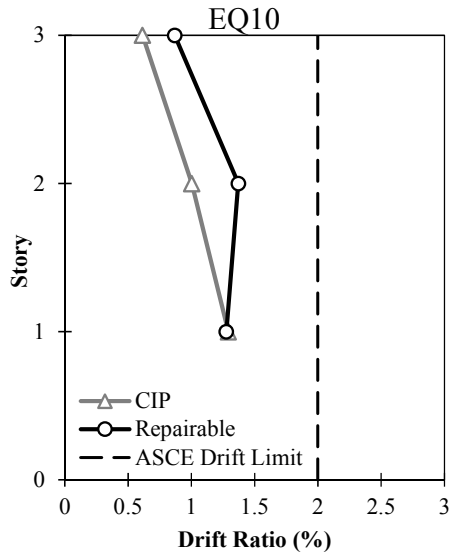

d) Story Drift Demands under EQ10

Figure 4-24. Roof Drift Ratios for Three-Story SMRF under Different Earthquakes (Continued)

4.3.5.2.2 Six-Story Frames

Figure 4-25 and 4-26 show the dynamic response for both CIP and repairable nine stories buildings under ten different strong ground motions. Table 4-14 shows the summary of the dynamic analysis. Similar to the results from three stories frames, six stories frames analysis results show that the repairable frame can withstand strong ground

motions and still have at least 43% reserved displacement capacity. The increase in displacement demand in six-story repairable frames was 7.8% higher than those demands in CIP frames.

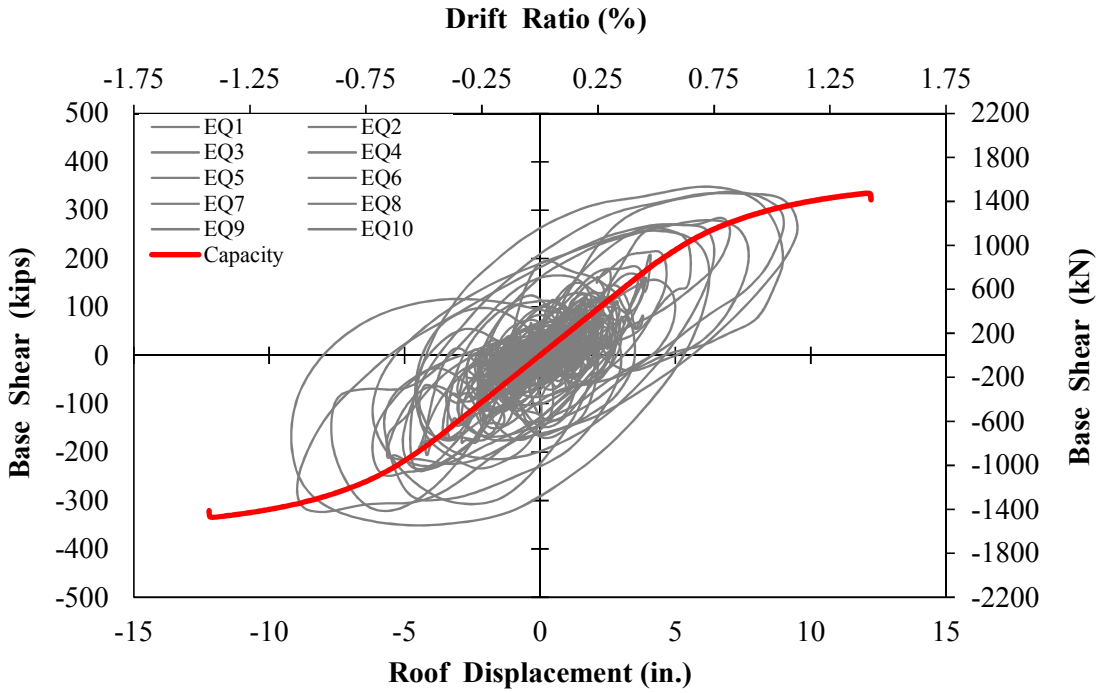

Figure 4-25. Dynamic Response of Six-Story CIP SMRF under Different Ground Motions

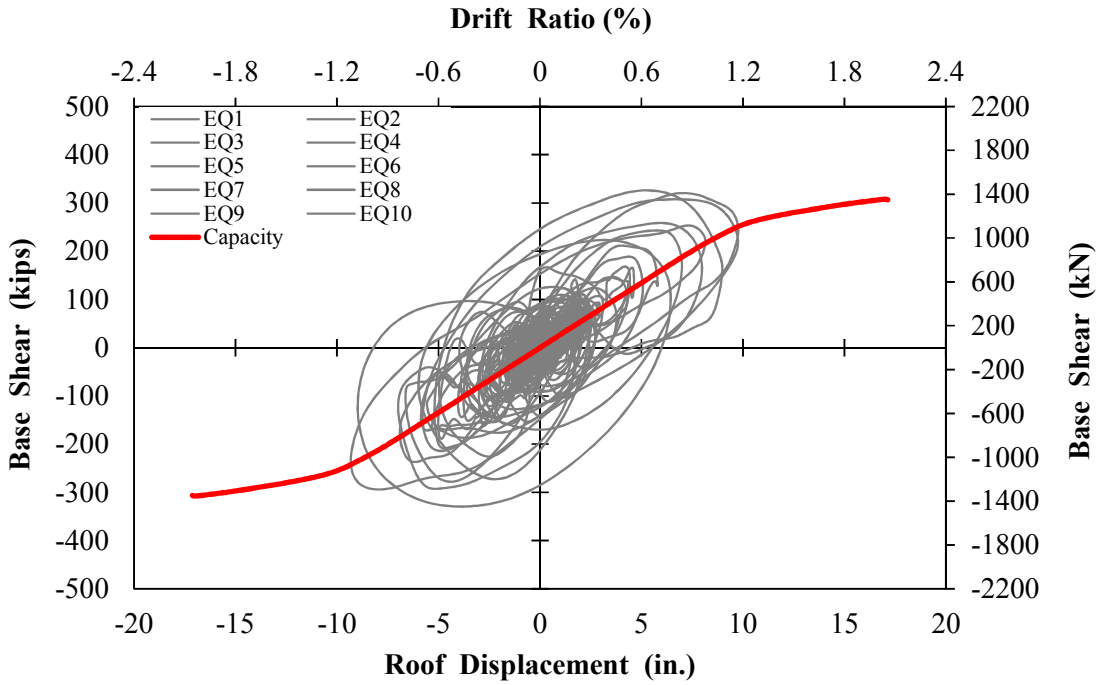

Figure 4-26. Dynamic Response of Six-Story Repairable SMRF under Different Ground Motions

Table 4-14. Summary of Dynamic Analysis for Six-Story CIP and Repairable Frames

Parameter	CIP		Repairable	
	Peak Roof Displacement (Drift)	Peak Base Shear (kips)	Peak Roof Displacement (Drift)	Peak Base Shear (kips)
Capacity	12.23 in. (1.42%)	334.84	17.13 in. (1.99%)	307.63
Demand-EQ1	4.24 in. (0.49%)	207.20	5.02 in. (0.58%)	166.70
Demand-EQ2	9.01 in. (10.45%)	337.97	9.76 in. (1.13%)	320.38
Demand-EQ3	9.51 in. (1.10%)	335.33	9.76 in. (1.13%)	307.5
Demand-EQ4	6.43 in. (0.75%)	270.62	6.98 in. (0.81%)	242.61
Demand-EQ5	5.65 in. (0.66%)	120.75	5.86 in. (0.68%)	106.99
Demand-EQ6	3.59 in. (0.42%)	107	4.05 in. (0.47%)	91.07
Demand-EQ7	8.98 in. (1.04%)	348.56	8.98 in. (1.04%)	325.98
Demand-EQ8	5.56 in. (0.12%)	262.31	5.79 in. (0.67%)	211.28
Demand-EQ9	9.19 in. (1.07%)	257.67	8.98 in. (1.04%)	222.97
Demand-EQ10	8.97 in. (1.04%)	283.95	9.33 in. (1.08%)	253.05

Note: 1 in. = 2.54 cm, 1 kip = 4.448 kN

Figure 4-27 and 4-28 show the maximum drift ratio and the residual drift for both CIP and repairable six-stories frames under different ground motions

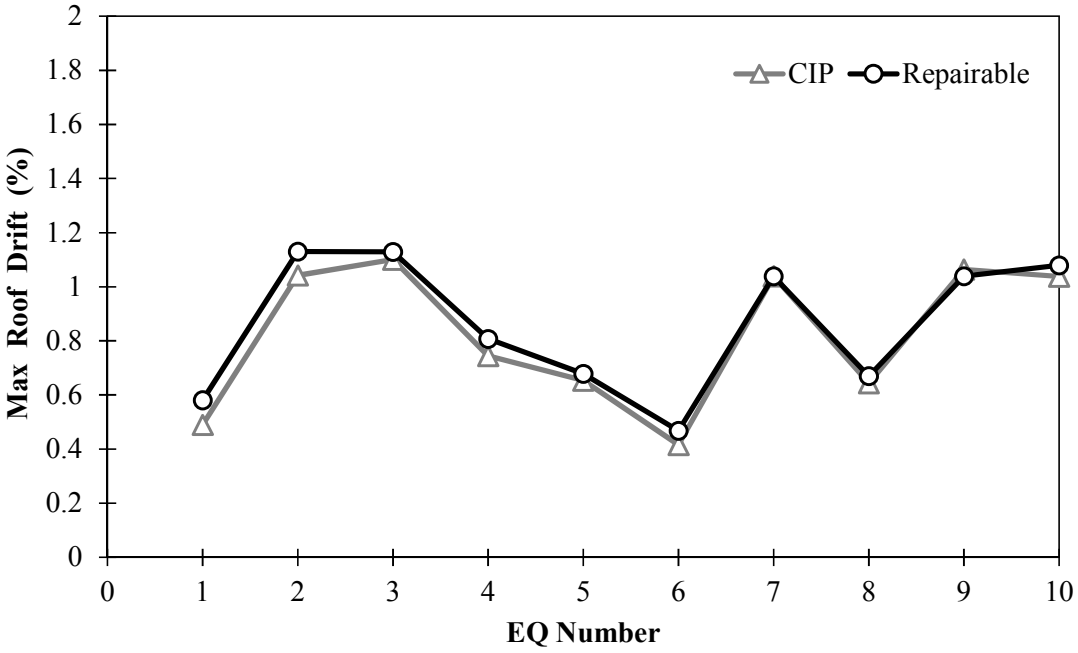

Figure 4-27. Maximum Drift Ratios of Six-Story SMRF under Different Ground Motions

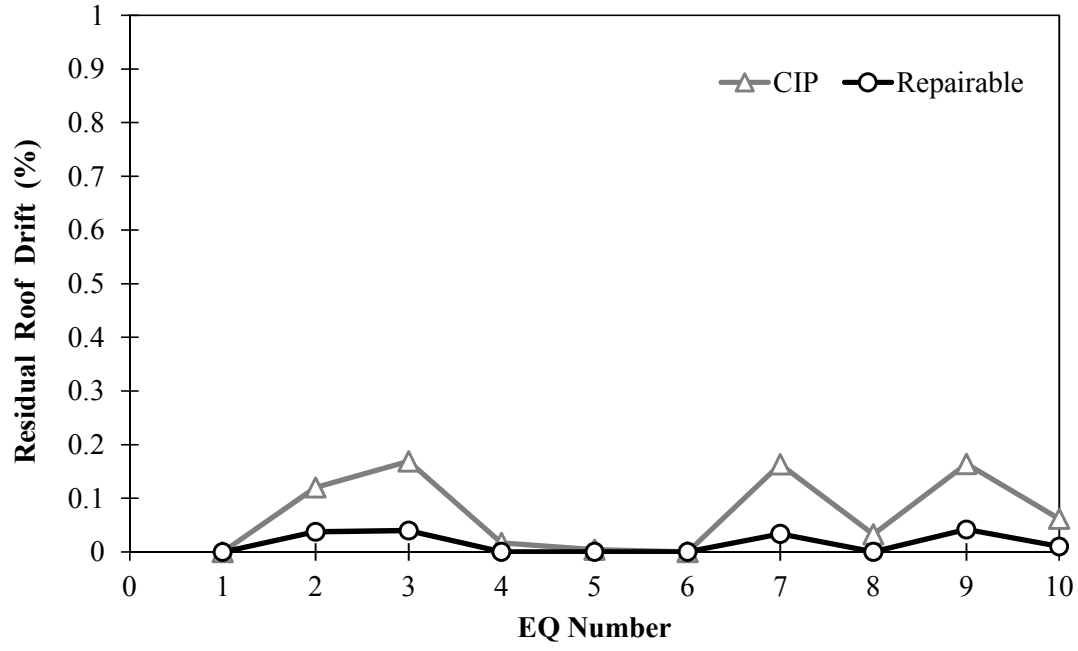

Figure 4-28. Residual Drift Ratios of Six-Story SMRF under Different Ground Motions

The story drift demands for the six-story CIP and repairable precast frames are shown in Fig. 4-29 for ten near-field ground motions. It can be seen that the repairable precast frame usually exhibit higher story drift demands than those in the CIP frame under the same ground motion. Nevertheless, the story drift demands for the six-story precast frame was always within the ASCE limit indicating that this frame is sufficient even without increasing the neck depth or the BRR sizes. Therefore, the lower initial stiffness for the six-story precast frame does not adversely affect the design and the precast building does not require larger sections to increase the stiffness.

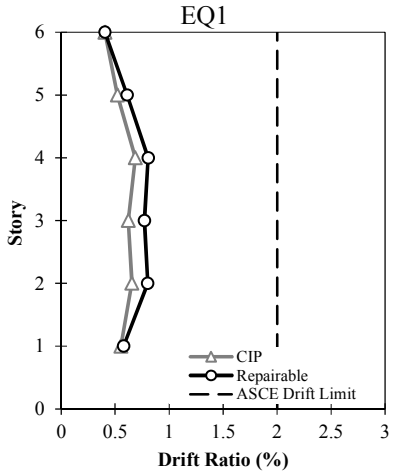

a) Story Drift Demands under EQ1

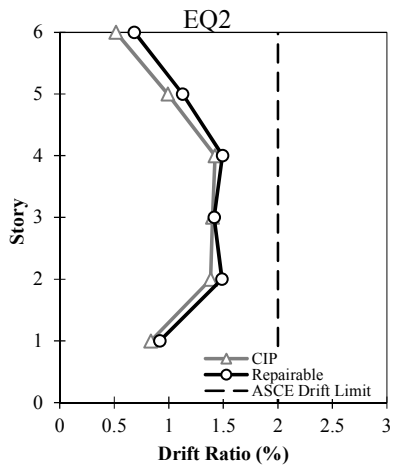

b) Story Drift Demands under EQ2

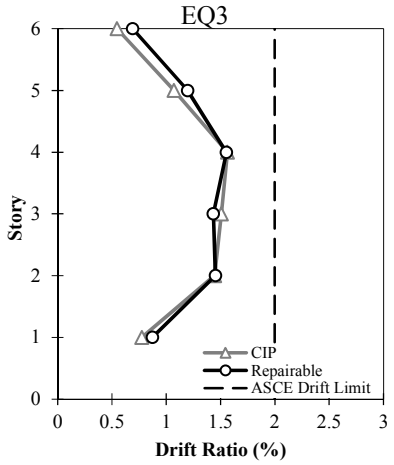

c) Story Drift Demands under EQ3

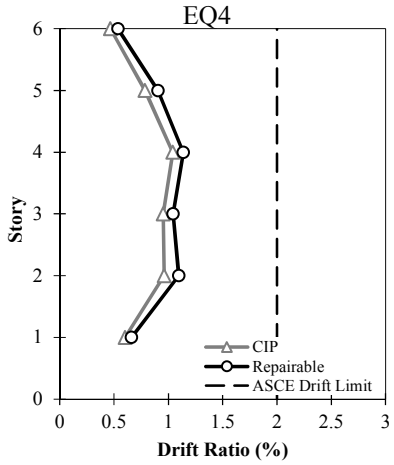

d) Story Drift Demands under EQ4

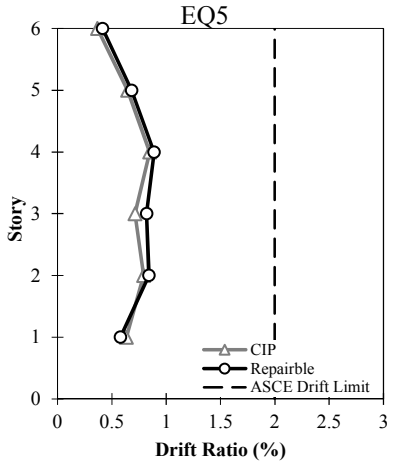

e) Story Drift Demands under EQ5

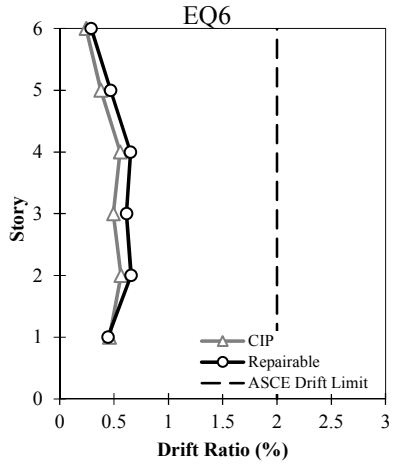

f) Story Drift Demands under EQ6

Figure 4-29. Roof Drift Ratios for Six-Story SMRF under Different Earthquakes

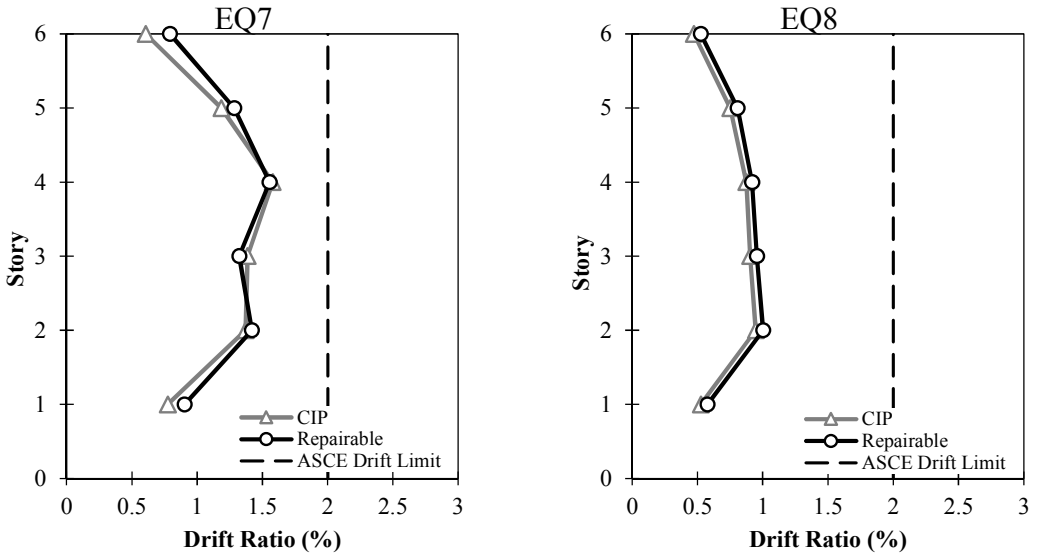

a) Story Drift Demands under EQ7

b) Story Drift Demands under EQ8

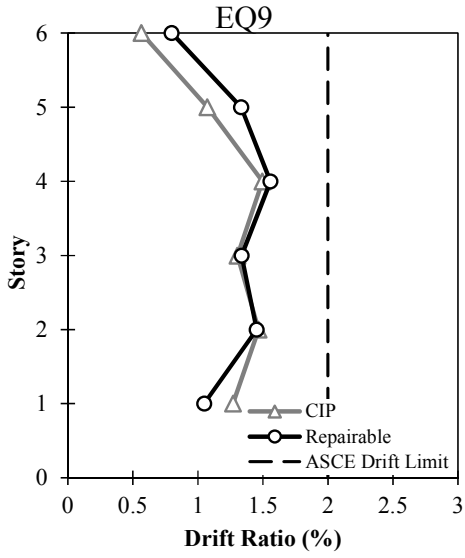

c) Story Drift Demands under EQ9

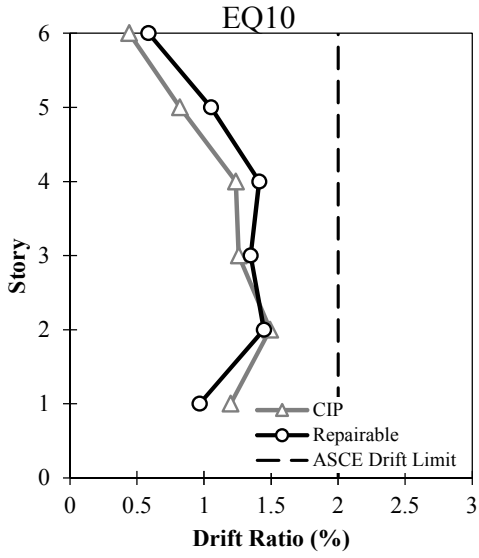

d) Story Drift Demands under EQ10

Figure 4-29. Roof Drift Ratios for Six-Story SMRF under Different Earthquakes (Continued)

4.3.5.2.3 Nine-Story Frames

Figure 4-30 and 4-31 show the dynamic response for both CIP and repairable nine stories buildings under ten different strong ground motions. Table 4-15 shows the summary of the dynamic analysis. It can be seen that the displacement demands for CIP frame under EQ3 and EQ4 reached the displacement capacity of the frame. Moreover, the

reference RC frame failed and the demand exceeded the frame capacity under EQ3 and EQ9. In contrast, the analysis results show that the repairable frame can withstand the same strong ground motions, in which the CIP frame failed, and still have at least 32.5% reserved displacement capacity. Another finding is that the repairable frames exhibited 22% higher displacement demands on average comparing to those demands in CIP frames.

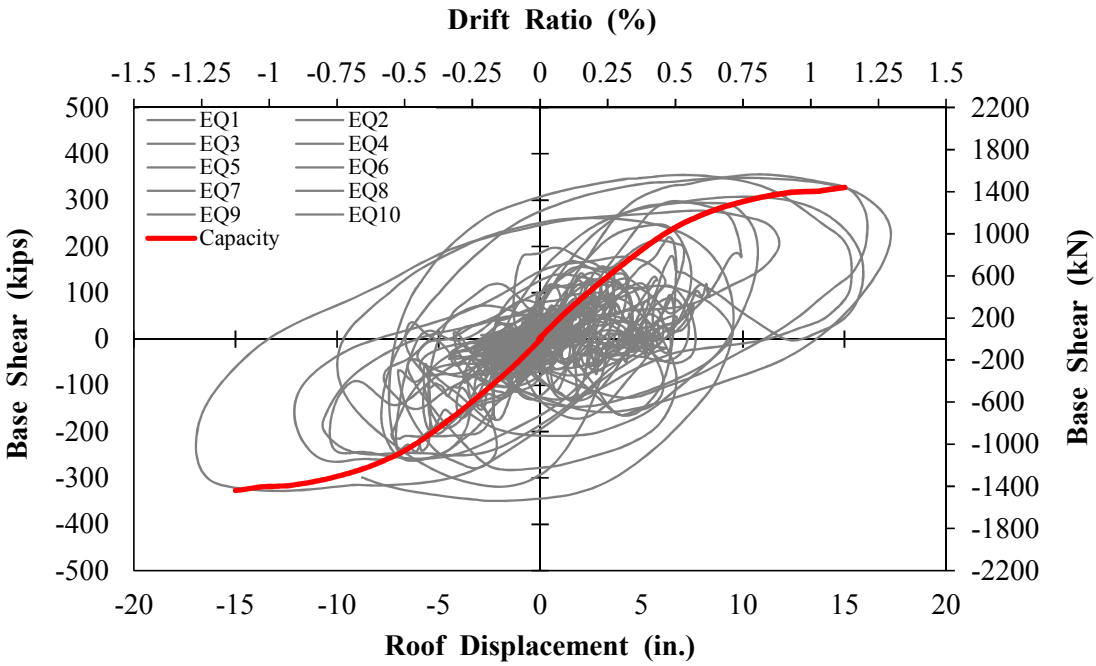

Figure 4-30. Dynamic Response of Nine-Story CIP SMRF under Different Ground Motions

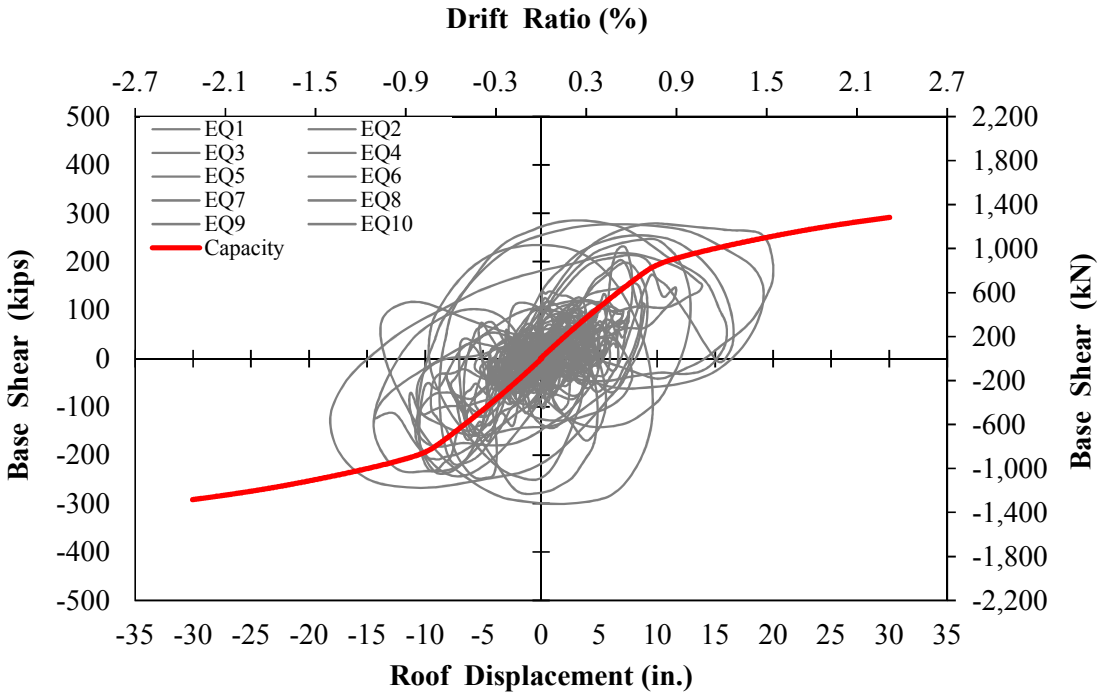

Figure 4-31. Dynamic Response of Nine-Story Repairable SMRF under Different Ground Motions

Table 4-15. Summary of Dynamic Analysis for Nine-Story CIP and Repairable Frames

Parameter	CIP		Repairable	
	Peak Roof Displacement (Drift)	Peak Base Shear (kips)	Peak Roof Displacement (Drift)	Peak Base Shear (kips)
Capacity	15.85 in. (1.22%)	327.05	29.78 in. (2.29%)	291.7
Demand-EQ1	7.10 in. (0.55%)	219.66	10.49 in. (0.81%)	203.39
Demand-EQ2	16.10 in. (1.24%)	355.6	20.01 in. (1.54%)	279.33
Demand-EQ3	16.10 in. (1.24%)	348.08	19.19 in. (1.48%)	277.69
Demand-EQ4	10.70 in. (0.82%)	294.86	12.88 in. (0.99%)	247.46
Demand-EQ5	10.40 in. (0.80%)	156.01	11.36 in. (0.87%)	133.56
Demand-EQ6	5.76 in. (0.44%)	155.77	7.36 in. (0.57%)	112.74
Demand-EQ7	15.30 in. (1.18%)	354.32	16.02 in. (1.23%)	285.62
Demand-EQ8	9.91 in. (0.76%)	297.64	11.64 in. (0.90%)	213.62
Demand-EQ9	9.99 in. (0.77%)	261.21	14.36 in. (1.11%)	234.67
Demand-EQ10	16.90 in. (1.3%)	277.31	17.97 in. (1.38%)	218.18

Note: 1 in. = 2.54 cm, 1 kip = 4.448 kN

Figure 4-32 and 4-33 show the maximum drift ratio and the residual drift for both CIP and repairable frames under different ground motions. The maximum drift ratios for repairable nine-story frame were higher than those in CIP frame.

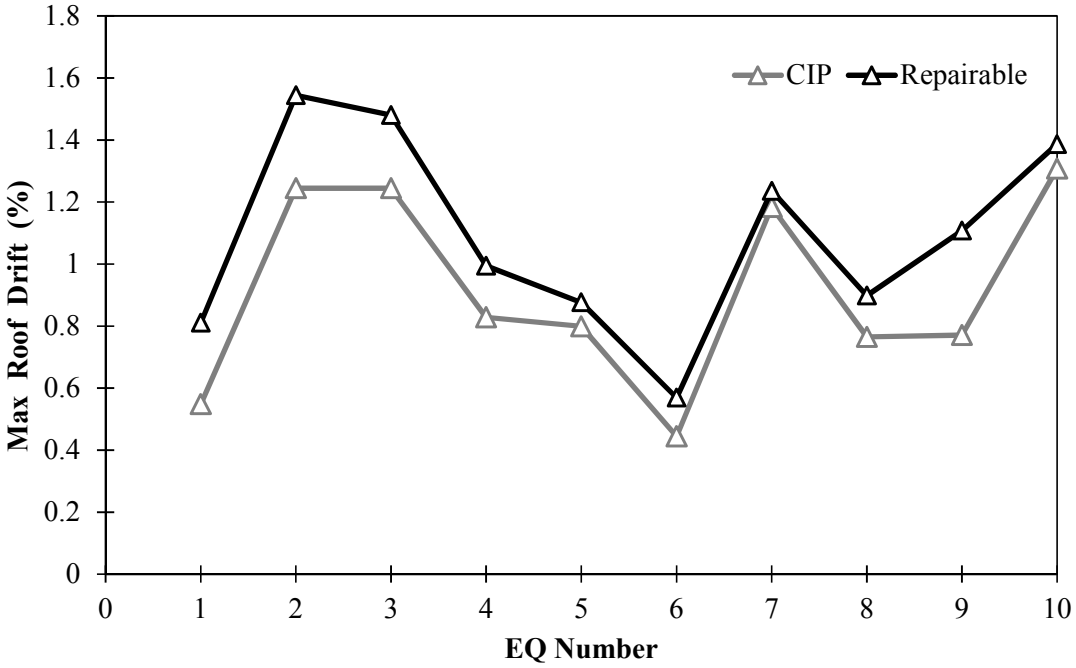

Figure 4-32. Maximum Drift Ratios of Nine-Story SMRF under Different Ground Motions

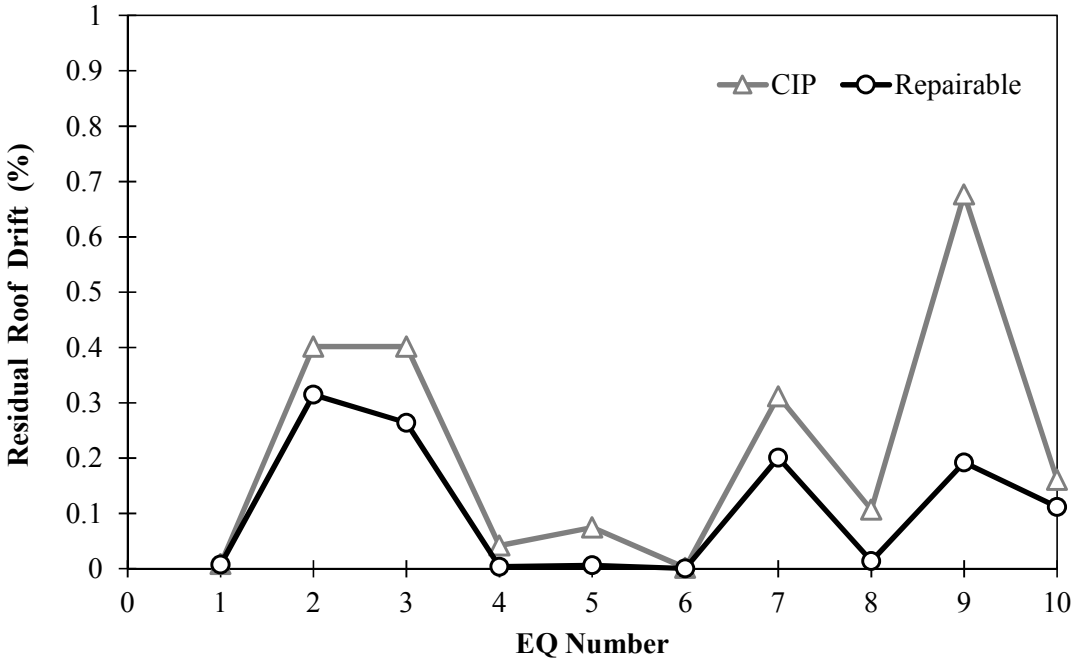

Figure 4-33. Residual Drift Ratios of Nine-Story SMRF under Different Ground Motions

The story drift demands for the nine-story CIP and repairable precast frames are shown in Fig. 4-34 for ten near-field ground motions. It can be seen that the repairable precast frame usually exhibit higher story drift demands than those in the CIP frame under the same ground motion. The story drift demands for the nine-story precast frame exceeded the ASCE limit for three strong ground motions indicating that this frame is insufficient for this case. Therefore, the lower initial stiffness for the nine-story precast frame must be addressed in the design and the precast building requires larger sections to increase the stiffness.

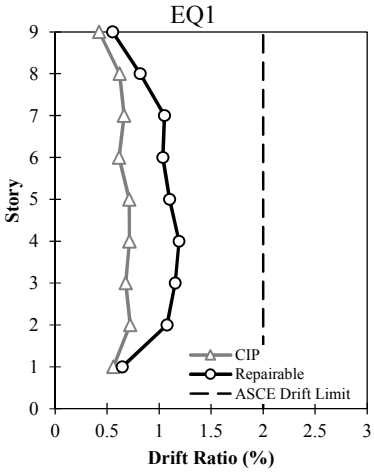

a) Story Drift Demands under EQ1

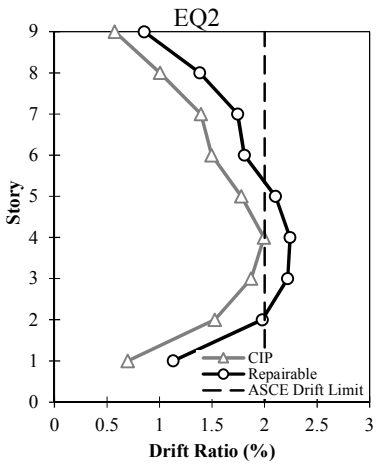

b) Story Drift Demands under EQ2

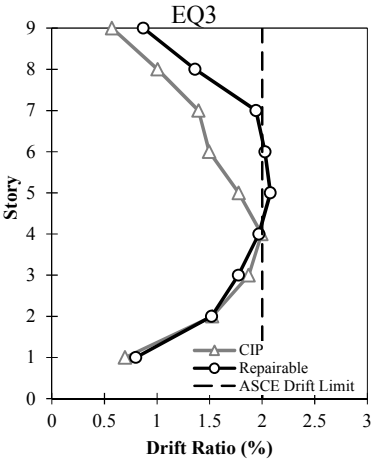

c) Story Drift Demands under EQ3

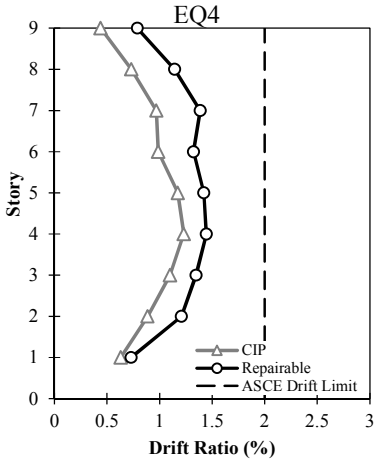

d) Story Drift Demands under EQ4

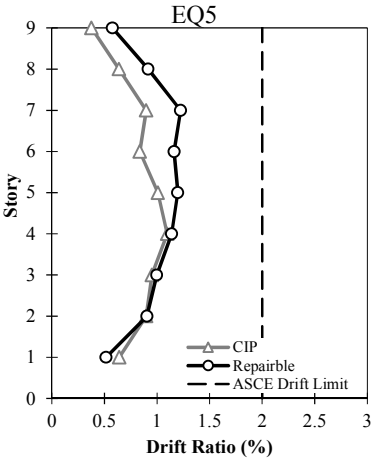

e) Story Drift Demands under EQ5

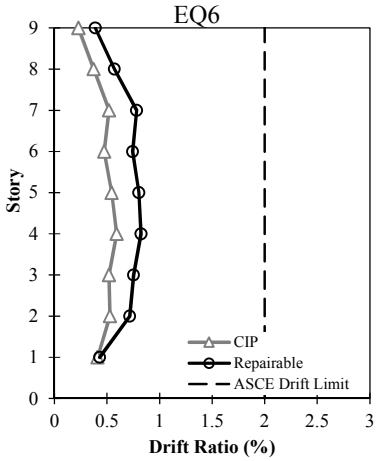

f) Story Drift Demands under EQ6

Figure 4-34. Roof Drift Ratios for Nine-Story SMRF under Different Earthquakes

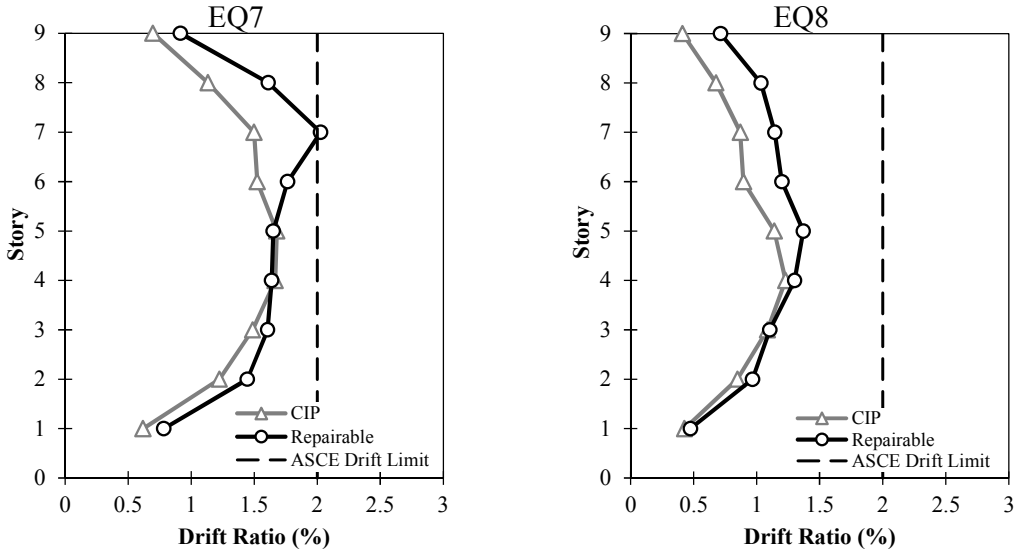

a) Story Drift Demands under EQ7

b) Story Drift Demands under EQ8

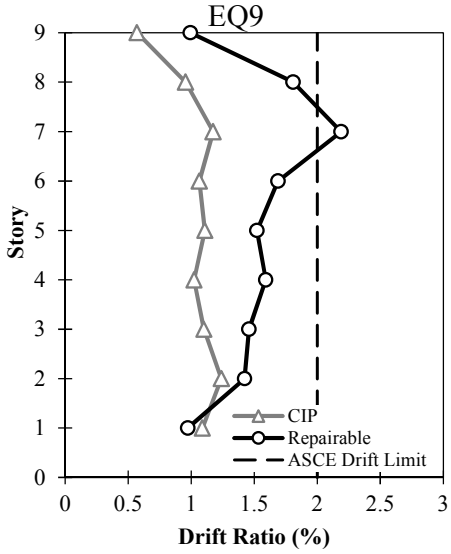

c) Story Drift Demands under EQ9

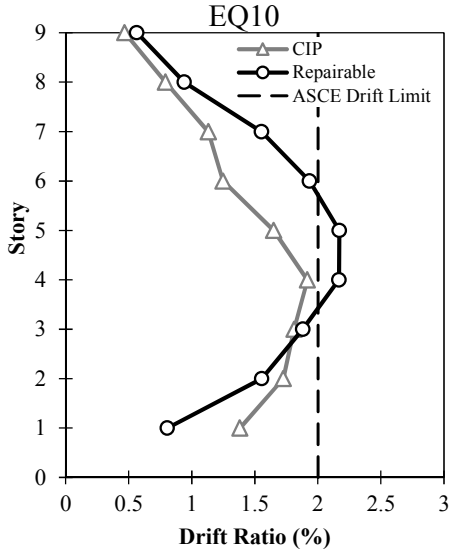

d) Story Drift Demands under EQ10

Figure 4-34. Roof Drift Ratios for Nine-Story SMRF under Different Earthquakes (Continued)

The effects of gap between the shear-pin and the steel socket on the precast frame performance was investigated through pushover analyses (Fig. 4.35). It was found that the gap has minimal effect on the frame performance when the floor system gravity loads were included in the analysis. Therefore, the lower initial stiffness of the precast frames

is mainly due to the geometry and mechanism of the new joint, and the gap effect is minimal.

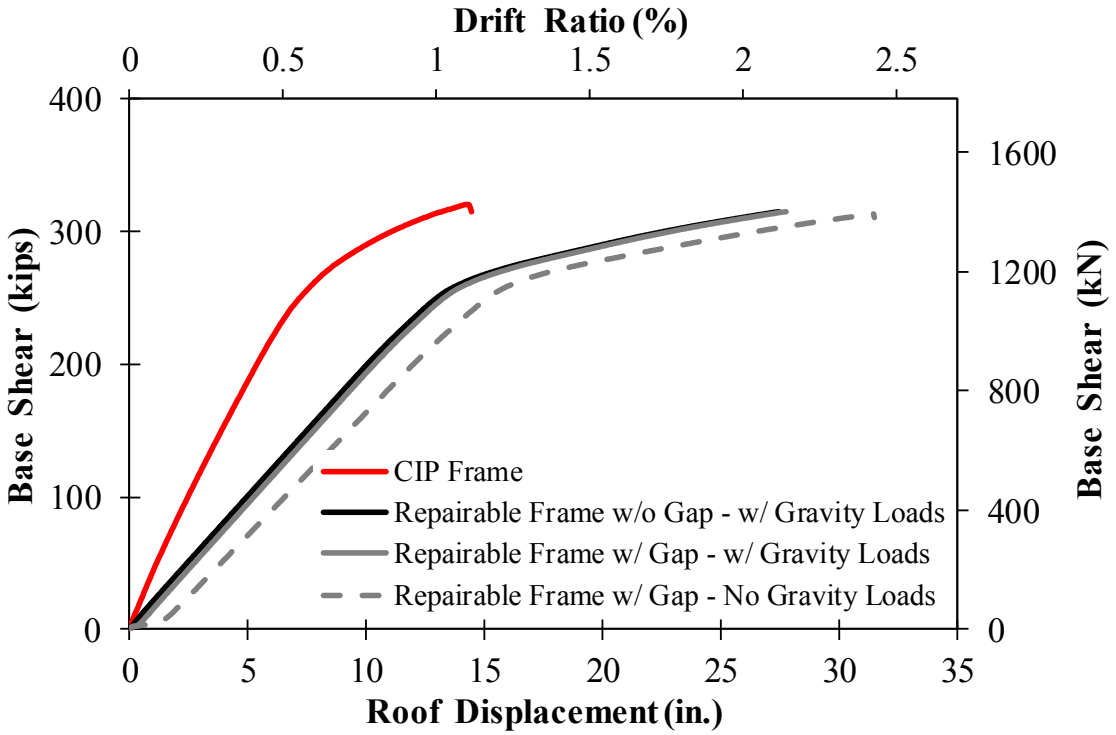

Figure 4-35. Effects of Shear Pin Vertical Gaps on Pushover Response of Nine-Story Frames

4.5 Summary and Conclusions

Pushover and dynamic analyzes were carried out to investigate the seismic performance of novel repairable precast buildings. First, modeling methods were proposed to capture the performance of all beam-column test specimens discussed in Ch. 3. The calculated and measured responses are compared to comment on the accuracy of the proposed modeling method. Then, the verified model was used to conduct the analytical study. Based on the analytical study, the following conclusions can be drawn:

- The new precast beam-column connections can increase the displacement capacity of precast buildings by a factor of three or more if BRR fuse with length of 0.75 of precast beam height were used.
- Longer BRR fuse lengths results in higher displacement capacities exceeding those of the corresponding conventional RC frames. The fuse length of 0.25 of the precast beam height is recommended
- Pushover analyses showed that the initial stiffness of the proposed precast buildings is 42% lower than that in CIP, on average.
- The repairable frames can withstand severe earthquakes with at least 30% reserved displacement capacity.
- The dynamic analysis showed that precast frames will lead to 21% increase in displacement (or story drift) demands on average. Nevertheless, the story drift demands for three- and six-story precast frames were always within the ASCE limit indicating that this frame is sufficient even without increasing the neck depth or the BRR sizes. However, Nine-story precast frame exhibits story drift demands higher than ASCE limit which requires the redesign of precast elements such as increasing the neck depth or the BRR sizes.

Overall, the proposed novel precast buildings are expected to exhibit significantly in higher displacement capacity over CIP buildings. However, large-scale experimental studies are needed to confirm these findings before field deployment.

4.6 References

1. OpenSees. (2016). “Open System for Earthquake Engineering Simulations,” Version 2.4.1, Berkeley, CA, Available online: http://opensees.berkeley.edu.
2. Al Hashib, A. (2017). “Effects of Mechanical Bar Splices on Seismic Performance of RC Buildings,” MSc thesis, South Dakota State University, Brookings, SD.
3. American Concrete Institute (ACI) Committee 318 (2014). “Building Code Requirements for Structural Concrete and Commentary,” ACI 318-14, ACI, Farmington Hills, MI.
4. ASCE Standard (2010). “Minimum Design Loads for Buildings and Other Structures,” American Society of Civil Engineers (ASCE), 1801 Alexander Bell Drive, Reston, Virginia 20191.
5. ASTM Standard A706/A706M-09b (2009). “Standard Specification for Low-Alloy Steel Deformed and Plain Bars for Concrete Reinforcement,” ASTM International, West Conshohocken, PA.
6. Mander, J., Priestley, M., and Park, R. (1988). "Observed stress-strain behavior of confined concrete," Journal of structural engineering, 114(8), 1827-1849.
7. Somerville, P., Smith, N. Punyamurthula, S. and Sun, J. (1997). “Development of ground motion time histories for phase 2 of the FEMA/SAC steel project.” *Rep. SAC/BD-97/04*, SAC Joint Venture, California.

Chapter 5: Repairable Reinforced Concrete Bridge Columns - Analytical Investigation

5.1 Introduction

Columns are usually the most important seismic-resistant element in bridges during severe earthquakes since the performance, ductility, and integrity of the bridge depend on the column performance. Bridge columns are currently designed to exhibit large displacement capacities through forming plastic hinges and damage of concrete and yielding of reinforcement. Connections between columns and their adjoining members are critical in accelerated bridge construction (ABC) in high seismic regions since they are subjected to large cyclic loads. A new bridge column detailing incorporating fully precast members and buckling restrained reinforcement (BRR) is proposed in this chapter in an attempt to develop a new generation of reinforced concrete (RC) bridge columns, which can be built quickly, exhibit better seismic performance compared to conventional RC columns, and can be repaired in a few hours after severe events with minimal cost and labor.

The seismic performance of the new detailing is investigated in this chapter through analytical studies. First, the proposed detailing is illustrated for a column-to-

footing connection. Second, modeling methods are discussed then the results of analytical studies including force-displacement relationship, failure mode, and displacement ductility are represented. Finally, a summary of findings is presented at the end of the chapter.

5.2 Research Objectives

Bridge columns dominate the performance of the entire bridge system during severe events. In addition, the design of connections between columns and other elements are important in ABC to ensure the integrity of the bridge structure. Novel columns are emerging to enhance the performance of bridges during seismic events and to improve safety and serviceability of bridges after the event.

The main objectives of this chapter are (1) to propose a fully precast novel bridge column detailing with improved seismic performance and quick repair scheme, and (2) to investigate the proposed bridge column performance through extensive parametric studies.

5.3 Conventional and Repairable RC Bridge Columns

Figure 5-1 illustrates the detail of a typical conventional and proposed novel column for a column-to-footing connection. Conventional reinforced concrete (RC) bridge columns (Fig. 5-1a) consist of core concrete, cover concrete, and longitudinal and transverse reinforcement. The ductility of a conventional column is through the use of confining (transverse) reinforcement and the strength of the column is provided by the core concrete strength and the amount and type of the longitudinal reinforcement.

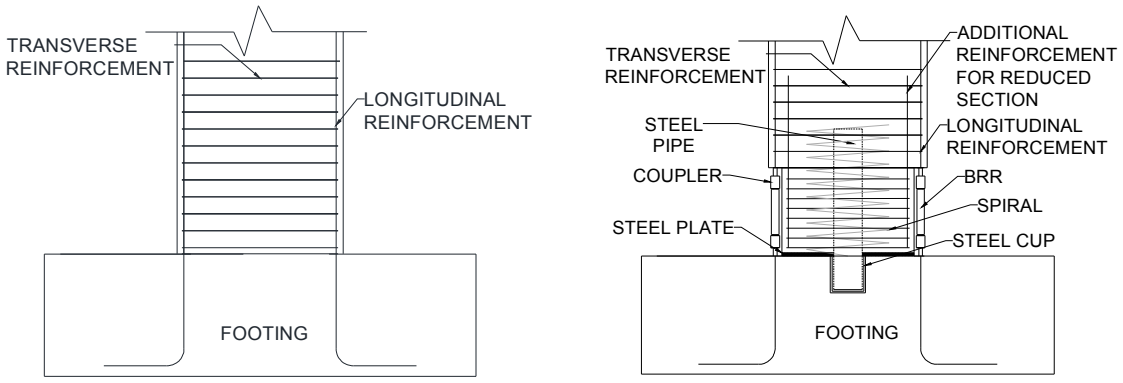

(a) Conventional Detailing (b) Repairable Detailing

Figure 5-1. Conventional versus Repairable RC Bridge Columns

Figure 5-1b shows the main components of the proposed detailing, which includes (1) a precast column with exposed longitudinal reinforcement, (2) a shear pin made of steel pipe to be inserted into a steel cup placed in the footing, (3) mechanical bar splices that can be detached, (4) external reinforcement to connect the precast column reinforcement to the footing dowels, and (5) a steel plate between the precast column and the footing to prevent damage during rocking. The proposed column is repairable since the exposed reinforcement can be replaced after a severe event if they are damaged.

The precast column is designed using current codes. A heavy-duty steel pipe embedded in the column is used as a pin to provide shear resistance. The steel pipe can be extended into the adjacent element (bent cap or footing) where a steel cup is embedded. A gap between the pipe and the cup will allow rotation of the pipe inside the cup. However, long pipes and minimal gaps result in dual-curvature of the pipe making the joint partially fixed. Performance of shear pipe-pin was experimentally and analytically investigated by Zaghi and Saiidi (2010). Shear pipe-pin design guidelines proposed in Zaghi and Saiidi were adopted in the present study. (Appendix C).

Any detachable mechanical bar splices (e.g. threaded and headed bar couplers) can be utilized to connect the column longitudinal reinforcement to that of the adjoining member. A steel plate can be utilized at the interface of the two concrete members to avoid damage of concrete during lateral movements.

Exposed reinforcing steel bars cannot resist compressive forces since they buckle at low compressive loads. Therefore, they should be restrained against buckling. Two different types of buckling restrained reinforcement (BRR) can be incorporated in the proposed repairable bridge columns: (1) BRR without any section reduction (Fig. 2a), which was discussed in detail in Chapter 2, and (2) dog-bone BRR (or BRRD) (e.g. energy dissipaters in Marriott et al., 2008). In BRR, the total length is allowed to yield while the reinforcement will mainly yield in the reduced sections of BRRD. Adjoining bars at the end of BRR can be oversized to prevent yielding and to limit the damage to only BRR. Note that buckling restrained reinforcement is to provide moment resistance in the joint by resisting both tensile and compressive loads.

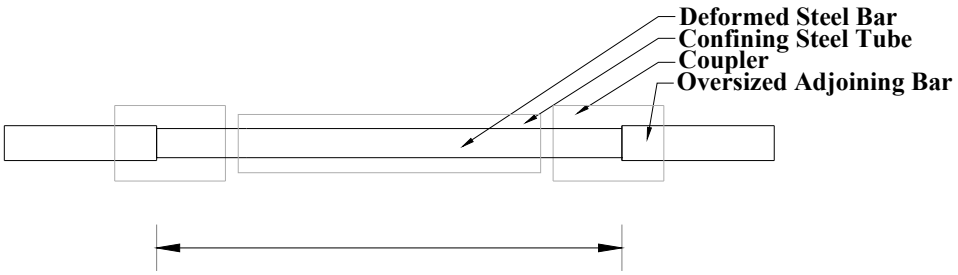

Yielding Region

(a) BRR without Section Reduction

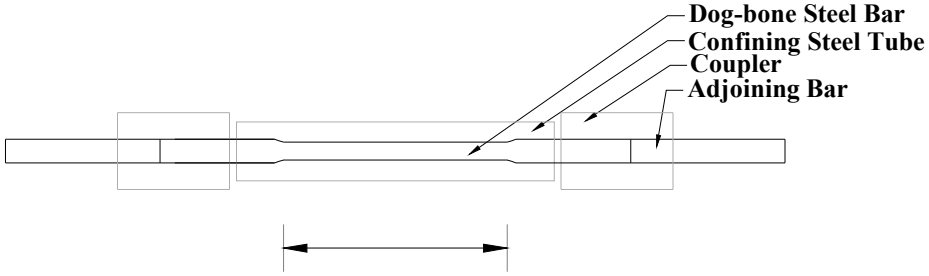

Yielding Region

(b) Dog-Bone BRR

Figure 5-2. Buckling Restrained Reinforcement

5.4 Modeling Methods for Conventional and Repairable RC Columns

5.4.1 Introduction

The seismic performance of conventional RC bridge columns and repairable precast columns is investigated through analytical studies. This section is dedicated to finite element modeling methods for the two column types. The modeling techniques, constitutive materials, and element types for conventional and repairable bridge columns are discussed herein.

5.4.2 Conventional RC Bridge Column Models

Conventional RC bridge columns were modelled based on the modeling method presented and verified in Tazarv and Saiidi (2014). OpenSees (2016) was used for the design and analysis of conventional RC columns. A three-dimensional fiber-section

model was utilized for RC columns in which the "forceBeamColumn" element with five integration points (distributed plasticity) was used to model the column element (Fig. 5-3).

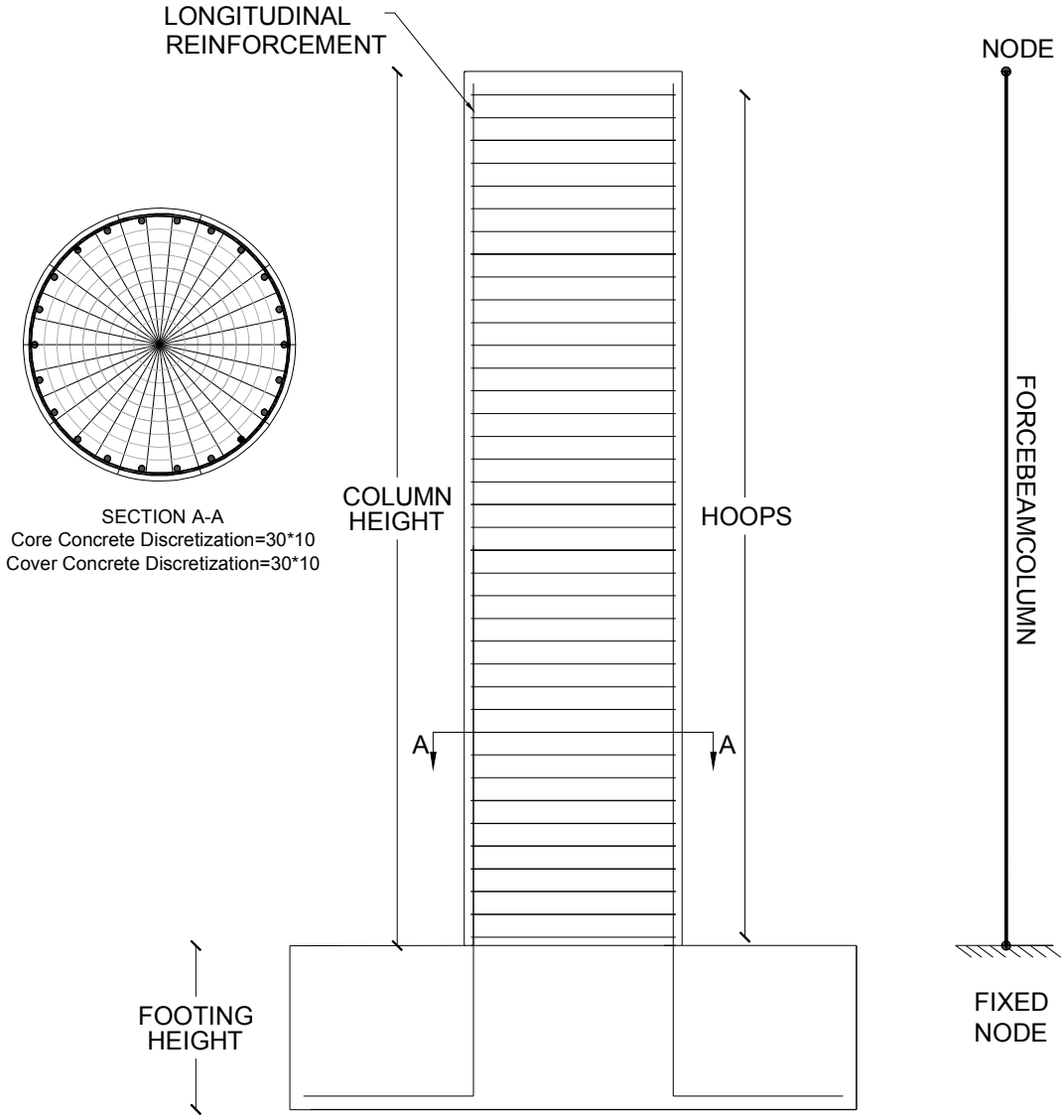

Figure 5-3. Conventional RC Bridge Column Analytical Model

The concrete cover and core were modeled using "Concrete01" and "Concrete04" material models, respectively. In OpenSees, "concrete01" is a uniaxial material model

with no tensile strength (Fig. 5-4a). However, "Concrete04" includes tensile properties of concrete and exhibit zero residual strength (Fig. 5-4b), which can be used to identify the failure mode due to core concrete failure. A uniaxial material, "ReinforcingSteel", was used to simulate the column reinforcement behavior (Fig. 5-5)

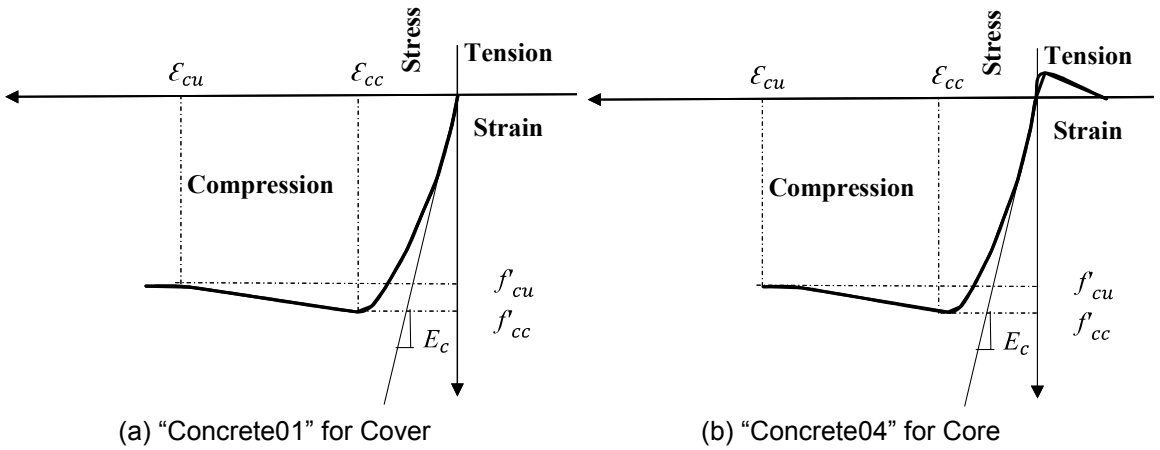

Figure 5-4. Concrete Material Models

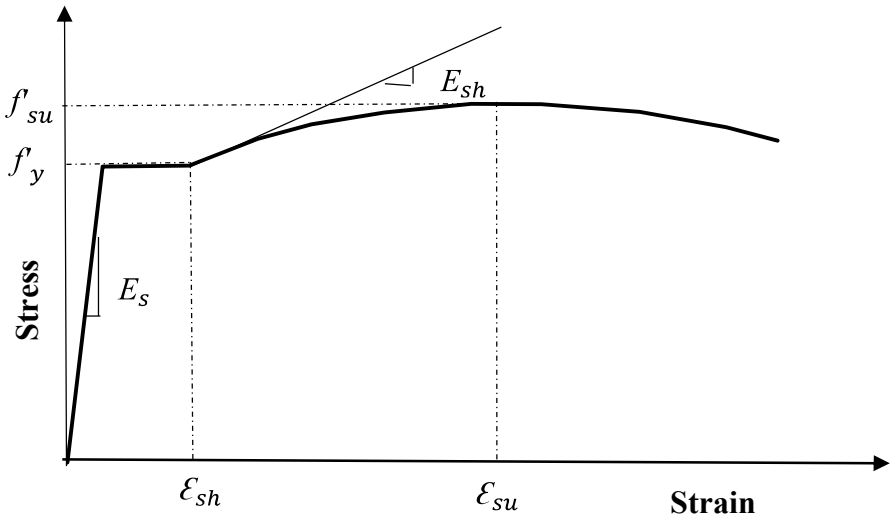

Figure 5-5. "ReinforcingSteel" Material Model

A fiber section with 30 circular and 10 radius segments was used to model both confined and unconfined concrete within the column section. Fibers for reinforcing steel

bars were also included (Fig. 5-3). Mander's model (Mander et al., 1988) was utilized to calculate properties of the confined concrete (Fig. 5-6). Since shear and torsional stiffness is not included in fiber-section models, the shear and torsional stiffness was aggregated to the section in the first integration point of the column model (at the base).

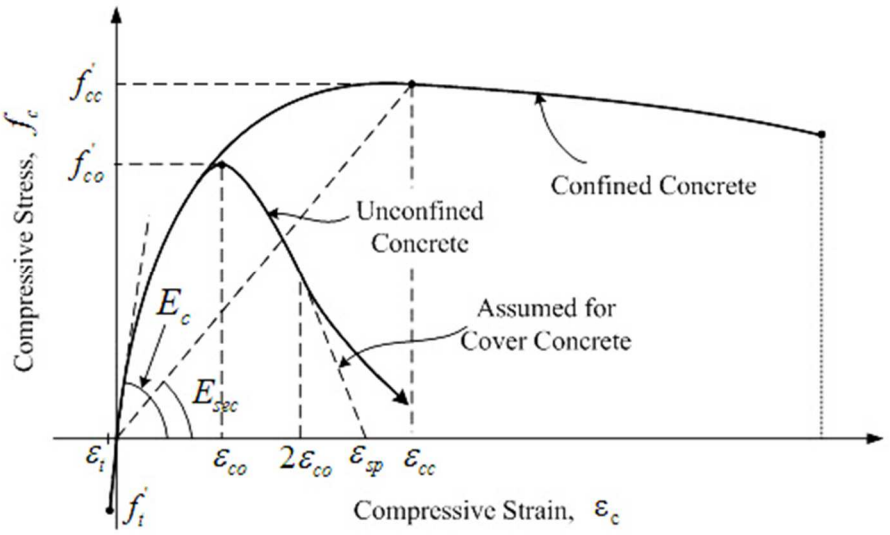

Figure 5-6. Stress-Strain Relationship for Confined Concrete (Mander et al., 1988)

5.4.3 Repairable RC Bridge Column Models

Similar to conventional RC columns, a three-dimensional fiber-section finite element model was developed to investigate the performance of repairable RC columns (Fig. 5-7). OpenSees was used for modeling. The column model can be generally divided into two submodules. The first module represents the portion of the column (reduced section, sec. B-B in Fig. 5-7) where yielding and damage of reinforcement are allowed. The second module is assumed to be damage-free (sec. A-A in Fig. 5-7). A "forceBeamColumn" element with five integration points was used to model the column elements in both modules. Since there was no longitudinal reinforcement inside the reduced column section to be extended into the footing (not developed), there was no

reinforcement fiber inside this section. The stiffness of the shear pin was aggregated with the section at the first integration point of module 1 (at the base). A uniaxial material model, "ReinforcingSteel", was used to simulate all reinforcing steel bars.

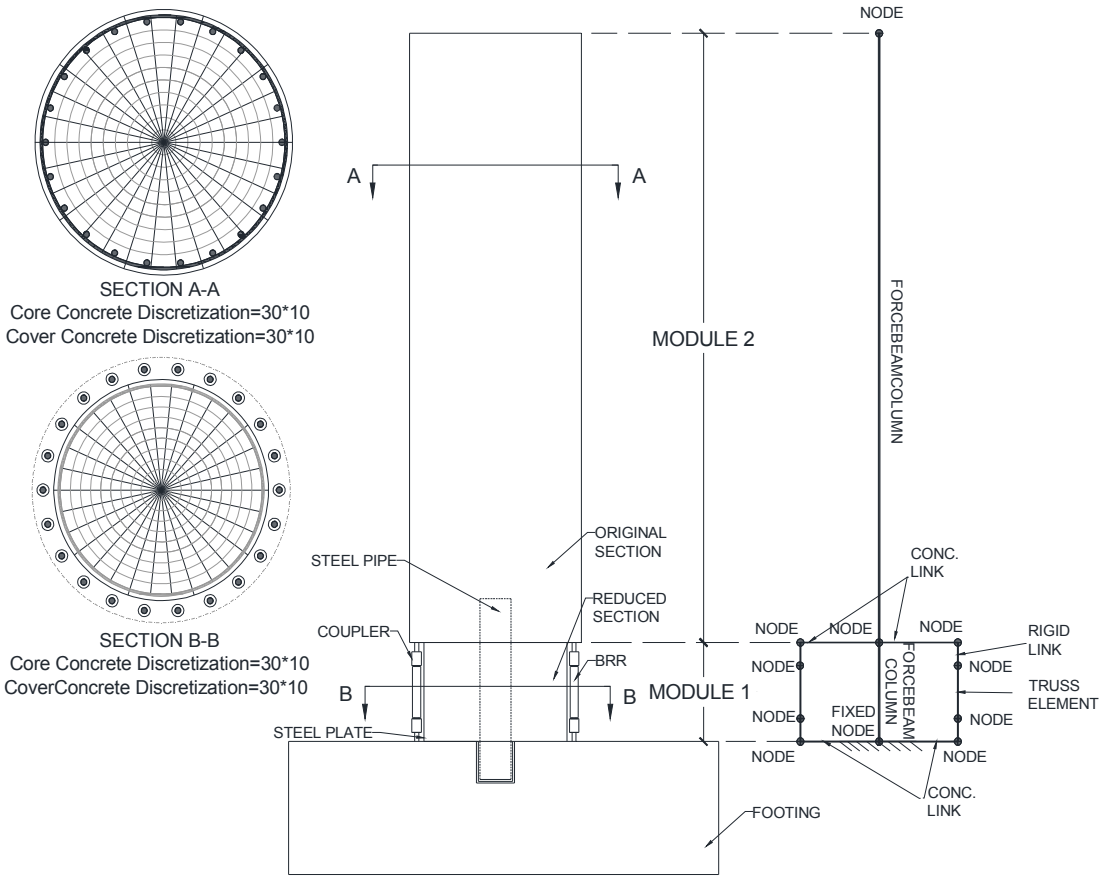

Figure 5-7. Repairable RC Bridge Column Analytical Model

The replaceable reinforcement (buckling restrained reinforcement) between the two couplers, which can be either BRR or BRRD, was modeled using truss elements with "ReinforcingSteel" material. The reinforcement portions between the BRRs and the adjacent concrete edge were modeled using rigid links to incorporate the rigidity of the couplers. Finally, the external reinforcement was connected to the column and the

footing using horizontal elastic elements with properties the same as those of the confined concrete.

Fiber sections with 30 circular and 10 radius segments were used to model the confined concrete within the two modules of the column element. The unconfined concrete was modeled with 10 circular and 10 radius segments. The axial load was applied to the top node of the column. The $P-\Delta$ effect was included in all analysis.

The lateral load was applied at the top node of the column using displacement control method. Each column model was pushed to failure. The column models were fixed against all translational and rotational degree of freedom at the base level.

5.4.3.1 Verification of Proposed Modeling Methods for Repairable RC Columns

No test data is available for the proposed repairable bridge columns. However, a few experimental studies investigated the cyclic behavior of hybrid rocking columns (defined as columns with unbonded post-tensioned tendons and internal or external reinforcement as energy dissipaters) with external energy dissipaters. Of which, column model HBD3 discussed in Marriott et al. (2009) was selected for further study. HBD3 had four unbonded post-tensioning tendons and four external energy dissipaters, two on each side of the square column. The column side dimension was 13.78 in. (350 mm) and the column height was 63 in. (1600 mm). The column was post-tensioned with a total force of 67.44 kips (300 kN). The column axial load due to dead load was 44.96 kips (200 kN) included in the posttensioning force. The test-day compressive strength of the column concrete was 7847 psi (54.1 MPa). The yield and the ultimate strength of the external energy dissipaters (BRRD) were 46.4 ksi (320 MPa) and 66.7 ksi (460 MPa), respectively.

An analytical model similar to that discussed in the previous section was developed in OpenSees to simulate the force-displacement relationship of the hybrid column. The only difference was an additional "corotational truss" element at the center of the column to represent the tendons. Table 5-1 shows the methods and parameters used in modelling the proposed robust model. Figure 5-8 shows the measured and calculated force-displacement relationships for HBD3. It can be seen that there is a good agreement between the measured and calculated response indicating robustness of the proposed modeling method.

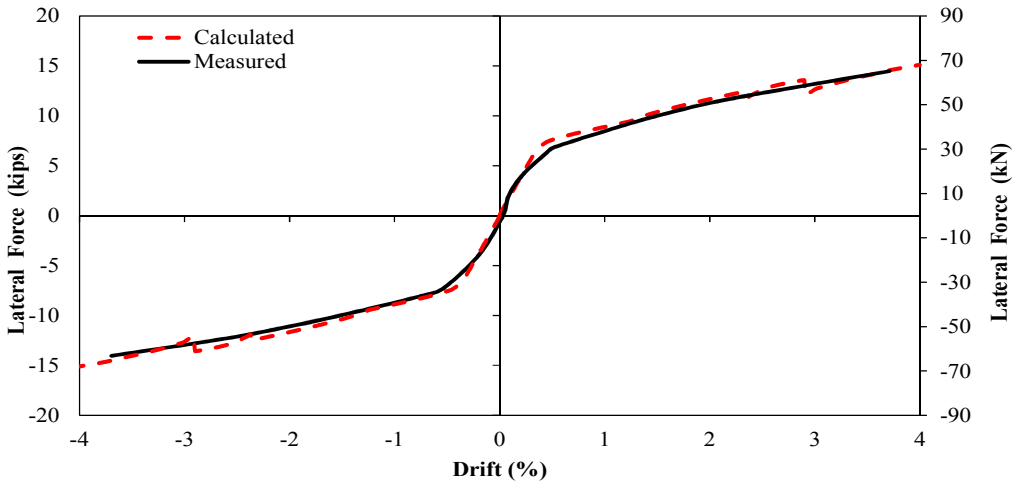

Figure 5-8. Measured and calculated force-displacement relationships for hybrid rocking column with external energy dissipaters

Table 5-1. Modelling Method for Proposed Robust Column

General Remarks	
Column Model: Element: *nonlinearBeamColumn* with 5 integration points for both modules Section: Fiber section Cover Concrete Discretization:10 radial by 10 circumference Core Concrete: Discretization:30 radial by 10 circumference $P-\Delta$ effect was included No bond slip effects	Energy Dissipaters Model: Element: *truss* Tendon Model: Element: *corotruss* with *InitStressMaterial* to represent the post tensioning force
Column Concrete Fibers	
Application: unconfined concrete Type: *Concrete01* F_{cc}= -7840 *psi* (54.1 *MPa)* $\mathcal{E}_{cc}$= -0.003 *in./in.* F_{cu}= 0.0 *psi* (0.0 *MPa)* $\mathcal{E}_{cc}$= -0.005 *in./in.*	Application: confined concrete based on Mander's model. Type: *Concrete01* F_{cc}= -10480 *psi* (72.2 *MPa)* $\mathcal{E}_{cc}$= -0.0086 *in./in.* F_{cu}= -9315 *psi* (64.2 *MPa)* $\mathcal{E}_{cc}$= -0.022 *in./in.*
Column Steel/Energy Dissipaters/tendons Fibers	
Application: Longitudinal reinforcement and dissipaters based on mild steel properties in Marriott Type: *ReinforcingSteel* F_y=46.4 *ksi* (320 *MPa)* F_{su}=66.7 *ksi* (460 *MPa)* E_s=27557 *ksi* (190000 *MPa)* E_{sh}=0.043 E_s $\mathcal{E}_{sh}$=-0.026 *in./in.* $\mathcal{E}_{su}$=-0.2 *in./in.*	Application: Post tensioned reinforcement/tendons Type: *Steel01* F_{py}=226.2 *ksi* (1560 *MPa)* F_{pu}=268.3 *ksi* (1850 *MPa)* E_{ps}=28587 *ksi* (197100 *MPa)*

5.5 Parametric Study

An extensive parametric study was conducted to investigate the seismic performance of conventional and repairable RC bridge columns.

A total of 27 RC bridge columns were designed according to the AASHTO Guide Specifications for LRFD Seismic Bridge Design (2015) with three key variables: the aspect ratio (4, 6, and 8), the axial load applied to the column (5%, 10%, and 15% of the product of the column sectional area and the column concrete strength, or the axial load index), and the displacement ductility capacity (3, 5, and 7).

The displacement ductility capacity is defined as the ratio of the column tip displacement to the effective yield displacement according to AASHTO SGS (2015).

The analytical plastic hinge length according to the AASHTO SGS (2015) is:

$$L_P = 0.08L + 0.15F_{ye}d_{bl} > 0.3\,F_{ye}\,d_{bl} \quad (5\text{-}1)$$

where

L_p = the equivalent length of column over which the plastic curvature is assumed constant for estimating the plastic rotation.

L = length of column from point of maximum moment to the point of moment contra-flexure (in.).

f_{ye} = expected yield strength of longitudinal column reinforcing steel bars (ksi)

d_{bl} = nominal diameter of longitudinal column reinforcing steel bars (in.)

The displacement capacity is defined as a displacement where (1) the column core concrete fails, (2) the column longitudinal reinforcement fractures, or (3) the column lateral load carrying resistance drops by 15% with respect to the peak lateral load. The drift ratio is defined as the column lateral displacement to the column height.

5.5.1 Conventional RC Columns

Twenty-seven conventional RC bridge columns were included in the parametric study (Table 5-2). Eighteen of which with aspect ratios of 4 and 8 were previously designed by Tazarv and Saiidi (2014), and nine columns with an aspect ratio 6 were designed in the present study. Different transverse reinforcing steel bars were utilized to achieve target displacement ductility capacity of 3, 5, or 7. The diameter of all the

columns was 48 in., to minimize the variations. ASTM A706 Grade 60 reinforcing steel bars were assumed for both longitudinal and transverse reinforcement. The compressive strength of concrete was 5000 psi (34.47 MPa) and the concrete cover was 2 in.

Table 5-2. Properties of Conventional Bridge Column Models

Column I.D.	Aspect Ratio	Axial Load Index (%)	Long. Reinf.	Trans. Reinf. (hoops)	Effective Yield Disp. (in.)	Disp. Ductility Capacity
RC-AR4-ALI5-D3	4	5	22-No. 9	No. 3 at 12 in.	1.01	3.02
RC-AR4-ALI5-D5			22-No. 9	No. 4 at 4 in.	1.11	4.95
RC-AR4-ALI5-D7			22-No. 9	No. 6 at 4 in.	1.17	7.05
RC-AR4-ALI10-D3		10	22-No. 9	No. 4 at 8 in.	0.98	2.92
RC-AR4-ALI10-D5			22-No. 9	No. 5 at 6 in.	1.02	4.98
RC-AR4-ALI10-D7			22-No. 9	No. 7 at 3.5 in.	1.07	6.93
RC-AR4-ALI15-D3		15	22-No. 9	No. 5 at 7 in.	0.96	3
RC-AR4-ALI15-D5			22-No. 9	No. 7 at 5.5 in.	1	5.04
RC-AR4-ALI15-D7			22-No. 9	No. 8 at 3 in.	1.04	7.11
RC-AR6-ALI5-D3	6	5	22-No. 9	No. 3 at 10 in.	2.25	3.16
RC-AR6-ALI5-D5			22-No. 9	No. 4 at 4 in.	2.39	5.12
RC-AR6-ALI5-D7			22-No. 9	No. 5 at 3.5 in.	2.42	7.33
RC-AR6-ALI10-D3		10	22-No. 9	No. 4 at 8 in.	2.02	30.7
RC-AR6-ALI10-D5			22-No. 9	No. 5 at 4 in.	2.1	5
RC-AR6-ALI10-D7			22-No. 9	No. 7 at 4 in.	2.13	7.19
RC-AR6-ALI15-D3		15	22-No. 9	No. 5 at 7 in.	1.98	3.05
RC-AR6-ALI15-D5			22-No. 9	No. 7 at 5 in.	2.04	4.93
RC-AR6-ALI15-D7			22-No. 9	No. 8 at 4 in.	2.02	7.08
RC-AR8-ALI5-D3	8	5	22-No. 9	No. 3 at 12 in.	3.88	3.03
RC-AR8-ALI5-D5			22-No. 9	No. 4 at 4.5 in.	3.96	5.1
RC-AR8-ALI5-D7			22-No. 9	No. 6 at 4 in.	4.03	7.12
RC-AR8-ALI10-D3		10	22-No. 9	No. 4 at 8 in.	3.57	3.11
RC-AR8-ALI10-D5			22-No. 9	No. 4 at 5 in.	3.53	5.15
RC-AR8-ALI10-D7			36-No. 11	No. 7 at 3 in.	5	7.02
RC-AR8-ALI15-D3		15	22-No. 9	No. 5 at 7 in.	3.46	3.13
RC-AR8-ALI15-D5			36-No. 9	No. 7 at 3 in.	4.15	5.02
RC-AR8-ALI15-D7			22-No. 9	No. 8 at 3 in.	5.18	6.04

Example of Specimen Identification: RC-AR4-ALI5-D3
RC: Reinforced Concrete Element,
AR4: Aspect Ratio = 4,
ALI5: Axial Load Index = 5%,
D5: Target Displacement Ductility Capacity = 5.

The name of each model consists of four components. The first component generally refers to the type of the column, which is reinforced concrete. The second component indicates the aspect ratio. The axial load index is identified in the third component. Finally, the number following the letter "*D"* indicates to the displacement ductility capacity of the column.

5.5.2 Repairable RC Columns

The 27 RC bridge columns discussed in the previous section were modified based on the proposed detailing for the repairable bridge columns. Figures 5-9 to 5-11 show the details of a typical repairable RC bridge column. Note that only the construction detailing was modified and the geometry, reinforcement, and material properties of the two column types were the same. In addition to the three main variables discussed for the RC columns, the yielding length of BRRs was varied with respect to the analytical plastic hinge length ($0.25L_p$, $0.5L_p$, $0.75L_p$, and $1.0L_p$). The plastic hinge length for the RC columns with the aspect ratios 4, 6, and 8 were 26.9 in. (86.2 cm), 34.5 in. (87.7 cm), and 42.2 in. (100.7 cm), respectively.

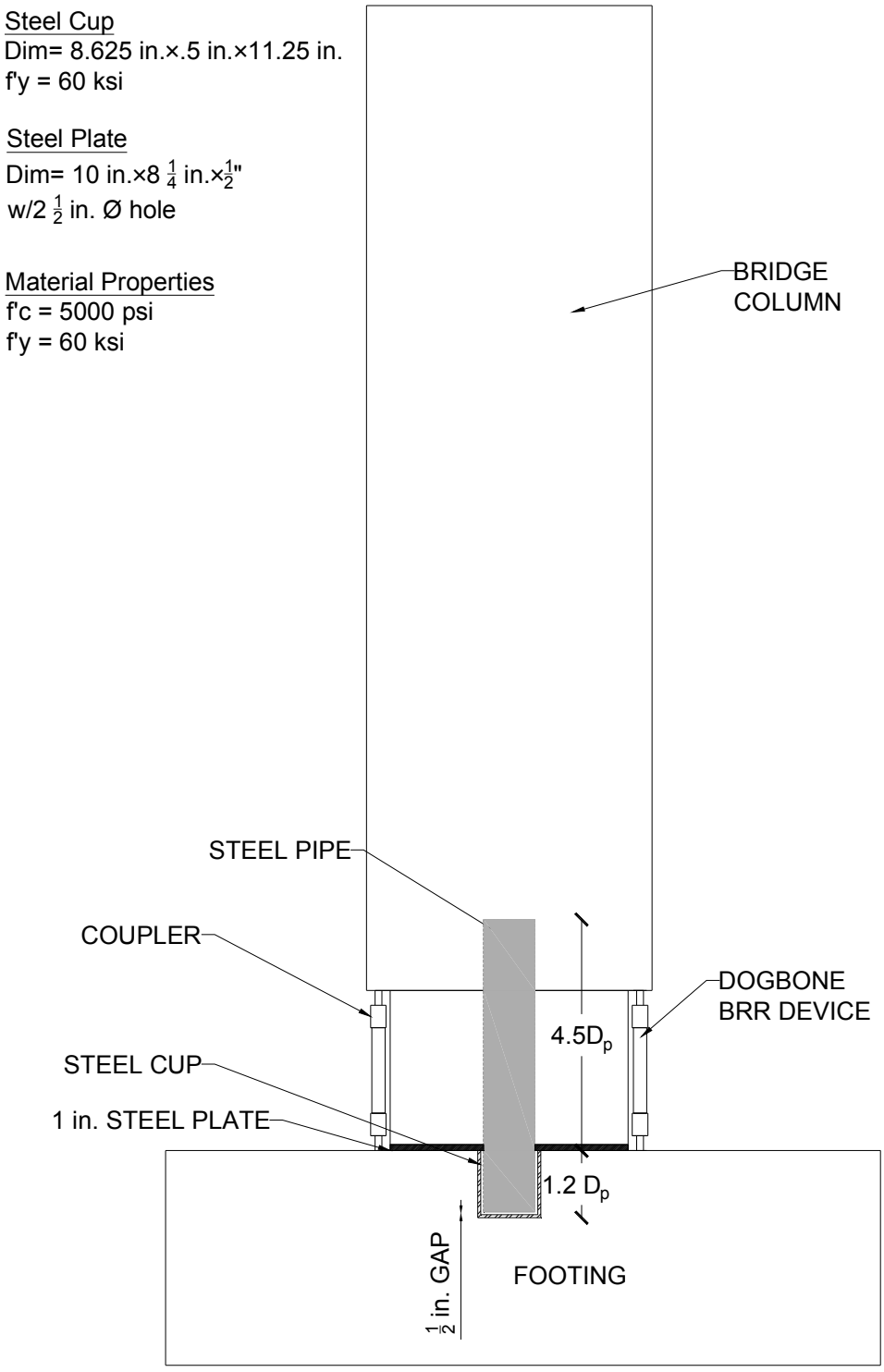

Figure 5-9. Repairable RC Bridge Column Details

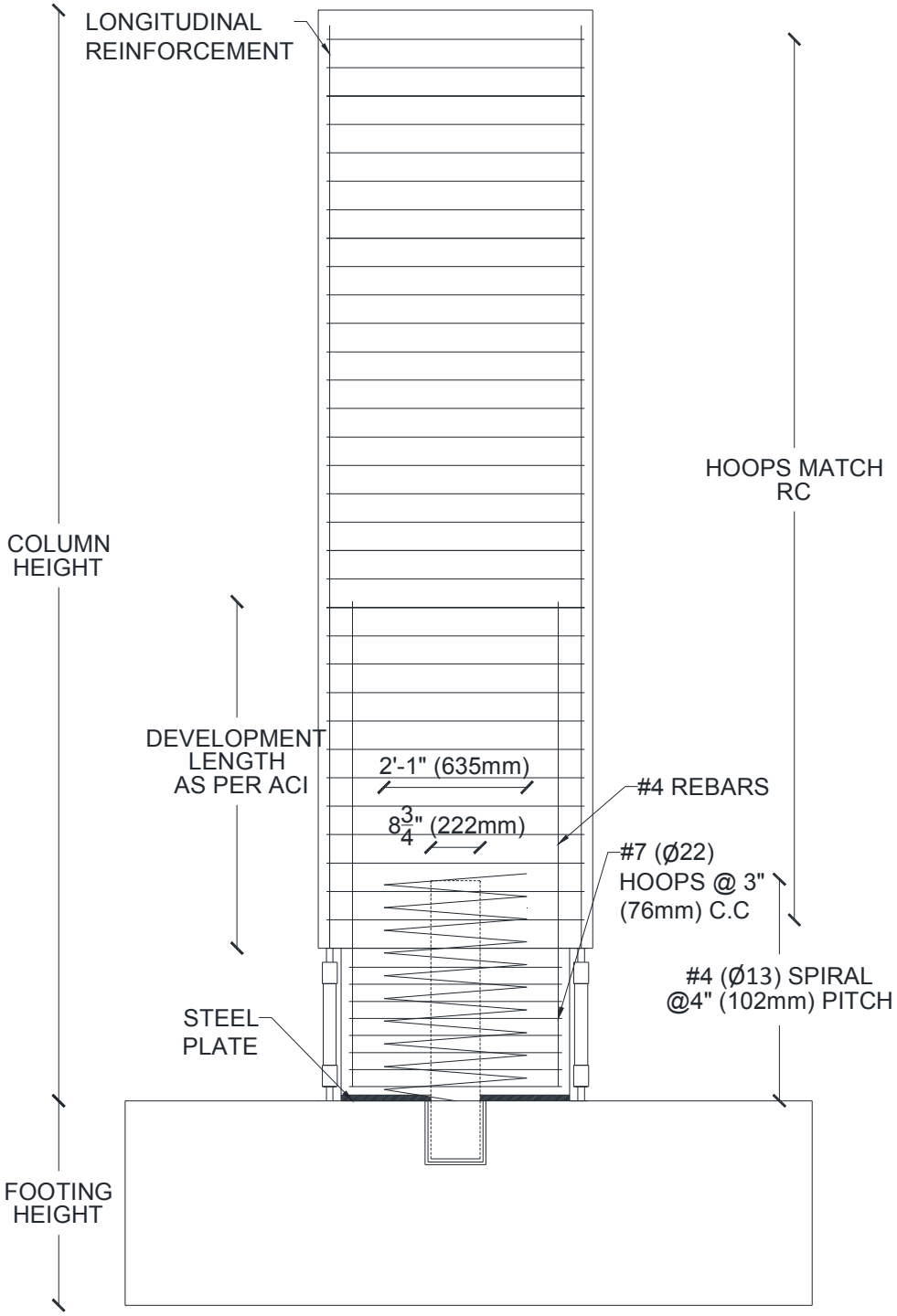

Figure 5-10. Repairable RC Bridge Column Reinforcement

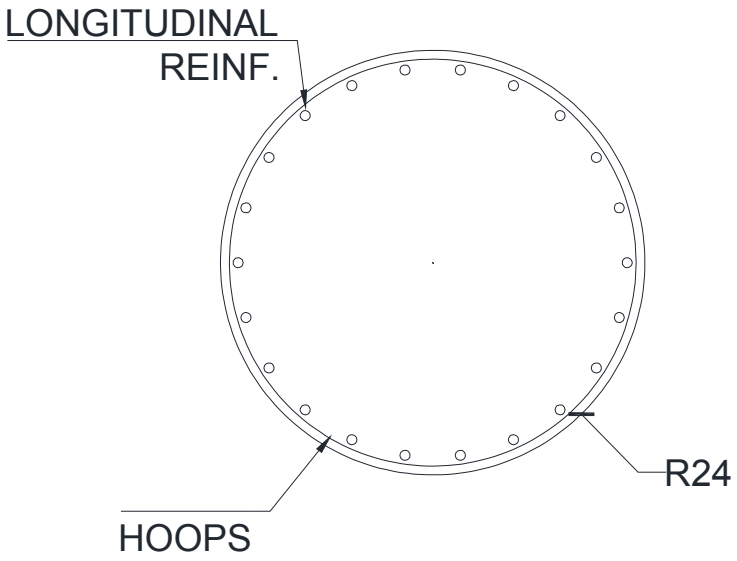

(a) Full Column Section

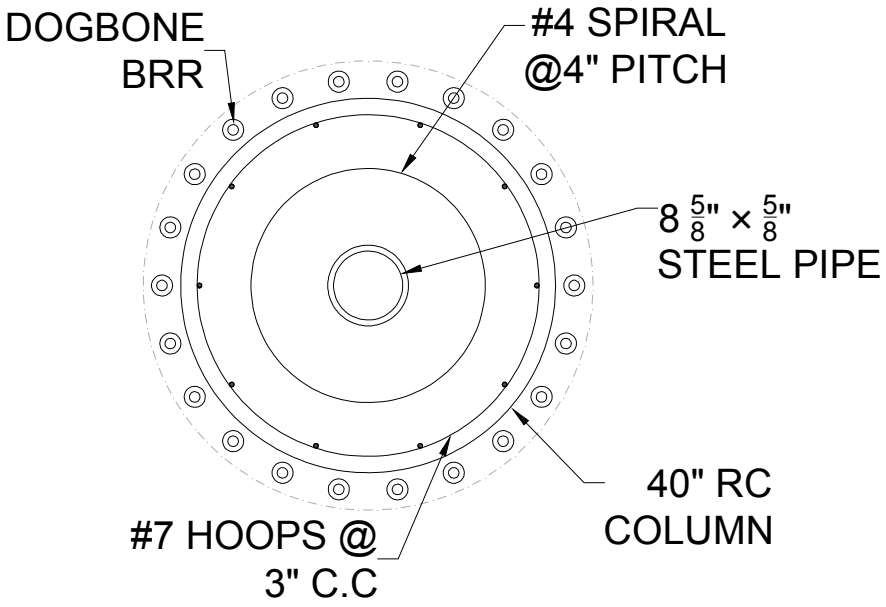

(b) Reduced Column Section

Figure 5-11. Different Cross Sections of Repairable RC Bridge Columns

In the repairable RC bridge columns, the column diameter at the column base was reduced from 48 in. (121.9 cm) to 40 in. (100.1 cm) to align BRRs with the column longitudinal reinforcement. Minimal longitudinal reinforcement was provided in the reduced column section to avoid compression failure. Transverse reinforcement with a

spacing of 3 in. (resulting in a volumetric transverse steel ratio of 2%) was provided in the reduced section to increase the confinement and to eliminate any concrete damage in compression. A steel plate was placed between the column and the footing to avoid damage during rocking.

In general, two techniques can be used to localize the yielding to the BRR and to avoid yielding of the column longitudinal reinforcement at the ends of a BRR: (1) utilize oversized reinforcement at the ends of BRRs, and (2) use dog-bone BRR (BRRD). In the former case, the yielding length of BRR is the total length. For the latter case, the yielding length is the length of the reduced section. The area of each BRR was the same as that for the longitudinal reinforcement in the corresponding conventional RC bridge column.

A steel pipe was incorporated at the column-to-footing interface to transfer the shear forces. The design of the shear pin was based on the guidelines proposed by Zaghi and Saiidi (2010). It was found that a steel tube with an area of 15 in^2 (96.8 cm^2) provides a shear capacity of 271.5 kips (1207.7 kN), which is sufficient for all repairable RC bridge column models. No. 4 spirals with a spacing of 4 in. was placed around the steel pipe to improve the confinement.

5.6 Results of Parametric Study

Twenty-seven conventional RC bridge columns were designed as discussed in the previous sections. The RC column detailing was modified to accommodate the new repairable detailing. The analytical results obtained from the pushover analysis for the 27 conventional and repairable column models are presented herein. The force-

displacement relationship, the drift capacity, the failure mode, and the displacement ductility capacity are presented in detail for each model.

5.6.1 Force-Drift Relationship

Pushover analysis was carried out for all bridge column models to investigate the seismic performance of the repairable bridge columns. Table 5-3 presents a summary of the analysis results. The calculated lateral force-drift relationships for the conventional and repairable precast columns are shown in Fig. 5-12 to 5-38.

Table 5-3. Summary of Analysis Results for Repairable RC Bridge Columns

Column I.D	Drift Ratio Capacity, % (Displacement Ductility Capacity) BRR Yielding Length (BRR-YL)				Mode of Failure	
	$0.25L_p$	$0.5L_p$	$0.75L_p$	$1.0L_p$	Conventional	Repairable
RC-AR4-ALI5-D3	2.29 (6.02)	4.09 (9.51)	5.88 (12.51)	7.69 (15.38)	Steel Fracture.	BRR Fracture.
RC-AR4-ALI5-D5	2.3 (5.92)	4.1 (9.32)	5.9 (12.29)	7.7 (15.1)	Steel Fracture.	BRR Fracture.
RC-AR4-ALI5-D7	2.32 (5.66)	4.12 (9.15)	5.9 (12.31)	7.7 (14.81)	Steel Fracture.	BRR Fracture.
RC-AR4-ALI10-D3	2.37 (6.58)	4.24 (10.6)	6.1 (14.2)	7.94 17.28)	Steel Fracture.	BRR Fracture.
RC-AR4-ALI10-D5	2.39 (6.29)	4.25 (10.37)	6.12 (13.61)	7.95 (16.93)	Steel Fracture.	BRR Fracture.
RC-AR4-ALI10-D7	2.41 (6.18)	4.27 (9.93)	6.13 (13.63)	7.95 (16.57)	Steel Fracture.	BRR Fracture.
RC-AR4-ALI15-D3	2.49 (6.92)	4.47 (11.19)	6.16 (14.34)	5.72 (12.18)	Steel Fracture.	BRR Fracture.
RC-AR4-ALI15-D5	2.52 (6.63)	4.49 (10.7)	6.17 (14.04)	5.73 (11.95)	Steel Fracture.	BRR Fracture.
RC-AR4-ALI15-D7	2.54 (6.35)	4.5 (10.47)	6.19 (13.47)	5.74 (11.73)	Steel Fracture.	BRR Fracture.
RC-AR6-ALI5-D3	3.1 (5.34)	5.4 (8.85)	7.71 (12.24)	8.55 (12.96)	Core Failure	BRR Fracture.
RC-AR6-ALI5-D5	3.13 (5. 21)	5.43 (8.62)	7.73 (12.08)	8.57 (12.79)	Core Failure	BRR Fracture.
RC-AR6-ALI5-D7	3.14 (5.14)	5.44 (8.37)	7.75 (11.92)	8.57 (12.6)	Core Failure	BRR Fracture.
RC-AR6-ALI10-D3	3.2 (6.15)	5.58 (10.34)	5.55 (9.57)	4.81 (7.76)	Core Failure	BRR Fracture.
RC-AR6-ALI10-D5	3.24 (5.89)	5.61 (9.84)	5.57 (9.29)	4.82 (7.53)	Core Failure	BRR Fracture.
RC-AR6-ALI10-D7	3.26 (5.82)	5.64 (9.73)	5.58 (9.15)	4.83 (7.43)	15% drop	BRR Fracture.
RC-AR6-ALI15-D3	3.36 (6.72)	4.48 (8.46)	3.93 (6.78)	3.46 (5.41)	Core Failure	15% drop
RC-AR6-ALI15-D5	3.4 (6.42)	4.5 (8.04)	3.95 (6.59)	3.48 (5.27)	Core Failure	15% drop
RC-AR6-ALI15-D7	3.43 (6.24)	4.52 (7.8)	3.97 (6.41)	3.49 (5.21)	15% drop	15% drop
RC-AR8-ALI5-D3	3.91 (5.21)	6.71 (8.94)	6.74 (8.75)	5.82 (7.1)	15% drop	BRR Fracture.
RC-AR8-ALI5-D5	5.38 (5.06)	6.75 (8.65)	6.76 (8.56)	5.83 (6.94)	Core Failure	15%drop
RC-AR8-ALI5-D7	5.44 (4.97)	6.78 (8.47)	6.78 (8.37)	5.85 (6.88)	15% drop	15% drop
RC-AR8-ALI10-D3	4.03 (6.2)	4.46 (6.66)	3.68 (5.18)	3.33 (4.21)	15% drop	15% drop
RC-AR8-ALI10-D5	4.08 (6)	4.49 (6.41)	3.71 (4.95)	3.35 (4.13)	15% drop	15% drop
RC-AR8-ALI10-D7	4.45 (4.54)	7.55 (7.78)	9.18 (9.56)	7.91 (7.98)	15% drop	15% drop
RC-AR8-ALI15-D3	3.78 (6.2)	3.24 (4.91)	2.83 (3.89)	2.72 (3.4)	15% drop	15% drop
RC-AR8-ALI15-D5	4.57 (5.37)	5 (5.88)	4.06 (4.51)	3.57 (3.71)	15% drop	15% drop
RC-AR8-ALI15-D7	5.71 (4.83)	8.64 (7.71)	8.2 (7.38)	6.8 (6)	15% drop	15% drop

Example of Specimen Identification: RC-AR4-ALI5-D3
RC: Reinforced Concrete Element,
AR4: Aspect Ratio = 4,
ALI5: Axial Load Index = 5%,
D5: Target Displacement Ductility Capacity = 5.

It can be seen that the pushover relationships vary significantly for different yielding lengths of the buckling restrained reinforcement (BRR-YL). Longer yielding lengths for BRR usually resulted in higher displacement capacities exceeding those of the corresponding conventional RC columns.

It was found that the precast columns with the proposed detailing can exhibit four times or higher displacement capacities than those seen in the corresponding conventional RC columns. This is especially true for columns with lower aspect ratios and lower axial load indexes. For instance, a precast column with an aspect ratio of 4 and an axial load index of 5% exhibited a displacement ductility capacity of 15.4 when the yielding length of the BRR was equal to the analytical plastic hinge length (Fig. 5-12). The displacement capacity for the proposed bridge column was 5.1 times higher than that for the corresponding conventional RC bridge column. Furthermore, columns with longer BRRs and higher aspect ratios exhibited lower lateral load carrying capacities mainly due to significant $P-\Delta$ effect. Overall, the lateral load capacity of the proposed repairable columns is expected to be lower than that in corresponding conventional columns due to the reduction in the column section close to the interface. For example, the column with an aspect ratio of 8, an axial load index of 15%, and the BRR yielding length equal to the analytical plastic hinge length (Fig. 5-36) exhibited 19% lower lateral load capacity compared to that of the corresponding conventional RC column (RC-AR8-ALI15-D3).

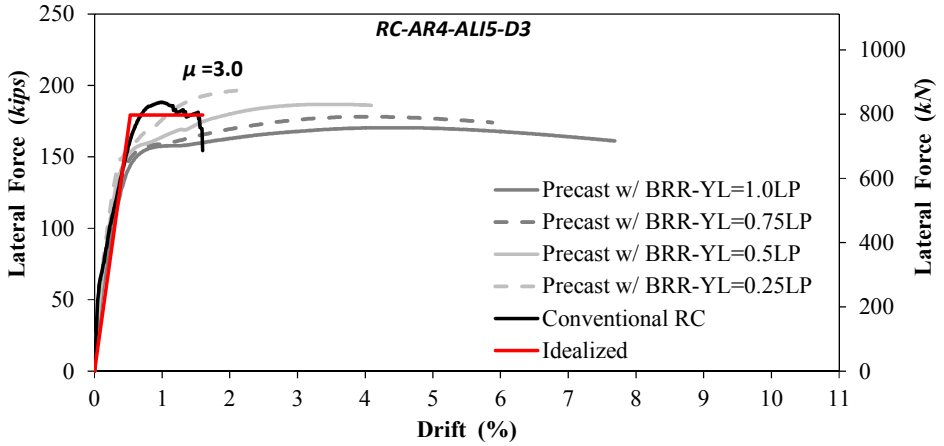

Figure 5-12. Pushover Analysis of RC-AR4-ALI5-D3 and Corresponding Repairable Precast Columns

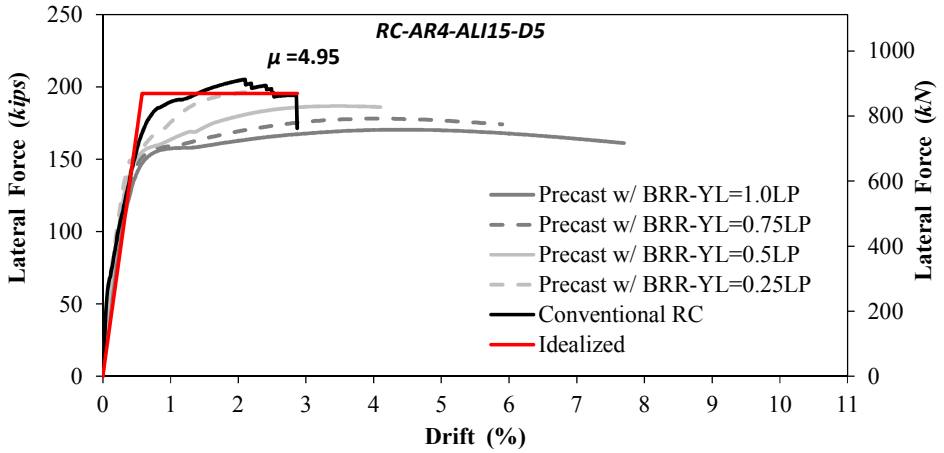

Figure 5-13. Pushover Analysis of RC-AR4-ALI5-D5 and Corresponding Repairable Precast Columns

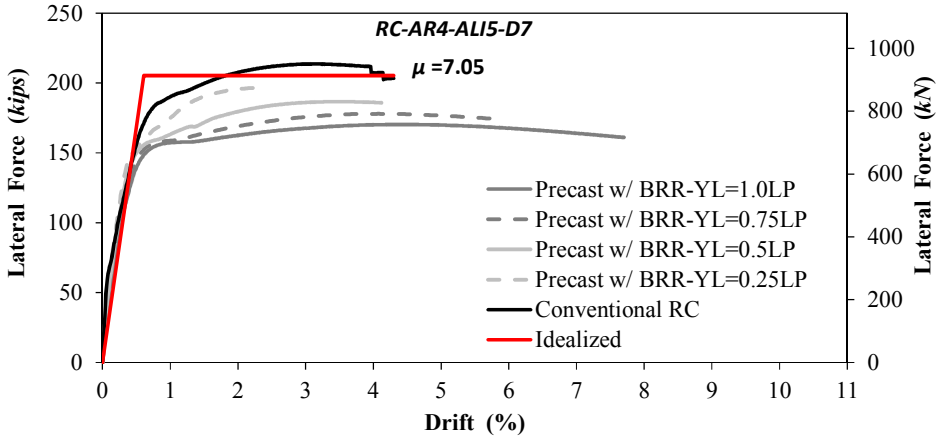

Figure 5-14. Pushover Analysis of RC-AR4-ALI5-D7 and Corresponding Repairable Precast Columns

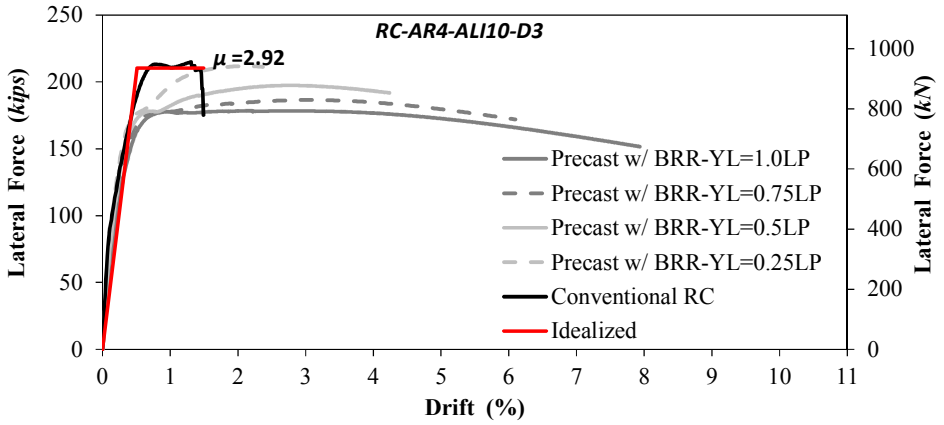

Figure 5-15. Pushover Analysis of RC-AR4-ALI10-D3 and Corresponding Repairable Precast Columns

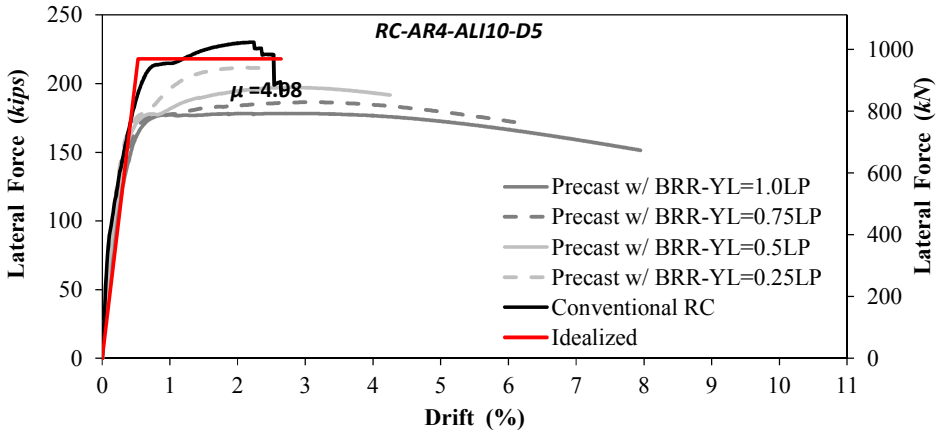

Figure 5-16. Pushover Analysis of RC-AR4-ALI10-D5 and Corresponding Repairable Precast Columns

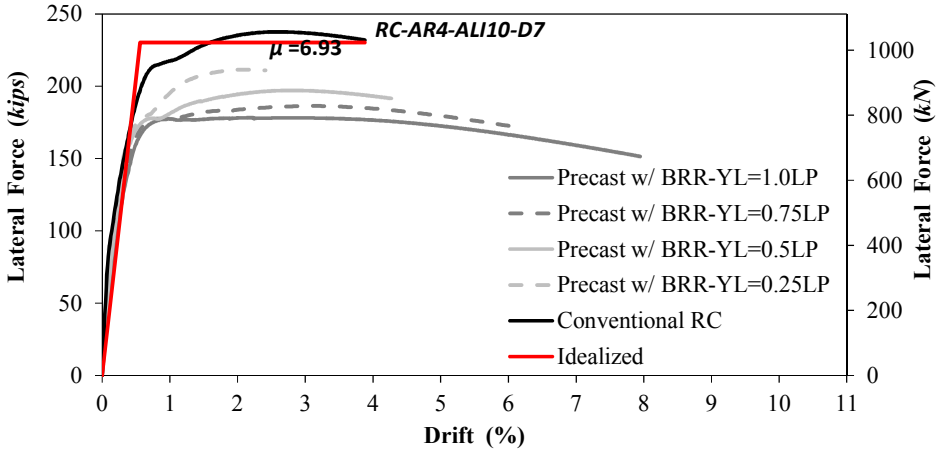

Figure 5-17. Pushover Analysis of RC-AR4-ALI10-D7 and Corresponding Repairable Precast Columns

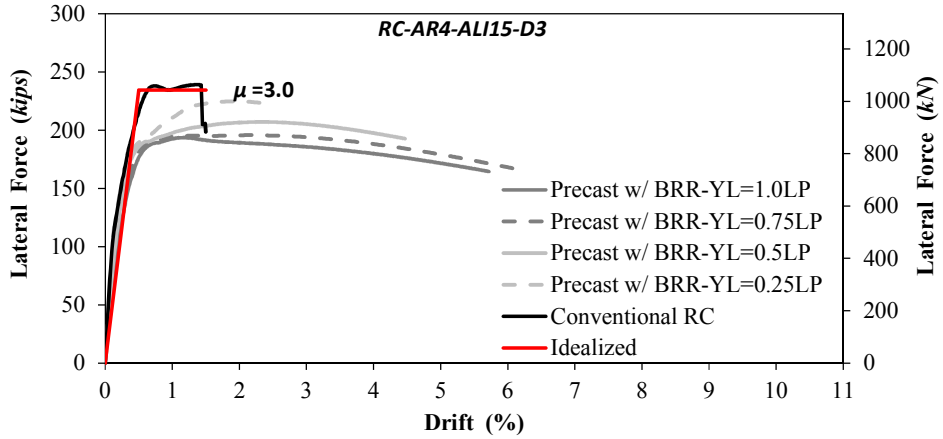

Figure 5-18. Pushover Analysis of RC-AR4-ALI15-D3 and Corresponding Repairable Precast Columns

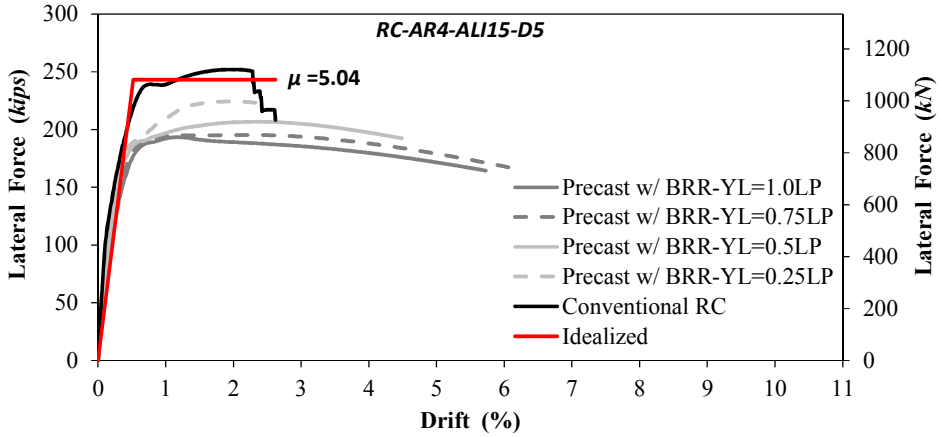

Figure 5-19. Pushover Analysis of RC-AR4-ALI15-D5 and Corresponding Repairable Precast Columns

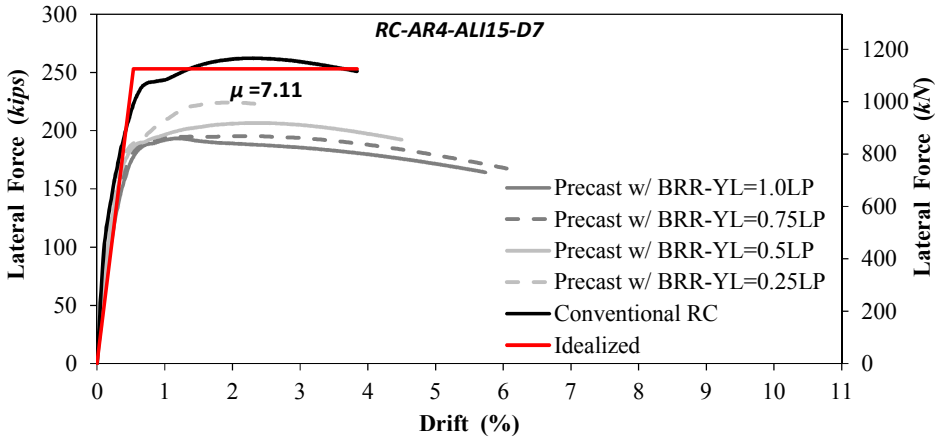

Figure 5-20. Pushover Analysis of RC-AR4-ALI15-D7 and Corresponding Repairable Precast Columns

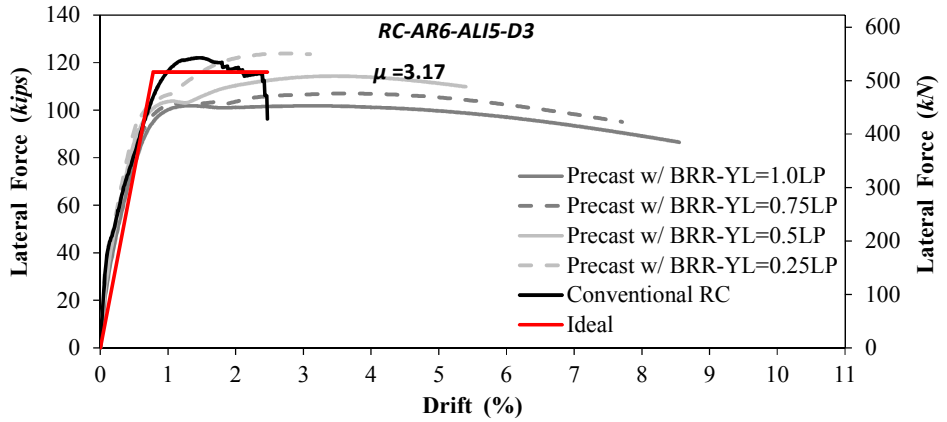

Figure 5-21. Pushover Analysis of RC-AR6-ALI5-D3 and Corresponding Repairable Precast Columns

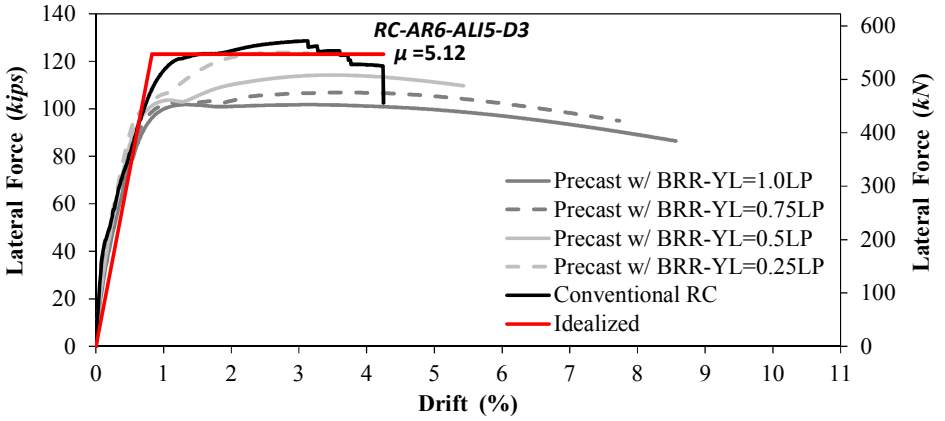

Figure 5-22. Pushover Analysis of RC-AR6-ALI5-D5 and Corresponding Repairable Precast Columns

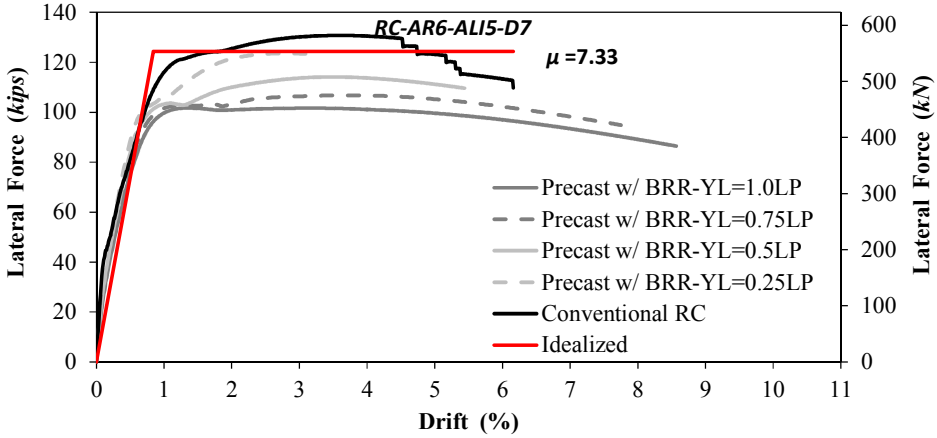

Figure 5-23. Pushover Analysis of RC-AR6-ALI5-D7 and Corresponding Repairable Precast Columns

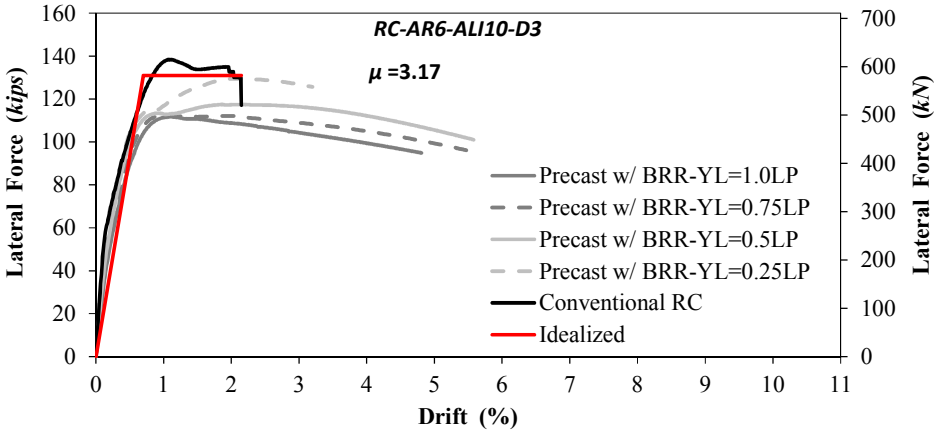

Figure 5-24. Pushover Analysis of RC-AR6-ALI10-D3 and Corresponding Repairable Precast Columns

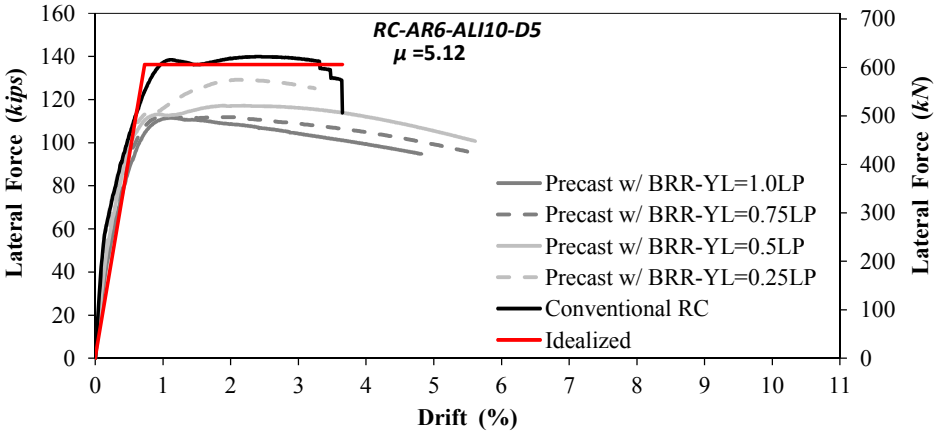

Figure 5-25. Pushover Analysis of RC-AR6-ALI10-D5 and Corresponding Repairable Precast Columns

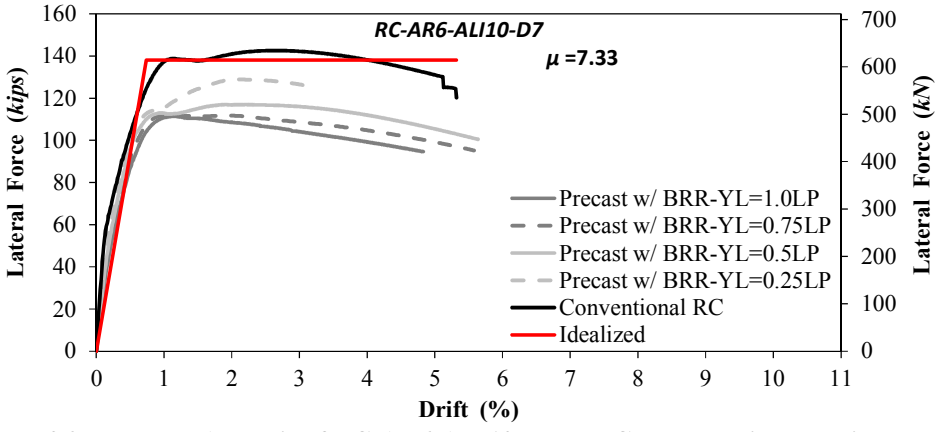

Figure 5-26. Pushover Analysis of RC-AR6-ALI10-D7 and Corresponding Repairable Precast Columns

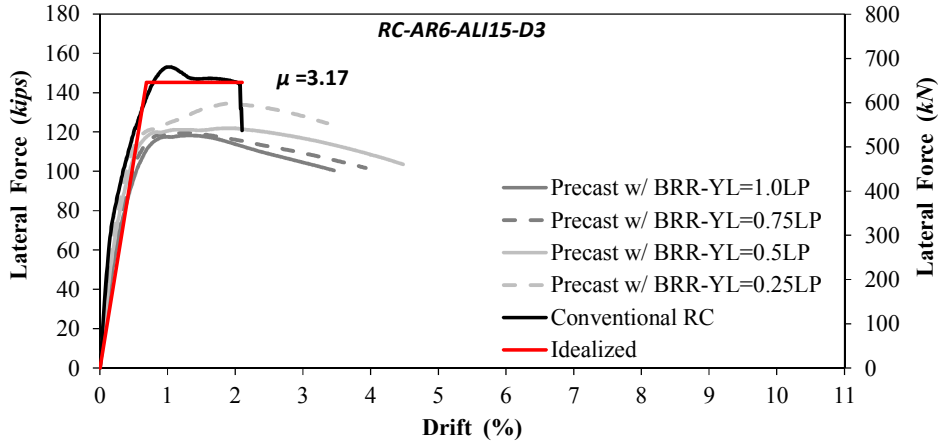

Figure 5-27. Pushover Analysis of RC-AR6-ALI15-D3 and Corresponding Repairable Precast Columns

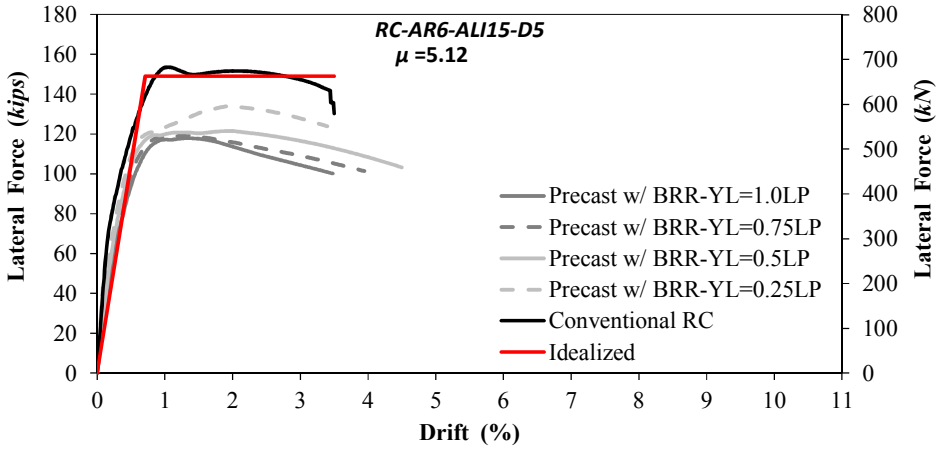

Figure 5-28. Pushover Analysis of RC-AR6-ALI15-D5 and Corresponding Repairable Precast Columns

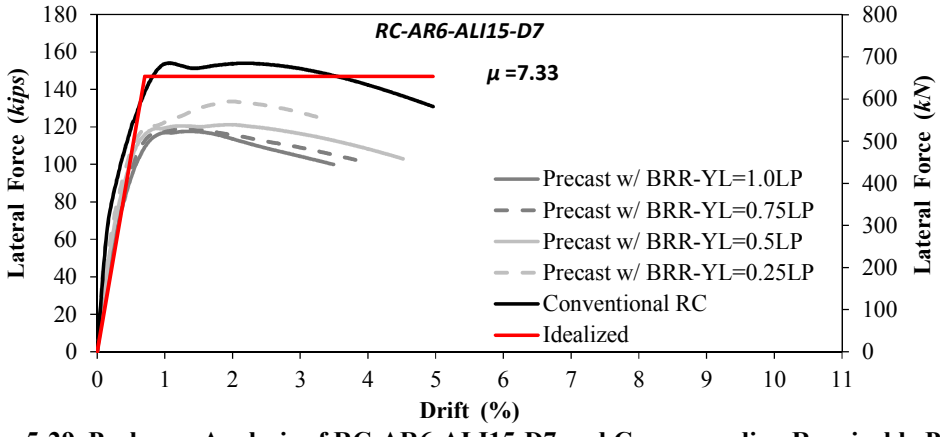

Figure 5-29. Pushover Analysis of RC-AR6-ALI15-D7 and Corresponding Repairable Precast Columns

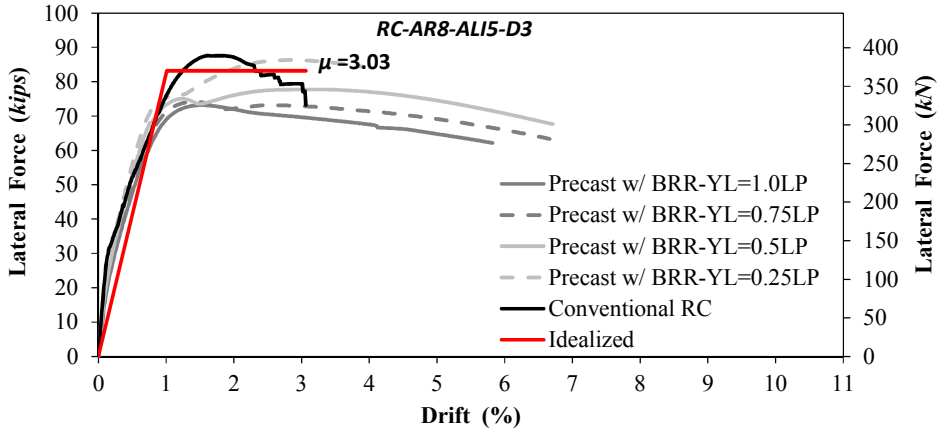

Figure 5-30. Pushover Analysis of RC-AR8-ALI5-D3 and Corresponding Repairable Precast Columns

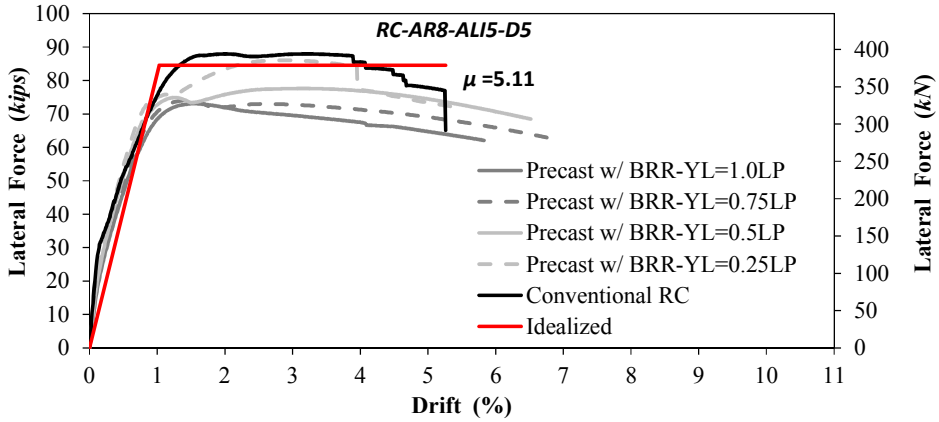

Figure 5-31. Pushover Analysis of RC-AR8-ALI5-D5 and Corresponding Repairable Precast Columns

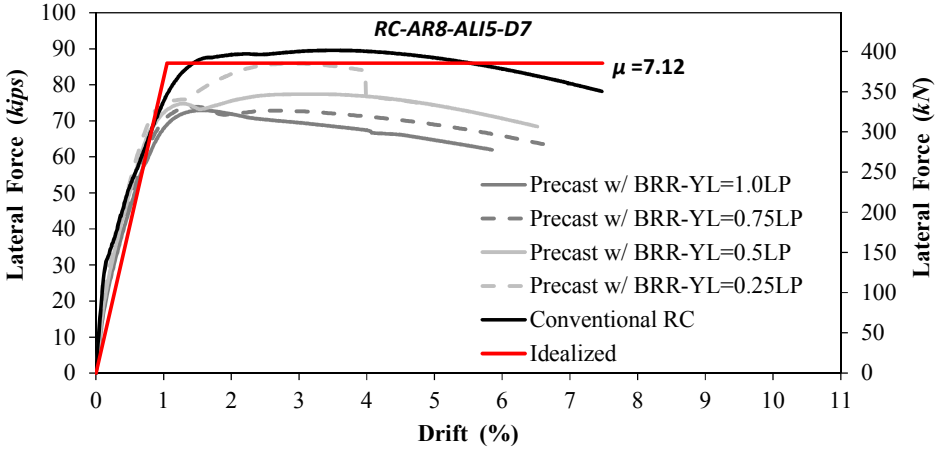

Figure 5-32. Pushover Analysis of RC-AR8-ALI5-D7 and Corresponding Repairable Precast Columns

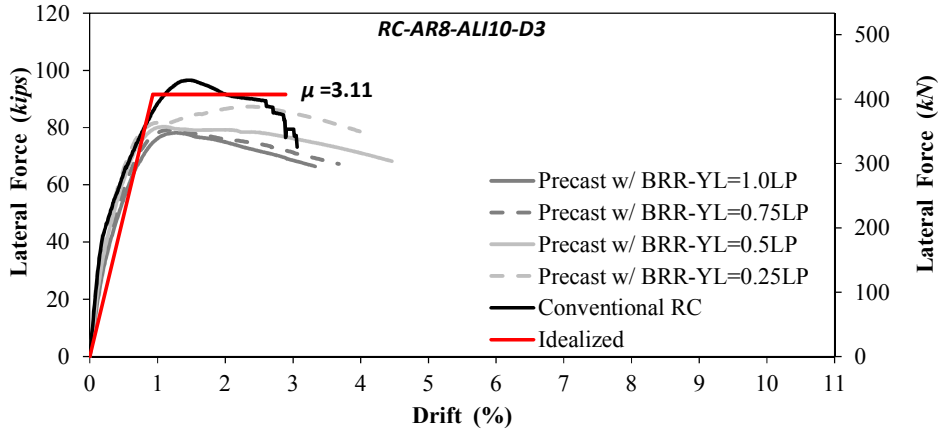

Figure 5-33. Pushover Analysis of RC-AR8-ALI10-D3 and Corresponding Repairable Precast Columns

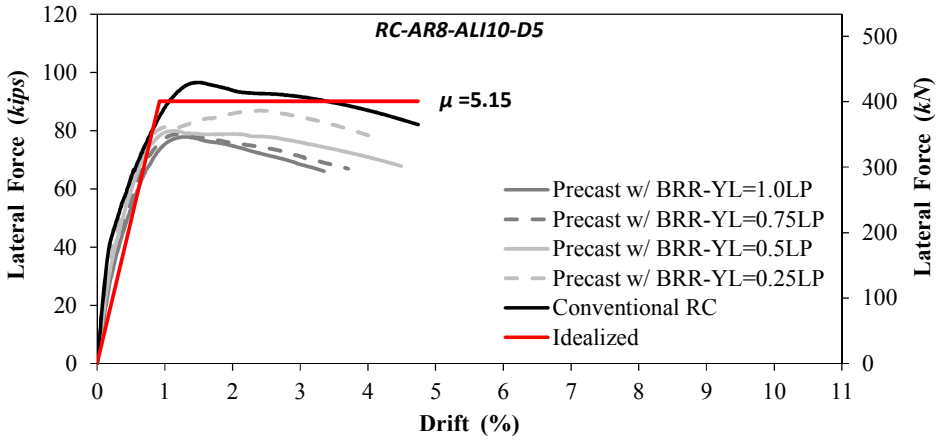

Figure 5-34. Pushover Analysis of RC-AR8-ALI10-D5 and Corresponding Repairable Precast Columns

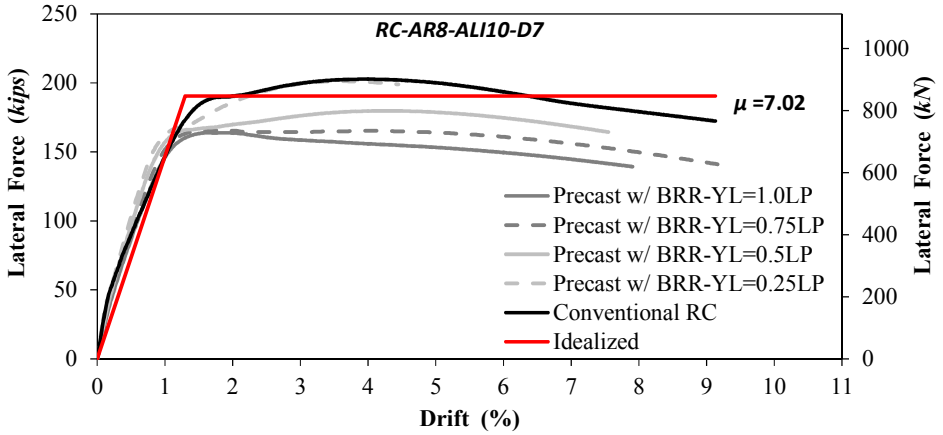

Figure 5-35. Pushover Analysis of RC-AR8-ALI10-D7 and Corresponding Repairable Precast Columns

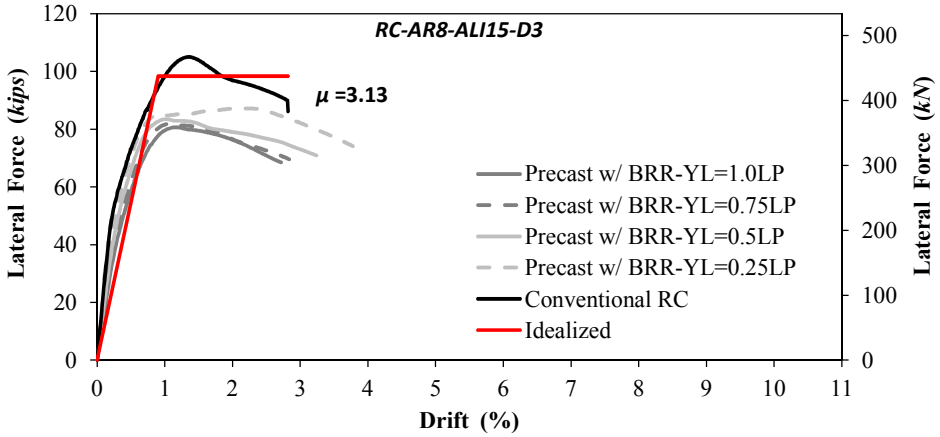

Figure 5-36. Pushover Analysis of RC-AR8-ALI15-D3 and Corresponding Repairable Precast Columns

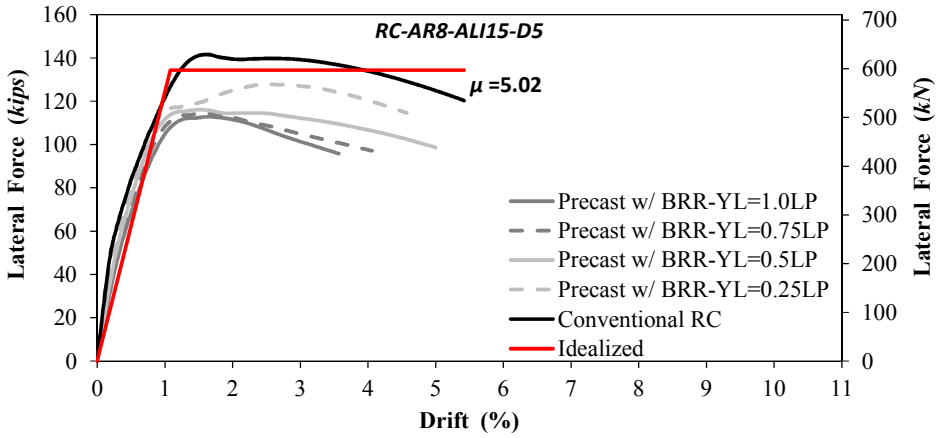

Figure 5-37. Pushover Analysis of RC-AR8-ALI15-D5 and Corresponding Repairable Precast Columns

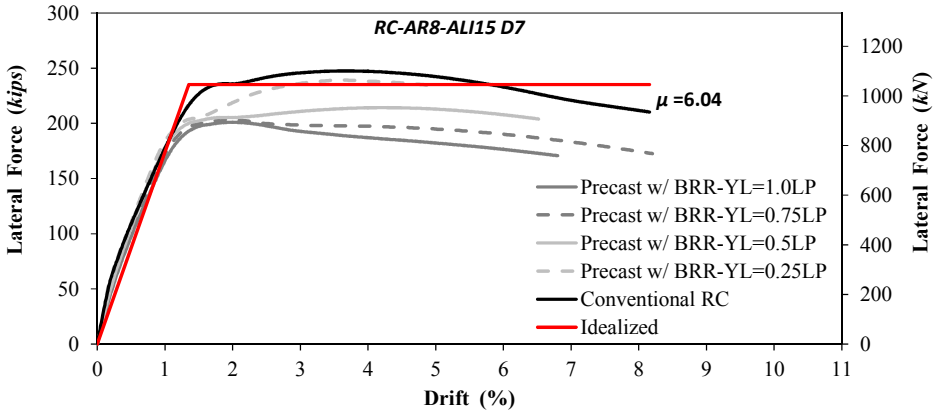

Figure 5-38. Pushover Analysis of RC-AR8-ALI15-D7 and Corresponding Repairable Precast Columns

Another finding was that a large displacement capacity can be achieved in the proposed repairable precast columns regardless of the confinement of the plastic hinge region. In other words, the displacement capacity of the proposed repairable columns is controlled by the yielding length of BRRs not the confinement. For examples, conventional columns of RC-AR4-ALI5-D3 and RC-AR4-ALI5-D5 and RC-AR4-ALI5-D7 (Fig. 5-12 to 5-14) are different because of their transverse reinforcement. *The precast version of these three RC columns is just one column.* It can be seen that the displacement capacities of the repairable precast column exceeded those of the corresponding RC columns when the yielding length of BRR was equal to or higher than $0.5L_p$.

5.6.2 Failure Mode

Table 5-3 presents the analytical failure modes for the reference RC columns as well as the repairable precast columns. It was found that the bar fracture was the dominant mode of failure for the conventional and repairable bridge columns with aspect ratio of 4. For aspect ratio of 6, the common mode of failure for the conventional RC columns was the core concrete failure while fracture of reinforcement was more often for the repairable precast columns. Significant $P-\Delta$ effect was seen for long columns with either conventional or the proposed detailing.

It is worth-mentioning that the failure of the core concrete is eliminated in the proposed repairable precast bridge columns by providing highly confinement at the column ends and by placing a steel plate at the column to adjoining member interface.

5.6.3 Remarks of Analytical Studies

An analytical model was developed in this chapter to investigate the performance of a novel fully precast RC bridge column which can also be repaired quickly with simple

tools. The damage is allowed only in the reinforcement which are restrained against buckling. The buckling restrained reinforcement (BRR) are installed within the plastic hinge region of the columns. The damaged reinforcement can be replaced easily after a severe event without the need of total replacement of the structure since they are connected to the column and the footing reinforcement through detachable mechanical bar splices.

Four different plastic hinge lengths were included in pushover analysis to optimize the length of BRRs. In addition to repairing feature, the analytical studies showed that the displacement capacity of the repairable columns can be four times higher than that of the corresponding reference conventional RC columns. The proposed detailing is most effective in terms of increasing the displacement capacity on the columns with low aspect ratios. For columns with high aspect ratios such as 6 and 8, the novel repairable columns exhibit higher or the same ductility as those of the reference RC columns. Overall, it was found that the precast columns with a BRR yielding length equal to the plastic hinge length exhibit equal to or larger displacement capacities compared to the conventional RC columns.

5.7 Summary and Conclusions

A new construction and design approach was proposed in the present study to improve the seismic performance of RC bridge columns and to accelerate construction. The proposed novel column incorporates (1) pipe-pin connections to transfer plastic shear forces, (2) exposed buckling restrained reinforcement to develop the plastic moment and to be replaced after a severe event, and (3) detachable mechanical bar splices for quick

replacement of damaged buckling restrained reinforcement (BRR). Based on the experimental and analytical investigations, the following conclusions can be drawn:

- The proposed column detailing can increase the displacement capacity of bridge columns by a factor of four or more especially for columns with low aspect ratios and low axial loads.
- Longer yielding lengths for BRR usually results in higher displacement capacities exceeding those of the corresponding conventional RC columns. The yielding (fuse) length does not need to be longer than the analytical plastic hinge length.
- Large displacement capacities can be achieved in the proposed repairable precast columns regardless of the confinement of the plastic hinge region.
- The proposed novel column is fast in construction since all components are prefabricated.
- The proposed novel column is repairable since the damage is limited to the BRR, which can be detached after an event through the use of detachable mechanical bar splices.

Overall, the proposed novel columns are expected to improve the seismic performance of bridges and to expedite the construction. The bridge total replacement after an earthquake will be eliminated since bridge columns are repairable. Large-scale experimental studies are needed to confirm these findings before field deployment.

5.8 References

1. Tazarv, M., and Saiidi, MS. (2014). “Next Generation of Bridge Columns for Accelerated Bridge Construction in High Seismic Zones,” CCEER Report No. 14-

06, Center for Civil Engineering Earthquake Research, University of Nevada, Reno, NV.

2. Zaghi, A., and Saiidi, M.S. (2010). “Seismic Design of pipe pin connections in Concrete Bridges,” Center for Civil Engineering Earthquake Research, University of Nevada, Reno, Nevada. CCEER Report No. 10-01.
3. Mander, J., Priestley, M., & Park, R. (1988). "Observed stress-strain behavior of confined concrete," Journal of structural engineering, 114(8), 1827-1849.
4. Marriott, D., Pampanin, S., and Palermo, A. (2009). “Quasi□Static and Pseudo□Dynamic Testing of Unbonded Post-Tensioned Rocking Bridge Piers with External Replaceable Dissipaters,” Earthquake Engineering & Structural Dynamics, 38(3), 331-354.
5. OpenSees. (2016). “Open System for Earthquake Engineering Simulations,” Version 2.4.1, Berkeley, CA, Available online: http://opensees.berkeley.edu.
6. ASTM Standard A706/A706M-09b (2009). “Standard Specification for Low-Alloy Steel Deformed and Plain Bars for Concrete Reinforcement,” ASTM International, West Conshohocken, PA.

Chapter 6: Summary and Conclusions

6.1 Summary

The main objective of this study was to develop a new precast connection that can accelerate construction of bridges and buildings, can improve their seismic performance, and can quickly repair them through replacement of exposed reinforcement. The following tasks were completed to achieve this objective

First, the feasibility and performance of buckling restrained reinforcement (BRR) that utilizes conventional deformed steel bars without any reduction of the section area were experimentally investigated. Nine BRR samples were tested in a collaboration with Tuhin (2016) to evaluate their uniaxial behavior. Conventional ASTM A706 Grade 60 deformed reinforcing steel bars were utilized in BRR. Various tube and bar lengths and two different bar diameters were included in the tests. Grade 1026 steel tubes were used as confining tubes. Non-shrink grout was utilized as filler material. A simple design method was proposed in the present study for both dog-bone and unreduced diameter BRR and was validated using test data.

Subsequently, the proposed moment-resisting connection was used in precast beam-column specimens and was tested under cyclic loading to investigate its feasibility and seismic performance. Two repairable precast specimens and one reference cast-in place beam-column specimen were constructed and tested. Each precast specimen was

tested twice to exercise the repair by bar replacement method. Each precast specimen was repaired after the first round of testing by simply replacing its buckling restrained reinforcement, BRR, and was retested under the same loading protocol.

Furthermore, the seismic performance of precast building incorporating the proposed connection detailing was analytically investigated. First a modeling method was proposed for the repairable beam-column connection, then the calculated responses of the beam-column test specimens were compared with those measured in the tests, to verify the accuracy of the proposed modeling method. Using the verified method, a comprehensive analytical study including pushover and dynamic analyzes were carried out to investigate the seismic performance of three-, six-, and nine-story precast buildings. The seismic performance of cast-in-place (CIP) buildings was also analytically investigated for comparison.

Finally, the seismic performance of precast bridge columns incorporating the proposed connection detailing was investigated through parametric study. First, the proposed detailing was modified for a column-to-footing connection. Twenty-seven conventional RC and their corresponding repairable precast bridge columns were modeled using OpenSees (2016). Three main variables were included in the design of the RC bridge columns: the axial load index, the aspect ratio, and the target displacement ductility capacity. In addition, four fuse lengths of BRR were included to optimize the length of BRR. The fuse length of BRR was varied with respect to the analytical plastic hinge length.

6.2 Conclusions

6.2.1 Buckling Restrained Reinforcement (BRR)

The following conclusions can be drawn from the experimental and analytical investigations on BRR:

- The total axial gap between the support and BRR tube significantly affects the overall performance of BRR.
- The strain of BRR corresponding to its peak stress can exceed 5%, which will be sufficient in most practical cases since the strain of compressive reinforcement in a concrete section is usually controlled by the core concrete strains.
- Bar length can affect the overall BRR stress and strain capacities in a way that shorter bars provide higher compressive capacities than longer bars.
- Tube thickness has insignificant effect on the BRR performance if the tube is designed properly according to the proposed design method.
- The proposed BRR design method is conservative and may be used for the design of dog-bone or unreduced BRR.

6.2.2 Repairable Precast Beam-Column Specimens – Experimental Study

The following conclusions can be drawn from the experimental study:

- No damage was observed in the plastic hinge regions of the precast specimens.
- The precast beam with improved detailing had insignificant concrete damage even at 13.5 times the design level earthquake.
- The displacement capacity of all precast specimens was higher than that in CIP.

- The lateral load carrying resistance of the precast specimens were lower than that in CIP at the same drift ratios due to lower reinforcement ratio and the reduced beam depth at the neck region.
- The initial stiffnesses of the precast specimens were lower than that in CIP due to the nature of the proposed detailing and the vertical gap between the steel pipe and the steel socket (cup) at the beam-column interface.
- All precast specimens showed lower residual displacements than those in CIP.
- The residual drift ratio for SMA reinforced precast specimen was less than 1%, which is insignificant. SMA will be able to bring back the building to its original position after severe earthquake.
- Building total replacement is prevented using the proposed method. Precast buildings can withstand severe earthquakes with minimal damage and ability to be repaired afterwards by replacing the damaged reinforcement.

6.2.3 Repairable Precast Buildings – Analytical Study

Based on the analytical study, the following conclusions can be drawn:

- The new precast beam-column connection can increase the displacement capacity of precast buildings by a factor of three or more if BRR with a fuse length of 75% of the precast beam height are used.
- Longer BRR fuse lengths results in higher displacement capacities exceeding those of the corresponding conventional RC frames.
- Pushover analyses showed that the initial stiffness of the proposed precast buildings is 42% lower than that in CIP, on average.

- The repairable frames can withstand severe earthquakes with at least 30% reserved displacement capacity.
- The dynamic analysis showed that displacement (or story drift) demands of the repairable precast buildings is 21% higher than those in CIP, on average. Nevertheless, the story drift demands for three- and six-story precast frames were always within the ASCE limit indicating that this frame is sufficient even without increasing the neck depth or the BRR sizes.

Overall, the proposed novel precast buildings will exhibit improved seismic performance, higher displacement capacities, and lower damage compared to CIP buildings. The precast buildings can be simply repaired after severe earthquakes by replacing BRR.

6.2.4 Repairable Precast Bridge Columns – Analytical Study

The following conclusions can be drawn from the analytical findings:

- The proposed column detailing can increase the displacement capacity of bridge columns by a factor of four or more especially for columns with low aspect ratios and low axial loads.
- Longer fuse lengths for BRR usually results in higher displacement capacities exceeding those of the corresponding conventional RC columns.
- Large displacement capacities can be achieved in the proposed repairable precast columns regardless of the confinement of the plastic hinge region.
- The proposed novel column will be fast in construction since all components are prefabricated.

- The proposed novel column is repairable since the damage is limited to the BRR, which can be detached after an event through the use of detachable mechanical bar splices.

Overall, the proposed novel bridge column is expected to improve the seismic performance of bridges and to expedite the construction. The bridge total replacement after an earthquake is eliminated since bridge columns are repairable. Large-scale experimental studies are needed to confirm these findings before field deployment.

Appendix A: Design of Shear-Pin

The shear-pins were design following the guideline proposed by Zaghi and Saiidi (2010). The design of shear-pins used in the beam-column specimens is listed here in

Known Information:

F_y = 40 ksi

F_{ys}= 60 ksi

F_c =5 ksi

B = 10 in.

D_P = 2.25 in.

T_P = 0.5 in.

$D_{Bearing}$ = 8 in.

A_{sp1} = 0.05 in. (#2)

A_{sp2} = 0.11 in. (#3)

S_1 = 5 in.

S_2 = 2 in.

D_1 = 6.5 in.

$D_2 = 3D_P = 3\times2.25 = 6.75$ in.; (use 6 in.)

$G = D_P/20 = 0.125$ in. use (1/8)

$M_u = 1.45 \times F_y \times (r_1^3 - r_2^3) = 1.45*40*(1.125^3 - 0.625^3) = 68.42$ K-in

$H_0 = 1.17 \times \sqrt{Mu \times Dp \times Fc} = 1.17*\sqrt{68.42 * 2.25 * 5}. = 32.46$ kips

- Upper Limit Lateral Load Capacity, H_{cr}:

Factor 1 $= 0.45 \times \frac{DBEARING}{B} + 0.6 = 8/10 + 0.6 = 0.96$

$A_C = 10*8.25 - \frac{\pi \times D2}{4} = \frac{2.25^2 * \pi}{4} = 78.52$ in^2

$H_{cr} = \text{Factor1} \times (0.16 \times A_C \times \sqrt{fc} + \frac{A_{sp1} \times F_{ys} \times D_1}{S_1}) + \frac{A_{sp2} \times F_{ys} \times 2}{S_2} + \frac{1.45 \times M_u}{D_{Bearing} + D_p}$

$= 0.96 \times (0.16*78.52 \times \sqrt{5} + \frac{0.05 \times 60 \times 6.5}{5}) + \frac{0.11 \times 60 \times 6}{2} + \frac{1.45 \times 68.42}{8+2.25} = 60.19$ kips

$N_a = \text{Factor1} \times A_C = 0.96 \times 78.52 = 75.37$

- Ultimate Capacity, H_n:

$H_n = H_0 + (H_{cr} - H_0) \times \frac{N}{Na} = 32.46 + (60.19 - 32.43) \times 0/75.37 = 32.46$ kips

$F_{impact} = 1.9 \times \frac{G \times EI}{Lc3} = 1.9 \times \frac{1*29000*1.138}{16*37.5^3} = 0.074$

Ø $H_n = V_0 + F_{impact}$

$V_0 = 0.75 \times 32.46 - 0.074 = 24.27$ kips > 16 kips (maximum shear force in beam-column connection specimens).

Appendix B: Design Guidelines for Repairable Precast Moment-Resisting Buildings

A novel repairable moment-resisting connection is developed for precast buildings and bridge columns. The connection (Fig. B-1) for buildings generally consists of (1) fully precast beams and columns with exposed longitudinal reinforcement, (2) a shear-pin made of steel pipe to be inserted into a steel cup, (3) mechanical bar splices that can be detached, (4) external reinforcement restrained against buckling (BRR) to connect the precast beam reinforcement to the column reinforcement, and (5) a steel plate between the precast column and the beam to prevent damage during lateral deformations.

Figures B-2 and B-3 show two practical detailing alternatives for repairable precast buildings. Both have all of the aforementioned components, but a fixed pipe is embedded in the column in Fig. B-2, which will be locked in the beam channel. A sliding pipe is used at the end of the precast beam in the second alternative (Fig. B-3) to be inserted into the column steel cup (sockets). The connection in Alternative No. 1 is completed by laterally sliding the precast beam. The connection using Alternative No. 2 is completed by placing the precast beam between the precast columns then sliding the pipe into the column steel cups (sockets).

Design guidelines and commentary are presented in this appendix for the repairable connections suited for precast buildings.

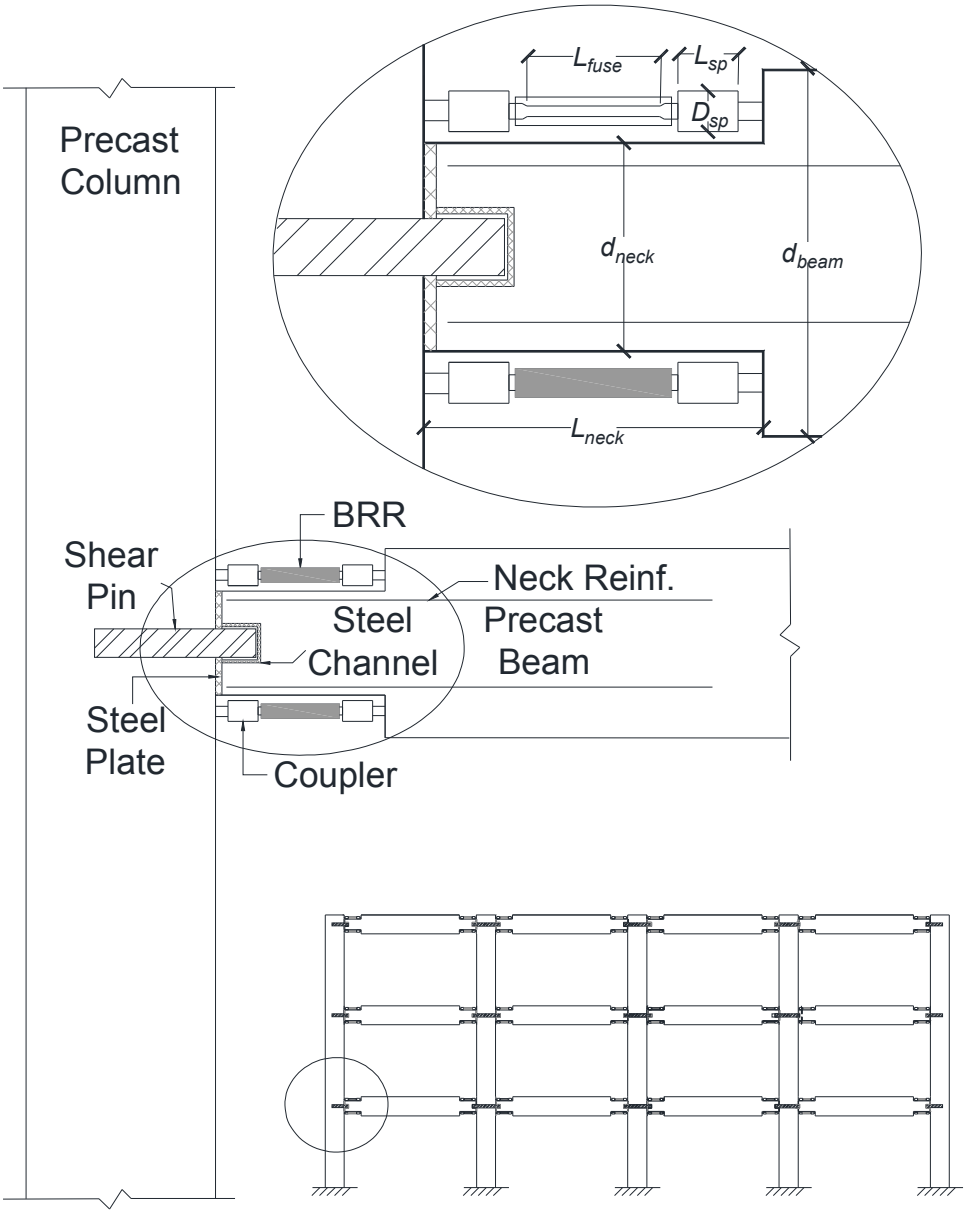

Figure B-1. Components of Repairable Precast Beam-Column Connections

Notations:
L_{neck}: The length of precast beam neck
L_{fuse}: The BRR fuse length
L_{sp}: The length of mechanical bar splice (or coupler)
D_{sp}: The diameter of mechanical bar splice (or coupler)
d_{neck}: The depth of precast beam neck
d_{beam}: The depth of the original precast beam/conventional CIP beam

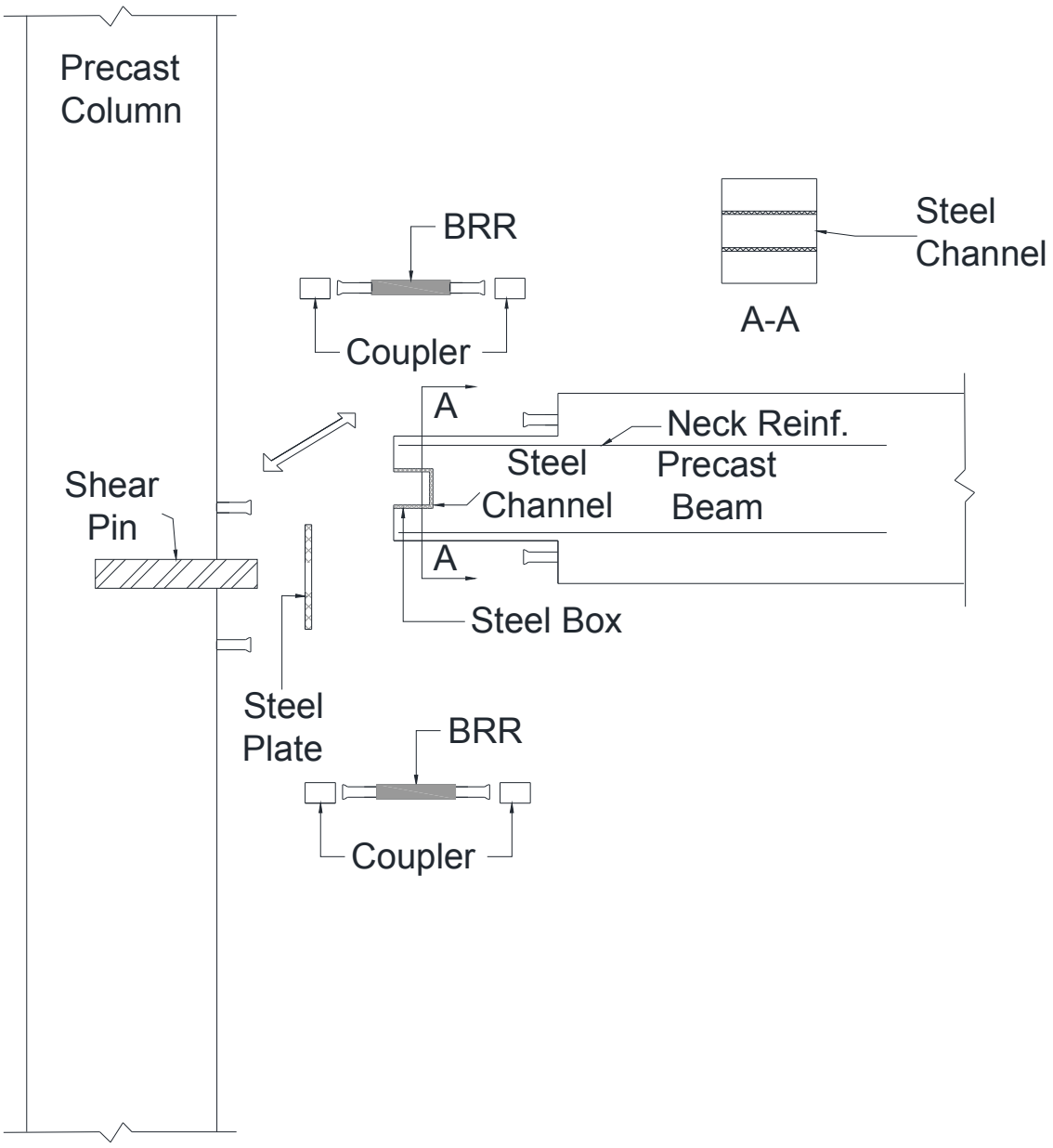

Figure B-2. Detailing Alternative No. 1 for Repairable Precast Buildings

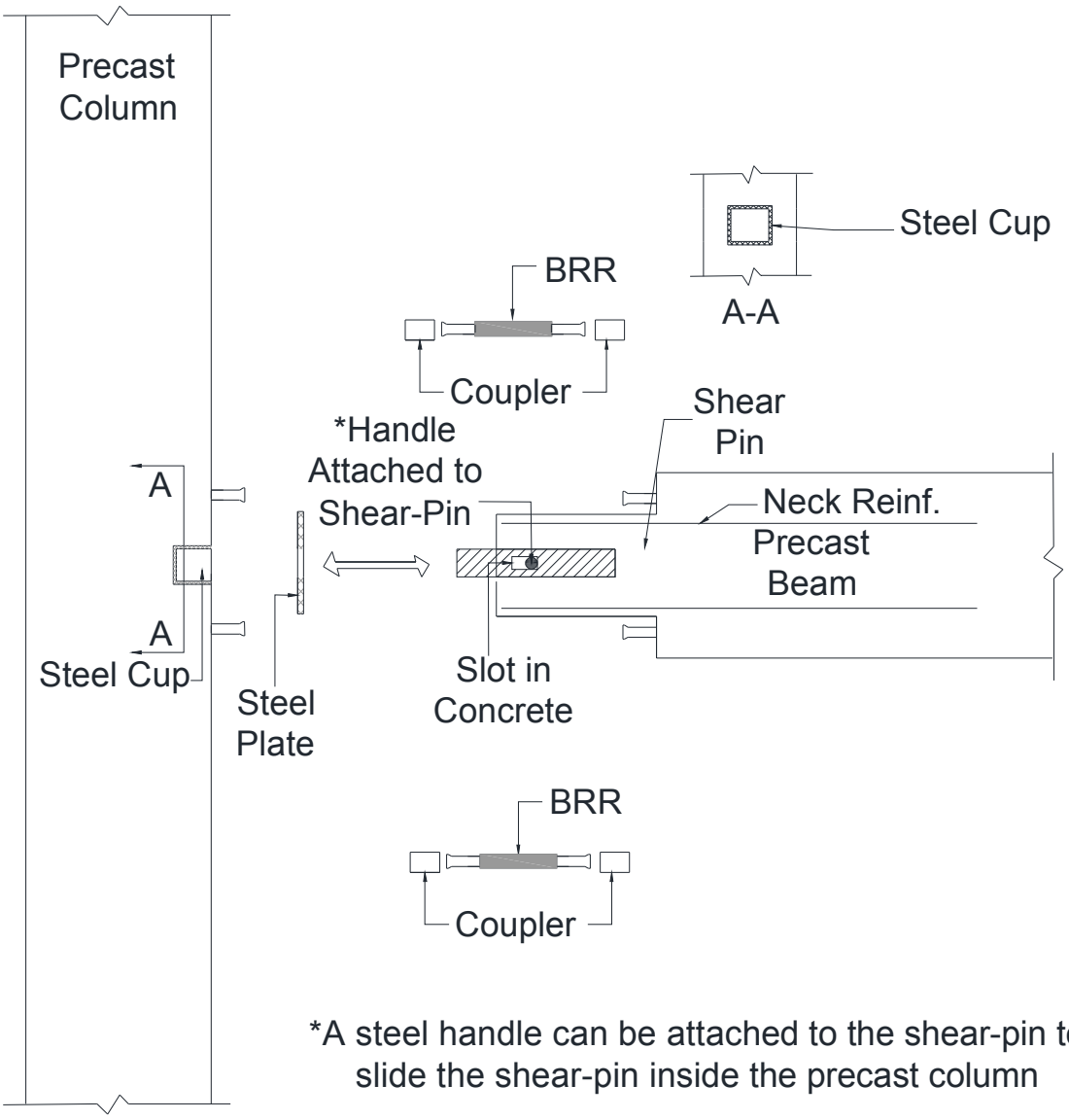

Figure B-3. Detailing Alternative No. 2 for Repairable Precast Buildings

Recommendations and Commentary

R.1. All structural members including beams and columns shall be designed according to current codes.

C.1. A cast-in-place building shall be designed first satisfying all current code requirements and then to be converted into a precast building following the recommendation listed in this guideline. All components can be designed according to current ASCE 7 and ACI318.

R.2. The neck length (L_{neck}) shall not be less than the BRR fuse length (L_{fuse}) plus four times the length of the coupler (L_{sp}). The neck depth (d_{neck}) shall not be less than the depth of the original beam (d_{beam}) less three times the coupler diameter (D_{sp}).

C.2. The geometry of the neck region should accommodate BRR, couplers, and bars beyond couplers.

R.3. The neck region reinforcement shall be designed to resist 1.25 of the plastic moment of the original beam and shall be developed inside the beam for a distance meeting current code development length requirement.

C.3. The neck region should remain capacity protected with minimal damage.

R.4. The precast beam longitudinal reinforcement shall be debonded from the concrete for a distance of $6d_b$.

C.4. Debonding of beam longitudinal reinforcement can be done by wrapping the bars with two layers of duct tape beyond the beam depth change inside the beam.

R.5. The BRR fuse length, which is defined as the length of the yielding portion of BRR, shall not be less than 0.25 the original (unreduced) depth of the precast beam (d_{beam}) and not to exceed 0.75 the depth of the precast beam (d_{beam}).

C.5. BRR fuse with a length of 0.25 the depth of the precast beam (d_{beam}) is recommended since this BRR fuse length can provide sufficient displacement capacity exceeding that in corresponding cast-in-place buildings.

R.6. The BRR fuse reinforcement area on the top and bottom of precast beams shall not be less than the top and bottom longitudinal reinforcement of the corresponding conventional cast-in-place beams at the same location. In addition, the reinforcement adjacent to BRR fuse reinforcement should have areas larger than the BRR fuse reinforcement areas to ensure the yielding within BRR fuse region.

C.6. The top and bottom longitudinal reinforcement (BRR fuse areas) in precast beam shall match the reinforcement design requirement to provide sufficient flexural strength.

R.7. Shear-pin and steel cup/socket should be designed in accordance with the guidelines proposed by Zaghi and Saiidii (2010).

C.7. Shear-pin details should provide sufficient strength to remain linear elastic.

R.8. Steel plates with a minimum thickness of 0.5 in. shall be placed at any beam-column interface to prevent concrete damage during lateral deformations.

C.8. Steel plates provide more uniform stress distribution at the beam-column interface and will minimize the concrete damage.

References

1. ASCE Standard (2010). “Minimum Design Loads for Buildings and Other Structures,” American Society of Civil Engineers (ASCE), 1801 Alexander Bell Drive, Reston, Virginia 20191.
2. American Concrete Institute (ACI) Committee 318 (2014). “Building Code Requirements for Structural Concrete and Commentary,” ACI 318-14, ACI, Farmington Hills, MI.
3. Zaghi, A., and Saiidi, M.S. (2010). “Seismic Design of pipe pin connections in Concrete Bridges,” Center for Civil Engineering Earthquake Research, University of Nevada, Reno, Nevada. CCEER Report No. 10-01.